Multi-Target Tracking with Phased Arrays : application to sonar bathymetry reconstruction

Augustin Alexandru Saucan

THÈSE / Télécom Bretagne
sous le sceau de l'Université européenne de Bretagne

pour obtenir le grade de Docteur de Télécom Bretagne
En accréditation conjointe avec l'Ecole Doctorale Sicma
Mention : Sciences et Technologies de l'Information et de la Communication

présentée par
Augustin Alexandru SAUCAN
préparée dans le département Image et Traitement de l'Information
Laboratoire Labsticc

Multi-Target Tracking with Phased Arrays: application to sonar bathymetry reconstruction

Thèse soutenue le 1er Décembre 2015
Devant le jury composé de :

Philippe Vanheeghe
Professeur, Ecole Centrale Lille / président

Sylvie Marcos
Directrice de recherche, LSS - Supelec – Gif/Yvette / rapporteur

Jérôme Mars
Professeur, GIPSA-lab - INP Grenoble / rapporteur

Ba-Ngu Vo
Professeur, Curtin University - Australie / examinateur

Philippe Pouliguen
Ingénieur de recherche, DGA/DS/MRIS – Paris / examinateur

Thierry Chonavel
Professeur, Télécom Bretagne / examinateur

Christophe Sintes
Directeur d'études, Télécom Bretagne / examinateur

Jean-Marc Le Caillec
Professeur, Télécom Bretagne / directeur de thèse

Dominique Fattaccioli
Expert DGA, DGA - Toulon / invité

Myriam Chabah
Ingénieur, Thales Underwater Systems - Brest /invitée

N° d'ordre : 2015telb0379

Sous le sceau de l'Université Européenne de Bretagne

Télécom Bretagne

En accréditation conjointe avec l'École Doctorale – Sicma

Multi-target Tracking with Phased Arrays: application to sonar bathymetry reconstruction

---

Thèse de Doctorat

Mention : STIC – Sciences et Technologies de l'Information et de la Communication

Présentée par **Augustin-Alexandru SAUCAN**

Département : Image et traitement de l'information

Laboratoire : Lab-STICC Pôle : Connaissance Information Decision

Soûtenu le 01 Décembre 2015 devant la Commission d'Examen composée de :

M. Philippe Vanheeghe - *Professeur Ecole Centrale Lille* (President)
Mme. Sylvie Marcos - *Directrice de recherche CNRS SUPELEC* (Rapporteur)
M. Jérôme Mars - *Professeur INP Grenoble* (Rapporteur)
M. Ba-Ngu Vo - *Professeur Curtin University, Australie* (Examinateur)
M. Jean-Marc Le Caillec - *Professeur Telecom Bretagne* (Directeur)
M. Thierry Chonavel - *Professeur Telecom Bretagne* (Examinateur)
M. Christophe Sintes - *Directeur d'études Telecom Bretagne* (Examinateur)
M. Philippe Pouliguen - *Ingénieur de recherche DGA* (Examinateur)
M. Dominique Fattaccioli - *Ingénieur de recherche DGA* (Invité)
Mme. Myriam Chabah - *Ingénieur Thales Underwater Systems* (Invitée)

Contents

List of Figures

List of Tables

Abbreviations and nomenclature

MSE	Mean Squared Error
MMSE	Minimum Mean Squared Error
MAP	Maximum A Posteriori
ULA	Uniform Linear Array
TWS	Track While Scan
TBD	Track Before Detect
PDA	Probabilistic Data Association
PDAF	Probabilistic Data Association Filter
IPDAF	Integrated Probabilistic Data Association Filter
IMM	Interacting Multiple Models
JPDAF	Joint Probabilistic Data Association Filter
JIPDAF	Joint Integrated Probabilistic Data Association Filter
NN-PDAF	Nearest Neighbor Probabilistic Data Association Filter
NN-IPDAF	Nearest Neighbor Integrated Probabilistic Data Association Filter
FHB	Flat and Horizontal Bottom
VO	Vertical Object
RW	Random Walk
UKF	Unscented Kalman Filter
PF	Particle Filter
IS	Importance Sampling
PHD	Probability Hypothesis Density
CPHD	Cardinalized Probability Hypothesis Density
PP	Point Process
RFS	Random Finite Set
OSPA	Optimum SubPattern Analysis
DBSCAN	Density-Based Spatial Clustering of Applications with Noise

The following notations are employed in this work:

$\mathbf{x}$	vector
$\mathbb{X}$	Space of vector $\mathbf{x}$
$\mathbf{X}$	matrix
X	set or point process

Acknowledgements

Anything I say. What a wonderful philosophy ...

Toecutter, *Mad Max, 1979*

During the three years of my PhD studies, I enriched my knowledge in the signal processing domain and acquired valuable research experience. All of these would not have been possible without the contribution of several persons with whom I have interacted during this period. First of all I have to thank my supervisors Christophe and Thierry for introducing me the subject of my PhD and for finding the funding necessary to conduct these three years of research. Furthermore, I would like to thank my supervisors for their advice and help throughout my PhD. Additionally, I thank my PhD director, Jean-Marc, whose guidance was detrimental to my work.

I conducted my research within the *Image and Information Processing Department*. I would like to thank all of my colleagues from the department for the pleasant moments and conversations we enjoyed together.

I am truthfully grateful to Mme. Sylvie Marcos and M. Jérôme Mars for undertaking the difficult task of reviewing my PhD dissertation and to M. Ba-Ngu Vo, M. Philippe Pouliguen, M. Dominique Fattaccioli and Mme. Myriam Chabah for taking part in my defense jury. Furthermore, I thank M. Philippe Vanheeghe for presiding the defense jury. I also thank the French *Direction Générale de l'Armement (DGA)* and the *Carnot Institute* for their financial support throughout my thesis.

I thank Aimée Johansen, Mary Daley, André Le Saout and Julien Schrek for their advice and help in the editing and writing of scientific papers.

The sonar data processed in this work was obtained with an EdgeTech 4600 side-scan sonar. We are grateful toward EdgeTech for supplying us with the sonar data and to Lisa Brisson, Steve Wright and Nick Lawrence for their scientific expertise.

Last but not least, I would like to thank my parents whose enduring love and nurturing formed me into the person I am today. Another big factor in my formation was played by the professors I had at Télécom Bretagne and at the Polytechnic University of Timisoara. I express my gratitude toward them. I thank my friends from Brest for the nice *soirées* spent together. I also thank Ramona for her support and for giving me enough time to work peacefully.

Résumé

Nature does not offer her problems ready formulated. They must be dug up with pick and shovel, and he who will not soil his hands will never see them.

John L. Synge

Mathematics : The Loss of Certainty

Contexte

Le système de transport maritime, défini comme l'union des ports, canaux et cours d'eau, est le pilier du commerce au niveau mondial. En 2005, 90% (par volume) du commerce international a été effectué par voie maritime [1]. Plus récemment, la sécurité portuaire et maritime a émergé comme une partie significative de la sécurité mondiale [2]. Le système de transport maritime a été conçu pour être efficace et rapide, ainsi toute perturbation amenée à ce système peut conduire à des pertes économiques importantes et/ou des pertes en vies humaines. En [2] un exemple à ce titre à été donné : la fermeture des ports sur la coté ouest des États Unis, pendant 5 jours consécutifs, entraînera des pertes de plus de 1 milliard US$. La plupart des analyses de sécurité montre les vulnérabilités des zones portuaires aux potentielles attaques qui pourront bloquer le port et causer des pertes économiques et en vies humaines. Comme souligné en [2], cela pourrait être obtenu par le naufrage de grands navires, tels que des porte-conteneurs, des navires de transport de gaz liquéfié ou même des ferries. Par conséquent, une attention très importante doit être apportée à l'inspection et l'imagerie des zones sous-marines dans les ports ainsi que dans les voies navigables.

Les systèmes sonar et des autres capteurs sous-marins sont de plus en plus employés pour la sûreté portuaire et la détection des intrusions [3–5], avec une prévalence pour les systèmes de sonar latéral acquérant des images sous-marines de haute qualité et à un prix abordable. Tous les sonars d'imagerie sont des systèmes actifs, ce qui signifie qu'ils émettent un signal et enregistrent le signal rétrodiffusé par l'environnement sous-marin. En effet, les sonars à balayage

latéral fournissent des images, de haute résolution, de l'amplitude du signal rétrodiffusé par fond marin. Par exemple, 6 cm pour la résolution en distance du sonar EdgeTech 4600 [6]. D'ailleurs les capacités de résolution des sonars latéraux peuvent être améliorées avec un traitement à synthèse d'ouverture [7, 8]. Des images provenant de systèmes sonar à balayage latéral à haute résolution sont nécessaires pour la détection des mines et des dispositifs explosifs improvisés [9]. La reconstruction en trois dimensions (3D) du fond marin, représentée par des cartes de profondeur (appelée aussi bathymétrie), est plus complexe et s'effectue traditionnellement avec l'aide des antennes sonars aux capteurs déphasés.

Dans les eaux profondes, la bathymétrie est habituellement réalisée avec des sondeurs multifaisceaux [10], qui sont constitués de deux réseaux des capteurs déphasés linéaires et orthogonaux. Tandis que dans les eaux peu profondes, comme les ports et les canaux, la bathymétrie est habituellement obtenue avec des sonars bathymétriques à balayage latéral [11, Ch.3.3.1], avec un unique réseau des capteurs linéaires. Pour un sonar bathymétrique latéral, un cycle émission réception (appelé *ping*) est présenté dans la Figure 1.

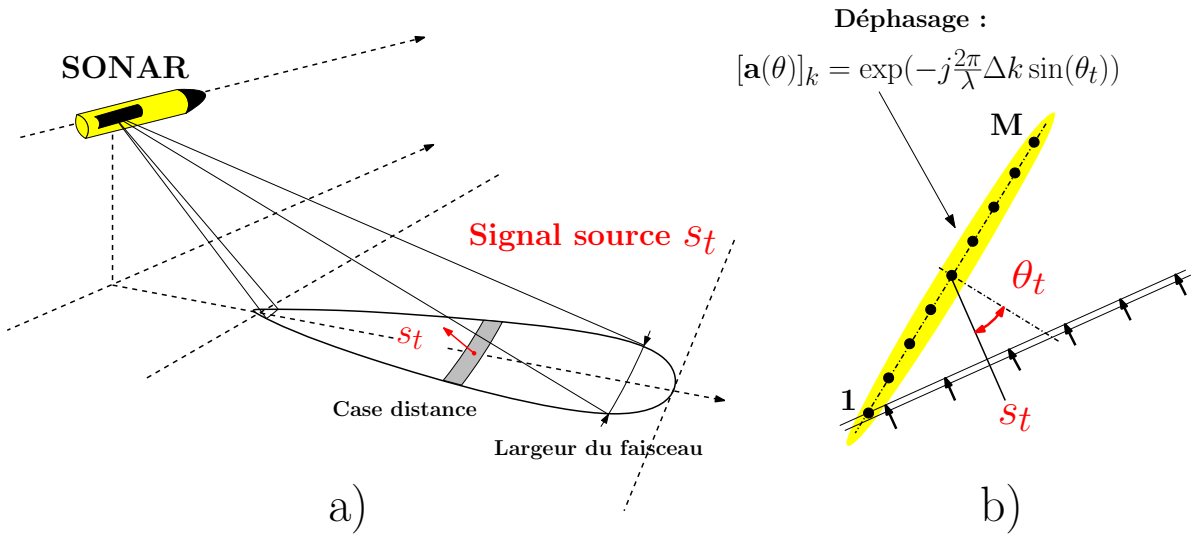

FIGURE 1 : Principe de l'imagerie sous-marine par sonar : a) Géométrie de la fauchée d'émission et le signal rétrodiffusé. b) Antenne réceptrice du sonar avec DOA du signal rétrodiffusé.

Un tel sonar est conçu pour insonoriser une fauchée fine sur le fond (ouverture à 1^o pour l'antenne EdgeTech 4600) et d'enregistrer le signal rétrodiffusé. L'allure de cette fauchée est présentée dans la Figure 1 a), où pour chaque instant d'échantillonnage t, la case distance correspondante génère un signal rétrodiffusé s_t, appelé signal source. L'antenne réceptrice contient M capteurs déphasés qui enregistrent le signal source s_t. Le retard et le déphasage du signal reçu par chaque capteur (par rapport au premier capteur) dépendent de l'angle d'arrivé (DOA) du signal source θ_t. On définit la trajectoire DOA de l'écho du fond comme la série temporelle des DOA θ_t des signaux sources rétrodiffusés tout au long de la fauchée sonar. La courbe de cette trajectoire DOA est modulée par le relief du fond contenu dans la fauchée sonar. Ainsi, la bathymétrie est obtenue par la triangulation (i.e. estimation DOA) de l'écho rétrodiffusé par des cibles étendues comme le fond marin ou diverses structures [12], [10]. L'interférométrie ainsi que des autres méthodes de traitement d'antenne sont employées pour estimer la DOA de la cible visée. La bathymétrie est ensuite obtenue par l'inversion de la relation entre le relief du fond et la trajectoire DOA, comme détaillé dans la Section II.1.

Il est à noter que aujourd'hui il y a une demande croissante pour des sonars bathymétriques à balayage latéral qui peuvent effectuer à la fois de l'imagerie 2D de l'amplitude rétrodiffusée

et de la reconstruction bathymétrique en 3D simultanément, sans la nécessité d'un recalage ultérieur, ce qui représente un avantage majeur dans les applications de détection de mines.

Les principaux défis

Les travaux menés dans cette thèse sont destinés à améliorer la poursuite des cibles multiples avec des antennes sonars aux capteurs déphasés pour atteindre une meilleure reconstruction du relief pour les eaux peu profondes. Les données réelles utilisées dans cette étude sont obtenues avec le sonar bathymétrique à balayage latéral EdgeTech 4600. Ces données ont été acquises dans un environnement peu profond, plus précisément dans le port des Everglades à Fort Lauderdale en Floride, USA. Les défis majeurs abordés dans notre travail seront présentés dans la suite.

- Les environnements marins peu profonds sont des milieux de propagation encombrés, qui présentent une propagation à trajets multiples et réverbération, ce qui limite l'efficacité des méthodes de traitement d'antenne classiques [13–15]. Comme indiqué dans le Chapitre II de cette thèse, la surface de la mer joue un rôle important dans la génération des multi-trajets. Le signal rétrodiffusé par le fond marin se propage à travers le guide d'onde formé entre les deux surfaces : le fond marin et la surface d'eau. La propagation du signal source, par un tel guide d'onde, génère plusieurs répliques : l'écho direct, des reflets ayant des DOAs distinctes et de la réverbération avec DOA diffuses. Les reflets et la réverbération représentent des interférences, la composante de réverbération étant considérée comme du bruit, tandis que les reflets cohérents sont modélisés comme des signaux sources à DOA distinctes. D'ailleurs, en fonction du phénomène de dispersion, les reflets et la réverbération montrent divers degrés de dépendance sur le signal de la source d'origine.

- Une autre difficulté provient de la non-stationnarité des signaux sources. En effet, pour l'estimation des positions des cibles cinématiques ou des échos bathymétriques, le signal antenne est un processus stochastique non-stationnaire. Dans la bathymétrie, les signaux d'intérêt sont les signaux rétrodiffusés par le fond marin ou par un certain objet d'intérêt. En conséquence, les caractéristiques des signaux sources, notamment leur DOA, évoluent avec le profil de l'environnement sous-marin. On peut dire que la trajectoire DOA de l'écho du fond est modulée par le relief du fond marin contenu dans la fauchée sonar. Cela est vrai même pour les surfaces horizontales et plates, où la trajectoire DOA de l'écho rétrodiffusé se présente sous forme d'une parabole. Ainsi, les DOAs de signaux source ne sont pas constantes, et forment des trajectoires spécifiques (des fonctions du temps). Cela implique que les statistiques de second ordre des signaux sources sont dépendantes du temps. Les méthodes de traitement d'antennes classiques nécessitent la stationnarité des signaux dans une fenêtre temporelle. Dans des environnements légèrement non-stationnaires, le traitement utilisant une fenêtre glissante peut encore être considéré. Cependant, les méthodes de traitement en ligne, i.e. méthodes de filtrage, sont nécessaires pour des situations plus générales, qui peuvent présenter des signaux fortement non-stationnaires.

- Des spécificités du traitement d'antennes sonar sont la présence des cibles angulairement distribuées et de signaux sources avec du bruit impulsifs. Les méthodes de traitement d'antennes considèrent l'estimation DOA des cibles angulairement distribués (ou étendus) dans le contexte stationnaire avec des cibles à étalement angulaire connu [16–18] ou inconnu [19]. La pertinence de signaux non-gaussiens et impulsifs dans le traitement radar/sonar est présenté dans [20]. Pour les signaux sonar présentés dans ces travaux, dans l'Annexe H, on démontre leur nature non-gaussienne et impulsionnelle. Dans le

traitement d'antennes, les signaux non-gaussiens et le bruit sont abordés dans [21–23] pour le cas stationnaire. Cependant, le traitement des cibles à étalement angulaire avec des signaux non-gaussiens et non-stationnaires n'a pas encore été abordé.

- Les cibles multiples peuvent survenir dans l'estimation des cibles cinématiques ainsi que dans les applications de bathymétrie. Pour la bathymétrie, des échos multiples peuvent provenir de la propagation à trajets multiples ou dans la situation où des objets verticaux de grande taille sont présents sur le fond marin, par exemple épaves, digues, poteaux, etc. Les trajectoires DOA des différents échos non-stationnaires doivent être estimées pour que les échos soient identifiés et séparés pour l'étape de reconstruction bathymétrique. Lorsque des modèles d'états sont utilisés pour représenter les états des cibles/échos, l'estimation de leurs états devient synonyme de pistage multi-cible. Dans ce travail, comme on s'intéresse à l'estimation des DOA des échos, les états associés aux différents échos vont contenir leurs DOA et potentiellement des autres paramètres. Le pistage multi-cible représente un domaine de recherche actif, avec des méthodes modernes s'appuyant sur des modèles de processus ponctuels et sur le filtre d'intensité. Dans une telle approche, une collection d'un nombre aléatoire des cibles/échos ayant des états Markoviens est associée à un processus ponctuel.

  Le filtre d'intensité est un filtre qui propage une approximation au premier ordre - la fonction d'intensité, au lieu de propager la densité du processus ponctuel [24], opération qui s'avère être difficile à mettre en place dans la pratique. Le filtre d'intensité, aussi connu comme le filtre Probability Hypothesis Density (PHD), est bien adapté pour traiter un nombre inconnu et variable de cibles avec états inconnus. Cependant, les filtres d'intensité existants ont été dérivés pour les modèles d'observation qui supposent une contribution déterministe de chaque cible. Dans le traitement d'antennes, il est courant de supposer les signaux sources, conditionnellement à leurs états, comme aléatoires. Ainsi la contribution à l'observation antenne d'une telle cible est aléatoire et les filtres d'intensité existants dans la littérature ne s'appliquent pas. C'est d'autant plus vrai pour la bathymétrie, où le signal source a une nature très fluctuante et qui est obtenue par la somme des signaux émis par des rétrodiffuseurs élémentaires contenus dans la cellule de résolution. Dans ce contexte, la proposition d'un filtre d'intensité pour le traitement des signaux sources aléatoires, sans faire appel à un état augmenté, n'a pas été proposé.

Dans cette partie, les possibles solutions aux défis précédemment énumérés sont présentées brièvement.

Objectifs et réalisations

Les modèles d'état pour le traitement d'antennes sont proposés dans un cadre de traitement général pour les signaux non-stationnaires, qui modélisent l'évolution de l'état d'une cible comme un processus de Markov caché. Les modèles d'état sont capables d'incorporer différentes connaissances *apriori* sur l'évolution des cibles. L'objectif de cette thèse est double, d'une part de proposer des filtres de poursuite multi-cibles pour les systèmes d'observation où la contribution d'une cible est aléatoire. Les méthodes proposées ont un caractère général, à savoir qu'ils ne comptent que sur une description de l'état avec un processus d'état Markovien. D'autre part, des modèles spécifiques pour la reconstruction bathymétrique sont proposés et les méthodes de poursuite sont appliquées aux données bathymétriques-sonar.

D'une manière générale, les systèmes de poursuite peuvent être classés en : Track While Scan (TWS) et Track Before Detect (TBD) [25]. Dans le cadre TWS, la poursuite est effectuée dans une étape de post-traitement, sur des observations ponctuelles obtenues par un pré-traitement appliqué au signal brut de l'antenne déphasée. L'étape de pré-traitement consiste généralement

en un module de détection et d'estimation qui détecte la présence des cibles et donne une estimation grossière de leur position. Par conséquent, dans TWS les observations consistent en un ensemble de points provenant de positions vraies des cibles, mais qui contiennent également des mesures fausses générées par l'encombrement. Pour les données sonar bathymétrique, l'encombrement est constitué par les échos interférents générés par la propagation multi-trajets et la réverbération volumique. De plus, même en l'absence de l'encombrement, l'ensemble d'observations est ambiguë parce que nous ne savons pas quel point d'observation appartient à quelle cible. La non-détection des cibles est également possible. L'ensemble des points d'observation obtenus par le pré-processeur alimente le filtre de poursuite. Le rôle du module de poursuite est d'éliminer les mesures erronées (i.e. fausses alarmes), de trouver des associations observations-cibles et de filtrer la trajectoire de chaque cible avec son observation associée. Les systèmes TBD ne recourent pas à un module de pré-traitement et considèrent directement le signal d'antenne comme l'observation du système. L'avantage des systèmes TBD, par opposition aux TWS, provient de l'absence d'opérations de seuillage présentes dans le module de pré-traitement et qui entraîneraient une perte d'information. Effectivement, dans l'approche TWS, le module de pré-traitement est non-adaptatif et il implique une certaine perte d'information. Cet avantage devient important lors du traitement de signaux à rapport signal sur bruit (SNR) faible. Cependant, cela se fait au prix d'une complexité importante des systèmes TBD, en raison du modèle d'état fortement non-linéaire qui intègre désormais le signal antenne comme observation.

Dans la première contribution aux méthodes de reconstruction bathymétriques, nous proposons un système TWS avec l'objectif de poursuivre les trajectoires DOA de différents échos impactant l'antenne déphasée, afin d'extraire uniquement les trajectoires correspondant au fond marin. Le pré-processeur donne un ensemble de DOA estimées qui représente une estimation grossière des DOA des échos présents dans le signal d'antenne. Cet ensemble est obtenu en deux étapes. D'abord, le pré-processeur utilise des critères d'information, e.g. Akaike information criterion (AIC), Minimum Description Length (MDL), pour estimer le nombre d'échos présents. Ensuite, les DOA sont obtenus comme les maxima locaux du spectrogramme du signal d'antenne. À noter que le spectrogramme est une densité angulaire de puissance du signal reçue par l'antenne et qui est obtenue avec un estimateur à fenêtre glissante, e.g. formation de voies, Capon, méthode haute-résolution. De plus, ces deux étapes qui consistent dans une pré-détection et une pré-estimation, peuvent être changées sans entraîner de modifications dans le modèle de poursuite ultérieur. Cette capacité d'adaptation présente un avantage majeur dans le cadre TWS, mais aussi un inconvénient car le module de pré-traitement est non-adaptatif. Cependant, la décomposition TWS dans le pré- et post-traitement est régulièrement utilisé dans les systèmes applicatifs et commerciaux [26], principalement en raison de sa mise en œuvre simple et de sa complexité faible. Dans notre approche, la poursuite d'écho est perçue comme une étape de post-traitement adaptatif par filtrage basée sur modèle. Le filtrage employé fait partie des filtres d'association données probabilistes et enlève l'ambiguïté de l'ensemble d'observation en donnant l'association optimale entre les cibles et les observations. L'association optimale est déterminée selon un critère probabiliste. Le modèle du filtre incorpore des informations *apriori* sur l'évolution temporelle des échos afin d'éviter les observations encombrées. Pour ce faire, nous développons plusieurs modèles géométriques, qui représentent l'information *apriori* incorporée dans l'étape de filtrage pour l'extraction de la bathymétrie. Une approche "modèle multiple", qui suppose plusieurs modèles en parallèle, est utilisée pour augmenter la capacité d'adaptation du filtre proposé sur les zones très irrégulières du fond marin. Une mesure de la qualité de trajectoire, la probabilité de l'existence de trajectoire, est utilisée pour détecter les zones d'ombrage acoustique et de terminer la poursuite. Plusieurs tests d'hypothèses sont employés pour valider la pertinence des modèles proposés, à la fois pour les images sonar réelles et simulées.

Des enjeux majeurs, auxquels les filtres d'association donnés ne fournissent pas des solutions rigoureuses, sont l'initialisation et la suppression de trajectoire/piste. Généralement, ce sont réalisé en utilisant des règles d'initialisation ad-hoc sur la base des observations ponctuelles. Dans le cadre de TBD ces méthodes d'initialisation ne sont pas facilement disponibles. Cependant, une approche différente qui implique des processus ponctuels et de filtres d'intensité (ou filtre PHD), peut intégrer d'une manière plus rigoureuse les processus de naissance et de décès. Les filtres d'intensité ont été d'abord proposés pour les systèmes TWS en [27]. Récemment, dans [28] un filtre TBD-PHD a été proposé pour les modèles d'observation superposés, où l'observation du système est donnée par la somme des contributions de chaque cible. Cependant, dans [28] les contributions individuelles de cibles, conditionnellement à leurs états, sont déterministes. En revanche, l'observation d'une antenne déphasée est la superposition des contributions aléatoires des différentes cibles.

En temps que deuxième contribution, basée sur le filtre PHD superposée, nous développons un filtre TBD-PHD qui permet de poursuivre plusieurs cibles à partir directement des observations d'antenne déphasées. Plus généralement, le filtre proposé peut être employé pour des systèmes TBD où la contribution d'une cible est aléatoire avec une distribution paramétrée par l'état de la cible. Dans le cadre de l'application bathymétrique, les contributions représentant les signaux sources qui, conditionnellement aux états des cibles, sont des variables aléatoires gaussiennes. D'ailleurs, nous interprétons le processus ponctuel, utilisé pour modéliser l'état multi-cibles, en conjonction avec les signaux sources comme un processus ponctuel marqué. Les signaux sources représentant les marques, tandis que la fonction de l'intensité du processus marqué intervient uniquement dans l'étape de mise à jour du filtre. Plus important encore, on montre qu'il suffit de propager la fonction d'intensité du processus ponctuel par opposition à l'intensité marquée qui est définie dans un espace de dimension plus élevée. En effet, la fonction d'intensité du processus ponctuel est définie dans l'espace d'état des cibles (positions), tandis que la fonction d'intensité marquée est définie dans l'espace produit - état et marques (l'espace des signaux sources). Nous montrons qu'augmenter les vecteurs d'état avec leurs signaux source n'est pas nécessaire, et que les marques peuvent être marginalisées dans les formules de mise à jour du filtre. Cela conduit à des implémentations particulaires plus efficaces par rapport aux solutions qui recourent aux vecteurs d'état augmenté. Ces dernières méthodes exigent un échantillonnage des particules à partir d'une distribution de dimensions supérieures. Le TBD-PHD proposé ne se limite pas uniquement aux applications bathymétriques, mais il est développé pour des cibles dynamiques génériques observé par une antenne déphasée.

Pour la troisième contribution, nous étendons le modèle du signal source pour les cibles étendues (i.e. angulairement dispersées) et pour des signaux à nature impulsionnelle (i.e. non-gaussiennes). Les deux notions sont couramment rencontrées dans le domaine du sonar. Dans la Figure 1 on peut remarquer que la cible, qui génère le signal source s_t, est un patch sur le fond marin et ainsi, une cible implicitement étendue. De plus, en milieux peu profonds, les distances antenne - cible sont faibles et la cible est vue sous un angle non-négligeable et qui entraine un étalement du signal source dans le domaine angulaire, implicitement dans le spectrogramme. Les signaux sonar traités dans cette thèse, ont des distributions à queue plus lourde que la distribution gaussienne, comme démontré dans l'Annexe H. Ce comportement des signaux sonar à été souvent rencontré dans la pratique [29–32] et relève leur nature impulsionnelle. En plus, pour améliorer les performances de poursuite, un filtre PHD Cardinalisé (CPHD) est considéré dans l'approche TBD pour le traitement d'antenne, menant au filtre TBD-CPHD. Le filtre TBD-CPHD propage, en plus de la fonction d'intensité, une distribution estimée sur le nombre de cibles, appelée distribution de cardinalité. La propagation de la distribution de cardinalité conduit à une inférence directe du nombre de cibles par des différents critères, par exemple *Maximum A Posteriori* (MAP) ou *Minimum Mean Squared Error* (MMSE). Comme indiqué précédemment, les signaux impulsifs sont fréquemment utilisés dans les applications de sonar

et radar, avec la famille de distributions Spherically Invariant Random Vector (SIRV) étant répandue dans la littérature. Par conséquent, un modèle joint-SIRV est utilisé pour des signaux sources et le bruit de réverbération qui est capable de faire face à une grande variété d'observations non gaussiennes. Par exemple, le modèle SIRV employé incorpore les distributions de Cauchy, de Laplace, la loi K mais aussi la lois Gaussienne. À cet égard, le filtre TBD-CPHD généralise le filtre TBD-PHD précédemment proposé, d'un coté méthodologique mais aussi du modèle du signal sonar. Du point de vue méthodologique, le filtre CPHD utilise une distribution de cardinalité générique, et par conséquent est plus flexible que le filtre PHD qui suppose une distribution de Poisson. De plus, l'estimation et la propagation de la distribution de cardinalité permet de améliorer l'estimation du nombre des cibles par rapport au filtre PHD. Du coté modèle, le modèle de cible ponctuelle et signal source gaussien auparavant employé, représente un cas particulier du modèle de cible étendue avec les signaux SIRV. En plus, nous proposons une implémentation particulaire complètement auxiliaire du filtre TBD-CPHD, qui utilise l'observation courante dans les étapes d'échantillonnage des particules persistantes (correspondant aux cibles déjà existantes) et des particules de naissance (correspondant aux cibles naissantes). L'implémentation complètement auxiliaire représente une amélioration des implémentations précédemment proposées dans la littérature, où l'observation courante est employée seulement pour les particules de naissance.

Plan détaillé de la thèse

Le Chapitre II présente des filtres de poursuite TWS basés sur les méthodes d'association données. Ces filtres sont employés pour reconstruire une image 3D à haute résolution du fond marin pour des applications en temps réel. La poursuite assure la formation et la séparation des trajectoires DOA bathymétriques et celles provenant des échos interférents (réverbération volumique et propagation multiple). Le repliement (*layover* en anglais) est un phénomène limitant pour les images 2D d'amplitude, où une partie de l'image n'est pas visible à cause d'un objet vertical de grande dimension, par exemple un poteau ou une digue. Le phénomène de repliement est résolu par la poursuite simultanée des échos du fond et de l'objet vertical. Cette approche TWS suppose un module de pré-traitement qui donne une première estimation grossière des DOA des échos présents dans le signal antenne. Plus précisément, le module de pré-traitement consiste en des méthodes de traitement d'antenne classique (e.g. formation de voie, Capon, MUSIC) et une méthode de détection du nombre des sources (e.g. AIC, MDL, BIC). La méthode de traitement d'antenne sert pour construire un spectrogramme du signal antenne, avec les pics de spectrogramme représentant des DOA estimés grossièrement des échos. L'ensemble ainsi formé est utilisé comme observation pour le module de poursuite par filtrage d'association donnée probabiliste (PDAF). Pour gérer l'association des observations multiples aux trajectoires multiples, une approche "plus proche voisin" (Nearest Neighbour) est employée. Ainsi le filtre est capable d'éliminer l'incertitude associée à l'ensemble des observations fourni par le module de pré-traitement et d'obtenir des trajectoires DOA régularisées et sans fausses détections. Des modèles géométriques sont utilisés pour caractériser les trajectoires DOA de cibles dans un contexte bathymétrique. Dans une approché *Interacting Multiple Models* (IMM), plusieurs modèles sont utilisés en parallèle afin d'augmenter la capacité d'adaptation du filtre proposé. De plus, ces modèles présentent également une segmentation de l'image 3D en fonction du modèle prédominant et fournissent des informations utiles pour l'identification des infrastructures. De plus, une probabilité d'existence de trajectoire est estimée de façon adaptative en parallèle avec le filtrage. Cette probabilité d'existence de trajectoire est utilisée pour détecter les zones d'ombrage acoustique et ainsi, la terminaison des trajectoires. Le filtre résultant est nommé filtre NN-IMM-IPDA-UKF et est implémenté en utilisant plusieurs filtres Kalman sans parfum (UKF). Des tests d'hypothèse (goodness of fit) sont utilisés pour valider les traitements et

différents modèles proposés. L'implémentation relativement simple de la NN-IMM-IPDA-UKF donne un algorithme adapté pour les applications temps réel. Cela constitue un avantage majeur de cette approche dans la poursuite des échos DOA. Cependant l'inconvénient réside dans le module de pré-traitement qui représente un module non-adaptatif et qui entraine une certaine perte d'information. De plus, le module de pré-traitement a besoin de traiter une fenêtre d'échantillons du signal antenne pour produire un spectrogramme significatif. En conséquence, le traitement TWS entraine une perte de résolution de l'image reconstruite.

Dans les chapitres suivants, nous proposons un schéma alternatif de traitement qui ne dépend pas d'un module de pré-traitement (détection/estimation), mais qui poursuit directement les échos à partir des observations de l'antenne sonar déphasée. Cette approche TBD permet de poursuivre les échos de faible SNR mais aussi de donner une estimation DOA filtrée pour chaque échantillon du signal antenne sonar, réalisant une bathymétrie à super-résolution. Néanmoins, les algorithmes de suivi TBD résultant, sont plus complexes que les méthodes TWS.

Dans le Chapitre III des filtres d'intensité sont développés pour la poursuite des cibles multiples directement des observations de l'antenne déphasée, dans un cadre TBD. La fonction d'intensité (ou la fonction PHD) est le moment de premier ordre de la densité d'un processus ponctuel (ou équivalente d'un ensemble fini aléatoire) et décrit à la fois le nombre aléatoire de cibles et leurs vecteurs d'états aléatoires. En conséquence, un filtre d'intensité est considéré comme un filtre de premier ordre, qui propage une approximation de la vraie distribution a posteriori. Le chapitre commence par l'introduction de quelques définitions et les résultats liés à la théorie processus ponctuels. Historiquement, le filtre PHD pour les systèmes TWS a été le premier filtre d'intensité proposé. Pour les systèmes d'observations superposées, où l'observation est une superposition des contributions des cibles individuelles, le filtre PHD superposé a été récemment proposé.

Basé sur le filtre PHD superposé, nous proposons un filtre TBD-PHD pour les antennes déphasées pour la poursuite de plusieurs cibles. On considère ici un modèle de cible ponctuelle. Les signaux sources, conditionnés par leurs états de cibles, sont des variables aléatoires gaussiennes, ce qui rend impossible l'application directe du filtre PHD superposé. Une solution possible est d'augmenter le vecteur d'état de chaque cible avec le signal source. Cependant une telle solution est inefficace, en particulier pour les implémentations à base de filtre particulaire. En effet, dans les filtres particulaires à état augmenté, l'échantillonnage des particules s'effectue à partir d'une densité définie sur l'espace correspondant au vecteur augmenté, ce qui est inefficace. En revanche, nous considérons un processus ponctuel de Poisson marqué qui est capable de caractériser le nombre de cibles, leurs vecteurs d'état et les signaux sources. Les marques représentent les signaux sources, supposés gaussiens conditionnellement aux états des cibles. Nous montrons que les marques de cibles peuvent être marginalisées analytiquement dans les équations de mise à jour du filtre TBD-PHD. En conséquence, le filtre doit uniquement propager la fonction intensité/PHD du processus ponctuel qui décrit les positions des cibles et évite la propagation d'un état augmenté. Plus généralement le filtre développé est utilisable pour tout système TBD super-positionnel où la contribution d'une cible, conditionnellement à son état, est aléatoire avec les paramètres de la distribution donné par l'état de la cible. Grâce aux formules marginalisées du filtre TBD-PHD proposé, le filtre admet une implémentation particulaire plus efficace que les filtres à état augmenté. Cependant, en raison d'une approximation gaussienne employée pour la pseudo-vraisemblance [voir Eq. (III.37)], le poids de la fonction d'intensité estimée devient très fluctuant et ne représente plus un estimateur efficace du nombre moyen des cibles dans une région spécifique. Par conséquent, une méthodologie de clustering est employée qui estime à la fois le nombre de clusters et les centres des clusters. Parmi les méthodes de clustering existantes, la méthode DBSCAN a été choisie. À notre connaissance, ceci est le premier filtre de poursuite à employer la méthode de classification DBSCAN. La DBSCAN a quelques avantages par rapport aux méthodes classiques basées sur la méthode

k-means. Tout d'abord, la DBSCAN ne nécessite pas la connaissance préalable du nombre de groupements, et fournit une estimation du nombre de cibles et de leurs vecteurs d'état respectifs. Deuxièmement, la DBSCAN considère l'existence de points aberrants (outliers en anglais) dans l'approximation particulaire de la fonction d'intensité. Les valeurs aberrantes représentant un problème pour les méthodes type k-means. De plus, la méthode de clustering DBSCAN est utilisable dans les scénarios à zéro-cible, autrement dit, où seulement des valeurs aberrantes sont présentes. En effet, l'utilisation de la méthode DBSCAN pour la poursuite multi-cible constitue une première et elle améliore considérablement les résultats par rapport à la méthode k-means-silhouettes proposée dans [28].

Le filtre cardinalisé PHD (CPHD) présente une solution à la problématique du poids très fluctuant de la fonction de PHD estimée. Le filtre TBD-CPHD est proposé pour la poursuite des cibles multiples à partir des observations d'antennes déphasées non-gaussiennes (modélisées comme processus SIRV) et générées par des cibles réparties angulairement. En plus de la fonction d'intensité, le filtre CPHD propage également la distribution de cardinalité, i.e. la distribution sur le nombre de cibles. Cela permet une estimation plus directe du nombre de cibles. Les deux quantités - l'intensité et la distribution de cardinalité sont interdépendantes, la distribution de cardinalité est employée dans l'estimation de la fonction d'intensité et réciproquement. Ainsi, la distribution de cardinalité améliore non seulement l'étape d'inférence des états de cible mais également la précision de la fonction d'intensité elle-même. Cela améliore considérablement les performances du filtre TBD-CPHD par rapport au filtre TBD-PHD. Le filtre TBD-CPHD et le modèle de signal source sont décrits davantage dans le Chapitre IV. De plus, dans un effort pour se rapprocher des scénarios réels, le TBD-CPHD est développé pour un modèle de cible angulairement distribuée (étendue) avec des observations impulsives. Les environnements acoustiques sous-marins présentent des signaux impulsifs ou même de distributions à queue lourde. Dans ce travail, nous employons le modèle général de signal SIRV capable de décrire à la fois les signaux impulsifs et celles à queue lourde, avec la distribution de Laplace multivariée plus spécifique pour les expériences sur des données réelles. Comme pour le filtre TBD-PHD, les signaux source sont analytiquement marginalisés dans les équations de mise à jour de l'intensité et de la distribution de cardinalité, ce qui assure une implémentation efficace du filtre.

Une implémentation particulaire améliorée du filtre TBD-CPHD est proposée en employant une étape auxiliaire pour les particules persistantes ainsi qu'une distribution IS adaptative pour les particules naissantes. L'implémentation résultante est nommée Completement Auxilière (CA-CPHD). Le CA-CPHD utilise l'observation courante dans l'étape d'échantillonnage des deux ensembles des particules - persistantes et naissantes. Les résultats sur des données simulées montrent une amélioration de la performance du filtre proposé par rapport aux méthodes récentes. De plus, le filtre proposé est appliqué à des données réelles issues d'un sonar bathymétrique.

Une des limitations majeures de tous les filtres d'intensité, comme indiqué dans la partie résultats TBD-CPHD sur données réelles, est l'incapacité d'identifier une piste entière (la ou les trajectoires). L'identification d'une trajectoire consiste à associer une étiquette unique à tous les états inférés qui appartiennent à la même cible tout au long de l'enregistrement sonar. Cette problématique est intrinsèque aux processus ponctuels, qui considèrent les cibles comme des points indissociables. L'identification des trajectoires entières, depuis leurs débuts jusqu'à leurs fins, est importante pour pourvoir ensuite classifier les trajectoires DOA en trajectoires pertinentes et non-pertinentes pour une application spécifique. La succession des ensembles de DOA inférées, offerts par les filtres TBD-PHD et TBD-CPHD, n'est pas suffisante pour réaliser cette identification et séparation des trajectoires. Les ensembles aléatoires étiquetés ont été récemment introduits dans [33, 34], et proposent d'utiliser un marquage unique pour les différentes cibles. Les marqueurs des cibles étant uniques, peuvent être utilisés pour reconstruire la trajectoire entière d'une cible spécifique.

Conclusions

Le sujet central dans cette thèse est la poursuite DOA des cibles multiples à partir des observations d'antenne déphasées. Plusieurs méthodes sont proposées et classées dans les approches TWS et TBD. Les solutions proposées sont testées sur des données sonar pour le problème de reconstruction du relief du fond sous-marin, autrement dit, la bathymétrie.

La première contribution présentée s'appuie sur la chaîne de traitement modulaire TWS. Dans cette approche une méthode de prétraitement est employée pour transformer l'observation antenne dans un ensemble d'observations ponctuelles et qui est ensuite filtré par le module de suivi. L'approche TWS suppose que le traitement adaptatif, i.e. le filtrage de suivi, se fait en post-traitement. Les systèmes TWS de poursuite sont les plus repandus et ont l'avantage d'avoir une complexité relativement faible et une implémentation simple. Le module de prétraitement utilise des méthodes classiques de traitement d'antennes pour obtenir un ensemble des estimées DOA. Cet ensemble sert d'observation pour le module de suivi. La poursuite est perçue comme un filtre basé sur un modèle et assure la formation des trajectoires. Ainsi on assure la séparation des échos bathymétriques des échos interférents, et ensuite une reconstruction 3D du fond marin. Des filtres Kalman sans parfum sont utilisés pour l'implémentation du module de suivi. Des modèles géométriques sont utilisés pour caractériser les trajectoires DOA d'échos dans un contexte bathymétrique. Plusieurs modèles sont utilisés en parallèle afin d'augmenter la robustesse du filtrage en conditions réelles. De plus, les modèles multiples permettent également une segmentation efficace de l'image 3D dès l'étape de formation d'image. Ainsi, les modèles géométriques fournissent des informations utiles à des fins d'identification de l'infrastructure. Des interruptions de trajectoire, dues à des ombres acoustiques, sont détectées par une mesure de la probabilité d'existence de la trajectoire.

Une deuxième contribution est représentée par un filtre TBD-PHD avec observations issues d'une antenne déphasée. Dans le cadre du filtre TBD, où aucun pré-traitement n'est effectué, de meilleures performances peuvent être atteintes mais au détriment d'une complexité plus élevée du filtre. Par opposition à l'approche TWS, le TBD rend également difficile la proposition de méthodes empiriques pour l'initialisation et de la terminaison des trajectoires. Par conséquent, nous optons pour un formalisme processus ponctuel et aux filtres d'intensité, permettant de contourner ce problème en tenant compte de l'état multi-cibles comme une collection non ordonnée de points (i.e. ensemble aléatoire). La fonction d'intensité (ou la fonction PHD) est la densité du moment de premier ordre d'un processus ponctuel, qui décrit à la fois le nombre aléatoire de cibles et leurs vecteurs d'état aléatoires. En conséquent, un filtre d'intensité est considéré comme un filtre de premier ordre, propageant une approximation de la distribution a posteriori. Basé sur le filtre PHD superposé, le filtre TBD-PHD est proposé, qui est capable de poursuivre plusieurs cibles directement des observations d'antennes déphasées. Le filtre proposé emploie la notion de marquage et les processus ponctuels marqués, où le signal source généré par une cible représente sa marque. Les marques sont marginalisées dans l'étape de mise à jour du filtre, ainsi évitant de propager un état augmenté. Cela conduit à une implémentation particulaire efficace et qui ne nécessite pas un échantillonnage à partir des distributions augmentées. De plus, le filtre proposé utilise un mécanisme de clustering amélioré où le nombre des clusters ainsi que leurs centres sont estimés en présence des outliers. Le filtre TBD-PHD proposé est utilisable pour toute sorte de cible qui admet une modélisation markovienne pour son état, sans aucune autre hypothèse sur sa cinématique. Ainsi, le filtre TBD-PHD est général et peut être employé pour des cibles cinématiques classiques ainsi que pour les échos bathymétriques. Le filtre TBD-PHD assume cependant des signaux de sources gaussiennes générées par des cibles ponctuelles, i.e. sans étalement angulaire. Ces hypothèses, bien que suffisantes dans diverses applications, sont trop restrictives pour les applications sonar.

Une troisième contribution est représentée par le filtre TBD-CPHD, qui améliore l'estima-

tion du nombre des cibles (i.e. la cardinalité) par rapport au filtre TBD-PHD précédemment proposé. Dans ce but, le filtre TBD-CPHD propage une estimation de la fonction d'intensité mais aussi une distribution de cardinalité estimée. Ici encore, le filtrage est obtenu sans augmentation du vecteur d'état de signaux sources, i.e. les marques. De plus, le filtre TBD-CPHD est développé pour des signaux sources impulsifs issues des cibles réparties angulairement. Des distributions SIRV sont employées pour modéliser les signaux sources et le bruit, dans un modèle joint-SIRV. La famille de distributions SIRV est très générale et englobe la plupart des distributions employées pour modéliser les signaux et l'encombrement dans les applications sonar/radar. Par exemple, dans les expériences sur des données réelles, nous employons la loi de Laplace multivariée comme la vraisemblance de l'observation antenne. Une meilleure implémentation particulaire est proposée pour le filtre, qui emploie une étape auxiliaire pour les particules persistantes et une distribution de naissance adaptative. Les performances du filtre TBD-CPHD sont évaluées par rapport à des méthodes classiques de traitement d'antennes et des filtres PHD de poursuite.

Perspectives

Les potentielles pistes de recherche peuvent être classées en deux axes interconnectés : l'enrichissement du modèle sonar et l'amélioration des méthodes de poursuite.

Comme il a été démontré dans l'Annexe H, les signaux sonar ont un degré d'impulsivité qui varie en fonction de l'angle d'incidence et/ou de la distance entre l'émetteur et l'antenne. En revanche, l'obtention d'avantage des données sonar est nécessaire pour la proposition d'une distribution adaptative, autrement dit une distribution qui prend en compte les dépendances avec l'angle d'incidence et la distance. Ces relevés des donnes doivent être menés dans en environnent contrôlé, fond et conditions de propagation homogènes. Par exemple, la loi K peut être employé avec un paramètre de forme dépendant de l'angle d'incidence et implicitement de la DOA du signal source. Une telle distribution peut conduire à une fonction vraisemblance plus "concentrée" et qui améliore le DOA estimé. L'emploi d'une distribution du signal source paramétré ne nécessiterait pas le changement des équations des filtres d'intensités proposés. Une autre voie d'amélioration, consiste à utiliser des distributions différentes pour le signal source et le bruit. Actuellement, un modèle joint-SIRV est employé, où la texture est prise identique pour tous les signaux sources et le bruit. Cette hypothèse est principalement motivée par la nécessite d'assurer une observation de type SIRV.

Des échantillons de signaux sources et du bruit ne sont pas disponibles indépendamment, en conséquence la caractérisation individuelle de chaque signal est difficile. En plus, la superposition des signaux non gaussiens et indépendants, n'admet pas en règle générale une forme analytique de la distribution résultante. Cependant, il existe quelques exceptions. Le cas où les signaux sont des variables aléatoires indépendantes de la famille CES (Complexes, Elliptiques et Symétriques) ayant la même matrice de dispersion, conduit après sommation à une nouvelle variable CES [35]. Malheureusement, ce modèle n'a pas d'intérêt en traitement d'antennes, car différentes sources ont forcement des matrices de dispersion distinctes (en raison de leurs DOA distinctes) tandis que le bruit blanc a une matrice de dispersion proportionnelle à la matrice identité. Une alternative plus prometteuse vient de la famille de distributions α-stable [36]. La propriété de stabilité des distributions α-stable exige que les signaux de sources et le bruit soient des variables aléatoires α-stable indépendantes avec le même paramètre α pour que leur somme soit α-stable. La contrainte, selon laquelle les signaux sources et le bruit ont le même paramètre α, est une condition moins stricte que de supposer une texture commune. En effet, le terme de texture du modèle joint-SIRV implique que les différents signaux sources et le bruit soient mutuellement décorrélés mais dépendants, tandis que les distributions α-stable supposent leur indépendance. Cependant, le passage aux distributions α-stable exige également des change-

ments dans les équations de filtrage. De plus, les distributions α-stable ne disposent pas des formes analytiques de leur densité pour tout valeur α, ce qui implique une augmentation de la complexité du traitement.

Le deuxième axe de recherche concerne l'amélioration de la méthode de filtrage. Comme remarqué pour les résultats TBD-CPHD sur données sonar réelles, les filtres d'intensité sont incapables d'identifier les pistes (ou les trajectoires). En général, les processus ponctuelles utilisé conduisent à des mesures du nombre moyen des cibles dans un région de l'espace mais qui ne permet pas de reconstruire l'historique des cibles. L'historique d'une cible permet de identifier sa trajectoire depuis sa naissance jusqu'à sa disparition. Cette séparation de trajectoire est la première étape dans un algorithm d'identification de la trajectoire. Afin de réaliser la séparation entre les échos bathymétrique pertinents et non pertinents, nous avons besoin d'une séparation claire et de l'identification des trajectoires. La nouvelle proposition des filtres basées sur un modèle de ensemble aléatoire (RFS) étiquetés [33,34] utilisent un étiquetage unique pour chaque cible. Les étiquettes sont uniques et peuvent être employées pour reconstruire la trajectoire entière d'une cible. Au contraire des filtres d'intensités, les filtres RFS étiquetés propagent une version tronquée de la densité a posteriori multi-cible. Par conséquent, les filtres RFS étiquetés sont en général plus exigeantes en termes du temps de calcul.

Chapter I

Introduction

In God we trust; all others must bring data.

W. Edwards Deming

Background

The maritime transportation system, defined as port, waterways and canals, is the backbone of the world trade. In 2005, 90% of the international trade (by volume), was conducted by the maritime transportation system [1]. In recent years, port and maritime security have emerged as a significant part of the global security effort [2]. Maritime transportation systems are designed for speed and efficiency, and any perturbation can lead to great economic and/or human loss. An example for this instance is given in [2], were the cost of closing the US West Cost ports for 5 consecutive days is estimated at approximately 1 billion US$. Most of the security analyses are aimed at highlighting the vulnerabilities of port areas to various attacks that would block the port and/or lead to the loss of human life. As pointed out in [2], this could result from sinking large ships such as container ships, liquid natural gas transport ships or even ferries, in a port. Therefore, an increased attention is shown toward the imaging and the inspection of underwater areas in ports and waterways.

Sonar systems and other underwater sensors have been increasingly employed for port security and intrusion detection [3–5], with the prevalence of side-scan sonar systems for high-quality and affordable underwater imaging [37]. All imaging sonars are active sensing systems, that is, they emit a signal and record the signal backscattered by the underwater environment. Indeed, side-scan sonars provide 2D amplitude images of the sea-floor backscatter at high-resolutions, e.g. 6cm range resolution for the EdgeTech 4600 sonar [6]. Furthermore, the resolution capabilities of side-scan sonars can be improved by a synthetic-aperture processing [7, 8]. High-resolution side-scan images are necessary for mine and improvised explosive device detection [9]. 3D reconstructions of the sea-floor, that is depth maps or bathymetry, are more involved and are traditionally conducted using phased-array sonars. In deep waters, bathymetry is usually achieved with multibeam echosounders [10], that consist of two orthogonal linear phased-arrays. While in shallow waters, such as ports and canals, bathymetry is usually obtained with bathymetric side-scan sonars [11, Ch.3.3.1], with a single linear phased array. In all sonar systems bethymetry is achieved by triangulating the echo backscattered by distributed targets such as the sea-floor or various structures [12], [10]. Interferometry and other array-processing methods are employed in estimating the Direction Of Arrival (DOA) of the desired target. Given the imaging geometry, DOA estimates can be converted to depth measures as described in Sec. II.1. Today, there is a growing demand for bathymetric side-scan sonars that can perform both 2D imaging and 3D bathymetry reconstruction simultaneously, and without the need for subsequent registration, which represents a major advantage in mine-detection applications.

Major challenges

The work conducted in this PhD thesis is aimed at improving multi-target tracking with phased-array sonar systems, to achieve improved bathymetry reconstruction in shallow waters. For real-data experiments, we employ data obtained with the EdgeTech 4600 bathymetric side-scan sonar, that have been acquired in shallow-water environment, more specifically in port Everglades, Fort Lauderdale, Florida USA. The major challenges addressed in our work are presented next.

- Shallow waters are encumbered propagation media, that exhibit multi-path propagation and reverberation, limiting the effectiveness of array-processing methods [13–15]. As shown in Chapter II, the sea-surface plays an important role in generating multi-path propagation. A source signal, propagating through a shallow-water wave guide, often generates several replicas: direct line-of-sight signal, reflections that have distinct DOAs, and reverberation with diffuse DOAs. Reflections and reverberation represent interferences, with the spatially-white reverberation component being regarded as noise, while coherent reflections being modeled as distinct source signals. Furthermore, depending on the scattering phenomena, reflections and reverberation show various degrees of dependency on the original source signal.

- An additional challenge arises from the non-stationarity of source signals. Indeed, whether estimating positions of kinematic targets or of bathymetric echos, the phased-array signal is non-stationary. In bathymetry, signals of interest are the signals backscattered by the sea-floor or some object of interest. Therefore, the characteristics of sources signals, notably their DOA, evolve with the profile of the underwater environment. This is true even for horizontal and flat surfaces, where the backscattered echo will exhibit an arched-shaped curve as DOA trajectory. Thus, the DOAs of source signals are not constant, and form specific trajectories (i.e. functions of time). This causes the second-order statistics of source signals to become time dependent. Classical array-processing methods require the stationary of signals in a window of time snapshots. In mildly non-stationary environments, sliding-window processing can still be considered. However, on-line signal processing, that is filtering methods are required for more general situations, which can exhibit highly non-stationary signals.

- Specific to sonar phased-array processing are the presence of angularly-distributed targets and impulsive source signals. Array-processing methods have considered DOA estimation of angularly-distributed (or extended) targets in the stationary context with known target extent [16–18] or unknown target extent [19]. The relevance of non-Gaussian and impulsive signals in radar/sonar processing is showcased in [20]. While for the sonar signals presented in this work, in Appendix H we demonstrate their non-Gaussian and impulsive character. In array processing, non-Gaussian signals and noise are addressed in [21–23] for the stationary case. However, processing extended targets with non-Gaussian and non-stationary signals has yet to be addressed.

- Multiple-targets can arise in kinematic-target estimation as well as in bathymetry applications. For bathymetry, multiple echoes can result from multi-path propagation or whenever tall objects are present on the sea-floor, e.g. pilings, poles etc. The DOA trajectories of the different non-stationary echoes need to be estimated in order for the echoes to be identified and separated for the bathymetric reconstruction stage. Estimating the DOAs of multiple non-stationary echoes, when conducted using state-space representations [38], becomes synonymous with multi-target tracking. Multi-target tracking represents an active area of research, with modern methods relying on point processes as the multi-target

process and the intensity filter as a first-order approximation [24]. Intensity filters, also known as Probability Hypothesis Density (PHD) filters, are well suited to handle varying number of targets. However, existing intensity filters have been derived for observation models not involving random source signals. In array processing, it is common to suppose source signals, conditioned on target states, as random. In this context, the proposal of a PHD filter not resorting to an augmented state (that would be overcomplex) has yet to be proposed.

In this work, possible solutions to the above-listed challenges are briefly presented next.

Objectives and achievements

State-space models for phased-arrays are proposed as a general processing framework for non-stationary signals, that models the evolution of the target state as a hidden Markov process. State-space models are capable of incorporating various *apriori* knowledge about the evolution of targets. The goal of this thesis is twofold, firstly to propose multi-target tracking filters for phased-array observation systems. The proposed methods are general, i.e. they only rely on a state-space description with a Markov state process. Secondly, specific models for bathymetry reconstruction are proposed and the tracking methods are applied to bathymetric-sonar data.

In general, tracking systems can be classified into Track While Scan (TWS) and Track Before Detect (TBD) [25]. In the TWS framework, tracking is conducted in a post-processing step, on point observations obtained by pre-processing the raw antenna observation signal. The pre-processing step usually consists in a detector and estimator module that detects the presence of targets and gives a rough estimate of targets positions. Therefore, in TWS the observations consist in a set of points originating from true-target positions but that also contains false measurements generated by clutter. Additionally, even in the absence of clutter, the observation set is ambiguous because we do not know which observation point belongs to which target trajectory. The set of observation points obtained by the pre-processor is fed to the tracking algorithm. The role of the tracking module is to eliminate false measurements, to find observation-to-target associations and to filter each target trajectory with its associated observation. TBD systems do not resort to a pre-processing module and directly consider the antenna signal as system observation. The advantage of TBD systems, as opposed to TWS, stems from the absence of thresholding at an early step of signal processing, that would result in information loss. This advantage becomes important when processing low Signal to Noise Ratio (SNR) signals, also called *dim* echoes. However, this comes at the cost of increased complexity for TBD systems, mainly due to the highly non-linear state-space model that now incorporates the phased-array signal.

As a first contribution to bathymetry reconstruction methods, we propose a TWS system with the objective of tracking the DOA trajectories of different echoes impinging the array in order to extract only the trajectories corresponding to sea-bottom and infrastructure. The pre-processor uses information-theoretic criteria to select a number of local maxima from the array (pseudo-)spectrogram as the point-set observation. Note that the array signal (pseudo-)spectrogram is obtained with a locally sliding window estimator and that it can be changed without incurring any modifications for the subsequent tracking model. This adaptability represents a major advantage of the TWS framework, but also a disadvantage since the evolutionary state-model is usually not employed in the pre-processing step. Nonetheless, the TWS decomposition in pre- and post-processing is regularly employed in practice and in commercial systems [26], mainly due to its straightforward and low-complexity implementation. In our approach, echo tracking is perceived as a model-based post-processing stage, incorporating prior information on the temporal evolution of echoes in order to avoid cluttered observations. We

develop several geometrical models, that represent the prior information incorporated into the filtering step for bathymetry extraction. A parallel-model framework is employed to increase the adaptability of the proposed filter over highly irregular sea-bottom areas. A measure of trajectory quality, the trajectory probability of existence, is employed to detect shadow areas and track extinction. Several goodness of fit tests are employed, that validate the adequacy of the proposed models both for simulated and real sonar images.

A major issue, to which TWS systems do not provide a rigorous solution, is trajectory/track initialization and deletion. Usually, this is achieved by employing ad-hoc initialization rules based on the point observations. In the TBD framework such initialization schemes are not readily available. However, a different approach that involves point processes and intensity (or PHD) filters, can integrate more rigorously birth and death processes. Intensity filters have been firstly proposed for TWS systems [27]. Recently, in [28] a TBD-PHD filter was proposed for superpositional observation models, i.e. the system observation is given by a noisy sum of individual target contributions. However, in [28] the individual target contributions are considered deterministic when conditioned on the target state, which is often not the case in array processing.

As a second contribution, based on the superpositional PHD filter, we develop a TBD-PHD filter that tracks multiple targets directly from phased array observations. The target contributions represent the source signals that, conditioned on target states, are assumed Gaussian random variables. Furthermore, we interpret the point process, used to model the multi-target state, in conjunction with the source signals as a marked point process. The source signals represent the marks, while the intensity function of the marked process intervenes in the update step of the filter. Most importantly, we show that it is sufficient to propagate the intensity function of the point process as opposed to the marked intensity which is defined in a higher dimensional space. Indeed, the intensity function of the ground point-process is defined on the space of target states (i.e. positions), while the marked intensity function is defined on the product space of target state-space and mark space (i.e. the space of source signals). We show that augmenting the state vectors with their source signals is not necessary, and that marks can be integrated-out of the filter update formulas. This leads to more efficient particle-filter implementations than augmented state-vector solutions that would require sampling from higher-dimensional posteriors. The proposed TBD-PHD is not restricted only to bathymetric applications, and is developed for generic target-dynamics and phased-array observations generated under the point-target model with Gaussian signals and noise.

As a third contribution, we extend the phased-array model to incorporate impulsive signals and noise, and angularly-distributed (extended) targets. Additionally, to improve tracking performance, a Cardinalized PHD (CPHD) filter is considered, leading to the TBD-CPHD filter. The TBD-CPHD filter propagates, additionally to the intensity function, the distribution of the number of targets, i.e. the cardinality distribution. Propagating the cardinality distribution leads to a direct inference of the number of targets from the cardinality distribution, e.g. via MAP or MMSE estimation. As noted earlier, impulsive signals are frequently encountered in both sonar and radar applications, with the family of Spherically Invariant Random Vector (SIRV) distributions being prevalent in the literature. Therefore, a joint-SIRV model is employed for source signals and reverberation noise that is able to cope with a wide variety of non-Gaussian observations, from the heavy-tailed Cauchy to the ubiquitous Gaussian. In this regard, the developed filter generalizes our previously proposed filter both methodologically and model-wise. Methodologically, the CPHD framework allows for an arbitrary cardinality distribution, and hence is more flexible than the PHD framework that is constrained to Poisson-distributed number of targets. Model-wise, the Gaussian point-target model previously employed represents a special case of the angularly-distributed (extended) target model with SIRV signals and noise. Additionally, we propose an improved particle-filter implementa-

tion of the TBD-CPHD filter, that employs the current observation in the sampling stages of both persistent particles, corresponding to previous targets, and birth particles, corresponding to newly-birthed targets. In previous particle implementations of superpositional filters, the current observation was only employed for birth particles.

Thesis organization

Chapter II presents the first contribution of our work, and addresses the development of a TWS system for adaptive DOA estimation of multiple echoes. It offers a post-processing module that extracts tracks from observations supplied by standard array-processors. The major issues encountered in shallow-water array-processing are detailed and exemplified over real sonar data. The modular TWS framework is given and specific models are proposed for bathymetry reconstruction. A parallel-model approach is considered and a measure of track quality is given in the form of the track probability of existence. The detailed derivation of the track probability of existence is given in Appendix A. Results on both simulated and real-sonar data are presented and validated via goodness-of-fit tests. A short presentation of goodness-of-fit tests is given in Appendices C and D.

Chapter III starts with a short introduction to point-process theory and provides, in particular, a physical interpretation of the intensity function which is extensively employed in PHD filtering. Several examples of point processes are given next and the TWS-PHD filter is briefly presented. The TBD-PHD filter for phased-array observations is derived for point-targets with Gaussian source signals and noise. The derivation of the TBD-PHD filter involves the notion of marked point processes, which is also briefly presented.

Chapter IV presents the TBD-CPHD filter for phased-array observations. The chapter presents the SIRV model and subsequently the joint-SIRV array model, which is validated by statistical tests conducted on real-sonar data. The test results are presented in Appendix H. The extended, or angularly-distributed, target model is presented next. The derivation of the CPHD filtering equations follow, and again involve marked point processes. The derivation of the importance distributions together with a detailed description of the particle filter implementation are given. Results on simulated phased-array data showcase the performance increase of the proposed filter as compared to state-of-the-art PHD and CPHD filters for array processing. Comparisons with classical array-processing methods are given in stationary and mildly non-stationary scenarios, as well as comparisons of tracking performance for rapidly evolving targets (highly non-stationary scenarios). Conclusions and perspectives are given in Chapter V.

Chapter II

Sonar echo tracking: a data-association approach

... essentially, all models are wrong, but some are useful ...

George Edward Pelham Box

II.1 Introduction: Objectives and challenges

In this chapter, we present a post-processing technique for reconstructing sea-bottom topography (i.e. the bathymetry) in a multi-path and highly-reverberant underwater environment. Bathymetry is defined as a 3-D reconstruction of the underwater sea-bottom, i.e. an estimated depth map. For sidelooking sonar arrays, bathymetry is achieved by estimating the Direction Of Arrival (DOA) of the echo backscattered by extended-targets such as the sea-floor or various structures [12], [10]. Interferometry [39] and other array-processing methods [40, 41] are employed to estimate the DOA of the sea-floor backscattered wave for each time sample t. As seen in Fig. II.1, from the estimated DOA $\hat{\theta}_t$ the local bathymetric height is recovered from the following equation

$$\hat{h}_t = H - d_t \cos\left(\Psi^c + \hat{\theta}_t\right), \tag{II.1}$$

where $\Psi = \frac{\pi}{2} - \Psi^c$ represents the tilt of the antenna array and H the sonar altitude. All variables presented in Fig. II.1 are taken to be positive. Notice the direct mapping between the time samples t and the slant-range bins $d_t = \frac{ct}{2}$, given the acoustic-wave celerity c.

Shallow-water environments present several issues, such as multi-path propagation [8] and reverberation, the latter representing a complex mixture of unpredictable reflections and acoustic-wave diffraction. The DOA of secondary echoes is not linked to the bathymetric height by means of Eq. (II.1), the latter being valid only for direct Line-Of-Sight (LOS) echoes. Indeed, the knowledge of the full echo trajectory, including sea-surface state and number of reflections is necessary for such an equation. Since such information is unavailable, only LOS echoes are considered informative. Other echoes are considered as interferences and are collectively referred by clutter. In sonar-imaging applications, the negative impact of multi-path propagation on side-scan images and bathymetric reconstructions has been noted in [13–15]. More specifically, secondary echoes lead to *spurious* (false) elevation points in the reconstructed surface, caused by the locally stronger intensity of the interfering echoes. Usually, such spurious points are eliminated by a bathymetry *clean-up step* [42]. Such procedures eliminate spurious elevation points from the estimated depth map. However, this leads to missing depth estimates that are interpolated from the neighboring points, leading to a loss in resolution. In [13] sonar-array design strategies are proposed that minimize the effect of sea-surface originated echoes. Other array-design methodologies are given in [43]. In [14], the authors investigate adaptive beamforming performance in multi-path shallow waters. A low-complexity multi-source beamforming and multi-target tracking algorithm is provided in [44]. The algorithm tracks a fixed number of targets starting from initial estimates of target locations.

In some cases [45–48], whenever environment parameters are known (or learned) beforehand, reverberation and multi-path are directly modeled and taken into account. However, such parameters are often unknown and possibly involve the desired bathymetry. For aerial acoustics, in [49], a single-speaker tracking algorithm is proposed for reverberant and multi-path indoor environments. In [50] a multiple speaker tracking and separation algorithm is proposed for reverberant environments.

We propose an adaptive signal post-processing filter for real-time high-resolution bathymetry. The filter is capable of extracting several echoes in clutter and hence resolve layover. The basic idea of our approach is to use the neighborhood information to determine the bottom, in a way that preserves resolution, instead of posteriorly removing incoherent bathymetry estimates. By

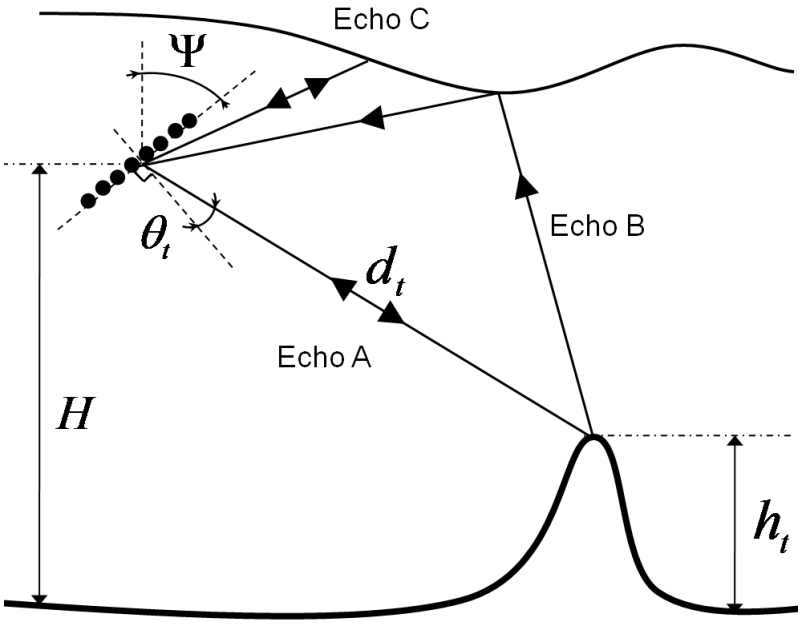

Figure II.1: Underwater scenario.

exploiting the spatial diversity of the receiving array, pre-processing methods achieve angular separation of the impinging echoes and yield a number of echo DOA estimates. Some of the pre-estimated DOA estimates represent the bathymetrically informative DOAs (i.e. DOAs belonging to the sea-floor or infrastructure echoes), while others represent false estimates caused by clutter. It is said that the measured DOAs present *origin uncertainty*, i.e. the DOA origin is unknown. The uncertainty is resolved by Probability Data Association (PDA) methods such as the Nearest-Neighbor PDA Filter (NN-PDAF). Hence, there is no resolution loss due to point interpolation, as long as the pre-processing module offers DOA estimates of bathymetric echoes and not just clutter. The NN-PDAF employs a predictive model for the evolution of echo DOA trajectories to effectively track bathymetric echoes. The proposed model takes into account the Signal to Noise Ratio (SNR) of sonar received signals, the existence of multiple DOA trajectories and the clutter generated by multi-path and volume reverberation. Also whenever persistent clutter is present [25], such as detections generated by secondary echoes, they should be considered as a secondary track alongside with the main sea-bottom track. Intuitively, whenever the secondary source is not taken into account, its power will contribute to the *background* noise and degrade the overall SNR ratio. To overcome this drawback, secondary sources are often modeled as separate tracks.

In practice, echo trajectories switch between several identifiable trends in accordance with the backscattering surface geometry: smooth horizontal or vertical, or highly irregular. In accordance, a parallel-model method for DOA tracking is needed, where each model is tuned for a specific trend. Thus, we derive novel geometrical models to cope with nearly flat and horizontal sea-bottoms and nearly vertical objects. Random walk (RW) models have been proposed for DOA tracking (see for instance [51]) and represent a robust prior with no preferred direction of evolution. An Interacting Multiple Model (IMM) fusion method is employed within the NN-PDAF, resulting in the NN-IMM-PDAF algorithm. IMM detects model switching and identifies the predominant model, thus offering supplementary information about the reconstructed surface, i.e. a geometrical segmentation of the surface. This geometrical segmentation could be employed as an aid for shape/object recognition algorithms.

A measure of trajectory quality, the trajectory existence probability, is employed to detect trajectory extinction over shadow areas, as discussed below, leading to the Integrated NN-IMM-PDAF (NN-IMM-IPDAF). Sonar data acquired in a shallow-water canal is processed with the proposed models and results are validated by goodness-of-fit tests. Goodness-of-fit test have the advantage of being conducted without the need of ground-truth data and thus provide an on-line evaluation of the models used for bathymetry reconstruction. In particular, the random-walk model, when employed solely, is shown to be inadequate and systematically rejected by goodness-of-fit tests.

To summarize, the novelty of our approach is threefold:

- Firstly, we propose real-time adaptive processing based on a state-space description. In other words, tracking the DOA trajectories of echoes impinging the sonar array to obtain a filtered (reduced-variance) 3D reconstruction and avoid multi-path and clutter problems (preserving resolution).

- Secondly, we derive several innovative geometrical models for the underlying DOA trajectories. The derived models are employed in a parallel framework to increase the adaptability of our processing.

- Thirdly, an Integrated NN-IMM-PDA filter is proposed to filter multiple targets (echoes) with the proposed multiple models and provide trajectory existence probabilities.

The proposed post-processing algorithm is based on the Unscented Kalman Filter (UKF), which has real-time implementations. Furthermore, since DOA estimates are often available at

the output of commercial echo-sounding systems, the proposed post-processing approach can be easily incorporated into the existing processing chain. The algorithm can be readily utilized in conjunction with already field-equipped SONAR systems, without the need of hardware or software modifications. This is possible, since the proposed method represents an additional processing module after raw-data array processing, which commercial sonar systems already use for real-time visualization purposes. Secondary echoes carry information linked to the sea surface that our proposed algorithm aims to retrieve.

The chapter is organized as follows. Sec. II.2 presents the challenges of shallow-water environments and the pre-processing module. In Sec. II.3 we develop the post-processing, i.e. tracking, module that consists in prediction (Sec. II.3.1), update (Sec. II.3.2), and the track existence probability (Sec. II.3.3). The geometrical models employed to track bathymetric echoes are introduced in Sec. II.4. Section II.5 showcases the results of the proposed filtering chain on simulated sonar data (Sec. II.5.1) and on real sonar data (II.5.2). We conclude in Sec. II.6.

II.2 Underwater environment and pre-processing module

Side-scan sonar systems have been an invaluable tool for providing high-resolution images of large swaths (e.g. 100 meters) of the sea-floor. Side-scan systems work by emitting a pulse - called ping. The array beam is is designed to be wide in the elevation plane but narrow in the azimuth plane, so as to insonify a fine strip of the sea floor at each emission. However, the beam being wide in the elevation plane, also interacts with the sea-surface, generating interference echoes (surface reverberation). Given the state of the sea-surface, interference echoes vary from specular reflections to diffuse scattering. The acoustic-wave propagation is nearly spherical, both forwards and backwards, and points located at the same distance are received at the same moment with different DOA. On the other hand, the acoustic wave does not insonify some parts of the bottom (e.g. in presence of tall objects), thus creating "acoustic shadows". Recently, constructors started fitting several receiving elements on side-scan systems, providing not only amplitude images of the sea-floor backscatter but also bathymetric estimates. Such systems are usually called interferometric or bathymetric side-scan sonars [11, Ch.3.3.1]. The sonar employed in this work is the EdgeTech 4600, which disposes of $N = 8$ half-wavelength, linearly spaced receivers. The sonar operates by emitting a linear frequency modulated pulse, where the pulse bandwidth was set to $10kHz$ with the carrier frequency being $540kHz$. Other sonar specifications are given in [6] and Appendix G.

Array processing algorithms are employed to estimate the DOA parameters θ_t^i with $i = 1, \cdots, n_t$, of n_t sources of acoustic waves, directly from the phased-array signal:

$$\mathbf{y}_t = \sum_{i=1}^{n_t} \mathbf{a}(\theta_t^i) s_t^i + \mathbf{n}_t, \tag{II.2}$$

where $\mathbf{y}_t \in \mathbb{C}^{N\times 1}$ represents the signal received at time t by the $N-$element array. s_t^i represents the $i-$th source signal and $\mathbf{n}_t \in \mathbb{C}^{N\times 1}$ the added noise. The array manifold vector $\mathbf{a}(\theta_t^i)$, for a far-field and narrow-band source[1], is defined as:

$$\mathbf{a}(\theta_t^i) \triangleq \begin{bmatrix} 1 & e^{-2\pi\jmath \frac{\Delta}{\lambda}\sin(\theta_t^i)} & \cdots & e^{-2\pi\jmath (N-1)\frac{\Delta}{\lambda}\sin(\theta_t^i)} \end{bmatrix}^T, \tag{II.3}$$

where $\{\cdot\}^T$ represents the transpose operator. Throughout this work, we assume a Uniform Linear Array (ULA) with N receivers and inter-receiver spacing of Δ. λ represents the acoustic wavelength.

[1] Verified for the EdgeTech 4600 sonar, see Appendix G.

Array processing algorithms, e.g. conventional beamforming, Capon beamforming or MUSIC [41], are used in conjunction with model-order selection tools to detect the number of sources (i.e. echoes) present in the array signal $\mathbf{y}_t$. Traditionally in the array-processing literature, the estimation of n_t is conducted by means of information theoretic criteria, e.g. Akaike Information Criterion (AIC), Bayesian Information Criterion (BIC), Minimum Description Length (MDL). Given the estimate $\hat{n}_t$ of the number of sources, the DOA estimates are obtained as the $\hat{n}_t$ highest "peaks" (i.e. local maxima) of some spectrogram $\mathcal{S}(\theta, t)$:

$$Z_t \triangleq \text{argmax}_{\theta_1,\cdots,\theta_{\hat{n}_t}} \mathcal{S}(\theta, t), \tag{II.4}$$

where the estimated DOAs are considered to form the set Z_t, called observation set. Note that other elements can be appended to the estimated DOAs, such as the values taken by the spectrogram at the local maxima. For simplicity however, such elements are not considered here. The spectrogram $\mathcal{S}(\theta, t)$, obtained from the phased-array signal $\mathbf{y}_t$, represents the time (or slant range) evolution of the angular distribution of power. $\mathcal{S}(\theta, t)$ is specific for each array-processing method, see [41] for the different constructions. $\text{argmax}_{\theta_1,\cdots,\theta_{\hat{n}_t}}$ has to be read "the arguments θ of the $\hat{n}_t$ highest peaks in $\mathcal{S}(\theta, t)$".

The proposed pre-processing module is composed by an information-theoretic criterion (either AIC, BIC or MDL) used in conjunction with MUSIC or the Capon beamformer in order to obtain an estimated DOA set Z_t in Eq. (II.4). As shown in Fig. II.2, which is analyzed in detail in the following paragraphs, the set contains spurious DOA estimates alongside the sea-floor echo DOA. If the DOAs of set Z_t are transformed to depth estimates, we obtain a spurious bathymetry map. Indeed, the role of the post-processor of section II.3 is to alleviate these problems without resolution loss. First shown in [52], the AIC and MDL involve the eigenvalue decomposition of the covariance matrix of the array signal. This operation is also required by the MUSIC algorithm [53] and the Capon beamformer [54]. They are preferred to conventional beamforming that offers poor angular resolution capabilities. Interchangeably, the Capon and MUSIC DOA estimators are used as the pre-processing module throughout Sec. II.5.2 to showcase the flexibility of the proposed post-processor. Also note that in [49] and [50], the authors propose a two stage processing algorithm. For [49], the first stage consists in Time Difference Of Arrival (TDOA) estimation. The authors also note the presence of clutter, or false TDOA estimates resulting from the presence of reverberation and multi-path. Subsequently, the estimated TDOA are filtered by an extended Kalman particle filter in the second stage. While in [50] the first stage comprises independent-component analysis to demix the the speaker signals, and a state coherence transform to obtain DOA estimates for the signals. Again, the noisy DOA estimates are uncertain, and contain clutter due to reverberation. Tracking is conducted by the probability hypothesis density filter in order to cope with a varying number of speakers.

In Fig. II.2 a) we can observe the angular spectrum (i.e. angular distribution of power) obtained with the Capon beamformer [54], of one ping of the array received signal, with the same configuration as in Fig. II.1. We can notice several highly-energetic echoes labeled from **A** to **D**. The main sea-floor echo is labeled **A**, and has an arch-like shape typical of a flat and horizontal sea floor. The echo labeled **B** represents the DOA of a wave resulting from a path involving scattering on the sea floor and a reflection over the sea surface, depicted in Fig. II.1. Such a path is slightly longer than the LOS path of the main sea-floor echo, amounting for the slight delay between the beginning of echoes **A** and **B**. Furthermore, echo **B** has an arch-like shaped DOA curve but in the opposite direction as compared to echo **A**, this is explained by the origin of echo **B** - the sea surface which generates an echo of opposite DOA variation as the bottom echo. A very weak echo **C** is seen in the water column zone (i.e. before the echo **A** reaches the array antenna) and exhibits the same reversed arch-like shape. The wide opening (of about 100^o) in the elevation plane of the emission beam, coupled with the pole-mounted configuration (i.e. close to the sea surface) of the sonar, leads to the scattering of the emitted

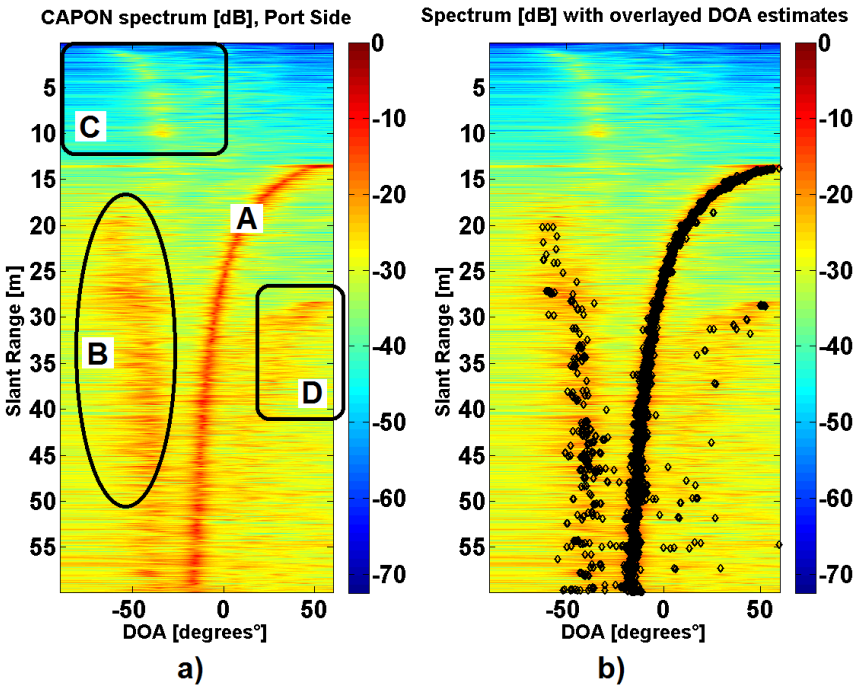

Figure II.2: Angular spectrum showing multiple echoes impinging the sonar array.

pulse from the sea surface, with the resulting echo **C** arriving before **A**. Echo **D** is a double sea-floor echo, that travels twice the round trip time of echo **A**.

In Fig. II.2 b) we observe DOA estimates overlaid on the same spectrum as before. The DOA estimates were obtained simply by selecting the maximum value for each slant range beam. Such a detection strategy is equivalent to that encountered in the frequency-estimation problem of time-series [55,56]. We observe the high number of spurious DOA estimates mainly caused by the persistent clutter which forms echo **B**. The full DOA trajectory of echo **A** cannot be retrieved only with the spectrum amplitude information, as we have seen the intensity of interfering echos is locally more stronger than the bathymetrical informative echo **A**. Additional *a priori* information is needed upon the evolution of the sea-floor backscattered wave in order to separate it from clutter echoes. Regularity conditions, such as limiting the allowed variation of the DOA estimates for echo **A**, effectively involve processing each DOA estimate in relationship to its preceding/following estimates by means of filtering/smoothing techniques. Such algorithms track only the desired DOA curve by employing a space-state description, thus avoiding clutter induced estimates. Space-state representations offer a Bayesian framework which easily takes into account prior models upon the evolution of the targets of interest (i.e. echoes) within the state-space equations. The set Z_t (see Eq. (II.4)) contains estimated DOAs, which represent observations in our state-space description. Thus, we refer to Z_t as a measurement or observation set. The observation set elements are said to suffer from origin uncertainty, since the exact origin (echo **A** or clutter), of each of the estimated DOA contained in Z_t is unknown. Bayesian state-space processors offer a framework that easily takes into account prior models upon the evolution of the targets of interest, i.e. the echoes of interest. The post-processor, derived in the next sections, relies on the observation sets provided by the pre-processor. This enables post-processing of spectrograms issued from the sonar data.

II.3 Post-processing module: the NNIPDA-UKF filter

This section presents the post-processing module, that is responsible with filtering multiple echoes (i.e targets) from the set of observations obtained by the pre-processor. We consider a number n_t of independent targets with system states denoted as $\{\mathbf{x}_t^i\}_{i=1}^{n_t}$. Since the trajectories of individual targets are considered independent, echo tracking can be conducted separately on each individual target state. For the $i-$th echo, the state system is given by the state-transition equation (II.5a) and the observation equation (II.5b)

$$\mathbf{x}_t^i = f_t(\mathbf{x}_{t-1}^i) + \mathbf{v}_t^i, \tag{II.5a}$$

$$\mathbf{z}_t^i = \mathbf{H}_t\mathbf{x}_t^i + \mathbf{w}_t^i, \qquad i = 1, \cdots, n_t, \tag{II.5b}$$

where the state vector $\mathbf{x}_t^i \in \mathbb{X}$ takes values in the state space $\mathbb{X}$. For the sake of generality, we consider $\mathbf{x}_t^i$ as a vector of dimension d_x and $\mathbb{X} \subseteq \mathbb{R}^{d_x}$. However, in sections II.4 and II.5, we will consider more specific models (e.g. $\mathbf{x} = \theta$). The state transition function $f_t(\cdot)$ represents an added prior, i.e. a model on the DOA trajectory. The covariance $\mathbf{Q}_t^i$ of the model noise $\mathbf{v}_t^i$ controls the confidence in the model. The notation $\mathbf{x}_t^i$ is kept for the sake of coherence with the tracking and dynamical-systems literature. $\mathbf{z}_t^i$ is the system noisy observation supplied by the pre-processing module, as discussed in the previous section. $\mathbf{H}_t$ is the observation matrix. Whenever, the observation $\mathbf{z}_t^i$ only consists in maxima locations of the spectrogram (as depicted in Eq. II.4), the observation reduces to a scalar and $\mathbf{H}_t = 1$. The observation noise $\mathbf{w}_t^i$ with variance $\mathbf{R}_t^i$ depends on the acquisition parameters and the pre-processing module. The noise sequences $\mathbf{v}_t^i$ and $\mathbf{w}_t^i$ are independent, white random processes characterized by their first two moments. Trajectory initialization is usually done by the "two out of three" heuristic rule, in other words, two observations falling inside a given gate within three consecutive range bins are assumed to represent a target. However, automatic trajectory initialization is beyond the scope of this chapter.

The pre-processing module detects the presence of a target (i.e. an echo) having state $\mathbf{x}_t^i$, with non-unitary probability of detection $p_D(\mathbf{x}_t^i)$, and estimates the DOA of the target. Conditioned on the target state, $p_D(\mathbf{x}_t^i)$ is by definition

$$p_D(\mathbf{x}_t^i) \triangleq Pr\{\mathbf{z}_t^i \in Z_t | \mathbf{x}_t^i\}. \tag{II.6}$$

$p_D(\mathbf{x})$ conveys the fact that $\mathbf{z}_t$ may not belong to the $\hat{m}_t$ maxima of $\mathcal{S}(\theta, t)$. In other words, the backscattering amplitude of the trajectory can be less than the largest $\hat{m}_t$ maxima. Furthermore, Z_t possibly contains clutter (false) DOA estimates since interfering echoes are present along the bathymetrically informative observation $\mathbf{z}_t$. Performance analysis of model-order estimators in array processing, involving AIC or MLD penalties, have been presented in [57, 58]. In [59], the dependence of p_D on the state $\mathbf{x}$ was analyzed and addressed at the expense of increased algorithmic complexity. For the applications considered in this chapter, employing $p_D = p_D(\mathbf{x}) = 0.9 \, \forall \, \mathbf{x} \in \mathbb{X}$ provides a compromise between performance and computational complexity.

The objective of model-based filters is to obtain an estimator $\hat{\mathbf{x}}_{t|t}^i \triangleq \mathbb{E}\{\mathbf{x}_t^i | Z_{1:t}\}$ of the state $\{\mathbf{x}_t^i\}_{i=1}^{n_t}$ given the sequence of current and past observations, denoted by $Z_{1:t}$. In the tracking literature, the sequence of filtered state vectors $\hat{\mathbf{x}}_{t|t}^i$ is usually called trajectory or track. All recursive filtering algorithms consist in two phases: prediction and update. Prediction aims to obtain an estimate $\hat{\mathbf{x}}_{t|t-1}^i$ by using the target model. The update step acts like a correction to the predicted state value $\hat{\mathbf{x}}_{t|t-1}$, by incorporating the current observation Z_t to obtain $\hat{\mathbf{x}}_{t|t}$. The magnitude of the correction takes into account the noise covariances $\mathbf{Q}_t$ and $\mathbf{R}_t$. In the case of Gaussian processes $\mathbf{w}_t$ and $\mathbf{v}_t$, and linear $f_t(\cdot)$, the Kalman [60] filter offers the Minimum Mean Squared Error (MMSE) estimator as closed-form equations for both the prediction and

the update step. Whenever the noises are only characterized by their first two moments, the Kalman filter supplies the optimal linear MMSE from the family of linear estimators. Furthermore, for non-linear systems, a sub-optimal but computationally attractive solution is given by the Unscented Kalman Filter (UKF) [61, 62]. The UKF only requires the first two moments of the noise terms $\mathbf{v}_t$ and $\mathbf{w}_t$. Indeed, the UKF only supposes uni-modal distributions, the Gaussian hypothesis not being strictly required. The mean-squared estimates supplied by the UKF amount to an approximate posterior distribution. To validate the model of Eqs. (II.5a) and (II.5b) and the aforementioned hypotheses, we employ Goodness-of-Fit (GoF) tests on simulated and real data.

Remote-sensing systems often produce measurements with uncertain origin, that might not originate from the target of interest. For example, the set Z_t [Eq. (II.4)] contains $\mathbf{z}_t^i$ with probability $p_D(\mathbf{x}_t^i)$. However, there is no information relating a specific element $\mathbf{z}_t^j \in Z_t$ to $\mathbf{x}_t^i$ and thus, the straightforward application of the Kalman or UKF filters is not feasible. Data association methods have been developed to deal with the ambiguities of single or multiple targets in clutter. Efficient filtering of single targets in cluttered environments often relies on the Probabilistic Data Association (PDA) filter [26], and the more recent Integrated PDA (IPDA) filter [63–65]. Both algorithms assume the following hypothesis: in one range bin, one target can produce at most one detection, spurious observations or clutter can also be detected inside the same bin. Note, that this hypothesis was also (silently) supposed in the introduction of this chapter. In [66] the aforementioned hypothesis is replaced by a many-to-one association: one target can spawn several observations in the same range bin caused by multi-path propagation in over-the-horizon radar applications. In our case this is deemed not possible, since the different paths have different lengths and will always create observations in different range bins. Furthermore, echo **B** is considered surface-originated rather than bottom-originated.

The aim of the PDAF is twofold. First, to regularize the sequence of DOAs given by the pre-processing module (see Sec. II.2), with the added prior of the state evolution equations. The magnitude of the regularization is given by the ratio of the two noise terms $\mathbf{v}_t$ and $\mathbf{w}_t$. And second, to "eliminate" false observations by means of the PDA module. To achieve this, the PDAF computes a sub-optimal conditional pdf of the filtered state $\hat{\mathbf{x}}_{t|t}^i$ using an MMSE approach: all observation-to-track associations are enumerated and assigned a probability. The overall estimated state is the weighted sum of individual association estimates with their respective probability. Such an estimation procedure is sometimes called *soft* association, as opposed to *hard* association where only the association with highest probability is employed [67, Ch.1]. Furthermore the state covariance matrix $\mathbf{P}_{t|t}^i \triangleq \mathbb{E}\{(\mathbf{x}_t^i - \hat{\mathbf{x}}_{t|t}^i)(\mathbf{x}_t^i - \hat{\mathbf{x}}_{t|t}^i)^T\}$ is increased to incorporate the origin incertitude of measurements. The optimal MMSE filter requires the propagation of a Gaussian mixture pdf [26] of the state vector while the PDAF propagates only a Gaussian approximation, i.e. mean and covariance approximations. This makes possible for the PDAF to compute the filter gain in a similar manner to the Kalman or UKF filters. An overview of the PDAF equations can be found in Appendix A.

In shallow waters, the ambient-noise levels are subject to large variations [68, Ch 7.3]. In order to increase the adaptability of our proposed filter, an estimator of the observation-noise covariance $\mathbf{R}_t$ is derived from the filtering residuals (see Proposition B of Appendix B). Indeed, the filtering residuals have a double purpose in our approach. On one hand their covariance is indicative of the observation noise variance $\mathbf{R}_t$, and on the other hand they are employed to validate the filters and models employed in our approach. Residual whiteness is indicative of the adequacy of the model in predicting the echo DOA. Model-validation results are presented in Sec. II.5. Adaptive estimators for the model noise covariance $\mathbf{Q}_t$ have also been proposed in [69] and [70, Ch. 8.4]. However, the adaptive estimator for $\mathbf{Q}_t$ is significantly more complex than for $\mathbf{R}_t$, thus we consider $\mathbf{Q}_t$ as a user defined parameter.

The IPDAF represents an extension of the PDAF, and employs the same PDA logic to

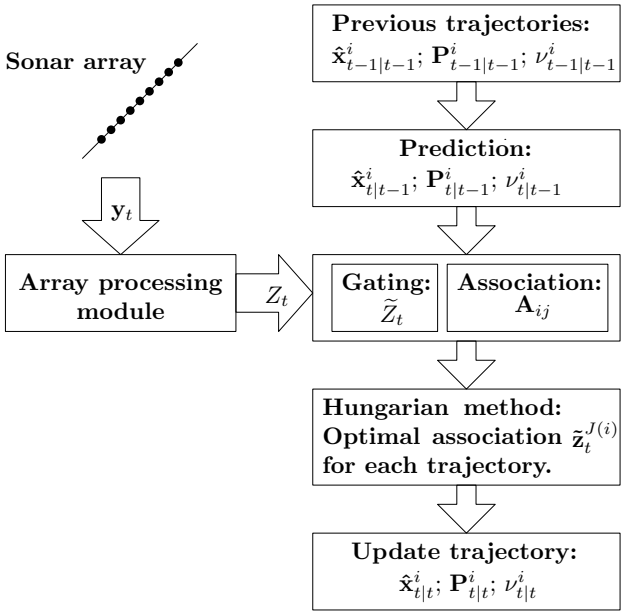

Figure II.3: Flowchart showcasing the different stages of the proposed algorithm.

alleviate observation uncertainty. The aim of IPDA filter is not only a recursive calculation of the state mean and covariance in presence of origin uncertainty, but also a recursive calculation of a track existence probability ν^i_t. Such a measure is useful in assessing the quality of the track and effectuate automatic track deletion whenever the track probability drops below a given threshold. This is useful for tracking bathymetry echoes over shadow areas, where the echo exhibits interruptions. The IPDAF computes $\nu^i_{t|t}$, given the set of observations $Z_{0:t}$, in a recursive manner. The IPDA prediction and update equations, and a detailed derivation of the existence probability $\nu^i_{t|t}$, are given in Appendix A. Based on the IPDAF, in the following section, a specific multiple target filter is derived.

To summarize, the aim of our multi-trajectory filtering approach is threefold:

- Firstly, to regularize DOA trajectories and reduce the state variance by employing convenient priors in the state-evolution Eq. (II.5a). This is achieved in the prediction step of Section II.3.1.
- Secondly, to resolve observation incertitude by observation-to-trajectory association and extracting only informative trajectories. Observation-to-trajectory association is carried out in the update step of Section II.3.2.
- Thirdly, to compute a trajectory quality measure $\nu^i_{t|t}$, in order to detect interruptions caused by acoustic shadows. This is achieved by a trajectory existence probability, presented in Section II.3.3.

A schematic representation of the proposed algorithm is given in Fig. II.3.

II.3.1 Prediction

Considering the non-linear state-transition function $f_t(\cdot)$, we employ the unscented transform to obtain approximate values for the predicted mean and covariance. The principle of the unscented transform is to use a small number of deterministic samples, called sigma points, to characterize the posterior at time $t-1$. The sigma points capture exactly at least the first two moments of the posterior, and are propagated through the non-linear system to obtain approximate values of the posterior moments at time t. The pair: $\left(\mathbf{x}^{i,k}_{t-1|t-1}, w^{i,k}_{t-1|t-1}\right)$ are referred to as a sigma point

and corresponding sigma weight. The set of sigma points and weights capture the first moments of the posterior pdf at time $t-1$ of the i-th target. Starting from the posterior estimates, mean $\hat{\mathbf{x}}^i_{t-1|t-1}$ and covaraince $\mathbf{P}^i_{t-1|t-1}$, the unscented transform [71, Ch.6.2] leads to the sigma points

$$\mathbf{x}^{i,k}_{t-1|t-1} = \begin{cases} \hat{\mathbf{x}}^i_{t-1|t-1} & \text{if } k = 0, \\ \hat{\mathbf{x}}^i_{t-1|t-1} + \left(\sqrt{(1+\mathcal{K})\mathbf{P}^i_{t-1|t-1}}\right)_k & \text{if } k = 1, \cdots, d_x, \\ \hat{\mathbf{x}}^i_{t-1|t-1} - \left(\sqrt{(1+\mathcal{K})\mathbf{P}^i_{t-1|t-1}}\right)_{k-d_x} & \text{if } k = d_x+1, \cdots, 2d_x, \end{cases} \tag{II.7}$$

where $\mathcal{K}$ is a scaling constant and $\left(\sqrt{\mathbf{M}}\right)_k$ represents the k-th column of the matrix squared-root of $\mathbf{M}$. d_x represents the dimension of the state $\mathbf{x}_t$. Note that for a scalar state, i.e. $\mathbf{x}_t = \theta_t$, only 3 sigma points are necessary resulting in very low complexity filters as compared to particle filter methods. The associated weights of the sigma points of Eq. (II.7) are given by:

$$w^{i,k}_{t-1|t-1} = \begin{cases} \frac{\mathcal{K}}{2(1+\mathcal{K})} & \text{if } k = 0, \\ \frac{1}{2(1+\mathcal{K})} & \text{if } k = 1, \cdots, 2d_x. \end{cases} \tag{II.8}$$

The predicted values for target i are obtained by averaging the propagated sigma points:

$$\hat{\mathbf{x}}^i_{t|t-1} = \sum_{k=0}^{2d_x} w^{i,k} f_t(\mathbf{x}^{i,k}_{t-1|t-1}), \tag{II.9a}$$

$$\mathbf{P}^i_{t|t-1} = \sum_{k=0}^{2d_x} w^{i,k} \left(f_t(\mathbf{x}^{i,k}_{t-1|t-1}) - \hat{\mathbf{x}}^i_{t|t-1}\right)^2 + \mathbf{Q}^i_t, \tag{II.9b}$$

$$\mathbf{S}^i_{t|t-1} = \mathbf{H}_t \mathbf{P}^i_{t|t-1} \mathbf{H}^T_t + \mathbf{R}^i_t, \tag{II.9c}$$

where $\hat{\mathbf{x}}^i_{t|t-1}$ is the predicted state; $\mathbf{P}^i_{t|t-1}$ is the predicted state covariance; $\mathbf{S}^i_{t|t-1}$ represents the covariance of the predicted measurement, or equivalently, the covariance of the innovation term. For the specific system of Eqs. (II.5a) and (II.5b), the Kalman filter gain is given by

$$\mathbf{K}^i_t = \mathbf{P}^i_{t|t-1} \mathbf{H}^T (\mathbf{S}^i_{t|t-1})^{-1}. \tag{II.10}$$

To further reduce computation time and provide real-time bathymetry estimates, gating is performed on the observation set. Only validated observations, i.e. observations falling inside some predefined volume centered on the predicted values $\mathbf{x}^i_{t|t-1}$, are considered for trajectory update.[2] Formulas for validation-gate volumes $\mathcal{V}_t$, and the probability of an observation falling inside the validation gate, called gate probability p_W, are given in [25, Ch. 6.3]. p_W is defined by the following equation

$$p_W = \int_{\mathcal{V}_t} p(\mathbf{z}|Z_{1:t-1}) d\mathbf{z}, \tag{II.11}$$

where $p(\mathbf{z}|Z_{1:t-1})$ represents the *apriori* pdf of the predicted observation at time step t. $p(\mathbf{z}|Z_{1:t-1})$ has first moment $\mathbf{H}_t \hat{\mathbf{x}}^i_{t|t-1}$ [from Eq. (II.9a)] and second moment $\mathbf{S}^i_{t|t-1}$ [from Eq. (II.9c)]. In practice, we suppose a Gaussian pdf for $p(\mathbf{z}|Z_{1:t-1})$ with the aforementioned moments. Now let the set $\widetilde{Z}_t$ of size $\tilde{m}_t$ denote the set of validated (also called gated) observations at time-step t and defined as

$$\widetilde{Z}_t = \{\tilde{\mathbf{z}}_t | \tilde{\mathbf{z}}_t \in Z_t \text{ and } p(\tilde{\mathbf{z}}_t|Z_{1:t-1}) \geqslant \mathcal{T}\}, \tag{II.12}$$

where $\mathcal{T}$ is a threshold corresponding to the gate volume $\mathcal{V}_t$. Thus, the set of gate-validated observations is a subset of the observation set, i.e. $\widetilde{Z}_t \subseteq Z_t$.

[2] Invalidated observations can be considered for creating new trajectories.

II.3.2 Update

Since in general there are several possible observations to update one trajectory, update is carried out using Probabilistic Data Association Filters (PDAF) proposed in [26] or the more recent Integrated PDAF (IPDAF) [63,65]. In the case of multiple trajectories, Joint PDA (JPDA) schemes have been developed. The JPDA association scheme employs a weighted average of observations to update each trajectory. As noted in [67, Ch.1], such updating procedures tend to cause closely spaced targets to coalesce, thus introducing bias. To counteract such situations, Nearest Neighbor PDA (NN-PDA) schemes were proposed in [67, Ch.1].

In order to associate an observation with a trajectory we propose a Nearest Neighbor Integrated PDA-UKF (NN-IPDA-UKF) that avoids trajectory coalescence problems. As proposed in [67, Ch.1], the probability $\mathbf{A}_{ij}$ of associating the gate-validated observation j to trajectory i, is approximated by

$$\mathbf{A}_{ij} = \frac{\mathbf{G}_{ij}}{a_{ti} + a_{oj} - \mathbf{G}_{ij}}, \tag{II.13}$$

where $\mathbf{G}_{ij}$ represents the Gaussian likelihood of the observation innovation:

$$\mathbf{G}_{ij} = \frac{1}{\sqrt{2\pi \det(\mathbf{S}^i_{t|t-1})}} \exp\Big(-\frac{1}{2} (\boldsymbol{\epsilon}^{i,j}_t)^T (\mathbf{S}^i_{t|t-1})^{-1} \boldsymbol{\epsilon}^{i,j}_t \Big), \tag{II.14}$$

where $\boldsymbol{\epsilon}^{i,j}_t = \tilde{\mathbf{z}}^j_t - \mathbf{H}_t \hat{\mathbf{x}}^i_{t|t-1}$ represents the innovation added by observation $\tilde{\mathbf{z}}^j_t$ to trajectory i; and $\mathbf{S}^i_{t|t-1}$ is the UKF innovation variance given in Eq. (II.9c). Once the $\mathbf{G}_{ij}$'s are computed for all n_t trajectories against all $\tilde{m}_t$ observations, the values of a_{ti} and a_{oj} in Eq. (II.13) are computed by

$$a_{ti} = \sum_{j=1}^{\tilde{m}_t} \mathbf{G}_{ij} \text{ and } a_{oj} = \sum_{i=1}^{n_t} \mathbf{G}_{ij}. \tag{II.15}$$

$\mathbf{A}_{ij}$ in Eq. (II.13) decreases whenever trajectory i correlates with observations other than j, or observation j correlates with trajectories other than i. In other words, whenever $\mathbf{G}_{ik}$ is high for observations $k \neq j$ or $\mathbf{G}_{kj}$ is high for trajectories $k \neq i$. a_{ti} and a_{oj} in Eq. (II.15) take into account these cross-correlations between trajectories.

We propose to update tracks with the most probable observations in the sense of $\mathbf{A}_{ij}$. Denoting by $\mathcal{D} = \{1, \cdots, n_t\}$ the set of all trajectory indices existing at time t and observations by $\mathcal{C} = \{1, \cdots, \tilde{m}_t\}$, the optimal measurement-to-trajectory association is given by the injective function $J : \mathcal{D} \longrightarrow \mathcal{C}$ that maximizes the functional:

$$\max \sum_{i=1}^{n_t} \mathbf{A}_{i\,J(i)} \tag{II.16}$$

The injective property for $J(\cdot)$ is necessary to prevent allocation of the same observation to multiple trajectories. Whenever $n_t > \tilde{m}_t$ this property cannot hold, thus additional null-observations are introduced, i.e. the empty-set $\emptyset$ association.

Such linear assignment problems are generally resolved with the Hungarian algorithm [72, Ch. 11]. The Hungarian algorithm finds the best one-to-one allocations given a set of allocation costs. Assignment is thus achieved with complexity $\mathcal{O}(\max(\tilde{m}_t, n_t)^3)$. In our case searching for the most probable allocations with the adaptation of the Hungarian algorithm is trivial. For any trajectory i, the best observation allocation is given by $\tilde{\mathbf{z}}^{J(i)}_t \in \widetilde{Z}_t$, or the empty set $\emptyset$. In the latter case no update is performed, while in the former case, update is carried out for each trajectory i:

$$\hat{\mathbf{x}}^i_{t|t} = \hat{\mathbf{x}}^i_{t|t-1} + \mathbf{K}^i_t \, \rho \, \boldsymbol{\epsilon}^{i,J(i)}_t, \tag{II.17a}$$

$$\boldsymbol{\epsilon}^{i,J(i)}_t = \tilde{\mathbf{z}}^{J(i)}_t - \mathbf{H}_t \hat{\mathbf{x}}^i_{t|t-1}, \tag{II.17b}$$

with $\boldsymbol{\epsilon}_t^{i,J(i)}$ representing the filter residual for trajectory i. This residual is also employed for goodness-of-fit tests, seen in Sec. II.4. The coefficient ρ is given in Eq. (II.18) and takes into account the non-ideal detection process [26]:

$$\rho = \frac{p_D \frac{\mathcal{V}_t}{\tilde{m}_t} \mathbf{G}_{iJ(i)}}{1 - p_D\, p_W + p_D \frac{\mathcal{V}_t}{\tilde{m}_t} \sum_{j=1}^{\tilde{m}_t} \mathbf{G}_{ij}}, \tag{II.18}$$

where $\mathcal{V}_t$ is the validation gate volume [25, Ch 6.3.2]. Observe that for an ideal detector, without gating and no clutter, i.e. $p_D = p_W = 1$ and $\tilde{m}_t = 1$, we have $\rho = 1$. ρ quantifies the likelihood of observation $\tilde{\mathbf{z}}_t^{J(i)}$ originating from trajectory i. Whenever this likelihood decreases, ρ decreases the Kalman gain $\mathbf{K}_t^i$ and the impact of the innovation term $\boldsymbol{\epsilon}_t^{i,J(i)}$ on the updated estimate. Equations for the "soft" update of the state vector and covariance are given in Appendix A. The "soft" update equations suppose a weighted average of all validated/gated observations, whereas in the aforementioned NN scheme, only the most probable observation is employed.

II.3.3 Trajectory quality measure

As stated in the introduction, an object on the sea bottom creates an acoustic shadow, where the corresponding trajectory estimates must not be considered for bathymetry reconstruction. In order to decide whether a trajectory is valid, we introduce an existence process. For trajectory i at time t, the trajectory existence process ζ_t^i is supposed to evolve according to a Hidden Markov Chain (HMC) with two internal states: TRAJECTORY EXISTS, denoted $\zeta_t^i = 1$ and TRAJECTORY DOES NOT EXIST, denoted $\zeta_t^i = 0$. The estimated trajectory existence probability is defined as $\nu_{t|t}^i = Pr\{\zeta^i = 1 | Z_{1:t}\}$ and represents a measure of quality associated with trajectory i. By thresholding $\nu_{t|t}^i$ we are able to extinguish trajectory estimates over shadow areas and terminate trajectories. The transitions between the Markov states are given by the transition matrix with elements $[\mathbf{\Pi}]_{kl} = \pi_{kl} \triangleq Pr\{\zeta_t^i = l | \zeta_{t-1}^i = k\}$ with $k, l \in \{0, 1\}$. Note that, for simplicity, we suppose a homogeneous HMC. However, IPDA filters can also cope with time-dependent transition probabilities. Typical values for these transition probabilities, also used throughout this chapter, are $\pi_{00} = \pi_{11} = 0.98$ [73]. In other words, transitions occur infrequently. $\mathbf{\Pi}$ is identical for all trajectories i.

A detailed derivation of the predicted and updated trajectory existence probability is given in Appendix A, while here we only recall the main results. The updated track existence probability $\nu_{t|t}^i$ is given by:

$$\nu_{t|t}^i = \begin{cases} \dfrac{1 - p_D\, p_W}{1 - p_D\, p_W\, \nu_{t|t-1}^i} \nu_{t|t-1}^i \text{ if } \quad \tilde{m}_t = 0, \\ \dfrac{1 - \delta_t^i}{1 - \delta_t^i\, \nu_{t|t-1}^i} \nu_{t|t-1}^i \text{ if } \quad \tilde{m}_t > 0, \end{cases} \tag{II.19}$$

where the predicted trajectory existence probability $\nu_{t|t-1}^i$ is given by:

$$\nu_{t|t-1}^i = \pi_{11} \nu_{t-1|t-1}^i + \pi_{01}(1 - \nu_{t-1|t-1}^i), \tag{II.20}$$

and $\delta_t^i = p_D\, p_W (1 - \frac{\mathcal{V}_t}{\tilde{m}_t} \sum_{j=1}^{\tilde{m}_t} \mathbf{G}_{ij})$. Note that the system-state estimate $\hat{\mathbf{x}}_{t|t}^i$ and trajectory existence probability $\nu_{t|t}^i$ are estimated separately from the observation sequence $Z_{1:t}$. Hence, the performance of the filter, in terms of $\hat{\mathbf{x}}_{t|t}^i$ efficiency, is not affected by the computation of $\nu_{t|t}^i$. The PDA module coupled with the trajectory quality measure, thus derived, is employed to track multiple echoes in cluttered environments and resolve shadow areas.

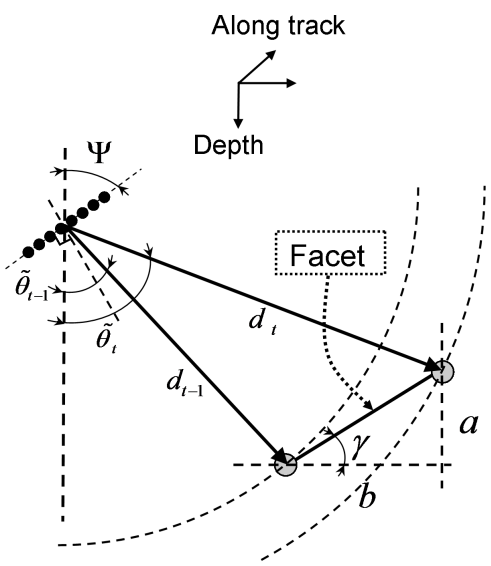

Figure II.4: Imaging geometry.

II.4 Geometrical models

In the previous section it was supposed that the target of interest, i.e. echo $\mathbf{A}$, behaves according to the model described in the state Eq. (II.5a). In this section we propose to derive such informative models, i.e. a model for $f_t(\mathbf{x}_{t-1})$, to describe the bathymetry, and propose a parallel-model framework to increase the adaptability of our system. The proposed models characterize the DOA trajectories of the bathymetry echoes. Furthermore, we consider the state of the system to represent the DOA trajectory, i.e. $\mathbf{x}_t = \theta_t$. In this case, the state noise $\mathbf{v}_t$ is a scalar random process. Furthermore, the observation set Z_t of Eq. (II.4) is comprised only of the local maxima of the spectrogram, hence the elements of Z_t and the observation noise $\mathbf{w}_t$ are scalars.

From Fig. II.2 we observe a clear trend in the evolution of the bottom DOA curve: an arch-shaped trend typical of flat-bottom returns. In such, an analytic relationship can be computed for this trend by considering the triangle of Fig. II.4

$$\tan(\gamma) = \frac{a}{b} = \frac{d_{t-1}\cos(\tilde{\theta}_{t-1}) - d_t\cos(\tilde{\theta}_t)}{d_t\sin(\tilde{\theta}_t) - d_{t-1}\sin(\tilde{\theta}_{t-1})}, \tag{II.21}$$

where γ represents the bottom slope. Note the relationship $\tilde{\theta}_t = \theta_t + \Psi^c$ between the DOA angle considered in this paragraph and the general DOA defined in Fig. II.1. The notation $\tilde{\theta}$ is employed to ease the interpretation of the angles in Fig. II.4. An equivalent writing of Eq. (II.21) is given by

$$d_t\cos(\tilde{\theta}_t - \gamma) = d_{t-1}\cos(\tilde{\theta}_{t-1} - \gamma). \tag{II.22}$$

The non-linear Eq. II.22 describes the transition function $\theta_t = f_t(\theta_{t-1})$ from the system Eq. (II.5a). In Fig. II.5 a) we observe the angular spectrum of a ping line with DOA estimates represented as black points and the red curve was generated using the perfectly flat and horizontal hypothesis for the bottom. Such a perfectly FHB is equivalent with using Eq. (II.22) as state-transition equation, with no model noise (i.e. $\mathbf{v}_t = \mathbf{0}$), for all t. The DOA estimates represent local maxima of the beamforming spectrum, the number of local maxima considered at one instant was given by the AIC criterion. Observe the large number of detections generated by the AIC in a reverberant environment. Indeed, in such environments, any small volume backscattering is detected by the AIC as a source of signal. Volume backscattering is usually

caused by a sharp change in the refraction index, e.g. generated by bio-mass in suspension, salinity and temperature gradients. Volume reverberation causes volume clutter, which forms the majority of the spurious DOA estimates. The surface clutter generated by the secondary echo **B**, often causes spurious bathymetry estimates (see Fig. II.2) since its intensity is stronger than that of the volume reverberation and occasionally stronger than the bottom backscatter. In Fig. II.5 b) we observe only the DOA estimates in black and the DOA curve generated by a perfectly FHB return in red. This model seems to offer a seemingly good fit for the DOA curve of echo **A**. Slight differences are noted at the beginning and end of the DOA curve. Intuitively, these could be dealt with by incorporating a non-zero model noise $v_t \neq 0$ forming the FHB-DOA model state equation:

$$\tilde{\theta}_t = \gamma + \arccos\{\frac{d_{t-1}}{d_t}\cos(\tilde{\theta}_{t-1} - \gamma)\} + v_t. \tag{II.23}$$

The model given in Eq. (II.23) incorporates a trend, capable of describing flat and inclined bottom returns. It also accounts for small deviations from constant slope. Indeed, depending on the noise magnitude $Q_t \triangleq \mathbb{E}\{v_t^2\}$, small deviations from the trend are allowed by the model noise. Note that the model noise v_t represents an angular noise and that an equivalent small-amplitude noise could be defined in Cartesian coordinates. In port and canal environments, nearly horizontal and nearly vertical slopes are often encountered. We propose to employ a nearly Flat and Horizontal Bottom (FHB) or a nearly Vertical Object (VO) model, corresponding to $\gamma = 0$deg and $\gamma = 90$deg in Eq. (II.23). Intuitively, both the nearly FHB and VO models are highly-informative priors for the evolution of the echo trajectories. Both FHB and VO are non-linear state-transition functions and require a UKF implementation of the IPDAF, presented in Sec. II.3.

FHB and VO models represent strong priors on the evolution of the echo DOA, and for moderate noise values, do not allow for strong deviations from a flat surface. In order to cope with such situations, a weak prior is proposed and employed in parallel with the aforementioned models. A random walk (RW) is employed as a weak prior on the evolution of DOA trajectories

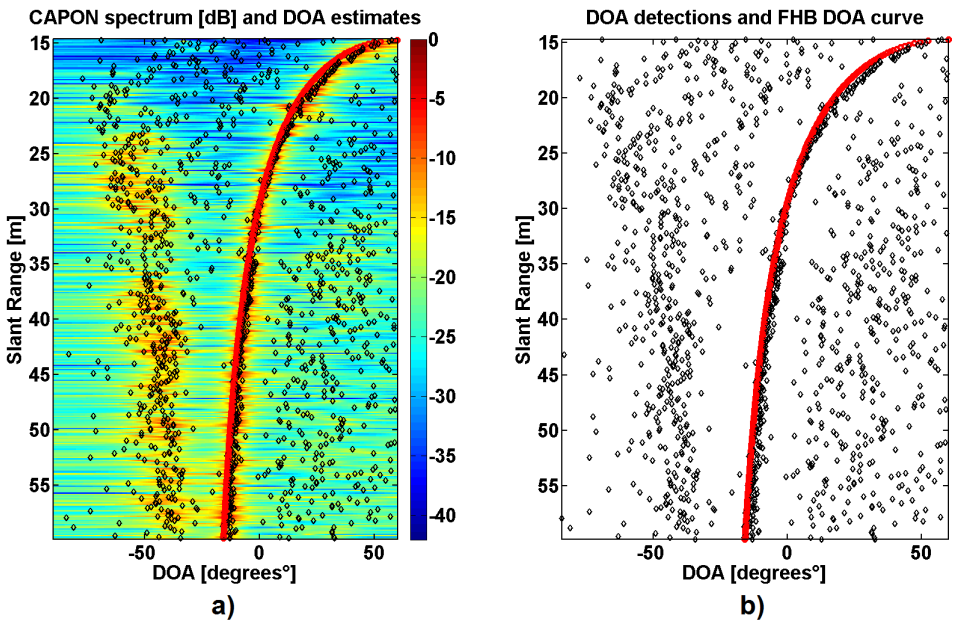

Figure II.5: a) Capon spectrogram with DOA observations (◊) and the perfect FHB trajectory (red curve). b) Only the DOA observations (◊) and the perfect FHB trajectory (red curve).

imposed by irregular sea-floor surfaces. The RW prediction equation is given by Eq. (II.24).

$$\theta_t^{\mathrm{RW}} = \theta_{t-1}^{\mathrm{RW}} + v_t^{\mathrm{RW}}. \tag{II.24}$$

The aforementioned RW-DOA model has been successfully used in the case of seismic echoes in [51]. Intuitively, the RW accepts with equal likelihood all values of θ_t equally distant from θ_{t-1}. In other words, the RW accepts any dynamical behavior that leads to a θ_t close to θ_{t-1} without any preferred direction. Except that it prohibits large magnitude jumps between consecutive θ_t values. Indeed, the RW model, being less informative than the FHB or VO model, represents a robust prior for the DOA evolution. However, RW models fail to precisely describe arch-like tendencies, clearly visible at the beginning of the sea-bottom echo in Fig. II.2 a). To ensure tracking of echoes over irregularities and capture the arch-like tendency, we propose to use a RW model alongside the two previously defined geometrical FHB and VO models.

Physical processes often evolve according to several identifiable trends, identified with different models. For example when tracking kinematic targets, such as aircraft or submarines, the usual models are constant speed, Wiener acceleration process or coordinated turn [25, Ch.4]. The generally accepted solution is to use all models working in parallel and processing the same sequence of observations. With each new observation, a measure of model adequacy, i.e. a probability is computed. Based on model probabilities, the instant of model switching can be estimated and also various schemes of model fusion can be defined. For example, in a MMSE approach the estimated state is a weighted combination of individual model-conditioned state estimates.

Several parallel-model processors have been proposed in the literature [74, Ch.11]. By far the most popular sub-optimal algorithm is the Interacting Multiple-Model (IMM) [73,75]. IMM supposes a bank of filters, each tuned to a specific model, processing the same observation time-series. The evolution of the DOA trajectory is supposed to evolve according to a HMC, where the internal states are the different models. In order to fuse individual model estimates, IMM computes model probabilities $\mu_{t|t}^i \triangleq Pr\{\text{Observation } \mathbf{z}_t \text{ generated by model } i | Z_{1:t}\}$ for each model i of the model set. The model-fused output of the IMM is a weighted mean of individual filters with the weights given by $\mu_{t|t}^i$. For a full algorithmic description we direct the reader to [74, Ch.11.6.6]. Useful information about the nature of the reconstructed bathymetry, i.e. flat-floor horizontal, vertical or irregular is obtained via the segmentation information conveyed by the model probabilities $\mu_{t|t}^i$ (see Fig. II.14 b)). In the presence of clutter PDA-type filters should be used to cope with clutter observation and non-unitary detection probability, giving birth to the IMM-PDA filter [76]. Also a track probability measure can be computed for the IMM-PDAF, in a similar fashion to the IPDAF, creating the IMM-IPDAF [64, 65]. Various multiple-target and multiple-model IPDA filters exist, we employ the NN-IPDAF (derived in Sec. II.3) with the IMM module to process real sonar data.

To validate the adequacy of our proposed model sets (FHB and RW for bottom, VO and RW for vertical objects), we employ Goodness-of-Fit (**GoF**) tests [77]. A review of major goodness-of-fit tests is presented in Appendix C. GoF tests the whiteness of the filtering residual sequence. The residual sequence is obtained as a filtering result (see Eq. II.17b), and is available for both simulated data and real data processing. Thus, GoF tests are usable for validating models in real data processing without the need for ground-truth data. Whenever the geometric model of Eq. (II.23) or the RW model of Eq. (II.24) proves inadequate at predicting the echo DOA trajectory, the residuals of Eq. (II.17b) increase and incorporate a trend: the difference between the hypothesized and observed trajectory. Such a trend introduces correlation between the residual samples. The whiteness of these residuals signifies that the model processor was successful in extracting the information contained in the observation time-series. The Box-Pierce [78] and the Ljung-Box [79] tests are considered. Both tests work by comparing the two hypothesis: H_0 white sequence and H_1 correlated sequence. In other words, H_0 conveys the fact

that there is no evidence against the models, while H_1 signals sufficient evidence against the employed models and perhaps a change is required. We also employ a simpler Out-of-Bound (OfB) test, first proposed in [80], and used extensively in [70, 71]. The OfB decides H_0 or H_1 whenever the number of times the residual-autocorrelation terms fall outside a given interval is less than, or grater than 5% of the total number of terms. Filtering results and GoF test results are presented in the following sections.

II.5 Results of NNIPDA-UKF

II.5.1 Simulated data results

Simulations are conducted to showcase clutter rejection, variance reduction of filtered DOA sequences, and more importantly model-validation results for the model-based processor. In the first scenario, a nearly flat and horizontal sea-floor is simulated. The signal $\mathbf{y}_t$ received by the antenna array, with DOA trajectory corresponding to the FHB model with $Q = 0.01\,\text{deg}^2$, is generated. In this way, the DOA trajectory resembles the arch-like curves observed in Fig. II.2. The SNR decreases from 20dB to 3dB from the beginning to the end of the echo, with the power variation taking into account geometrical spreading due to propagation and Lambertian scattering on the sea-bottom [81, Ch. 12.3.7]. Also the sonar array altitude is set to $H =$ 15m, and other parameters are matched with those of EdgeTech 4600 sonar used for the real data experiment. The MUSIC algorithm is employed to estimate the DOA, leading to the noisy observations z_t, see Eq. (II.4). Clutter is added to form the observation set Z_t so as to induce origin uncertainty. The clutter location is uniformly distributed in the observation space $[-90, 90]\,\text{deg}$, with the number of cluttered observations being a Poisson process with parameter $\lambda = 1.5$. The model based filter is conducted with the NN-IPDA-UKF algorithm with only one trajectory. The overall simulation, comprised of generating the signal $\mathbf{y}_t$, DOA estimation with MUSIC and DOA trajectory filtering, is performed 1000 times. Two cases of

Table II.1: Type I error of different tests, evaluated from 1000 trials.

Test	α (False positive rate)					
	0.5	0.4	0.3	0.2	0.1	0.05
Box-Pierce	0.506	0.394	0.306	0.217	0.119	0.058
Ljung-Box	0.531	0.439	0.342	0.246	0.148	0.082
Out of Bound	0.065					

interest are considered. In the first one, the model used for simulation is employed to filter the noisy observations. Goodness-of-fit tests, such as the Box-Pierce [78], Ljung-Box [79] and the Out-of-Bound [80] tests are applied on the residuals of the filters to assess their whiteness. The tests are conducted with different α, also known as *Type I error* or the *false positive rate*. In the first scenario, α represents the proportion of tests that reject the whiteness hypothesis, although the sequences are white. Indeed, since the filter employs the exact same model used to create the DOA trajectories, the residual sequences are necessarily white. Table II.1 presents the averaged results for the estimated false positive rate given a specified α. Observe the relative good match between the number of rejected sequences and the corresponding α. The out-of-bound test does not offer user parameter, with the false positive rate being fixed to 5%.

In the second case, a noisy FHB echo trajectory is generated but intentionally processed with a flat and inclined bottom of slope $\gamma = 5\,\text{deg}$. The model noise is increased to $Q = 1\,\text{deg}^2$ to avoid the divergence of filters. In this case, all innovation sequences are necessarily correlated,

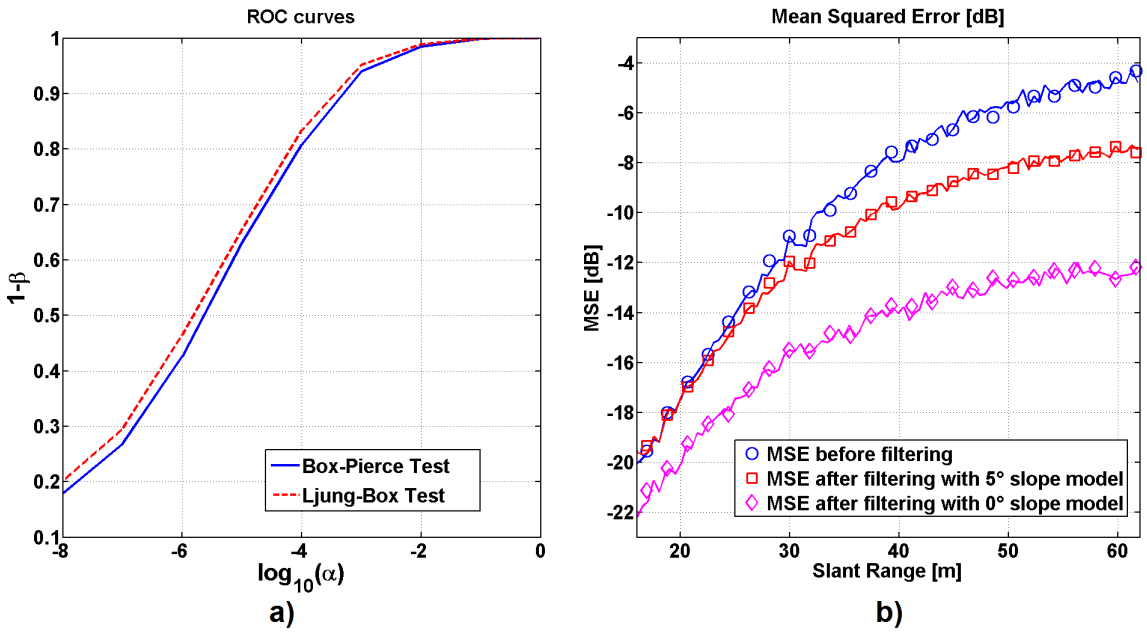

Figure II.6: a) Receiver operating curves for Box-Pierce and Ljung-Box tests. b) Noisy trajectory generated with FHB model. MSE of raw observation sequence(before filtering). MSE after filtering with the correct FHB model and an incorrect slopped model.

thus revealing the inadequacy of the filtering model. GoF tests results are presented in Fig. II.6 a), as Receiver Operating Characteristic (ROC) curves. The ROC curves are obtained by plotting the test power in function of the logarithm of α. The test power, also known as sensitivity, is obtained as $1-\beta$, where β is called *Type II error* or the *false negative rate* and represents the proportion of tests that fail to reject the whiteness hypothesis. For values of $\alpha \in [0.05, 0.1]$ both tests offer high-rejection rates of the residual whiteness whenever the models are inadequate. We observe that the Ljung-Box test is slightly more powerful than the Box-Pierce test, as also noted in [79]. The out-of-bound test fails severely, only rejecting 0.54% the whiteness hypothesis, from the 1000 trials. Hence, only the Box-Pierce and Ljung-Box will be considered for tests on real-sonar data with the choice of $\alpha = 0.05$ offering a powerful test.

Curves showing Mean-Squared Error (MSE) between the simulated and filtered DOA estimates are given in Fig. II.6 b). They show the MSE before filtering (i.e. the MSE of observations z_t), MSE of filtered DOA trajectory with the correct FHB model, and MSE of filtered estimates with the (intentionally incorrect) inclined model. We observe the coincidence of the minimum MSE with the model validated by GoF tests. Indeed, a small mismatch, such as a 5 deg slope, might not generate a noticeable error in the filtered bathymetry; however GoF tests immediately detect this model inadequacy and systematically reject the whiteness of incorrectly filtered residuals. Also notice the improvement, i.e. reduced MSE, of post-filtering DOA sequences, implying an increased accuracy of bathymetry reconstructed by Eq. (II.1). For high range d_t values, the imaging geometry causes the received signal to be less sensitive to the sea-floor slope, in other words, if $d_{t-1}/d_t \approx 1$ the slope γ of Eq. (II.23) cancels out. This explains why even the MSE of the filter with the incorrect model is improving for increased range values, as compared with the raw observation MSE.

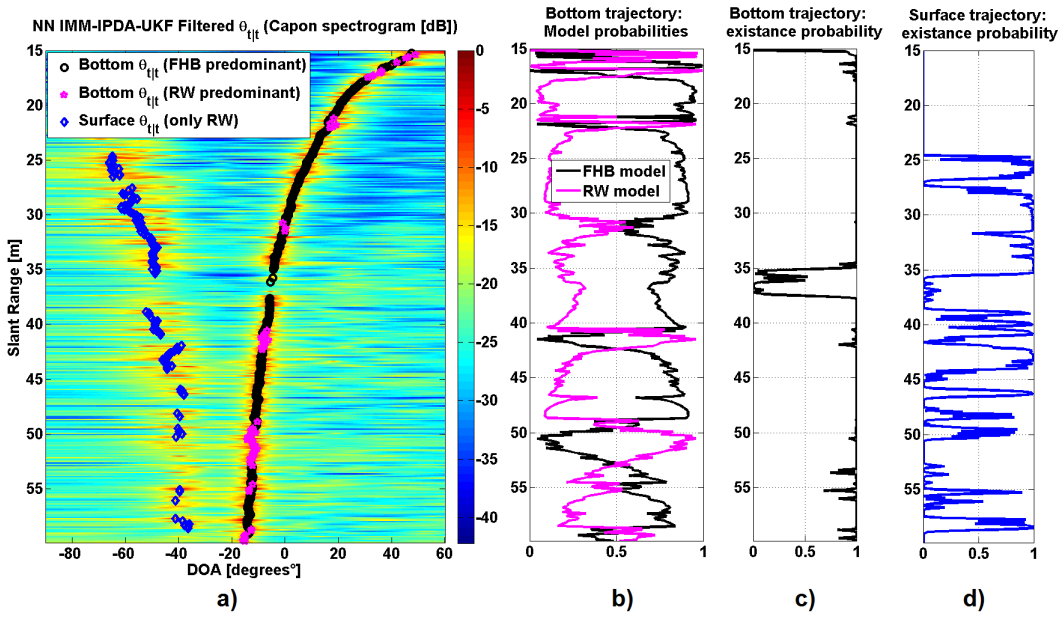

Figure II.7: NN-IMM-PDA-UKF echo separation: a) $\hat{\theta}_{t|t}$ overlay-ed on the Capon spectrogram. b) Bottom FHB and RW model probabilities $\mu_{t|t}$. c)/d) Bottom/sea-surface trajectory existence probability $\nu_{t|t}$ Eq. (A.17).

II.5.2 Real data results

In this section we present filtering results of real-sonar data. Sonar data were acquired with an EdgeTech 4600 sonar (see [6] and Appendix G), in a shallow-water canal near Fort Lauderdale, Florida. Depth varies between 10m and 20m. The extent of the imaged area is given by a maximum slant range of 60m. The state of the sea was calm, resulting in important sea-surface reflections. Sec. II.5.2.a showcases the ability of the proposed filter to eliminate clutter and separate the bottom echo from the sea-surface echo. In Sec. II.5.2.b we present the batymetry reconstruction of a man-made object - a mooring pole (also referred to as a piling or pile), and in Sec. II.5.2.c a full-survey bathymetric reconstruction is achieved with the proposed filter. Capon and MUSIC are used interchangeably as the pre-processing module.

II.5.2.a Multi-path echoes separation

In Fig. II.7 a) we observe NN-IMM-IPDA results for bottom and sea-surface echoes overlaid onto the Capon spectrogram of the corresponding ping line. Pre-processing was done with the Capon beamformer and the AIC [52] method for number of sources estimation. Observe the echo separation achieved by the multiple-trajectory filter with the nearest neighbor association scheme. The separation of the bottom and the sea-surface echoes ensures spurious-free bathymetric reconstruction. Bottom-echo tracking is conducted using the set of models: FHB (II.23) with model noise variance $Q^{\text{FHB}} = 0.01\,\text{deg}^2$, and RW model (II.24) with $Q^{\text{RW}} = 0.1\,\text{deg}^2$. The IMM [74, Ch.11.6.6] framework that merges the two model estimates, employs sequentially-estimated model probabilities $\mu_{t|t}$ showcased in Fig. II.7 b). Model probabilities $\mu_{t|t}^{\text{FHB}}$ and $\mu_{t|t}^{\text{RW}}$ indicate the model likelihood given current and past observations, thus providing a geometrical segmentation of the underlying bottom profile. Since the bottom echo has an arch-shaped curve typical of flat and horizontal bottoms, the FHB model is, for most of the times, more likely than the RW model. The bottom trajectory existence probability $\nu_{t|t}$, given by Eq. ((A.17)) and presented in Fig. II.7 c) is also computed sequentially and indicates trajectory quality. Whenever $\nu_{t|t}$ decreases below the threshold value, set to 0.5, the trajectory estimates are extinguished (for

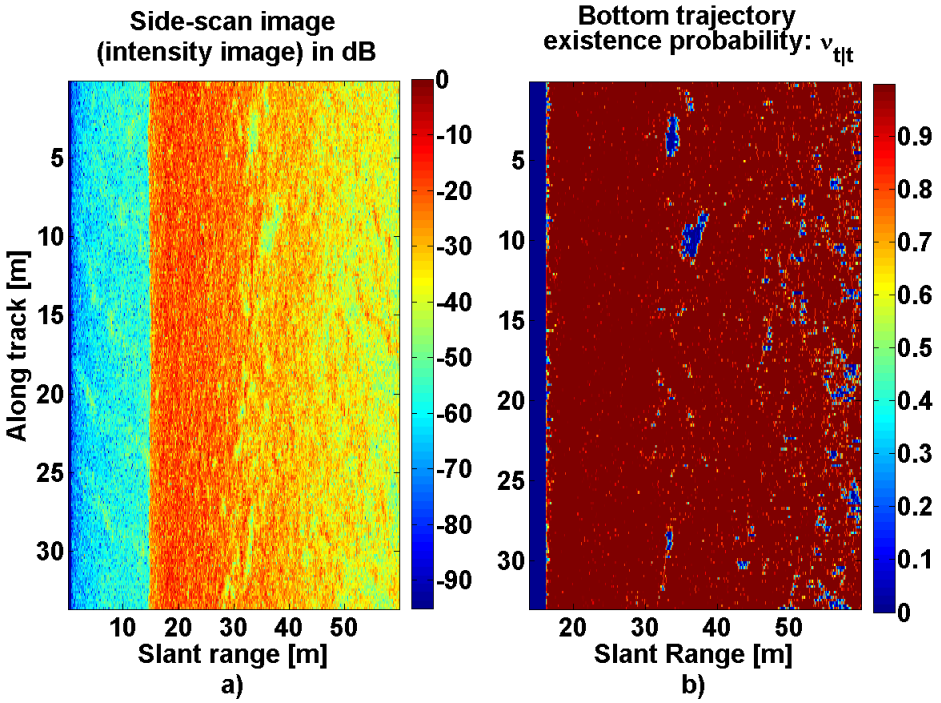

Figure II.8: Side-scan (amplitude) image of 200 adjacent ping lines. b) Trajectory existence probabilities for the 200 ping lines.

slant range values between $35-40$ m). The filtering residuals given by Eq. (II.17b) are employed for GoF tests yielding the acceptance of the whiteness hypothesis with $p-$values of 0.318 and 0.283 for the Box-Pierce and Ljung-Box tests, respectively. Since the sea-surface echo exhibits high variations, with a less evident trend, a single RW model was employed with $Q^{\text{RW}} = 1\,\text{deg}^2$ for DOA trajectory estimation. Sea-surface echo trajectory existence probability is given in Fig. II.7 d). GoF tests for the surface echo yield the acceptance of the whiteness hypothesis with $p-$values of 0.439 and 0.346 for the Bow-Pierce and Ljung-Box tests, respectively. In order to better visualize the trajectory existence probabilities $\nu_{t|t}$ we present the results for 200 adjacent ping lines forming Fig. II.8. In Fig. II.8 a) we observe the lateral (or side-scan) amplitude image, while in Fig. II.8 b) we observe the corresponding instantaneous trajectory quality, $\nu_{t|t}$. Notice the correspondence between the two figures, notably concerning the two acoustic shadows where the trajectory existence probability is low. The ping line processed in Fig. II.7 is obtained from the set of ping lines presented in Fig. II.8 at the along track marker of $10m$. Notice the echo interruption from Fig. II.7 a) caused by an acoustic-shadow patch. Thresholding $\nu_{t|t}$ ensures acoustic-shadow detection, where tracking is stopped and bathymetric points are not reconstructed (lack of bottom-backscattered signal).

II.5.2.b Man-made object reconstruction

Another interesting case of double target tracking is showcased in Fig. II.9 a), where the primary trajectory is the sea-bottom DOA echo and the secondary trajectory corresponds to the echo backscattered from a vertical mooring pole (also called piles or pilings). Note, that the two echoes are received simultaneously, since the two echoes are situated at the same distance (slant range) from the sonar array. This leads to the layover phenomenon in side-scan images, effectively obstructing the area in front of the pole. Pre-processing is done by MUSIC coupled with AIC and require a computation time of 0.9s. The post-filtering has a computation time of 1.3s on a 3.6GHz processor in MATLAB. Compiling the code would enable real-time survey-

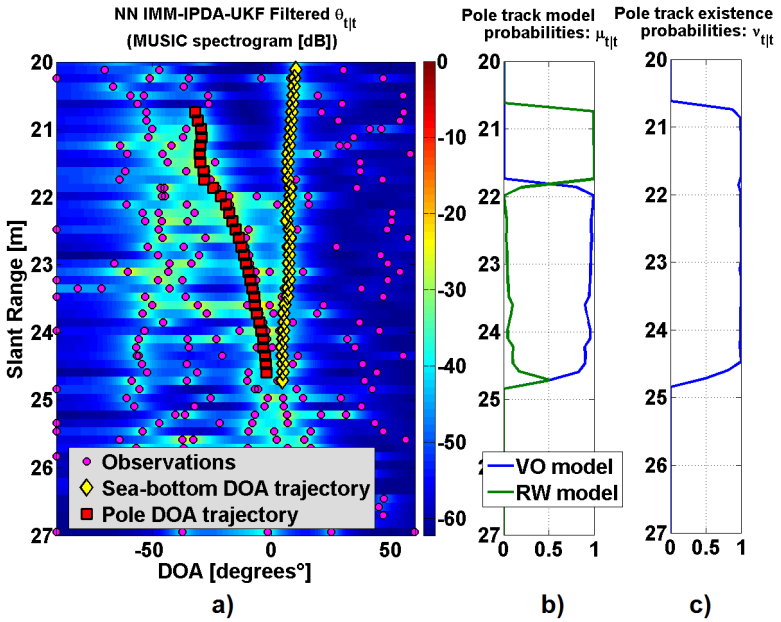

Figure II.9: Man-made object scenario: a) NN-IMM-IPDA-UKF estimates overlayed on the MUSIC pseudo-spectrogram. b) Pole VO and RW model probabilities. c) Pole trajectory existence probability $\nu_{t|t}$, Eq. (A.17).

ready processing. The models employed to track the pole echo are the VO model with $Q^{\text{VO}} = 0.1(^o)^2$, and a RW model with $Q^{\text{RW}} = 1(^o)^2$. The sea-bottom echo was tracked with the same parameters as in the previous figures. In Fig. II.9 b) we observe the evolution of the $\mu_{t|t}^{\text{VO}}$ and $\mu_{t|t}^{\text{RW}}$ model probabilities. Observe the pertinence of the RW model for the start of the pole trajectory and the later switch to the VO model. Tracking the pole trajectory is stopped when its existence probability $\nu_{t|t}$, given by Eq. (A.17) and presented in II.9 c), drops below the threshold value of 0.5. GoF tests were conducted for the sea-bottom echo yielding the acceptance of the whiteness

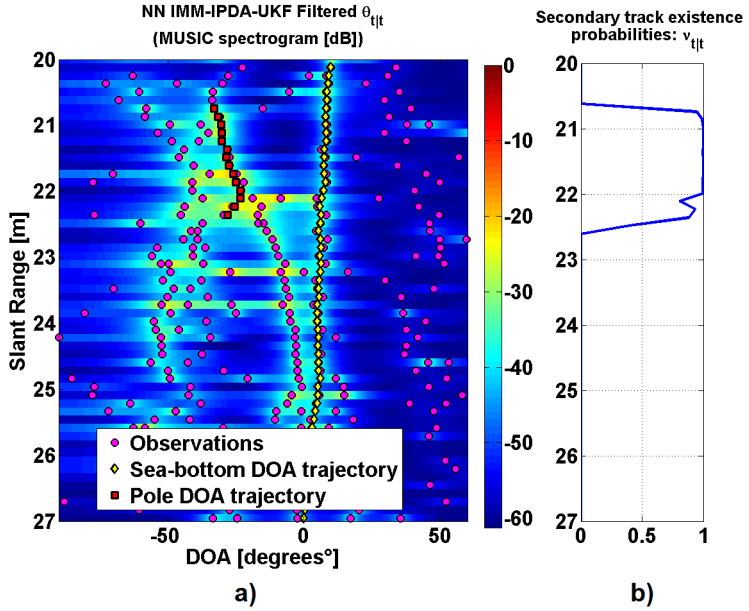

Figure II.10: Trajectory loss: a) Tracking with only the RW model. b) Pole trajectory existence probability.

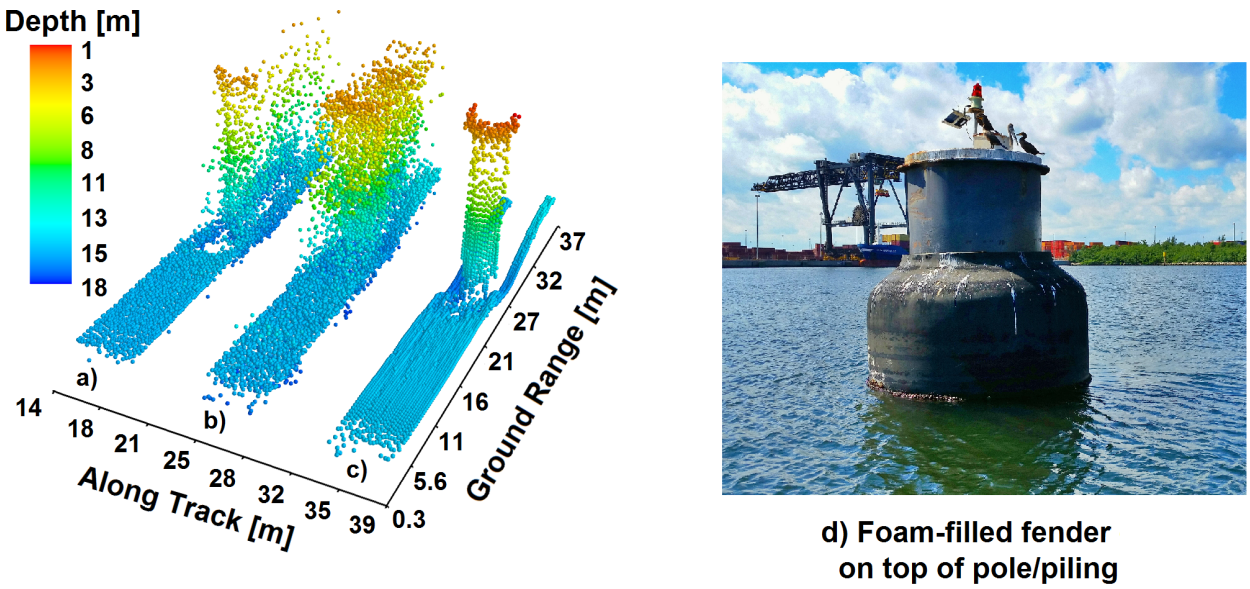

Figure II.11: Man-made object reconstruction comparison: a) Interferometry b) MUSIC c) NN-IMM-IPDA-UKF. Figure d) shows an image of the foam-filled fender, which is mounted on top of the pole (courtesy of *EdgeTech*). Notice the partial submersion of the fender, which makes it visible in the reconstructed sonar bathymetry of figure c).

hypothesis with $p-$values of 0.34 and 0.18 for the Box-Pierce and the Ljung-Box tests. GoF tests for the pole echo also accept the whiteness hypothesis, with $p-$values of 0.76 and 0.59 for the Box-Pierce and the Ljung-Box tests.

For comparison reasons, the RW model alone is also employed to track the pole echo. However, since the RW has no preferred dynamical evolution situations occur were any clutter induced DOA estimate close to the pole DOA trajectory can cause the trajectory to be irretrievably lost, as seen in Fig. II.10 a). Again the trajectory existence probability, Fig. II.10 b) is employed to stop the tracking process.

Bathymetry reconstruction is achieved by employing Eq. (II.1) with the various DOA estimates of each ping line. Thus transforming several adjacent ping lines we obtain the full reconstructed bathymetry. The bathymetry corresponding to the pole area is reconstructed in Fig. II.11 a) using interferometry DOA estimates, in Fig. II.11 b) using the raw MUSIC DOA estimates and in Fig. II.11 c) the reconstruction is carried out using the proposed filter. Observe the regularized reconstruction obtained with the proposed filtering algorithm as opposed to the MUSIC reconstruction which is buried in clutter. Since in our experiment 8 receivers are available, the interferometry estimate is given by the means of the phase differences taken between the 7 pairs of adjacent receivers. Interferometry only offers one DOA angle estimation at each instant t, so it appears less cluttered but also it is not capable to reconstruct the pole and the area just in front of it. Indeed, for the bottom and pole backscattered echoes that impinge on the sonar array at the same instant, interferometry only offers one DOA estimate which is biased toward the more powerful pole echo. The MUSIC algorithm is used with the AIC [52] criterion to select the number of echoes. Hence the number of DOA estimates (also bathymetry points) at each range bin in Fig. II.11 b) is given by AIC. Notice an image of the foam-filled fender in Fig. II.11 d), which is mounted on top of the pole/piling. An aerial view of the survey area and the pole is given in Fig. II.12, which represents the turning notch of Port Everglades in Fort Lauderdale, Florida. Large container ships traveling down the river/canal are turned 180^o in this turning notch. The piling serves as a turning piling (also called turning dolphin), while the fender protects ship hulls from getting damaged in the turning process. Since the fender is

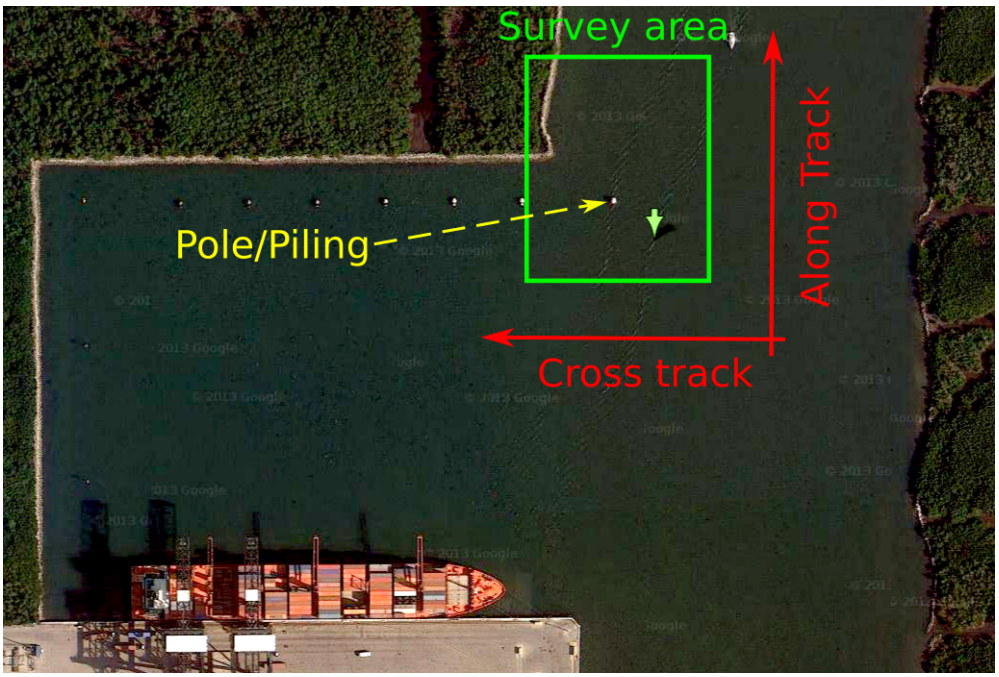

Figure II.12: Turning notch of Port Everglades, Fort Lauderdale, FL (GPS coordinates 26.074920, −80.115201). Courtesy of *Google Maps*, date 14.11.2013. The canal is called *Stranahan River*. Note the encircled survey area and the turning piling. Large container ships are turned inside this turning notch, with the help of the turning piling.

partially submerged, part of it is visible in the reconstructed bathymetry. Note that the fender is free to rise/descend with the incoming/outgoing tide. A cylinder is fitted to the points representing the main body of the mooring pole in Fig. II.11 c), using the Pratt method [82]. The inferred pole diameter is $2.23m$ with a 95% confidence interval of $[2.14, 2.3]m$. The inferred value corresponds well with the typical 7.5 foot ($2.28m$) diameter of the mooring pole. In Fig. II.13, the points corresponding to the main body of the pole are projected onto the plane of the along-track and ground-range axes. Additionally, on the same plane a projection of the fitted

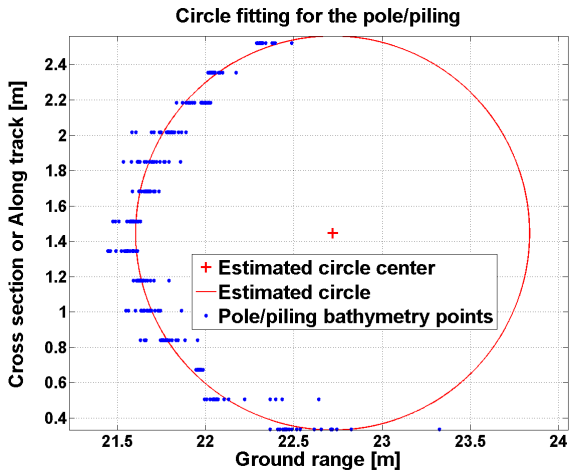

Figure II.13: Pole/pilling diameter inference. The bathymetry points comprising the main body of the pole are projected onto the plane of the along-track and ground-range axis. Note the fitted circle, corresponding to the inferred diameter and center, and the projected points.

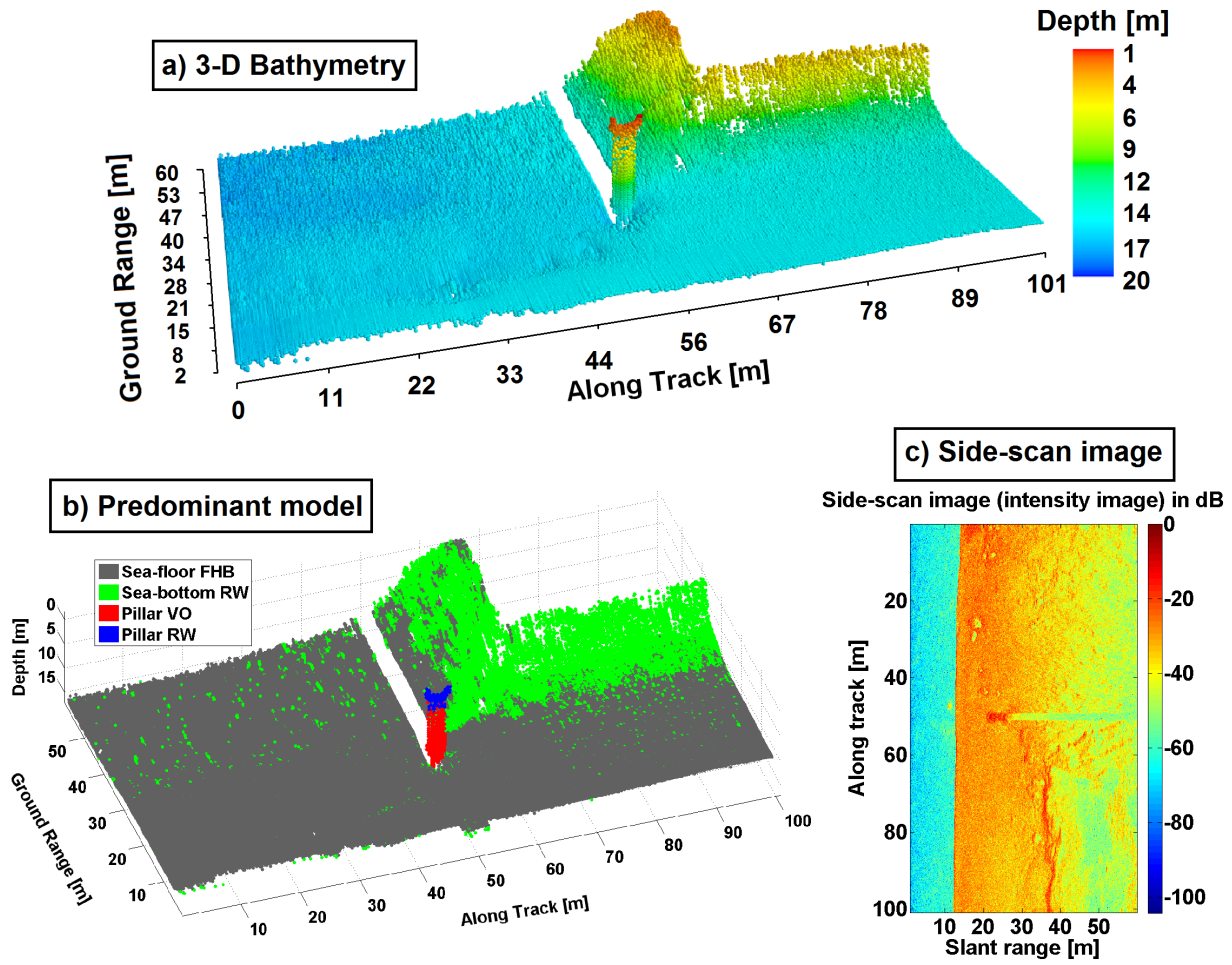

Figure II.14: a) Bathymetry reconstruction with the proposed filtering algorithm. b) Predominant models (geometrical segmentation). c) Side-scan image (signal amplitude).

cylinder is represented as a red circle. Note the presence of bathymetric points only on the left semicircle, the right semicircle corresponding to the acoustic shadow generated by the pole.

II.5.2.c Bathymetric survey

A fully reconstructed bathymetry with the NN-IMM-IPDA-UKF is presented in Fig. II.14 a) where the point color code represents depth. 600 adjacent ping lines are processed and employed for the bathymetry reconstruction. Bathymetry estimates are extinguished based on the various trajectory probabilities. Observe the pole in the middle of the reconstructed bathymetry image with the resolved layover. Next to the pole, observe the canal bank. Bathymetry was reconstructed with the RW and FHB models for the sea-bottom echo and the VO and RW models for the pole echo. In both cases, the RW model is employed to provide tracking in highly irregular areas, complementary to the geometrically informative models FHB and VO. Thus, multiple-model processing, carried out by the IMM module of the proposed NN-IMM-IPDA-UKF, offers better adaptability of the filtering algorithm and avoids filter divergence. Furthermore, multiple model processing offers image-segmentation information as early as the image reconstruction stage. By image-segmentation information we refer to the model probabilities $\mu_{t|t}$ adaptively computed by the IMM. A simple thresholding mechanism of model probabilities is presented in Fig. II.7 a), where we affect the class FHB or RW to a filtered DOA estimate (implicitly to the bathymetry-point estimate) whenever the corresponding model probability $\mu_{t|t}$ is predom-

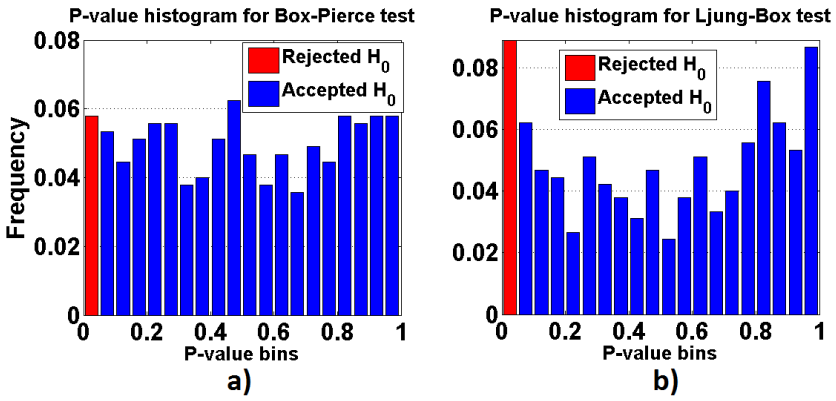

Figure II.15: GoF $p-$value histogram of ping lines composing the bathymetry in fig. II.14: a) Box-Pierce test b) Ljung-Box test

inant. Proceeding in such a manner for the entire reconstructed scene, we obtain Fig. II.14 b), where the bathymetry is effectively segmented according to the geometrical models employed for each of the processed echoes: bottom and pole. Observe the occurrence of the RW model for the bottom echo, describing mainly the sloped canal bank, not captured by the FHB model. The RW model is active in describing the upper section of the pole, not covered by the VO model. This corresponds to the foam-filled fender discussed above. Indeed, the VO model is active only for describing the pole body, which constitutes a vertical object. This represents a rough segmentation based on the simple selection mechanism of the most probable model. Improved segmentation mechanisms could be envisaged by incorporating inter-ping processing. The different predominant models visible in Fig. II.14 b) illustrate the need for a multiple model approach, where strong priors such as FHB and VO are coupled with the less restrictive RW model. Multiple model filtering increases the flexibility of the proposed method in real scenario bathymetry processing. In Fig. II.14 c) we present the side-scan image of the same area, i.e. the intensity of the backscattered signal. Observe the mooring pole with the layover phenomenon, obstructing the area in front of the pole. In Fig. II.12 an aerial view of the surveyed area is provided. Note the good match between the bathymetry reconstruction (Fig. II.14 a)), the side-scan image (Fig. II.14 c)) and the aerial view of the surveyed area (Fig. II.12). GoF tests are conducted for the ping lines composing fig. II.14 a), and are synthesized in Figs. II.15 a) and b). The $p-$values obtained by the Box-Pierce and Ljung-Box tests for each ping line are arranged in the normalized histograms. Given a level of significance of $\alpha = 0.05$, the percentage of rejected ping lines are represented by the red bin in the aforementioned figures. With the

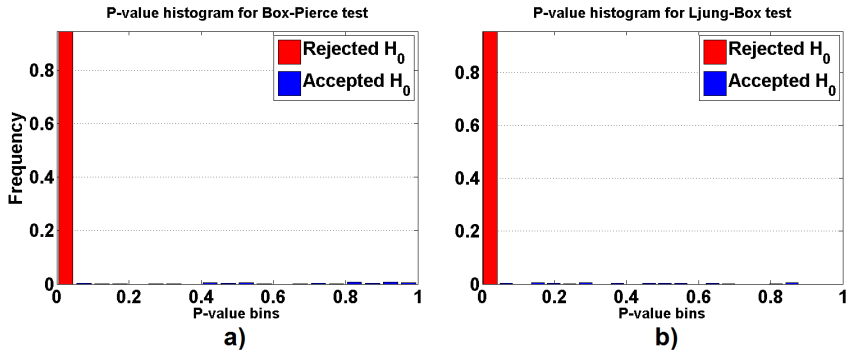

Figure II.16: GoF $p-$value histogram for RW model only: a) Box-Pierce test b) Ljung-Box test

Box-Pierce test 6% of ping lines are rejected, while for the Ljung-Box 9% are rejected. This shows that acceptable model validation rates are achieved with the proposed multiple-model framework. $p-$values are expected to be uniformly distributed under the H_0 hypothesis (see Appendix D and [83]), which seems to be the case more for the Bow-Pierce histogram (fig. II.15 a)) than for the Ljung-Box p-values histogram (fig. II.15 b)). In fact, the tested ping lines do not rigorously constitute independent realizations of the same stochastic process, thus inducing that the percentage of rejected ping lines are not expected to be equal to α. However, from a practical point of view, a small number of rejected ping lines is relevant to validate the proposed geometrical models whenever ground-truth data is lacking. Furthermore, GoF tests used actively during survey operations offer the possibility to detect when the reconstruction method fails (failed GoF tests) and switch the system to a supervised reconstruction involving operator input.

For the sake of comparison, bathymetry reconstruction was also conducted solely with the RW model. Unfortunately, in the pole case presented in Fig. II.10 a) showcases the inadequacy of the RW model for the reconstruction of the pole body. Filtering only the sea-bottom with the RW model is achieved without divergence. However, the GoF test results presented in Fig. II.16, reject the majority of processed ping lines at about 90%. We conclude with the inadequacy of the RW model, when used solely, for bathymetry extraction.

The proposed post filtering method is employable for multibeam sonar and synthetic-aperture systems. However, the pre-processing module needs to be modified in function of the sonar system under consideration. Multibeam systems dispose of roughly 10 times the number of receiver elements as conventional interferometric side-scan sonars, hence conventional beamforming is preferred to the MUSIC algorithm. The latter requires a temporal window larger than the number of receivers for the estimation of the sample covariance matrix. Simple thresholding of the beamforming spectrum offers the DOA observation set Z_t. For synthetic aperture sonars, once the synthetic-aperture formation is carried out for each of the N receivers, DOA estimates forming the observed set Z_t can be inferred from the N synthetic aperture images. Then, the observation set of DOAs can be post-filtered with the proposed method in order to obtain clutter-free bathymetry reconstructions of the sea-floor.

II.6 Chapter conclusions

In this chapter, model-based adaptive filters are employed to achieve high-resolution 3D imaging of the sea-bottom for real-time applications. Tracking ensures trajectory formation and separation of echoes from clutter and interfering multi-path for image reconstruction. Also layover, a limiting phenomenon of side-scan images, is resolved by simultaneously tracking the multiple echoes. The proposed NN-IMM-IPDA-UKF forms echo DOA-trajectories from DOA estimates obtained with classical array processing methods such as MUSIC. Geometric models are employed to characterize the DOA trajectories of echoes in a bathymetric context. Multiple models are employed in parallel in order to increase the adaptability of the proposed filter. Furthermore, such models are also shown to effectively segment the 3D image and provide useful information for infrastructure identification purposes. Goodness of fit tests are provided as a means to validate the proposed model processors on simulated and real data.

The relatively simple implementation of the NN-IPDA-UKF yields an algorithm suited for real-time applications. This constitutes one major advantage of such an approach to tracking DOA echoes. However, the disadvantage lays in the pre-processing module that needs to process a window of signal samples to produce a meaningful spectrogram and subsequently DOA estimates. In the following chapters, we will propose an alternative processing scheme that does not rely on a pre-processing (detection/estimation) module, but tracks echoes directly from the

phased-array measurements. This provides a depth estimate for each array sample, thus achieving super-resolution bathymetry. Such tracking algorithms, referred to as Track Before Detect (TBD), are more complex than Track Wile Scan (TWS) methods such as the PDAF. Furthermore, TBD algorithms are capable of tracking low SNR echoes. This is achievable by delaying the detection thresholding process as long as possible in order to integrate (and subsequently track) dim echo intensity over time/slant range.

Chapter III

Sonar echo tracking: an intensity function approach

Far better an approximate answer to the right question, which is often vague, than an exact answer to the wrong question, which can always be made precise.

John Tukey

III.1 Point-process formalism for target tracking

In this chapter we investigate algorithms aimed at adaptively estimating both the number of echoes impinging the sonar array and their associated DOAs. In a similar way to the previous chapter, a state-space formalism is employed, in which the system state, or multi-state, represents the collection of individual target states. Targets represent acoustic echoes and are

characterized by a state vector that contains target-position parameters (e.g. DOA, Cartesian coordinates) and possibly other parameters (e.g. echo strength, angular dispersion).

In the previous chapter, a varying number of targets was not explicitly accounted for. Instead, tracks were considered already formed and data association is employed to find the most probable observation-to-track allocations. With this approach, track update is carried out once the pairs between observations and tracks are optimally determined. Methods are employed to explicitly add new tracks by considering each unassociated observation to form a *tentative track*. Since false, i.e. clutter, observations are present, a confirmation logic is required for the newly-formed tentative tracks. A typical confirmation rule requires that at least M detected observations fall within a pre-specified vicinity of one another in N successive samples [25, Ch. 1.3.2]. An often used rule is the 2 out of 3 rule. Explicit track deletion can be carried out whenever a specific track has not been updated for several time samples, or based on a track-score function such as the probability of existence in the IPDAF. By employing a track-score function for each track, the Joint IPDAF [84] is employed to achieve multi-target filtering with a varying number of targets. Note that in IPDA-based filters, the number of targets is not modeled as a random variable. In Reversible Jump Markov Chain Monte Carlo (RJ-MCMC) algorithms, a variable number of targets is accounted for by introducing birth and death moves that increase the statistical diversity of particles. Such an RJ-MCMC method has been developed in [38] for DOA tracking directly from phased-array observations, that is, no pre-processing is required in order to form a set of detections. Alternatively, the proposed RJ-MCMC can be interpreted as an algorithm that estimates the model order and other parameters of the observation process.

A different approach consists in considering the multi-state as an unordered collection of objects or points representing individual targets, where the number of points and their locations are random. The individual point states take values in a specific space, referred to as the single-target space. Compared to the previously mentioned filters, the major difference of this approach consists in modeling the number of targets as a random variable. This allows for prior densities to be defined on both target number and target locations, and the rigorous derivation of Bayesian filters. Bayesian multi-target filters, that estimate both the number of targets and their state vectors, have received an increasing interest in recent years. The mathematical concepts dealing with a random number of points as well as random point locations are modeled by the theory of point processes [85]. In general, targets are assumed to have no specific ordering. Point processes offer a natural representation of multi-target states as unordered collections of individual states. Because of the ordered nature of elements in a vector, augmented vectors as multi-target states are not a natural representation. This problem clearly arises when using the ordinary euclidean distance for computing errors between an estimated and a ground-truth multi-target state vector: a different ordering of elements, in the estimated multi-target state as opposed to the ground-truth vector, yields an unjustified increase in error. Thus, at least from the point of view of mathematical formalism, a correct representation of a multi-target state is an unordered collection, or a set whenever duplicate elements are not present.

In most applications, we only consider finite and simple point processes, i.e. with realizations having a finite number of distinct points, both properties holding almost surely. In the tracking literature, such processes are also known as Random Finite Sets (RFS) [27]. A finite and simple Point Processes (PP) description of the multi-state allows for an implicit account of target birth and death in the recursive propagation of the PP posterior distribution. A practical multi-target tracking filter, propagating the intensity function or Probability Hypothesis Density (PHD) (i.e. first-order moment density of the PP), has been proposed in [27], and is referred to as the PHD filter. The intensity or PHD function is defined on the single-target space and has two interesting properties that make it attractive for multi-target tracking. Firstly, integrating the PHD over any region of the single-target space leads to the average number of points/targets in that region. Secondly, target positions or states can be inferred from the local maxima of

the intensity function. Hence the PHD filter recursively estimates the intensity function of the corresponding multi-target PP given past and current observations. Intensity based filters such as the PHD filter have several advantages as compared to classical PDA-based filters:

- Firstly, data association is carried out implicitly during the update stage of the intensity function, and no explicit enumeration of observation-to-track associations is needed. The latter being computationally intensive.
- Secondly, target births are accounted for simply by algebraically adding a birth intensity to the existing intensity[1].
- Thirdly, target survivals (or equivalently target deaths) are accounted for by multiplying the intensity function with the probability of target survival[2].
- Fourthly, an estimate of the number of targets is obtained by integrating the intensity function, while target states can be inferred from the local maxima of the intensity function.

The aforementioned advantages apply to both TWS and TBD filtering strategies. Since in TBD there are no ad-hoc target-initialization procedures, such as the "M out of N" rule from TWS, the aforementioned advantages of intensity filters become more interesting. Furthermore, in [28,86,87] intensity filters based on point-process theory are shown to outperform RJ-MCMC algorithms for multi-target tracking with sensor arrays. Therefore, in this work, we focus on developing intensity based filters for phased-array sensors.

Historically, the TWS-PHD filter was the first PP-based filter developed for multi-target tracking in TWS systems. TBD-PHD filters have only recently been proposed in [86], for sensor arrays in which the observation model is completely specified by the target states, that is, the observation equation is a deterministic function of the target states. For phased-arrays on the other hand, the target states only specify the parameters of a stochastic observation model and the PHD filters of [86] are not directly applicable. More specifically, the observation is a sum of target-generated source signals and noise, with source signals being modeled as stochastic processes with parameters given by the target states. To cope with the phased-array model, we introduce a novel marked point-process model, that integrates the multi-target point-process with the stochastic source signals. In the proposed model, source signals represent the marks generated by the individual points. Moreover, we show that marks can be marginalized-out in the update process of the TBD-PHD, leading to an efficient filter that only propagates the intensity function relative to target states. Thus, we avoid augmented-state solutions (such as the RJ-MCMC [38]), that lead to less efficient particle-filter implementations. The proposed TBD-PHD filter is capable of tracking multiple Gaussian point-targets directly from phased-array observations, that is, with no pre-processing. Observation extraction in TWS systems implies thresholding operations, potentially missing low-SNR echoes. To validate our TBD approach, the proposed TBD-PHD filter is shown to outperform stat-of-the-art TWS-PHD filters for phased-array processing [87]. Moreover, the TWS-PHD filter of [87] was shown to outperform the RJ-MCMC method of [38], and with a reduced computational cost. Indeed, RJ-MCMC methods exhibit a burn-in period required by the Markov process to reach stability, which occurs at each time sample in on-line estimators. The phased-array TBD-PHD filter was the subject of publications [88, 89].

This chapter is organized as follows. In Sec. III.2, we present several definitions related to PP theory and introduce the PHD filter notations. Next, in Sec. III.3, several PP examples are given that serve as priors for multi-target filters developed in subsequent sections. In Sec. III.4,

[1] Whenever the birth points are independent from existing points.
[2] Whenever the survival of one point is independent from other points.

the error metric employed to quantify the estimation error of multi-target states is given. We give a short presentation of the TWS-PHD filtering equations in Sec. III.5, which will prove useful for the development of TBD filters. The proposed TBD-PHD filter is developed in Sec. III.6. We conclude in Sec. III.7.

As a side-note, in [90,91] we proposed single-target TBD filters for phased arrays. Additionally, in [92] we proposed a TBD filter that models the array observation process as a process switching between an order 1 and an order 2 model, the resulting filter being capable of tracking at most 2 simultaneous targets. In such, these filters constitute special cases of the methods presented in the following, the latter being capable of tracking (at least theoretically) a generic number of targets.

III.2 Point-process theory

In this section we state the main definitions and develop the notations employed throughout the following sections. The main elements presented here involve basic point-process theory, required in multi-target tracking methods. Good texts on general point-process theory are [85,93], on spatial point processes and simulation methods [94,95] and on applications of point processes [96].

A Point Process (PP) is defined as a collection of indistinguishable points distributed randomly in a locally compact Hausdorff space whose topology has a countable basis, e.g. $\mathbb{R}^d$. Typically, we are interested in *finite point processes*, defined as point processes for which the total number of points is finite with probability 1. Furthermore, in target tracking, points represent target states and it is reasonable to suppose that there are no two points with the same state vector. In such, we define *simple point processes* as point processes that have distinct points with probability 1. Since the ordering of points has no meaning, an equivalent *Random Finite Set* (RFS) terminology is possible for simple, finite point processes [24]. For equivalences between PP and RFS, we direct the reader to [27, Sec. II.D] and [97, Sec. II]. Some parallels between the two concepts will be drawn in this document, which help to interpret different notions (e.g. the probability hypothesis density function). Indeed, we consider the point-process construction of densities and factorial moment measures to be rewarding in terms of interpretability. Nonetheless, the more compact notations introduced by RFS, specifically the set integral and PHD, will be employed in the majority of this work.

The following sections are organized as follows: in Sec. III.2.1 we present several preliminary definitions, in Sec. III.2.2 we define a probability measure for PP, in Sec. III.2.3 we introduce the random finite set and the set integral terminology, and in Sec. III.2.4 we introduce moment measures and moment densities for PP.

III.2.1 Preliminary definitions

For a finite point process X the following conditions hold:

- The points are located in a complete separable metric space $\mathbb{X}$, e.g. $\mathbb{X} = \mathbb{R}^d$, referred to as the single-target space.

- A distribution $\{p_n\}$ with $n \in \mathbb{N}^+$ with $\sum_{n=0}^{\infty} p_n = 1$ exists and determines the distribution of the total number of points.

- For each $n \geq 1$, a probability distribution $\Pi_n(\cdot)$ exists on the Borel sets $\mathcal{B}(\mathbb{X}^n)$ of $\mathbb{X}^n = \mathbb{X} \times \cdots \times \mathbb{X}$, and it determines the joint distribution of process points, conditioned on the total number of points being n.

The previous conditions offer an insightful and constructive definition of finite PP. That is, in order to generate a realization of the finite PP X, one needs to first choose the number of points n with probability p_n and then sample the collection $(\mathbf{x}_1, \cdots, \mathbf{x}_n)$ from the distribution $\Pi_n(\cdot)$. Furthermore, since we assume that we deal with unordered points, the distribution $\Pi_n(\cdot)$ needs to assign the same probability mass to all $n!$ permutations of coordinates $\mathbf{x}_1, \cdots, \mathbf{x}_n$. In other words, $\Pi_n(\cdot)$ should be symmetric. Whenever this is not the case, a symmetrical measure is obtainable by imposing on any partition $(A_1 \times A_2 \times \cdots \times A_n)$ of $\mathbb{X}$:

$$\Pi_n^{\text{sym}}(A_1 \times \cdots \times A_n) = \frac{1}{n!} \sum_{\sigma \in \text{Perm}(n)} \Pi_n(A_{\sigma(1)} \times \cdots \times A_{\sigma(n)})$$

where $\text{Perm}(n)$ denotes the set of the $n!$ permutations of the first n positive integers. Hence, $\sum_{\sigma \in \text{Perm}(n)}$ is taken over all $n!$ permutations $(\sigma(1), \cdots, \sigma(n))$ of integers $(1, \cdots, n)$. Observe that the new symmetrical distribution has total mass unity.

Janossy measures are defined as [85, Eq. 5.3.2]:

$$\begin{aligned} J_n(A_1 \times \cdots \times A_n) &= p_n \sum_{\sigma \in \text{Perm(n)}} \Pi_n(A_{\sigma(1)} \times \cdots \times A_{\sigma(n)}) \\ &= n!\, p_n\, \Pi_n^{\text{sym}}(A_{i_1} \times \cdots \times A_{i_n}). \end{aligned}$$

Janossy measures capture both the target number distribution as well as their spatial distribution on $\mathbb{X}$, and therefore provide a concise characterization of a PP. Observe that the probability of a realization of the PP X having n points is given by:

$$p_n = \frac{1}{n!} J_n(\mathbb{X}^{(n)}), \tag{III.1}$$

since $\Pi_n((\mathbb{X}^n)) = 1$. Also note that:

$$\sum_{n=0}^{\infty} \frac{1}{n!} J_n(\mathbb{X}^n) = 1.$$

An application of Janossy measures is to construct probability distributions of the number $N(A_i)$ of points falling inside the subset $A_i \in \mathbb{X}$. Considering $(A_1, A_2, \cdots, A_r)$ as a finite partition of $\mathbb{X}$, the probability of finding exactly n_i points in each A_i, with $i = 1, \cdots, r$ and $n = \sum_{i=1}^r n_i$, is given by:

$$\begin{aligned} Pr\{N(A_i) = n_i, i = 1, \cdots, r\} &\triangleq P_r(A_1, A_2, \cdots, A_r; n_1, n_2, \cdots, n_r) \\ &= \frac{1}{n_1! n_2! \cdots n_r!} J_n(A_1^{n_1} \times \cdots \times A_r^{n_r}) \\ &= p_n \binom{n}{n_1 \ \cdots \ n_r} \frac{1}{n!} \sum_{\text{perm}} \Pi_n(A_1^{n_1} \times \cdots \times A_r^{n_r}), \end{aligned}$$

where $\binom{n}{n_1 \ \cdots \ n_r} \triangleq \dfrac{n!}{n_1! n_2! \cdots n_r!}$ is the multinomial coefficient that represents the number of ways of grouping n points in r distinct sets with n_i points in A_i, for $i = 1, \ldots, r$.

A simple interpretation of Janossy measures is possible whenever derivatives exist. In such a case, let $j_n(\mathbf{x}_1, \cdots, \mathbf{x}_n)$ represent the density (Radon-Nikodym derivative) of $J_n(\cdot)$ with respect to the Lebesgue measure on $\mathbb{X}^n$, whenever $\mathbb{X} = \mathbb{R}^d$ and $\mathbf{x}_i \neq \mathbf{x}_j$ for $i \neq j$. In such, the Janossy density $j_n(\mathbf{x}_1, \cdots, \mathbf{x}_n)$ is interpreted as:

$$\begin{aligned} Pr\left\{ \begin{array}{c} \text{exactly } n \text{ points, each located in} \\ \text{the distinct intervals } (\mathbf{x}_i, \mathbf{x}_i + d\mathbf{x}_i) \\ \text{and none elsewhere.} \end{array} \right\} &= J_n(d\mathbf{x}_1 \times \cdots \times d\mathbf{x}_n) \\ &= j_n(\mathbf{x}_1, \cdots, \mathbf{x}_n) d\mathbf{x}_1 \cdots d\mathbf{x}_n \end{aligned} \tag{III.2}$$

Finite point processes become simple, whenever $\mathbb{X} = \mathbb{R}^d$ and for all n the Janossy measures admit densities $j_n(\cdot)$ with respect to the $n \cdot d$ Lebesgue measure [85, Prop. 5.4.V]. Hence, finite-simple PP are commonly encountered in tracking applications where at least one dimension of $\mathbb{X}$ is $\mathbb{R}$.

III.2.2 A probability measure for PP

Characterizing a PP can be achieved by specifying the family of Janossy measures $J_n(\cdot)$ with $n \geq 0$, from which we can obtain the distribution of the number of points p_n (see Eq. III.1) and a set of symmetric probability distributions $\{\Pi_n^{\text{sym}}(\cdot)\}$ defined on $\mathcal{B}(\mathbb{X}^n)$, and conversely. From [85, Prop. 5.3.II], either specification is equivalent to a probability measure on the Borel sets of the countable union

$$\mathbb{X}^{\cup} = \bigcup_{n=0}^{\infty} \mathbb{X}^n, \tag{III.3}$$

where $\mathbb{X}^0 = \emptyset$ denotes the empty set configuration. Clearly, $\mathbb{X}^{\cup}$ represents the space of outcomes of X.

The construction of a measurable space from $\mathbb{X}^{\cup}$ requires the introduction of several notions. Thus, let us introduce the measure space $(\mathbb{X}, \mathcal{A}, \lambda)$, λ an atomless finite measure, and λ^n be the $n-$fold product measure on $\mathbb{X}^n$ for $n \geq 1$ and $\lambda^0(\mathbb{X}^0) = 1$, by convention. In what follows, we assume that $\mathbb{X} = \mathbb{R}^d$, $\mathcal{A}$ is the Borel σ algebra of $\mathbb{R}^d$ and λ is the Lebesgue measure over $\mathbb{X}$. We denote with $\mathcal{B}(\mathbb{X}^{\cup})$ the σ algebra in $\mathbb{X}^{\cup}$ inherited from $\mathcal{A}$. In particular, for each set $\mathcal{S}$ of $\mathcal{B}(\mathbb{X}^{\cup})$, we verify $\mathcal{S} \cap \mathbb{X}^n \in \mathcal{A}^n$, for any n. With the above defined notions, in [95, Ch. 3.5], for any $\mathcal{S} \in \mathcal{B}(\mathbb{X}^{\cup})$ the dominating measure was proposed[3]

$$\begin{aligned} \mu(\mathcal{S}) &= \sum_{n=0}^{\infty} \frac{\lambda^n(\mathcal{S} \cap \mathbb{X}^n)}{n!} \\ &= \sum_{n=0}^{\infty} \frac{1}{n!} \int_{\mathbb{X}^{(n)}} \mathbb{1}_{\mathcal{S}}(\{\mathbf{x}_1, \cdots, \mathbf{x}_n\}) d\mathbf{x}_1 \cdots d\mathbf{x}_n, \end{aligned} \tag{III.4}$$

The probability of X can be connected to Janossy measures, and their densities (when they exist), as follows

$$\begin{aligned} Pr\{X \in \mathcal{S}\} &= \sum_{n=0}^{\infty} p_n \, Pr\{X = (\mathbf{x}_1, \cdots, \mathbf{x}_n) \in \mathcal{S}\} \\ &= \sum_{n=0}^{\infty} \frac{1}{n!} \int_{\mathbb{X}^n} \mathbb{1}_{\mathcal{S}}(\{\mathbf{x}_1, \cdots, \mathbf{x}_n\}) J_n(d\mathbf{x}_1 \times \cdots \times d\mathbf{x}_n) \\ &= \sum_{n=0}^{\infty} \frac{1}{n!} \int_{\mathcal{S} \cap \mathbb{X}^n} j_n(\mathbf{x}_1, \cdots, \mathbf{x}_n) d\mathbf{x}_1, \cdots, d\mathbf{x}_n \\ &\triangleq \int_{\mathcal{S}} p(x) \mu(dx) \end{aligned} \tag{III.5}$$

where $\mathbb{1}_{\mathcal{S}}(U)$ denotes the indicator function ($\mathbb{1}_{\mathcal{S}}(U) = 1$ if $U \in \mathcal{S}$ and 0 otherwise).

Equation (III.5) defines the mixed probability distribution for the finite PP X. Indeed, the family of Janossy densities represent the probability density of the PP X with respect to the measure $\mu(\cdot)$ defined in Eq. (III.4). Observe that $\mu(\mathbb{X}^{\cup}) = 1$, hence $(\mathbb{X}^{\cup}, \mathcal{B}(\mathbb{X}^{\cup}), \mu)$ is a probability space. In this work, probability densities for finite PP are defined with respect to the dominating measure $\mu(\cdot)$ given by Eq. (III.4).

[3] In [95, Ch. 3.5], the measure $\mu(\cdot)$ is introduced as the unnormalized distribution of a Poisson point process with intensity $\lambda(\cdot)$, however this requires a more involved presentation, which is avoided here.

III.2.3 RFS and set integral

In the literature devoted to tracking, finite and simple point processes X are often referred to as Random Finite Sets (RFS). Since realizations of X can be seen as finite subsets[4] of $\mathbb{X}$, the probability of X can be reformulated in terms of the probability that elements of X belong to sets $A \in \mathcal{A}$, which writes [27]

$$Pr\{X \subseteq A\} = \sum_{n=0}^{\infty} \frac{1}{n!} \int_{A^n} j_n(\mathbf{x}_1, \cdots, \mathbf{x}_n) d\mathbf{x}_1, \cdots, d\mathbf{x}_n, \tag{III.6}$$

for $A \in \mathcal{A}$. In the literature this the following set integral notation [24, Ch. 11.3.3.1] was introduced

$$\int_{\mathbb{X}} f(X)\delta X \triangleq \sum_{n=0}^{\infty} \frac{1}{n!} \int_{\mathbb{X}^n} f(\{\mathbf{x}_1, \cdots, \mathbf{x}_n\}) d\mathbf{x}_1 \cdots d\mathbf{x}_n, \tag{III.7}$$

for any set function $f(\cdot)$, defined on the set of all finite subsets of $\mathbb{X}$, denoted $\mathcal{F}(\mathbb{X})$. From Eqs. (III.6) and (III.7) we have

$$Pr\{X \subseteq A\} = \int_A p(X)\delta X, \tag{III.8}$$

for a non-negative function $p(\cdot)$ defined on $\mathcal{F}(\mathbb{X})$ as

$$p(\{\mathbf{x}_1, \cdots, \mathbf{x}_n\}) \triangleq j_n(\mathbf{x}_1, \cdots, \mathbf{x}_n). \tag{III.9}$$

Observe that $Pr\{X \subseteq A\}$ actually repackages the probability measure $Pr\{X \in \mathcal{S}\}$ introduced in Eq. (III.5), where $\mathcal{S} = \cup_{n=0}^{\infty} A^n$. Moreover, $\int p(X)\delta X = 1$. A detailed presentation of the link between PP and RFS is presented in [97, Sec. II]. In the following sections, we shall employ the common term of *multi-target process* for both finite-simple PP or RFS.

III.2.4 Moment measures of point processes

Let us now consider that the total population of the finite PP has finite k-th moment $\mathbb{E}\{(N(\mathbb{X}))^k\}$, for $k \in \mathbb{N}^+$. Where $N(A)$ denotes the random number of points of the PP falling in A. Then, for any Borel set $A \in \mathcal{A}$ we can define [85, Ch. 5.4, Eq. (5.4.1)] the expectation

$$M_k(A^k) = \mathbb{E}\{(N(A))^k\}.$$

Similarly, k-th factorial-moment measures $M_{[k]}(\cdot)$ can be defined on arbitrary rectangle sets of the form $A_1^{[k_1]} \times \cdots \times A_r^{[k_r]}$ with $\{k_1, \cdots, k_r\}$ representing a partition of k (i.e. $\sum_{i=1}^{r} k_i = k$):

$$M_{[k]}(A_1^{[k_1]} \times \cdots \times A_r^{[k_r]}) = \mathbb{E}\{(N(A_1))^{[k_1]} \cdots (N(A_r))^{[k_r]}\}.$$

Whenever $M_{[k]}(\cdot)$ exists, the densities $m_{[k]}(\cdot)$ and $j_n(\cdot)$ are related by the equation

$$m_{[k]}(\mathbf{x}_1, \cdots, \mathbf{x}_k) = \sum_{n=0}^{\infty} \frac{1}{n!} \int_{\mathbb{X}^n} j_{k+n}(\mathbf{x}_1, \cdots, \mathbf{x}_k, \mathbf{y}_1, \cdots, \mathbf{y}_n) d\mathbf{y}_1 \cdots d\mathbf{y}_n. \tag{III.10}$$

In multi-target tracking the first-order moment density is also referred to as the intensity function or the Probability Hypothesis Density (PHD) function [27]. The term of PHD is preferred, since the term of intensity has a multitude of meanings in the signal processing literature. Note, that in Mahler's set-integral notation of Eq. (III.7), the PHD is denoted as $D(\mathbf{x})$ and is equivalently defined as [24, Ch. 16.2.3]:

$$D(\mathbf{x}) = \int p(\{\mathbf{x}\} \cup X)\delta X, \tag{III.11}$$

[4] We are considering a simple PP, that is all elements of the outcomes of X are district a.s.

where $p(\cdot)$ is the probability density of the RFS X, Eq. (III.9).

In multi-target tracking and medical applications, the first-order moment density $m_1(\cdot) = m_{[1]}(\cdot)$ is of practical importance. Several arguments are presented in the following paragraphs. Firstly, for Poisson PP, the first-order moment density completely characterizes the process, thus estimates of $m_1(\cdot)$ represent sufficient statistics for the process. Secondly, the propagation of the first-order moment density is practically achievable either by Gaussian mixture approximations [98] or Sequential Monte Carlo (SMC) methods [97]. Currently, there are no practical implementations of higher-order filters in the tracking literature. Similarly to the Janossy density (III.2), the kth fractional-moment density has the following physical interpretation:

$$Pr\left\{\begin{array}{l}\text{one point located in each of the}\\ k \text{ distinct intervals } (\mathbf{x}_i, \mathbf{x}_i + d\mathbf{x}_i)\end{array}\right\} = m_{[k]}(\mathbf{x}_1, \cdots, \mathbf{x}_k)d\mathbf{x}_1 \cdots d\mathbf{x}_k. \tag{III.12}$$

Note the differences between the interpretation of the kth fractional moment density of Eq. (III.12) and the kth Janossy density of Eq. (III.2). From this interpretation, an important property of the PHD is easily derived for any Borel set $A \in \mathcal{A}$:

$$M_1(A) = \mathbb{E}\{N(A)\} = \int_A m_1(\mathbf{x})d\mathbf{x}. \tag{III.13}$$

This property makes the PHD extremely interesting for target tracking, since the expected number of targets/points in any given region of space is obtained simply by integrating the PHD over that region. Note that the value of $M_1(A)$ does not affect the expected number of targets for any other element of $\mathcal{A}$.

As noted in [85, p.137], from a practical point of view the fractional-order densities are more interesting than Janossy densities. That is, fractional-order densities of Eq. (III.11) can be estimated from the results of k observations at specific places, whereas the Janossy densities require indefinitely many observations to determine the exact and total number of occurrences.

III.3 Examples of finite point processes

In this section we present several examples of finite PP, or equivalently RFS, defined on $\mathbb{X} = \mathbb{R}^d$. The processes represent the basis for most tracking filters and algorithms and incorporate different priors on the number of targets, referred to as the cardinality distribution, and their distributions. Specialized processes, such as marked or labeled processes, are constructed from these examples and will be introduced in the sections dealing with their application. Since both terminologies of PP or RFS can be employed interchangeably in this chapter, from hereon, we will collectively refer to them as *multi-target processes*.

III.3.1 Independent and identically distributed cluster (iidc)

In the case of iid clusters [85, Ex. 5.3(a), p. 125], the points are considered as independent and identically distributed according to a probability distribution $V(A) = \int_A v(\mathbf{x})d\mathbf{x}$ for $A \in \mathcal{A}$. Consider the number of points, i.e. cardinality, as a random variable with distribution p_n. In such, the Janossy density of an iid cluster is

$$p(X = \{\mathbf{x}_1, \cdots, \mathbf{x}_n\}) \triangleq j_n(\mathbf{x}_1, \cdots, \mathbf{x}_n) = p_n\, n!\pi_n(\mathbf{x}_1, \cdots, \mathbf{x}_n) = p_n\, n!v(\mathbf{x}_1) \cdots v(\mathbf{x}_n), \tag{III.14}$$

where $\pi_n(\cdots)$ represents the symmetric joint probability density of n points at $\mathbf{x}_1, \cdots, \mathbf{x}_n$. The factorial $n!$, gives the number of ways we can associate the n points to $\mathbf{x}_1, \cdots, \mathbf{x}_n$. $j_n(\cdots)$ gives the probability density of finding n points at $\mathbf{x}_1, \cdots, \mathbf{x}_n$, and none elsewhere.

An exponential RFS notation, equivalent to Eq. (III.14), is

$$\begin{aligned} p(X) &= p_n\, n!\, [v(\cdot)]^X \\ &= p_n\, n!\, \prod_{\mathbf{x}\in X} v(\mathbf{x}), \end{aligned} \tag{III.15}$$

where the RFS exponential $[f(\cdot)]^X \triangleq \prod_{\mathbf{x}\in X} f(\mathbf{x})$ will be employed throughout the following sections.

Observe that the first-order moment density of Eq. (III.10) for an iid cluster, denoted hereon $D(\mathbf{x})$, is given by:

$$\begin{aligned} D(\mathbf{x}) \triangleq m_1(\mathbf{x}) &= \sum_{n=0}^{\infty} \frac{1}{n!} \int_{\mathbb{X}^{(n)}} p_{n+1}\, (n+1)!\, v(\mathbf{x}) \prod_{i=1}^{n} v(\mathbf{y}_n) d\mathbf{y}_1 \cdots d\mathbf{y}_n \\ &= v(\mathbf{x}) \sum_{n=0}^{\infty} (n+1) p_{n+1} \\ &= v(\mathbf{x}) \bar{N}, \end{aligned} \tag{III.16}$$

where $\bar{N} = \sum_{n=0}^{\infty} n p_n$ represents the mean number of points in $\mathbb{X}$. Hence, the knowledge of the individual point probability density $v(\cdot)$ on the space $\mathbb{X}$ coupled with the cardinality distribution p_n is sufficient and completely characterize the iid cluster. The iidc multi-target process has been employed to derive the Cardinalized PHD (CPHD) filter in [99].

III.3.2 Poisson process

Poisson point processes represent a very important class of multi-target processes, mainly due to the multitude of properties they possess. The Poisson process is a special case of the iid cluster, where the number of points contained in any subset $A_i \in \mathcal{A}$ is Poisson distributed with mean $N(A_i) = \int_{A_i} v(\mathbf{x}) d\mathbf{x}$. Furthermore, the Poisson random variables $\{N(A_i)\}_{i=1}^{k}$ are independent whenever the sets are disjoint: $\cap_{i=1}^{k} A_i = \emptyset$. As for the iidc process, the Poisson process has iid targets with pdf given by $v(\cdot)$, and probability density given by

$$p(X) = e^{-\bar{N}} \left[\bar{N} v(\cdot)\right]^X, \tag{III.17}$$

where we employed the exponential RFS notation of Eq. (III.15). By analogy to the iidc case, the intensity or PHD function is given by: $D(\mathbf{x}) = \bar{N} v(\mathbf{x})$. Note that the PHD function completely characterizes the Poisson multi-target process, that is, it captures both the parameters of the cardinality distribution and the individual target distribution. Given the PHD function, one estimates the mean number of targets $\hat{n}$ in $\mathbb{X}$ by integrating the PHD over $\mathbb{X}$, while target states are inferred from the first $\hat{n}$ local maxima of the PHD function. Based on the Poisson process, the first RFS multi-target filter was proposed in [27].

III.4 Error metrics for multi-target tracking

Performance evaluation of algorithms estimating multi-target states is more difficult than in the single-target case. The main difficulty is caused by the need to evaluate the number of points as well as point locations within the space $\mathbb{X}$. Consider a ground truth multi-target process consisting in the set of points $X = \{\mathbf{x}_1, \cdots, \mathbf{x}_n\}$ and an estimate $\hat{X} = \{\hat{\mathbf{x}}_1, \cdots, \hat{\mathbf{x}}_{\hat{n}}\}$. Note that even when the cardinals of the two sets are equal, i.e. $|X| = |\hat{X}|$, a direct application of a Mean Squared Error (MSE) metric is not possible since X and $\hat{X}$ are unordered. Instead, the MSE should be evaluated for all pairwise associations between the elements of both sets,

with the minimum MSE representing the MSE of the estimated set. However, when cardinals are different, a penalty term should also be incorporated in the final MSE. A metric taking into account the aforementioned issues, called the Optimum SubPattern Analysis (OSPA) was proposed in [100]. The OSPA is a standard tool in evaluating the performance of multi-target tracking filters [28, 101]. The OSPA metric requires two parameters, denoted $1 \leq p < \infty$ and $0 < c$. Let us note $d^c(\mathbf{x}, \hat{\mathbf{x}}) = \min(c, \|\mathbf{x} - \hat{\mathbf{x}}\|)$, with $\|\cdot\|$ representing the euclidean distance and $\text{Perm}(n)$ the set of all permutations of integers $1, \ldots, n$. Then, the OSPA distance [100] between X and $\hat{X}$ is

$$d_p^c(X, \hat{X}) \triangleq \left[\frac{1}{\hat{n}} \left(\min_{\sigma \in \text{Perm}(n)} \sum_{i=0}^{n} (d^c(\mathbf{x}_i, \hat{\mathbf{x}}_{\sigma(i)}))^p + c^p(\hat{n} - n) \right) \right]^{\frac{1}{p}}, \tag{III.18}$$

whenever $n \leq \hat{n}$, and $d_p^c(X, \hat{X}) = d_p^c(\hat{X}, X)$ otherwise. The first term of the sum of Eq. (III.18) gives the error in point location while the second term captures the cardinality miss-match between the two sets of points. The p parameter controls the impact of location errors on the OSPA metric, more specifically, increasing p increases the impact of large location errors. The cut-off parameter c weights cardinality errors and also acts as a threshold on the euclidean distance between two points $\|\mathbf{x} - \hat{\mathbf{x}}\|$. That is, the two points are paired together whenever the distance between them is smaller than the cut-off parameter, otherwise they are considered as unrelated. The OSPA metric will be employed throughout the chapter to evaluate the performance of multi-target tracking filters.

III.5 The PHD filter for TWS systems

In this section, the PHD filter for TWS systems is presented. TWS is common in radar and sonar systems and hence tracking methods were first developed in this context. As in all TWS systems, a pre-processor detects the presence of targets and estimates their associated locations, with the resulting observation set containing noisy target locations and possibly false alarms (called clutter). PDA filters, presented in Chapter II, were historically the first to be proposed for TWS systems. The first practical filter based on RFS (or simple-finite PP), dubbed the PHD filter, was proposed by Mahler in [27]. In this work, we shall refer to Mahler's PHD filter as the TWS-PHD, in order to distinguish it from the later TBD-PHD filters. The TWS-PHD filter propagates only the PHD function associated with the Poisson multi-target process conditioned on the set of current and past observations. The multi-target Poisson process was chosen to model the multi-target state due to the properties that these specific processes verify and that facilitate the derivation of the filtering equations. Furthermore, the PHD function completely characterizes the Poisson multi-target process (see Sec. III.3.2), and thus is sufficient for target inference. Whenever, the Poisson prior is not verified, the TWS-PHD filter represents an approximating filter, only propagating the first-order moment density (the PHD) of that multi-target process. In such cases, the estimated PHD of the TWS-PHD is an approximation to the true multi-target posterior, and in this sense, the TWS-PHD filter is similar to steady-state filters, such as the $\alpha - \beta$ and the $\alpha - \beta - \gamma$ filters [74, Ch. 6.5]. Generally, tracking algorithms consider the different targets as being independent, that is, no interaction among targets is present. This is also the case for the TWS-PHD filter since the Poisson multi-target process considers iid targets.

We consider n_t independent targets in a space $\mathbb{X} = \mathbb{R}^{d_x}$, where the index t denotes the discrete time samples. For each target i, with state vector $\mathbf{x}_t^i \in \mathbb{X}$ at time t, we employ the following state-space model

$$\mathbf{x}_t^i = f_t(\mathbf{x}_{t-1}^i) + \mathbf{v}_t^i, \tag{III.19a}$$
$$\mathbf{z}_t^i = h_t(\mathbf{x}_t^i) + \mathbf{w}_t^i, \tag{III.19b}$$

where we observe the vector $\mathbf{z}_t^i \in \mathbb{R}^{d_z}$. The possibly non-linear functions, $f_t(\cdot)$ and $h_t(\cdot)$, are referred to as the state-transition and observation functions. Noise vectors $\mathbf{v}_t^i$ and $\mathbf{w}_t^i$ are the state-model and observation noise, taken to be centered random processes with covariance matrices $\mathbf{Q}_t$ and $\mathbf{R}_t$. The observation set Z_t is formed by the detected observations $\mathbf{z}_t$, where the probability of detection is $p_D(\mathbf{x})$, to which false observations (clutter) is added (see Eq. III.22).

As in all filtering methods, we are interested in estimating the posterior density $p_{t|t}(X)$ of the multi-target process $X_{t|t}$, that is, X_t given all the observations $Z_{0:t}$ up to and including time t. Propagation of such densities on $\mathcal{F}(\mathbb{X})$ is not achievable, except in some specific cases [102], where restrictions are imposed on the variation of the number of points. As stated, for the specific case of the Poisson prior on the multi-target process, the intensity or PHD function is sufficient and of practical interest. The TWS-PHD filter aims for the recursive computation of the PHD function $D_{t|t}(\cdot)$ corresponding to the posterior distribution of the Poisson process $X_t|Z_{0:t}$, referred to as posterior distribution, with expression [Eq. (III.17)]:

$$p_{t|t}(X) \triangleq p(X_t|Z_{0:t}) = e^{-\int_{\mathbb{X}} D_{t|t}(\mathbf{x})d\mathbf{x}} \prod_{\mathbf{x}\in X} D_{t|t}(\mathbf{x}). \tag{III.20}$$

Note that $p_t(X)$ represents a probability density with relationship to the measure $\mu(\cdot)$ of Eq. (III.4). Similarly to the Kalman filter, the recursive estimation of $D_{t|t}(\cdot)$ is achieved through two stages: prediction and update. In the prediction stage, presented in Sec. III.5.1, the kinematic model of Eq. (III.19a) is applied to the multi-target process alongside with processes accounting for the death and birth of targets. While in Sec. III.5.2, the update of the predicted PHD is obtained by incorporating the new observation set Z_{t+1}.

III.5.1 TWS-PHD prediction

In the PHD prediction stage, we aim at obtaining the PHD $D_{t|t-1}(\cdot)$ corresponding to the process $X_{t|t-1} \triangleq X_t|Z_{t-1}$, which incorporates target deaths, kinematics and births. Target spawning, that is, a target "giving birth" to a secondary target, is not considered in this work since such situations are not of interest in bathymetrical applications.

Target death is achieved by a process called independent (Bernoulli) *thinning* ([94, Prop. 3.7] and [96, Ch. 2.8]), where the points of $X_{t-1|t-1}$ are retained independently with probability $p_{S,t-1}(\mathbf{x})$. A point not retained represents a target death. The process of retaining for one specific point is independent from the process of retaining other points. As shown in [96, Ch. 2.8], the thinned process is also Poisson with intensity (and PHD) of $p_{S,t-1}(\mathbf{x})D_{t-1|t-1}(\mathbf{x})$. Each point of the thinned process undergoes a kinematic transformation as dictated by the transition density $f_{t|t-1}(\mathbf{x}|\boldsymbol{\xi}) = \mathcal{N}(\mathbf{x}; f_t(\boldsymbol{\xi}), \mathbf{Q}_t)$ of the kinematic model in Eq. (III.19a). The resulting process is again a Poisson multi-target process [96, Ch. 2.11.1]. Furthermore, to account for target births, an independent Poisson process with intensity $\gamma_t(\cdot)$ is superposed to the transformed process. In virtue of the superposition theorem [93, Ch. 2.2], the predicted intensity (and PHD) of $X_{t|t-1}$ is given by

$$D_{t|t-1}(\mathbf{x}) = \gamma_t(\mathbf{x}) + \int_{\mathbb{X}} f_{t|t-1}(\mathbf{x}|\boldsymbol{\xi})\, p_{S,t-1}(\xi)\, D_{t-1|t-1}(\boldsymbol{\xi})d\boldsymbol{\xi}. \tag{III.21}$$

The predicted PHD model captures target death, birth and kinematics. Since the measurement does not intervene in the prediction stage, the predicted process and PHD are independent of the observation model. Hence, the same prediction equations apply for TBD-PHD filters.

III.5.2 TWS-PHD update

The pre-processing module detects the presence of targets and constitutes the set of detected observations Z_t^D. The detection process involves a non-unity probability of detection $p_D(\mathbf{x})$,

possibly depending on the position of the target, as defined in the previous chapter in Sec. II.2. Furthermore, the detection process of one target is supposed independent from the other targets. Hence, the detected or "thinned" target observations belong to the set Z_t^D with probability $p_D(\mathbf{x})$, just as defined in Eq. (II.6). Furthermore, clutter is present and modeled as a Poisson multi-target process K_t with intensity $\kappa_t(\cdot)$. Therefore, the complete observation set at time $t+1$, denoted Z_t, is given by:

$$Z_t \triangleq Z_t^D \cup K_t. \tag{III.22}$$

The observation set Z_t is said to be *uncertain*, that is, the origin of an observation $\mathbf{z}_t^i \in Z_t$ (clutter or a specific target) is unknown. In the PHD update stage, we aim at estimating the PHD $D_{t|t}(\cdot)$ corresponding to the posterior $p_{t|t}(X)$ of the process $X_{t|t}$, conditioned on all observations up-to and including time t.

Several PHD derivations are presented in the literature. In [27], Mahler was the first to derive the PHD filter explicitly aimed for multi-target tracking applications. The author employed the RFS formalism to derive $D_{t|t}(\cdot)$, indirectly, via the probability generating functional (p.g.fl.) of the updated process $X_{t|t}$. This is a rather technically-involved derivation, but provides a general result. In [103], the authors use the point process formalism and employ the specific properties of Poisson PP to derive the distribution of the process $X_{t|t}$, with the PHD obtained by the first-order moment density formula (III.10). Furthermore, the authors in [103] also give an equivalent probability generating functional derivation of the PHD filter, similar to [27], however within the PP framework. Also using the Poisson PP formalism, in [104] and subsequently [96, Appx. D], Streit employs Bayes's theorem to derive the posterior density of $X_{t|t}$ incorporating the new observation set Z_t. The PHD (or intensity), of this posterior is obtained by the mean field approximation [105, pp. 35-36]. In [106], Streit provides an alternative derivation to the PHD filter, by employing marked Poisson PP.

In all of the preceding works, their respective authors arrive at the same update formulas for the PHD, which we provide here without proof:

$$D_{t|t}(\mathbf{x}) = \left[1 - p_D(\mathbf{x}) + \sum_{i=1}^{|Z_t|} \frac{p_D(\mathbf{x}) p_t(\mathbf{z}_t^i|\mathbf{x})}{\mathcal{Z}_{t,i}}\right] D_{t|t-1}(\mathbf{x}), \tag{III.23}$$

where $|Z_t|$ is the cardinal of the current observation set, that is, the number of current observations. $\mathbf{z}_t^i$ is the i-th element of the observation set and $p_t(\mathbf{z}_t^i|\cdot)$ is the observation likelihood. The normalization constants are given by

$$\mathcal{Z}_{t,i} = \kappa_t(\mathbf{z}_t^i) + \int_{\mathbb{X}} p_D(\mathbf{x}) p_t(\mathbf{z}_t^i|\mathbf{x}) d\mathbf{x}.$$

Note that the updated posterior $p_{t|t}(X)$ does not factorize to the form of Eq. (III.20), hence $X_{t|t}$ is not a Poisson multi-target process. However, the PHD $D_{t|t}(\cdot)$ does represent the first-order moment density of the updated multi-target process, and it was shown in [27], that it represents the best approximation, in the Kullback-Leibler divergence sense, to the updated posterior. Hence, $D_{t|t}(\cdot)$ is employed as the intensity function of a Poisson approximation to $X_{t|t}$ that serves as the prior for the next iteration of the filter. This first-order approximation strengthens the comparison of the TWS-PHD filter and steady-state filters mentioned at the beginning of Sec. III.5. Indeed, the $\alpha-\beta$ and $\alpha-\beta-\gamma$ are steady-state filters [74, Ch. 6.5], i.e. constant Kalman gain, and only propagate the mean of the posterior distribution. In comparison, the TWS-PHD recursion propagates the first-order moment density of the multi-target posterior distribution.

The interpretation of $D(\mathbf{x})d\mathbf{x}$ as the probability of having a target at $\mathbf{x}$ [see Eq. (III.12)], gives another interesting interpretation of the PHD filter. The propagation of a function defined on $\mathbb{X}$ that respects the aforementioned property, is equivalent to a filter that propagates all

points of $\mathbb{X}$ (by prediction and update stages) and evaluates for each points a probability of existence, in a similar manner to the IPDAF (see Appendix A). The function relating the point state $\mathbf{x}$ to the target probability of existence at that state location, represents the PHD function. Hence the name of probability density function over $\mathbb{X}$ for the PHD function. Such an interpretation of the PHD filter, gives a "practical feel" of the PHD function and justifies the process of inferring target states from the maxima of the PHD function. Integrating the probability of existence function (PHD) over $\mathbb{X}$ does not yield 1. Instead the mean number of targets on $\mathbb{X}$ is "encoded" in the normalizing constant of the PHD function. Additional parallels between the IPDAF and RFS-based filters are drawn in [107].

III.6 TBD-PHD filter for phased arrays: a Gaussian point-target case

In this section we propose a Track Before Detect (TBD) filter aimed at tracking the Direction Of Arrival (DOA) of multiple targets from phased-array observations. In the TBD framework, the array signal is fed directly to the tracking module, without the need of pre-processors that detect targets and form observation sets. Indeed, detection and estimation of targets is conducted entirely by the TBD filter. This leads to more complex tracking filters that circumvent the loss of information incurred by the observation-set formation, i.e. thresholding, of the array-signal spectrograms (see Sec. II.2). The phased-array model poses a new problem since each target emits a signal, called source or target signal. Bathymetric sonars are active systems, hence the source signals are actually signals backscattered by resolution cells on the sea-bottom. However, the method we propose can be employed for passive sonars or more generally, for targets that emit signals, either target-backscattered or target-generated signals. Additionally, the targets considered in this section are modeled as point targets with Gaussian source/target signals. Existing methods consider the source signal as part of an augmented system state. This is inefficient, especially for particle approximations of posteriors, where samples are drawn from the higher-dimension posterior of the augmented state. To address these problems, we propose a novel Marked Poisson multi-target model and derive the Probability Hypothesis Density (PHD) filter that adaptively estimates target DOA directly from phased-array observations. The proposed model accounts for variations of both the number and the location of points representing targets. The mark of a point represents the source/target signal, without the need of an augmented state. Recursive formulas for the marked process PHD filter are derived with simulations showcasing improved performance over state-of-the-art methods.

III.6.1 Introduction

Modern radar and sonar systems employ antenna or hydrophone arrays in order to detect, localize and track various targets. Target localization is achieved by estimating the Direction Of Arrival (DOA) of the source signal. DOA tracking is traditionally achieved through a two-stage process referred to as Track While Scan (TWS). Firstly, targets are detected and a set of DOA estimates is formed [see Eq. (II.4)]. The resulting DOA estimates suffer from origin uncertainty, that is, the origin of observations (clutter or target) is unknown. Secondly, filtering the DOA estimates with the kinematic model and resolving the origin uncertainty problem is dealt with probabilistic data association filters, as described in Ch. II of this manuscript. In [108, 109] we proposed a TWS system for a sonar image-reconstruction application. The advantage of such TWS systems for image reconstruction applications is the relative low-complexity implementations. The downside of TWS is the reliance on the pre-processing module aimed at forming the observation set Z. The bias and variance introduced by the pre-processor should be reduced

by the TWS filtering post-processor. Furthermore, the set of observations Z is usually formed form on a small time-sample window of array snapshots. Hence, the TWS filter has a reduced resolution effect, that is, only offers one filtered DOA estimate corresponding to the window of array snapshots. Unlike PDAF-based methods, the PHD filter offers a rigorous framework for target birth and death processes. The PHD filter in the TWS configuration (TWS-PHD) [see Sec. III.5] has found numerous applications in diverse fields [110–113]. In [50] DOA tracking of multiple speakers is achieved by a two-stage processing chain. In the pre-processor, a set of DOA measurements is extracted form a short time-block of microphone array data by means of the independent component analysis and the state-coherence transform. Based on the detected DOAs, a Gaussian Mixture PHD (GM-PHD) filter is employed to perform tracking of the time-varying number of speakers. In [102], a Bayesian RFS filter that tracks the speaker locations and number of speakers is performed.

Track Before Detect (TBD) filters, are aimed at tracking targets directly from the antenna signal, i.e. without performing any pre-detection or estimation procedures. Furthermore, the proposed marked multi-target process is capable of taking into account target birth and death, i.e. a variable number of targets. The TWS-PHD filter of Sec. III.5, with implementations given in [97], is derived for TWS systems and is not directly applicable for TBD. A first TBD-Multi-Bernoulli filter was proposed in [114], for a specific case of separable likelihood: multiple non-overlapping objects in image sequences. In contrast, the phased-array observation likelihood is not separable. A TBD-PHD filter for amplitude sensors was derived in [28], and since the sensor observation is the algebraic sum of individual target contributions, the resulting filter was named the superpositional PHD. However in array processing, the DOA information is contained in the phase differences between the signals received by the phased array, and in general, we are not directly interested in signal amplitudes. Furthermore, array observations result from the superposition of individual source contributions that, unlike in [28], are unknown and modeled as randomly fluctuating complex signals. Thus, [28] cannot be directly used for the standard DOA tracking problem, and further refinements of the superpositional PHD filter must be conducted in order to tackle this problem. A possible work-around solution would be to augment the state of each target with its source signal. Such a solution is undertaken in [38], coupled with a reversible-jump MCMC algorithm to handle fluctuations in target number. Furthermore, for augmented-state particle filters, sampling from higher-dimensional posteriors is inefficient. In [115] the authors propose a multi-Bernoulli filter coupled with the MUSIC [56, Ch. 4.5] pseudo-spectrum in order to track several targets from array observations.

The novelty of our approach is the proposal of a marked multi-target model and the derivation of the first-order moment density filter (PHD or intensity) for DOA tracking. The marked formalism naturally describes targets that generate a *mark*, here a stochastic signal representing the individual source/target contribution. Thus, we extend in the case of marked processes (formally introduced in Sec. III.6.2) the aforementioned superpositional TBD-PHD filter. A Poisson multi-target process, referred to as the ground process, describes target number and target location in the single-target space $\mathbb{X}$. The PHD or intensity function of a Poisson process is sufficient to describe the process, see section III.3.2 of this chapter. Hence, the filter that adaptively estimates target DOA, given the current and previous observations, only needs to propagate the PHD corresponding to the posterior distribution. Furthermore, in section III.6.3 we show that the propagation of the ground-process PHD (defined on the single-target space) is sufficient. Thus, we avoid the propagation of the a density function in the single-target and mark spaces, leading to a more efficient particle-filter implementation of the filter. In the update step of all superpositional filters a Gaussian approximation is employed for the distribution of the superpositional observation. A similar approximation is employed here, while in the Appendix F we justify this Gaussian approximation. To our knowledge, such a justification has yet to be made available for the supperpositional observation model [28, 86, 116].

We argue that the marked model introduces a distinction between points and marks that has physical meaning, that is, a point generates the mark. The marked-process model captures this point-mark relationship, which would be otherwise lost in an augmented state formalism. We emphasis the ability of the proposed filter to deliver target DOA estimates for each array observation. This is required in array-processing algorithms for high-resolution image-formation algorithms, e.g. sonar bathymetry reconstruction [109]. In contrast, the method of [115] and most TWS methods (including the one presented in Ch. II) process several array observations to produce one DOA estimate. Thus, generally resulting in a reduced resolution effect in imaging applications.

In the following, we present the phased-array observation model alongside the marked multi-target process in Sec. III.6.2. In Sec. III.6.2 the phased-array observation model is developed for point targets with Gaussian source signals and Gaussian additive noise. In section III.6.3 we derive the approximate PHD/intensity filtering equations for the phased-array TBD-PHD filter. In section III.6.4 we showcase the phased-array TBD-PHD filtering results and we conclude in section III.7.

III.6.2 Array signal and marked multi-target process

We assume a Poisson multi-target process X_t at time t that describes both the number of targets and their locations. Consider $\{\mathbf{x}_t^1, \cdots, \mathbf{x}_t^{n_t}\}$ the realization of X_t, with n_t a realization of a Poisson random variable of mean $\int_{\mathbb{X}} D_t(\mathbf{x})d\mathbf{x}$, see Sec. III.3.2. Conditional to the number of points, individual elements of $\{\mathbf{x}_t^1, \cdots, \mathbf{x}_t^{n_t}\}$ are independent and identically distributed in the single-target space $\mathbb{X} \subset \mathbb{R}^{d_x}$. The probability distribution (referenced to the measure $\mu(\cdot)$ of (III.4)) of X_t can be specified by the distribution of the number N_t of targets and the joint distribution of the target positions, conditional on the total number of targets $N_t = n_t$. Thus, using the RFS notation of Sec. III.2.3, X_t has an associated probability density (III.17) of:

$$p_t(X) = \mathrm{e}^{-\int_{\mathbb{X}} D_t(\mathbf{x})d\mathbf{x}} \prod_{\mathbf{x}\in X_t} D_t(\mathbf{x}), \tag{III.24}$$

where $D_t(\cdot)$ represents the PHD/intensity function defined on the single-target space $\mathbb{X}$. Targets are presented as peaks of $D_t(\cdot)$, and thus target locations can be inferred from $D_t(\cdot)$. Next, we consider that each point $\mathbf{x}_t$ generates a mark s_t in a mark space $\mathbb{K} \subseteq \mathbb{C}$. The point process $\{(\mathbf{x}_t^i, s_t^i)\}$ on $\mathbb{X} \times \mathbb{K}$ is Poisson and represents a Marked Poisson PP or marked multi-target process, which we denote $\widetilde{X}_t$. With X_t usually called ground process [85, Ch. 6.4]. In this work, marks represent the source signals generated by the targets, and conditioned on the target states, the marks are taken to be centered and circular Gaussian random variables with power $P((\mathbf{x}_t))$: $s_t|\mathbf{x}_t \sim \mathcal{CN}(0, P(\mathbf{x}_t))$. Note that the source-signal power $P(\cdot)$, is a function of the target state vector. The marked process $\widetilde{X}_t$ is Poisson with points $\tilde{\mathbf{x}} = (\tilde{\mathbf{x}}, s)$ and intensity function $\widetilde{D}_t(\tilde{\mathbf{x}}) = D_t(\mathbf{x})\mathcal{CN}(s; 0, P(\mathbf{x}))$, as given by the Marking Theorem [94, Prop. 3.9] and [93, p. 55].

We assume a point-target model with an array signal $\mathbf{y}_t \in \mathbb{C}^{M\times 1}$ by an $M-$element array as the random sum

$$\mathbf{y}_t = \sum_{\tilde{\mathbf{x}}\in\widetilde{X}_t} \mathbf{g}(\tilde{\mathbf{x}}) + \mathbf{n}_t, \tag{III.25}$$

where $\mathbf{g}(\tilde{\mathbf{x}}_t) = \mathbf{a}(\mathbf{x}_t)s_t$. $\mathbf{a}$ is the array-manifold vector, having the form given in Eq. (III.27), typical of point targets. The additive noise $\mathbf{n}_t \in \mathbb{C}^{M\times 1}$ is $\mathbf{n}_t \sim \mathcal{CN}(\mathbf{0}, \sigma_t^2\,\mathbf{I}_M)$. The Signal to Noise Ratio (SNR) is given by $SNR = \frac{P}{\sigma_t^2}$.

Generally, target tracking is conducted in the Cartesian coordinate system, with several kinematic models such as the nearly constant velocity or the Wiener acceleration model [74, Ch. 6.3]. For distant targets, tracking in polar coordinates becomes adequate since pseudo-acceleration is small [117, Ch. 1.5]. In this chapter, we consider a first-order kinematic model,

i.e. a nearly constant angular-velocity model:

$$\mathbf{x}_t = \mathbf{F}_t \mathbf{x}_{t-1} + \mathbf{v}_t, \tag{III.26}$$

where $\mathbf{x}_t = [\theta_t, \dot{\theta}_t]^T \in \mathbb{X}$ presents the single-target state vector. $\mathbf{v}_t \sim \mathcal{N}(\mathbf{v}_t; \mathbf{0}, \mathbf{Q})$ represents the white model noise. $\mathbf{F}_t$ is a transition matrix specific for a constant-velocity model [74, Ch. 6.3.1].

Assuming a ULA with far-field, narrow-band point targets, the array manifold vector $\mathbf{a}(\mathbf{x}_t)$ is defined as:

$$\mathbf{a}(\mathbf{x}_t) \triangleq \begin{bmatrix} 1 & e^{-j\,k\Delta\sin(\theta_t)} & \cdots & e^{-j\,k(M-1)\Delta\sin(\theta_t)} \end{bmatrix}^T, \tag{III.27}$$

where $\{\cdot\}^T$ represents the transpose operator. $k = \frac{2\pi}{\lambda}$ represents the wave number, λ the wavelength and Δ the inter-receiver spacing.

In order to infer target positions from the marked process $\widetilde{X}_t$, the knowledge of $D_t(\mathbf{x})$ is sufficient. The number of targets in any region $A \subseteq \mathbb{X}$ is given by $\int_A D_t(\mathbf{x})d\mathbf{x}$. Target DOAs can be obtained from the locations of the main peaks of $D_t(\cdot)$. The aim of the proposed filter is to adaptively detect targets and estimate target states $\mathbf{x}_t$ from the marked process posterior $p_{t|t}(\widetilde{X}) \triangleq p(\widetilde{X}_t|\mathbf{y}_{0:t})$, given the sequence $\mathbf{y}_{0:t}$ of past and current array observations. In order to achieve this goal, propagation of the corresponding PPP PHD $D_{t|t}(\mathbf{x})$ is sufficient, while the marked process occurs naturally in the observation likelihood. In such, the propagation of $D_{t|t}(\mathbf{x})$ is conducted in the state-space $\mathbb{X}$, avoiding the propagation in the augmented space $\mathbb{X} \times \mathbb{K}$ [38]. Approximate propagation formulas for $D_{t|t}(\mathbf{x})$ are derived in the following section.

III.6.3 Approximate PHD filter for marked multi-target process

In this section, we derive the filtering equations for the array-processing problem. Given the intensity $D_{t-1|t-1}(\mathbf{x})$ at time $t-1$, we aim at deriving the PHD $D_{t|t}(\mathbf{x})$ corresponding to the posterior distribution of the ground multi-target process, given the phased-array observations up to and including time t. The resulting filter will be referred to as the TBD-PHD filter in this manuscript. The TBD-PHD filter comprises two stages: prediction (Sec. III.6.3.a) and update (sec. III.6.3.b). Since the observation is not involved in the prediction process, the predicted PHD $D_{t|t-1}(\mathbf{x})$ for TBD-PHD is identical to the one of the TWS-PHD filter of Sec. III.5.1. The predicted PHD takes into account target kinematics, as dictated by the law of motion of Eq. (III.26), and target death and birth. The update stage intends to correct the predicted intensity with the current observation $\mathbf{y}_t$. Closed-form expressions are not available for the updated intensity, and an approximation similar to [28] is proposed.

III.6.3.a Phased-array TBD-PHD Prediction

Consider at time $t-1$ the intensity or PHD function $D_{t-1|t-1}(\cdot)$, corresponding to the posterior density $p_{t-1|t-1}(X)$ of the ground process,[see Eq. (III.24)]. The ground process describes target locations at time $t-1$ and undergoes a stochastic transformation induced by target death and movement of the surviving targets. Both the process at time $t-1$ and the prediction process are Poisson processes. In other words, the prediction operation is exact and $D_{t|t-1}(\cdot)$ is a sufficient statistic for the prediction process. In this section, all arguments for the specific form of the predicted intensity of the TWS-PHD filter apply. In the following, we will only recall the prediction parameters and their impact in the predicted intensity. For a detailed construction of the predicted intensity function see Sec. III.5.1.

Target death is modeled by a process of independent thinning. That is, targets present at time $t-1$ are retained with probability $p_s(\mathbf{x})$. Inclusion (or equivalently retention) of targets is independent of each other. Each point of the thinned process undergoes a kinematic transformation as dictated by the transition density $f_{t|t-1}(\mathbf{x}|\boldsymbol{\xi}) = \mathcal{N}(\mathbf{x}; \mathbf{F}_t\boldsymbol{\xi}, \mathbf{Q}_t)$ of the kinematic model

in Eq. (III.26). Target birth is accounted for by an independent multi-target Poisson process with intensity $\gamma_t(\cdot)$. From Sec. III.5.1, the form of the predicted intensity is given by

$$D_{t|t-1}(\mathbf{x}) = \gamma_t(\mathbf{x}) + \int_{\mathbb{X}} f_{t|t-1}(\mathbf{x}|\boldsymbol{\xi})\, p_s(\boldsymbol{\xi})\, D_{t-1|t-1}(\boldsymbol{\xi}) d\boldsymbol{\xi}. \tag{III.28}$$

The predicted PHD model captures target death, birth and kinematics. Marking the process $X_{t|t-1}$ supposes appending to each element $\mathbf{x}$ of a realization of $X_{t|t-1}$ the mark s, in order to obtain the pair $\tilde{\mathbf{x}} \triangleq (\mathbf{x}, s)$. The marked process, denoted $\widetilde{X}_{t|t-1}$, has the same number of points as the $X_{t|t-1}$. Conditionally on the target state $\mathbf{x}$, the mark s is sampled from $\mathcal{CN}(0, P(\mathbf{x}))$, as explained in Sec. III.6.2. Hence, the marked process $\widetilde{X}_{t|t-1}$ has the same Poisson distribution as $X_{t|t-1}$ but with intensity (or PHD) function given by

$$\widetilde{D}_{t|t-1}(\tilde{\mathbf{x}}) = D_{t|t-1}(\mathbf{x})\mathcal{CN}(s; 0, P(\mathbf{x})). \tag{III.29}$$

As shown in the following section, the propagation of $D_{t|t}(\mathbf{x})$ is sufficient, with the marked PHD intervening in the array likelihood model. This leads to an efficient implementation, that propagates only a particle approximation of $D_{t|t}(\mathbf{x})$.

III.6.3.b Phased-array TBD-PHD Update

By the definition of (III.10), $D_{t|t}(\cdot)$ is given by

$$D_{t|t}(\mathbf{x}) = \sum_{n=0}^{\infty} \frac{1}{n!} \int \cdots \int p_{t|t}(\{\mathbf{x}, \mathbf{w}_1, \cdots, \mathbf{w}_n\}) d\mathbf{w}_1 \cdots d\mathbf{w}_n.$$

Or more compactly, by using the set integral [Eq. (III.11)] representation

$$D_{t|t}(\mathbf{x}) = \int p_{t|t}(\{\mathbf{x}\} \cup W)\delta W \tag{III.30}$$

where $W = \{\mathbf{w}_1, \cdots, \mathbf{w}_n\}$ is a multi-target process with density $p_{t|t}(\cdot)$. Applying the Bayes rule for the posterior $p_{t|t}(W)$ we obtain

$$\begin{aligned} D_{t|t}(\mathbf{x}) &= \frac{\int p_t(\mathbf{y}_t|\{\mathbf{x}\} \cup W) p_{t|t-1}(\{\mathbf{x}\} \cup W)\delta W}{p_t(\mathbf{y}_t|\mathbf{y}_{0:t-1})} \\ &= \frac{\sum_{n=0}^{\infty} \frac{1}{n!} \int_{\mathbb{X}^n} p_t(\mathbf{y}_t|\{\mathbf{x}, \mathbf{w}_1, \ldots, \mathbf{w}_n\}) \mathrm{e}^{\left(-\int D_{t|t-1}(\mathbf{z}) d\mathbf{z}\right)} D_{t|t-1}(\mathbf{x}) \prod_{i=1}^{n} D_{t|t-1}(\mathbf{w}_i) d\mathbf{w}_1 \ldots d\mathbf{w}_n}{\int p_t(\mathbf{y}_t|W) p_{t|t-1}(W)\delta W} \end{aligned}$$

where, in the last equality, we have employed the Poisson expression of Eq. (III.17) for $p_{t|t-1}(W)$. By separating the intensity $D_{t|t-1}(\mathbf{x})$ from the ratio, we obtain

$$D_{t|t}(\mathbf{x}) = D_{t|t-1}(\mathbf{x})\; L_{\mathbf{y}_t}(\mathbf{x}). \tag{III.31}$$

The ratio $L_{\mathbf{y}_t}(\mathbf{x})$, referred to as pseudo-likelihood, is given by

$$L_{\mathbf{y}_t}(\mathbf{x}) = \frac{\int p_t(\mathbf{y}_t|\{\mathbf{x}\} \cup W) p_{t|t-1}(W)\delta W}{\int p_t(\mathbf{y}_t|W) p_{t|t-1}(W)\delta W}. \tag{III.32}$$

The array likelihood involves target positions and associated marks (source signals), and can be further written as

$$p_t(\mathbf{y}_t|\{\mathbf{w}_1, \ldots, \mathbf{w}_n\}) = \int_{\mathbb{X}^n} p_t(\mathbf{y}_t|\{(\mathbf{w}_1, s_1), \ldots (\mathbf{w}_n, s_n)\}) \prod_{i=1}^{n} \mathcal{CN}(s_i; 0, P(\mathbf{w}_i)) ds_1 \cdots ds_n. \tag{III.33}$$

The construction of the marked set now becomes evident. Let $\{(\mathbf{w}_1, s_1), \dots (\mathbf{w}_n, s_n)\}$ be a realization of the multi-target process $\widetilde{W}$, referred to as marked multi-target process. Note that the marked multi-target process $\widetilde{W}$ is obtained by marking of the ground process W. Both the ground and marked processes are Poisson and have the same cardinality, denoted by $|W|$ and $|\widetilde{W}|$, respectively.

The denominator of the pseudo-likelihood of Eq. (III.32) can be written in terms of the marked process $\widetilde{W}$ as

$$\begin{aligned}\int p_t(\mathbf{y}_t|W)p_{t|t-1}(W)\delta W &= \sum_{n=0}^{\infty}\frac{1}{n!}\int_{(\mathbb{X}\times\mathbb{K})^n} p_t\left(\mathbf{y}_t|\{(\mathbf{w}_i,s_i)\}_{i=1}^n\right)\\ &\quad\times \mathrm{e}^{(-\int_{\mathbb{X}} D_{t|t-1}(\mathbf{x})d\mathbf{x})}\prod_{i=1}^{n}\left[D_{t|t-1}(\mathbf{w}_i)\mathcal{CN}(s_i;0,P(\mathbf{w}_i))\right]d\mathbf{w}_1 ds_1\cdots d\mathbf{w}_n ds_n\\ &= \int p_t(\mathbf{y}_t|\widetilde{W})p_{t|t-1}(\widetilde{W})\delta\widetilde{W},\end{aligned}$$

where the set integral of marked multi-target processes is defined as

$$\int f(\widetilde{W})\delta\widetilde{W} = \sum_{n=0}^{\infty}\frac{1}{n!}\int_{(\mathbb{X}\times\mathbb{K})^n} f\left(\{(\mathbf{w}_1,s_1)\cdots,(\mathbf{w}_n,s_n)\}\right)d\mathbf{w}_1 ds_1\cdots d\mathbf{w}_n ds_n.$$

Proceeding in a similar manner for the numerator of Eq. (III.33) we obtain:

$$L_{\mathbf{y}_t}(\mathbf{x}) = \frac{\iint p_t(\mathbf{y}_t-\mathbf{a}(\mathbf{x})s|\widetilde{W},\,\tilde{\mathbf{x}})\mathcal{CN}(s;0,P(\mathbf{x}))p_{t|t-1}(\widetilde{W})\delta\widetilde{W}ds}{\int p_t(\mathbf{y}_t|\widetilde{W})p_{t|t-1}(\widetilde{W})\delta\widetilde{W}},$$

where the integration order was interchanged. This operation does not pose any issues since the integrated functions are all non-negative.

By employing the change of variables formula proposed in [118, Prop 4., p.180], that is, denoting $\mathbf{z} \triangleq \sum_{\tilde{\mathbf{w}}\in\widetilde{W}}\mathbf{g}(\tilde{\mathbf{w}})$ we obtain

$$L_{\mathbf{y}_t}(\mathbf{x}) = \frac{\iint \mathcal{CN}(\mathbf{y}_t-\mathbf{a}(\mathbf{x})s;\mathbf{z},\sigma_t^2\mathbf{I}_M)p(\mathbf{z})d\mathbf{z}\,\mathcal{CN}(s;0,P(\mathbf{x}))ds}{\int \mathcal{CN}(\mathbf{y}_t;\mathbf{z},\sigma_t^2\mathbf{I}_M)p(\mathbf{z})d\mathbf{z}}. \tag{III.34}$$

Observe that in Eq. (III.34) the set integrals are now reduced to ordinary integrals, where $p(\mathbf{z})$ is the distribution induced by the change of variables. As proposed in [28], if we approximate $p(\mathbf{z}) \approx \mathcal{CN}(\mathbf{z},\tilde{\mu},\widetilde{\mathbf{\Sigma}})$ with a Gaussian distribution, then we are able to obtain an analytic formula for the updated PHD. In Appendix F, we justify the Gaussian approximation for superpositional observations by employing Campbell's theorem [93, Ch. 3.2]. To our knowledge, such a justification has yet to be made available for the supperpositional observation model [28,86,116]. The first and second order moments of $p(\mathbf{z})$ are obtainable from the marked predicted distribution $p_{t|t-1}(\widetilde{X})$ by means of the Marking Theorem [93, Ch. 5.3]:

$$\begin{aligned}\tilde{\mu} &= \int_{\mathbb{X}\times\mathbb{K}}\mathbf{g}(\tilde{\mathbf{x}})\,\widetilde{D}_{t|t-1}(\tilde{\mathbf{x}})d\tilde{\mathbf{x}}\\ &= \int_{\mathbb{X}}\mathbf{a}(\mathbf{x})\left(\int_{\mathbb{K}} s\,\mathcal{CN}(s;0,P(\mathbf{x}))ds\right)D_{t|t-1}(\mathbf{x})d\mathbf{x} = \mathbf{0} &\text{(III.35a)}\\ \widetilde{\mathbf{\Sigma}} &= \int_{\mathbb{X}\times\mathbb{K}}\mathbf{g}(\tilde{\mathbf{x}})\mathbf{g}^H(\tilde{\mathbf{x}})\,\widetilde{D}_{t|t-1}(\tilde{\mathbf{x}})d\tilde{\mathbf{x}}\\ &= \int_{\mathbb{X}}\mathbf{a}(\mathbf{x})P(\mathbf{x})\mathbf{a}^H(\mathbf{x})\,D_{t|t-1}(\mathbf{x})d\mathbf{x}, &\text{(III.35b)}\end{aligned}$$

where $\widetilde{D}_{t|t-1}(\tilde{\mathbf{x}})$ is the predicted marked PHD given by Eq. (III.29), and $\{\cdot\}^H$ represents the transpose conjugate operator. The formula for combination of quadratic terms, given in Appendix E, is employed to solve the denominator and inner integral of the numerator in the ratio

of Eq. (III.34). Thus yielding

$$L_{\mathbf{y}_t}(\mathbf{x}) \approx \frac{\int \mathcal{CN}(\mathbf{y}_t; \mathbf{a}(\mathbf{x})s, \sigma_t^2\mathbf{I}_M + \widetilde{\mathbf{\Sigma}})\mathcal{CN}(s; 0, P(\mathbf{x}))ds}{\mathcal{CN}(\mathbf{y}_t; \mathbf{0}, \sigma_t^2\mathbf{I}_M + \widetilde{\mathbf{\Sigma}})}. \tag{III.36}$$

Solving again the numerator of Eq. (III.36) becomes

$$L_{\mathbf{y}_t}(\mathbf{x}) \approx \frac{\mathcal{CN}(\mathbf{y}_t; \mathbf{0}, \mathbf{a}(\mathbf{x})\, P(\mathbf{x})\, \mathbf{a}^H(\mathbf{x}) + \sigma_t^2\mathbf{I}_M + \widetilde{\mathbf{\Sigma}})}{\mathcal{CN}(\mathbf{y}_t; \mathbf{0}, \sigma_t^2\mathbf{I}_M + \widetilde{\mathbf{\Sigma}})}. \tag{III.37}$$

The final form of the pseudo-likelihood, given in the above equation, used in conjunction with Eq. (III.31) yield the updated intensity function $D_{t|t}(\mathbf{x})$.

III.6.4 Results on simulated phased-array data

The final form of the pseudo-likelihood is given in Eq. (III.37), were $\widetilde{\mathbf{\Sigma}}$ is given by Eq. (III.35b). This analytic relationship facilitates the update of the predictive PHD with Eq. (III.31). Since we employ a Gaussian approximation of $p(\mathbf{z})$, the integral of the PHD is no longer a reliable estimate for the number of targets. Hence, target-state inference requires clustering methodology that extracts the number of targets and their state estimates from the estimated intensity function. In [28], this is achieved by iterating the $k-$means clustering algorithm for different numbers of clusters and evaluating the cluster separation with the silhouette method [119]. However, the silhouettes exist only when there are two or more clusters, hence there is no state inference when there are less than two clusters. In fact, the authors of [28] notice the increased error of this method whenever there is only one target present. Here, we propose to use the DBSCAN clustering algorithm [120], which does not require *apriori* knowledge of the number of clusters and considers the existence of particles not belonging to any cluster, i.e. outliers. This is necessary since a number of particles, corresponding to the birth process $\gamma_t(\cdot)$, are expected to be dispersed whenever there are no birthed targets. Note that the $k-$means aims to minimize the within-cluster sum of squares and hence behaves poorly in presence of such outliers.

A test scenario involving crossing targets was envisaged. Similarly to [28], the proposed TBD-PHD filter is implemented using a particle filter, that employs an auxiliary step to resample birth particles. The particles corresponding to the surviving targets (also called persistent particles), are propagated through a bootstrap particle filter, that is employing the

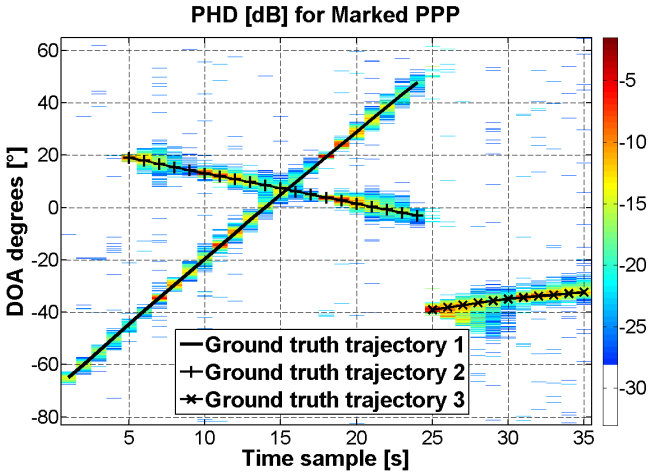

Figure III.1: Logarithm of estimated intensity function, for the proposed TBD-PHD filter.

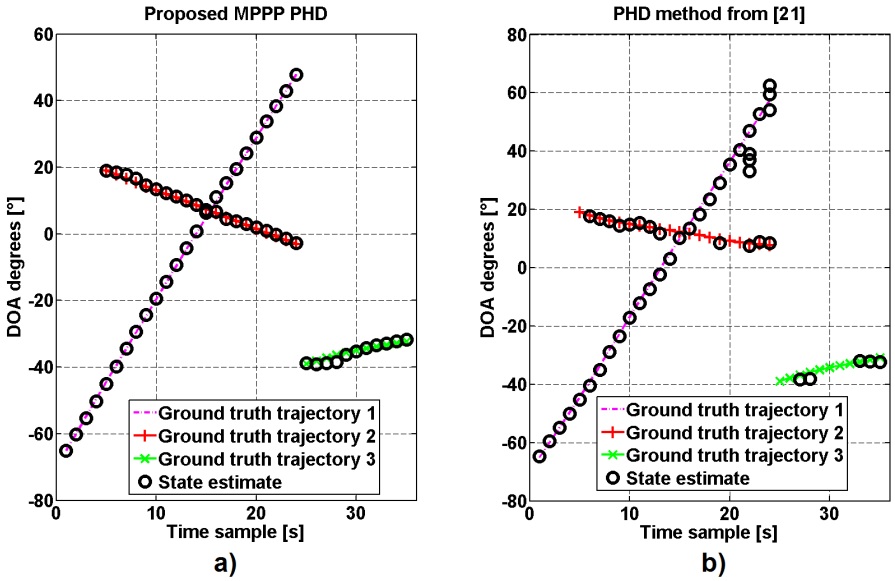

Figure III.2: DBSCAN clustering results: a) for the proposed TBD-PHD filter b) for the reference phased-array TWS-PHD.

state-transition Eq. (III.26) as importance distribution. A number of 1000 particles per target was considered. The kinematic model in Eq. (III.26) is employed with $\mathbf{v}_t \sim \mathcal{N}(\mathbf{0}, \mathbf{Q}_t)$ and covariance $\mathbf{Q}_t = \mathbf{h} q_t^2 \mathbf{h}^T$ with $q_t = 0.5^o/s^2$ representing an acceleration noise [74, Ch. 6.3.1]. Accordingly, $\mathbf{h} = [T_s^2/2, T_s]^T$ and $T_s = 1$s represents the sampling period. PHD prediction is performed with Eq. (III.28) where the probability of target survival is a constant $p_s = 0.9$. The intensity $\gamma_t(\cdot)$ for birth location is chosen uniform over $[-\pi, \pi]$, while for speed we use $\mathcal{N}(0, 3)$. The whole birth intensity integrates to 0.2, amounting to the mean number of targets born in $\mathbb{X}$ at one time sample. The array consists of $M = 30$ receivers and targets are generated with the same source signal power, so that SNR = 5dB. Here, for simplicity, we consider the source-signal power as a known constant. However, the marked point-process framework allows a generic state-dependent power function, i.e. $P(\mathbf{x})$. For example, we could employ the Capon spectrogram to represent the signal power $P(\mathbf{x})$, thus allowing different power levels for targets. TBD-PHD update is performed using Eq. (III.31) and the pseudo-likelihood of Eq. (III.37). The resulting point-mass approximation of the PHD is seen in Fig. III.1, where the logarithm of particle weights are shown for better visualization. Observe the relatively good fit of the particle clouds with the three target trajectories. From the particle approximation of the

Table III.1: Average OSPA error over 1000 Monte Carlo runs.

	OSPA error for SNR 5dB			OSPA error for SNR 0dB		
Algorithm	$c = 1.5$	$c = 2.5$	$c = 5$	$c = 1.5$	$c = 2.5$	$c = 5$
Proposed TBD-PHD	0.46	0.54	0.67	0.58	0.69	0.87
Method in [87]	1.07	1.43	2.19	1.53	2.44	4.67

intensity function, target number and state estimation is performed via DBSCAN clustering. DBSCAN requires two parameters: the minimum number of particles needed to form a cluster (set here to 50), and the neighborhood distance (set here to 1). In Fig. III.2-a) clustering of the intensity function of Fig. III.1 is depicted. In Fig. III.2-b), results of the method proposed in [87] for the same simulated scenario and parameters are depicted. Observe a better adequacy of the proposed TBD-PHD filter, while the method of [87] struggles with crossing targets and short tracks. The phased-array PHD filter of [87] employs the TWS-PHD of Sec. III.5 to track the peaks of the array-signal spectrogram. Thus, whenever targets cross only one

peak is present in the spectrogram (one observation) leading to track loss. Furthermore, the approximations conducted in [87], in order to arrive to a separable-likelihood function, are not valid for closely-spaced targets.

A Monte Carlo analysis is carried out by simulating 1000 times the same scenario described above at SNR values of 5dB and 0dB. The latter representing a very low SNR scenario in order to test the proposed TBD filter. The optimal subpattern assignment (OSPA) error metric of Sec. III.4 is employed to quantify the differences between the estimated target set and ground-truth set. The results are synthesized in Table III.1, again showcasing the superiority of the proposed TBD-PHD filter, even in very-low SNR conditions.

III.7 Chapter conclusions

In this chapter, intensity based filters are developed for tracking multiple targets directly from phased-array observations, i.e. in a track-before-detect framework. The intensity function (or PHD function) is the first-order moment density of a point process (or equivalently of a random finite set) and describes both the random number of targets and their random-state vectors. Therefore, an intensity filter is viewed as a first-order filter, that propagates an approximation to the true posterior distribution. The chapter starts with the introduction of a few definitions and results related to point-process theory. Historically, the PHD filter for TWS systems was the first intensity filter to be proposed. For superpositional-observation systems, where the observation is a superposition of individual target contributions, the superpositional PHD filter was only recently proposed.

Based on the supperpositional PHD filter, we propose a phased-array TBD-PHD filter for tracking multiple point targets in a Gaussian context. The target or source signals, conditioned on their target states, are Gaussian processes, rendering infeasible the direct application of the superpositinal PHD filter. A possible solution is to augment the target-state vector with the source signal. However this is inefficient, in particular for particle-based implementations of the filter. Indeed, in augmented-state particle filters, due to the higher-dimensional distribution of the augmented vector. Alternatively, we consider a marked Poisson point-process that is capable of characterizing the number of targets, their state vectors and the source signals. The marks represent the source/target signals, that conditionally to the target states are Gaussian random variables. We show that target marks can be analytically integrated-out in the proposed TBD-PHD filter update equations. Therefore, the filter only needs to propagate the intensity/PHD function of the ground process that describes target positions on the single-target space $\mathbb{X}$, and avoids the propagation of an augmented state. Therefore, the proposed filter has an efficient particle-filter implementation. However, due to a Gaussian approximation employed for the pseudo-likelihood [see Eq. (III.37)], the updated-intensity function no longer integrates to the average number of targets in a specific region. Integrating the updated intensity function leads to a highly-fluctuant estimator for the number of targets. Hence, a clustering methodology that estimates both number of clusters and cluster centers is proposed in the form of the DBSCAN method. To our knowledge, this is the first tracking filter to employ the DBSCAN clustering method. The DBSCAN has some advantages over classical k-means based methods. Firstly, DBSCAN does not require prior knowledge of the number of clusters, and actually provides an estimate of the number of targets and of their respective state vectors. Secondly, DBSCAN considers the existence of outlier points in the particle approximation of the intensity function. Outliers are a nuisance especially for k-means methods. Furthermore, the DBSCAN clustering methodology is employable in zero-target scenarios, i.e. where only outliers are present. This vastly improves clustering performance as compared to the k-means-silhouettes method proposed in [28].

A Cardinalized PHD filter (CPHD) represents a different solution to the problem of the highly-fluctuant integral of the PHD function. Along with the intensity function, the CPHD filter also propagates the cardinality distribution, i.e. the distribution of the number of targets. This allows a more direct estimation of the number of targets, for example by employing a MAP estimator. The CPHD filter also improves the estimation of $\widetilde{\mathbf{\Sigma}}$, by renormalizing the highly-fluctuant intensity estimate with the mean-estimated number of targets. In turn, an improved estimate of $\widetilde{\mathbf{\Sigma}}$ provides a better pseudo-likelihood $L_{\mathbf{y}_t}(\cdot)$, and eventually an improved intensity estimate. Further details as well as the derivation of the TBD-CPHD filter will be given in the following chapter.

Chapter IV

Sonar echo tracking: the case of extended and impulsive targets

Laplace [used] ... Bayes' theorem ... to help him decide which astronomical problems to work on.... in which problems is the discrepancy between prediction and observation large enough to give a high probability that there is something new to be found?

E. T. Jaynes

Bayesian Methods: General Background [121]

In this chapter we propose a novel phased-array Track Before Detect (TBD) filter for tracking multiple distributed (extended) targets from impulsive observations. Since the targets are angularly spread, we track the centroid Direction Of Arrival (DOA) of the target-generated (or backscattered) signal. The main challenge stems from the random target signals that, conditional to their respective states, constitute non-deterministic contributions to the system

observation. The novelty of our approach is twofold. Firstly, we develop a Cardinalized Probability Hypothesis Density (CPHD) filter for tracking multiple targets with non-deterministic contributions, more specifically, Spherically Invariant Random Vector (SIRV) processes. This is achieved by analytically integrating the SIRV and angularly distributed target signals in the update step. Thus, ensuring a more efficient implementation than existing solutions, that generally consider augmenting the target state with the target signal. Secondly, we provide an improved auxiliary particle CPHD filter and clustering methodology. The auxiliary step is carried out for persistent particles, while for newly birthed particles an adaptive importance distribution is given. This is in contrast with existing solutions that only consider the auxiliary step for birthed particles. Simulated data results showcase the improved performance of the proposed filter. Results on real sonar phased-array data are presented for underwater 3D image reconstruction applications.

IV.1 Introduction

TBD filters track targets directly from the phased array signal, without the need for pre-processing (detection and estimation) procedures. In order to achieve multi-target filtering we resort to the PHD filter and to the Cardinalized PHD (CPHD) filter [122], which also propagates the distribution of the number of targets. For superpositional amplitude sensors a TBD-CPHD filter was proposed in [28]. For radar/sonar applications, signal amplitudes are modeled as Spherically Invariant Random Vector (SIRV) processes, for which the method in [28] is not directly applicable. As mentioned in Sec. III.6.1, an inneficient solution is to augment the state of each target with the source signal.

On the other hand, signals in radar/sonar applications are rarely Gaussian. Experimental clutter measurements, conducted in [123], showcased the non-Gaussian nature of radar clutter. For example, the K-distribution is often employed to model the envelope (magnitude of matched filter output) of radar clutter [124–126], while heavy-tail behavior is also reported in [127]. In aerial acoustics, the heavy-tail behavior of reverberation was noted in [128], with the proposal of an $\alpha-$stable distribution for the target signals.

Moreover, in the underwater acoustic literature [129,130], high-resolution sonar systems are noted to have impulsive signals, with the $K-$distribution shown to provide a good fit for the magnitude of the signal backscattered by the sea-floor. Furthermore, a multivariate complex Laplace distribution is shown to provide a good fit for the complex (in phase and quadrature) signals involved in underwater target detection in sonar imagery [131]. In the appendix of [92], goodness-of-fit tests were conducted on high-resolution sonar signals that highlighted the impulsive nature of the complex phased-array signal, with a multivariate complex Laplace distribution proving to be a better fit than the Gaussian. The Spherically Invariant Random Vector (SIRV) [132] provides a general, elegant model for impulsive signals and encompasses a large number of non-Gaussian and heavy-tail distributions. In view of the aforementioned reasons, the SIRV model is nowadays employed in remote sensing signal processing [133]. Furthermore, SIRV processes have found applications in other areas, such as speech processing [134], array processing [135] or financial engineering models [136].

The novelty of our approach is twofold. On one hand, we derive the CPHD filter for superpositional systems where the target contributions are non-deterministic functions of their state vectors. In other words, the target state only specifies the parameters for the distribution of its contribution to the overall observation. In array processing, target/source signals are highly-fluctuant and are modeled as random vectors with probability distribution determined by the state of the target. For localization purposes, we show that source signals can be marginalized-out from the filtering equations of the proposed filter. Thus, we achieve a more efficient particle

filter implementation as opposed to implementations that consider an augmented state, particularly since there is no predictive model for source signals conditional to their corresponding target states. On the other hand we adapted the aforementioned CPHD filter for DOA tracking of extended targets from observations modeled as an impulsive (non-Gaussian) SIRV process. Furthermore, we provide an improved auxiliary particle implementation of the filter. The auxiliary step is carried out for persistent particles by selecting only the previous particles that fit the current observation. In addition, we propose an adaptive-birth importance distribution based on the current observation. This is in contrast with [28], where an auxiliary step is only carried out for birthed particles, while persistent targets are propagated through a bootstrap filter. An improved clustering method is also provided. Results are supplied for simulated and real sonar data. The TBD-CPHD filter developed in this chapter is the subject of the article [137]. Furthermore, the TBD-CPHD filter extends the TBD-PHD filter developed in Chapter III and presented in [88, 89].

The subsequent sections are organized as follows: Sec. IV.2 presents the general SIRV model for impulsive signals and the specific joint-SIRV model for phased-arrays; Sec. IV.3 presents the impulsive and extended-target signal model. In Sec. IV.4 we derive the approximate CPHD filtering equations for phased-array observations. In sections IV.5 and IV.6, we showcase the results of our proposed filter on simulated and real sonar data, followed by our conclusions in section IV.7.

IV.2 Impulsive Sonar-signal distributions

Usually in applications considering the localization of targets with phased arrays, the source signals are of no direct interest. In passive-sensing systems, the nature of source signals is unknown and signals are modeled as random processes for localization purposes. Given the estimated DOA of a specific source signal, an adapted filter can be developed for the array signal that provides an estimate of the source signal, and subsequently of the source message. The filter used to recover the source signal should be designed to attenuate all directions (specifically other target DOAs) except the DOA of the target under study. In active-sensing systems the source signal represents the signal backscattered by the target surface. Although the precise form of the backscattered signal is not known, the shape of the emitted signal is exploited in the matched filter of the receiver. However, due to the random nature of the scattering process, the matched-filter output signal is modeled as a stochastic process. Therefore, for the sake of generality, the source signals will be modeled as random processes in this work. Considering several targets simultaneously present, the phased-array signal is obtained by the superposition (i.e. addition) of the individual target/source signals. In addition, noise of various origins is also received.

For bathymetric sonars, the targets of interest represent patches (i.e. projected resolution cells) on the sea-floor or some object of interest. Hence, source signals represent surface backscattering (see [68, Ch. 5.8] and [138, Ch. 1]). In this context, noise is a generic term for all undesired signals received alongside the signals of interest, i.e. the source signals. Sources of noise are the electronic receiver noise and ambient acoustic noise. The acoustic noise [139, Ch. 10] can be further decomposed in volume backscattering, sea-surface backscattering, multi-path propagation, ship noise (both self and other ships), etc. Shallow-water environments are echoic environments that involve multi-path propagation and hence, generate an important reverberation-noise component. Therefore, the array observation signal is written as

$$\mathbf{y}_t = \sum_{i=1}^{n} \mathbf{g}_{i,t} + \mathbf{w}_{r,t} + \mathbf{w}_{n,t}, \tag{IV.1}$$

where $\{\mathbf{g}_{i,t}\}_{i=1}^{n}$ represent source signals generated by n targets; $\mathbf{w}_{r,t}$ represents the reverberation-noise component due to multi-path propagation and the noise $\mathbf{w}_{n,t}$. The noise $\mathbf{w}_{n,t}$ term contains truly ambient noise, such as ship noise, and receiver electronic noise. Reverberation $\mathbf{w}_{r,t}$ is signal related, that is $\mathbf{w}_{r,t}$ is only present whenever source signals are present. Indeed, without targets emitting source signals there wouldn't be any multi-path propagation and sea-surface reflections. This leads to the justification of $\mathbf{w}_{r,t}$ as signal-dependent, whereas $\mathbf{w}_{n,t}$ is non-signal dependent. This specific factorization of noise terms, justifies the joint-SIRV model presented in Sec. IV.2.2. Spherically Invariant Random Vector (SIRV) signals, are formally introduced in Sec. IV.2.1, and characterize a family of random vectors with a wide range of probability density functions. These density functions range from the ubiquitous Gaussian to more impulsive distributions such as inverse-Gaussian distributions [140]. The impulsive character of the sonar signals processed in this work, is highlighted in Appendix H. The Laplace and K-distributions are shown to provide a better fit to sonar signals than the Gaussian distribution.

IV.2.1 The SIRV model

An important class of distributions is that of Spherically Invariant Random Vectors (SIRV). They have been widely considered in the engineering literature e.g., for modeling radar [123–126, 133, 133] and sonar [129, 130] clutter. Radar and sonar applications have mainly employed the K-distribution, which represents a particular case of SIRV distribution. Other domains, such as speech processing [134], array processing [135] or financial engineering models [136] have also found applications for SIRV distributions. SIRV processes, also known as compound-Gaussian distributions, are part of a more general family of complex elliptically symmetric distributions [20, Sec. III.E]. In the statistics literature, SIRV processes are known as *scale mixtures of normal distributions*.

A SIRV random vector $\mathbf{y} \in \mathbb{C}^m$ can be written as

$$\mathbf{y} \overset{d}{=} \boldsymbol{\mu} + \sqrt{u}\mathbf{n}, \tag{IV.2}$$

where $\overset{d}{=}$ means equality in distribution; $\boldsymbol{\mu}$ represents a location parameter; u is called texture and is a positive random variable and $\mathbf{n}$ is a circular Gaussian random vector called speckle, i.e. $\mathbf{n} \sim \mathcal{CN}(\mathbf{0}, \boldsymbol{\Sigma})$. Most importantly, u and $\mathbf{n}$ are independent.

We denote by $F_u(\cdot)$ the cumulative distribution of the texture u and assume that $\text{rank}(\boldsymbol{\Sigma}) = m$. As $\mathbf{n}$ is Gaussian, the distribution of $\mathbf{z}$ is given by

$$p_{\mathbf{y}}(\mathbf{y}) = \pi^{-m}\det(\boldsymbol{\Sigma})^{-1} h_m\left((\mathbf{y}-\boldsymbol{\mu})^H \boldsymbol{\Sigma}^{-1}(\mathbf{y}-\boldsymbol{\mu})\right), \tag{IV.3}$$

where the nonlinear function $h_m(\cdot)$, called *density generator*, is defined as

$$h_m(v) = \int_0^\infty u^{-m} \exp\left(-\frac{v}{u}\right) dF_u(u). \tag{IV.4}$$

Note that the circular complex Gaussian distribution is obtained for the degenerate case of $u = 1$. The texture u, plays the role of a variance term, while $\boldsymbol{\Sigma}$ characterizes the specific correlation structure between the elements of $\mathbf{y}$. Indeed, $\text{Cov}(\mathbf{y}) = \mathbb{E}(u)\boldsymbol{\Sigma}$. Note that replacing the pair $(u, \boldsymbol{\Sigma})$ with $(ua^2, \boldsymbol{\Sigma}/a)$ for any $a > 0$ does not change the distribution of $\mathbf{z}$. Hence, for uniqueness, we will consider a unit variance for the texture, i.e. $\text{Var}(u) = 1$, the covariance matrix of $\mathbf{y}$ being $\boldsymbol{\Sigma}$. The major interest of employing a random texture is the ability to obtain distributions with heavier tails than that of the Gaussian. Processes exhibiting distribution tails heavier than the Gaussian are referred to as impulsive [20]. These are not to be confused with *heavy-tailed distributions*, for which the tails cannot be bounded by any exponentially

decreasing function [141, Ch. 1], or stated otherwise, who exhibit tails heavier than the exponential distribution. More specifically, the family of impulsive distributions includes the class of heavy-tailed distributions.

It is clear, from the definition in Eq. (IV.3), that any (possibly multivarite) marginal distribution of a SIRV belongs to the SIRV distributions family. This property is called *consistency* [142]. as a result, the study of univariate components of a multivariate SIRV are useful in the study of the distribution tails. In [143] and [127], fitting SIRV models to real data is addressed: the authors show that either one of the marginal envelopes $r_i = |z_i| = \sqrt{y_i y_i^*}$ $(i \in 1, m)$ or the scalar quadratic form $\alpha = \mathbf{y}^H \boldsymbol{\Sigma}^{-1} \mathbf{y}$ can be employed as a sufficient statistic for identifying the multivariate SIRV distribution. The marginal envelope r and the quadratic α are univariate random variables and hence, require fewer independent samples than fitting the entire $m-$variate vector $\mathbf{y}$. Moreover, the approach of fitting the marginal envelope is preferred the method of fitting α, since the latter requires the covariance matrix $\boldsymbol{\Sigma}$. Supposing that y_i is centered and has variance $\text{var}(y_i) = \sigma_i^2$, we can write the density of the marginal envelope as

$$p_{R_i}(r) = 2\frac{r}{\sigma_i^2} h_1\left(\frac{r^2}{\sigma_i^2}\right), \tag{IV.5}$$

In [143] it is shown that, by identifying $h_1(\cdot)$ we can construct higher-order versions $h_m(\cdot)$ by successive derivations. Examples of impulsive SIRV processes are given next.

- **The complex multivariate Laplace distribution** has numerous applications in finance, engineering, astronomy and biology (see [144, Ch. 7-10] and references herein). In [131] the complex multivariate Laplace distribution is employed to model sonar signals. It is demonstrated in [145] that the distribution of speech samples, during voice activity periods, is well described by a Laplacian distribution. Furthermore, the coefficients of speech signals, using the discrete cosine transform or the Karhunen-Loeve transform, are shown to obey a multivariate Laplace distribution. In [146], the authors employ Laplace-Gaussian mixtures for speech denoising. In [147], the wavelet-transform coefficients of images are found to have sparse distributions (i.e. Laplacian distributions), a property that has been extensively exploited in coding and denoising. The complex multivariate Laplace distribution is obtained by considering an exponential distribution for the texture $u \sim \text{Exp}(1)$. In order to ensure a unitary second-order moment for the texture, the parameter of the exponential distribution is fixed to 1. From distributions $p(u_t)$ and $p(\mathbf{y}_t|u_t)$, we obtain (see [131] and [144, Ch. 5.2.2]) the complex multivariate Laplace distribution

$$p_{\mathbf{y}}(\mathbf{y}) = \frac{2}{\pi^M \det(\boldsymbol{\Sigma})} \frac{K_{m-1}\left(2\sqrt{(\mathbf{y}-\boldsymbol{\mu})^H \boldsymbol{\Sigma}^{-1}(\mathbf{y}-\boldsymbol{\mu})}\right)}{\left[(\mathbf{y}-\boldsymbol{\mu})^H \boldsymbol{\Sigma}^{-1}(\mathbf{y}-\boldsymbol{\mu})\right]^{(m-1)/2}} \tag{IV.6}$$

  where $K_\nu(\cdot)$ is the modified Bessel function of the second kind and of order ν [148, Ch. 9.6] [144, Eq. A.0.4, p. 315] and [149, p. 183], defined as

$$K_\nu(x) = \frac{1}{2}\left(\frac{x}{2}\right)^\nu \int_0^\infty t^{-\nu-1} \exp\left(-t - \frac{x^2}{4t}\right), \tag{IV.7}$$

  with $\nu \in \mathbb{R}$ and $\text{Re}\{x^2\} > 0$. With the above definition, it is easy to show that $K_\nu(x) = K_{-\nu}(x)$ for $x \in \mathbb{R}^+$, i.e. the modified Bessel function of the second kind is even in the order. From hereon we shall denote such a complex multivariate Laplace distribution with $\mathcal{L}(\cdot; \boldsymbol{\mu}, \boldsymbol{\Sigma})$ where $\boldsymbol{\mu}$ and $\boldsymbol{\Sigma}$ represent the location and covariance as given in Eq. (IV.6).

- **The complex multivariate *K*-distribution** is obtained with a Gamma-distributed texture, i.e. $u \sim \mathrm{Gam}(\nu, 1/\nu)$. Hence, the texture is Gamma distributed with shape parameter $\nu > 0$ and scale parameter $\theta = 1/\nu$. Hence, insuring that $\mathbb{E}\{u^2\} = \nu\theta = 1$ or in other words, a unitary-variance texture. The probability density function of u is

$$p_u(u;\nu) = \begin{cases} \frac{\nu^\nu}{\Gamma(\nu)} u^{\nu-1} \mathrm{e}^{-\nu u} & \text{if } u \geq 0 \\ 0 & \text{if } u < 0, \end{cases} \tag{IV.8}$$

where $\Gamma(\cdot)$ is the Gamma function. by employing Eq. (IV.3) and Eq. (IV.4), one can write the probability density of a K-distributed random vector $\mathbf{z}$ as

$$p_{\mathbf{z}}(\mathbf{z}) = \frac{2\nu^{\frac{m+\nu}{2}}}{\pi^M \det(\boldsymbol{\Sigma})\Gamma(\nu)} \frac{K_{\nu-m}\left(2\sqrt{\nu(\mathbf{z}-\boldsymbol{\mu})^H \boldsymbol{\Sigma}^{-1}(\mathbf{z}-\boldsymbol{\mu})}\right)}{\left[(\mathbf{z}-\boldsymbol{\mu})^H \boldsymbol{\Sigma}^{-1}(\mathbf{z}-\boldsymbol{\mu})\right]^{(m-\nu)/2}}, \tag{IV.9}$$

where $K_\nu(\cdot)$ denotes the modified Bessel function of the second kind, as defined in Eq. (IV.7). From hereon, we shall denote such a complex multivariate K-distribution with $\mathcal{K}_\nu(\cdot; \boldsymbol{\mu}, \boldsymbol{\Sigma})$ where ν, $\boldsymbol{\mu}$ and $\boldsymbol{\Sigma}$ represent the order, location and covariance as given in Eq. (IV.9). The aforementioned multivariate Laplace distribution, is only a special case of the K-distribution. Indeed, we observe that a K-distribution with $\nu = 1$ yields the Laplace distribution of Eq. (IV.6). Note that the Gamma-distributed texture for shape $\nu = 1$ and scale $\theta = 1$ yields the exponentially distributed texture used to generate the Laplace SIRV. Considering the centered marginal y_i, Eq. (IV.5) gives the probability density of the marginal envelope R_i as

$$p_{R_i}(r) = \frac{4\sqrt{\nu}}{\Gamma(\nu)} (\sqrt{\nu} r)^\nu K_{\nu-1}(2\sqrt{\nu} r), \tag{IV.10}$$

which represents the univariate K-distribution for unit-variance envelopes, i.e. $\mathbb{E}\{R_i^2\} = 1$. The univariate K-distribution of Eq. (IV.10) is the usual K-distribution employed to model clutter in radar and sonar applications; for radar see [20, Sec. IV.B] and references herein, while for sonar see [129,130]. Note that for a K-distributed envelope R_i, a different factorization [150] is possible: $R_i = \sqrt{u\, z_i}$. Where $u \sim Gam(\nu, 1/\nu)$ and $z_i \sim \mathrm{Exp}(1)$ are independent. This result is immediate, since envelopes of complex-circular Gaussian random variables ($\mathbf{n}$ of Eq. (IV.2)) are Rayleigh distributed, while the squared envelope is exponentially distributed.

IV.2.2 The joint-SIRV model

We now introduce joint-SIRV models in order to provide an impulsive characterization to both source signals and additive noise. Note that various specific cases of a joint-SIRV model have been proposed in the array-processing literature. Considering the superpositional model of the phased-array observation given in Eq. (IV.1), the authors of [151] and [128] introduce the following model

$$\begin{cases} \mathbf{g}_{i,t} = \sqrt{u_t}\mathbf{s}_{i,t} & \forall i = 1, \ldots, n \\ \mathbf{w}_{r,t} = \sqrt{u_t}\mathbf{n}_t, \end{cases} \tag{IV.11}$$

where $\mathbf{s}_{i,t} \sim \mathcal{CN}(\mathbf{0}, \boldsymbol{\Sigma}_{i,t})$ for $i = 1, \ldots, n$ and $\mathbf{n}_t \sim \mathcal{CN}(\mathbf{0}, \boldsymbol{\Sigma}_{n,t})$ are independent. In [151] and [128], the texture u_t is supposed to obey a Lévy distribution in order to ensure a Cauchy multivariate distribution for $\mathbf{y}_t$. The shared texture u_t ensures the desired SIRV distribution for the phased-array observation $\mathbf{y}_t$, i.e. the likelihood. The case of different and independent textures involves computing $n-1$ multivariate convolutions of SIRV densities, which in general, has no analytic expression. An exception is the Gaussian probability density (i.e. $u_t = 1$), which is of little interest in impulsive-signal modeling.

The main argument of the joint model of Eq. (IV.11), also invoked in [151] and [128], stems from the characteristics of an echoic environment, i.e. a multi-path and reverberant environment. As we have seen in Sec. IV.2, in echoic environments the additive noise can be decomposed into two categories: signal-dependent and non-signal dependent. Considering echoic environments, where the signal-dependent reverberation is more important than electronic and ship noise, we neglect $\mathbf{w}_{n,t}$ [see Eq. (IV.1)] in the following paragraphs. Source signals $\mathbf{g}_{i,t}$ are generated by scattering from target surfaces while $\mathbf{w}_{r,t}$ is generated by volume reverberation or diffuse scattering from the sea-surface. Furthermore, the same scattering phenomenon lies at the generation of the source signals $\mathbf{g}_{i,t}$ and of the reverberation $\mathbf{w}_{r,t}$. Hence, the source signals and signal-dependent reverberation share the same distribution family. The source signals and the reverberation noise propagate simultaneously through the same rapidly-changing and echoic environment, with the resulting signals being dependent. Existing studies, conducted in [129–131], demonstrate the impulsive nature of underwater acoustic signals, with impulsive and dependent signals and reverberation . Even in the case of a single signal $\mathbf{g}_t$ propagating through the echoic environment and undergoing $k-1$ reflections, this leads to the reception of k dependent signals (direct and reflections) from different directions of arrival.

The joint-SIRV model can also be justified as a robust model for the observation $\mathbf{y}_t$. Indeed, in bathymetric sonar applications, we only have access to snapshots of the signal $\mathbf{y}_t$, containing source signals, reverberation and noise. There are no recordings of the source signals or the reverberation individually. This stems from the generation process of Sec. IV.2, where reverberation and signal only exist together. Furthermore, the impulsive nature of the phased-array signal comprising of the sum of signals and noise is showcased in Sec. H. Therefore, fitting a SIRV model to the phased-array signal can be interpreted as a robust localization method. This approach is presented in [20, Sec. VII] and [22], where $\mathbf{y}_t$ is supposed to be a centered SIRV process with covariance matrix $\text{cov}(\mathbf{y}_t) = \sum_{i=1}^{n} \text{cov}(\mathbf{s}_t) + \text{cov}(\mathbf{n}_t)$. However, this leads to the following parametrization of the observation signal

$$\mathbf{y}_t \overset{d}{=} \sqrt{u_t} \left(\sum_{i=1}^{n} \mathbf{s}_{i,t} + \mathbf{n}_t \right), \tag{IV.12}$$

where u_t is a texture that ensures the desired SIRV for $\mathbf{y}_t$. $\mathbf{s}_{i,t}$ and $\mathbf{n}_t$ are independent complex circular Gaussian processes that ensure the desired covariance structure for $\mathbf{y}_t$. However, this parametrization of $\mathbf{y}_t$ is equivalent in distribution to the model presented in Eq. (IV.11). Thus, the authors of [20] and [22] implicitly employ a joint-SIRV model for the phased-array observation. Given the SIRV model of Eq. (IV.12), they provide an optimal covariance estimator, which is further eigen-decomposed in order to construct the MUSIC pseudo-spectrum function or to construct the Capon MVDR beamforming filter. The model of Eq. (IV.12) is also employed in [152] and referred to as the *unconditional model*. Therefore, both models presented in Eq. (IV.11) of [128, 151] and Eq. (IV.12) of [20, 22, 152] are identical and suppose a joint-SIRV model, albeit sometimes not-explicitly.

IV.3 Phased-array signal and multi-target formalism

Throughout this work, a multi-target process (RFS or an equivalent PP) is employed to model a random number of targets with random state (location) vectors. We denote by X_t the random multi-target process with realizations of the form $\{\mathbf{x}_{1,t}, \ldots, \mathbf{x}_{n_t,t}\}$, where both the number n_t of targets and target-state vectors $\mathbf{x}_{k,t}$ are random. Target-state vectors take values in the single-target space: $\mathbf{x} \in \mathbb{X}$, usually some subspace of $\mathbb{R}^{d_x}$.

As described in Sec. IV.2, array observations consist in a noisy sum of individual target contributions, called target or source signals, which are also modeled as random processes. The

statistics of the target contributions and array observation are detailed in Sec. IV.3.1. The marked point process that describes the number of targets, their location and contributions is presented in section IV.3.2.

IV.3.1 Extended and impulsive target model

Section III.6.2 introduced the phased-array model for point targets with Gaussian source signals. In this section we generalize the aforementioned model in two different directions. First, we consider extended targets, that is, targets that have a certain angular extent and that generate a source/target signal with a corresponding angular distribution. Such targets are typically encountered in sonar applications that either exhibit low resolution-cells (i.e. large footprint) or small target-to-sonar distances. For shallow water bathymetry, the latter in encountered. The point-target model is only a special case of the extended-target model. Secondly, an impulsive source/target signal is considered that also generalizes the Gaussian model employed in Sec. III.6.2. The SIRV-signal model that we employ is capable of characterizing a wide range of impulsive signal distributions that are often encountered in sonar and radars.

Let $\mathbf{x}_{i,t}$ denote the state of the i-th extended target. Each extended target emits (or backscatters) a signal $\mathbf{s}_{i,t}$ which, in point-process terminology, represents a mark. Given the nature of extended targets, the mark [17] is given by

$$\mathbf{s}_{i,t} \triangleq \mathbf{s}(\mathbf{x}_{i,t}) = \int_{-\pi}^{\pi} \mathbf{a}(\phi)\, \mathcal{S}(\phi; \mathbf{x}_{i,t}) d\phi, \tag{IV.13}$$

which explicitly models the extended target signal as the superposition of elementary backscattered signals $\mathcal{S}(\phi; \mathbf{x}_{i,t}) \in \mathbb{C}$ with DOA ϕ. Each elementary backscattered signal is a narrow-band plane wave with DOA ϕ and array manifold vector $\mathbf{a}(\phi)$. For plane waves (narrowband condition verified verified in Appendix G) impinging a ULA, we have

$$\mathbf{a}(\phi) \triangleq \begin{bmatrix} 1 & e^{-j\,\phi} & \cdots & e^{-j\,(M-1)\phi} \end{bmatrix}^T,$$

where M is the number of array receivers and $\{\cdot\}^T$ represents the transpose operator. The DOA ϕ is linked to the physical angle θ by: $\phi = \frac{2\pi}{\lambda}\Delta \sin(\theta)$, with λ representing the wavelength and Δ the receiver spacing. For linear arrays, the physical angle spans $\theta \in [-\pi/2, \pi/2]$, while $\phi \in [-\pi, \pi]$ (if $\Delta = \lambda/2$). The terminology of *speckle* [153, Ch. 14.8] is employable for $\mathbf{s}_{i,t}$ and is motivated by the fact that $\mathbf{s}_{i,t}$ is the sum of complex random contributions, in Eq. (IV.13). The individual scatterers exhibit a uniformly distributed phase, hence their sum yields a highly-fluctuant signal. The power of $\mathbf{s}_{i,t}$ is given by the power of the incident signal, the surface area of the reflector and the incidence angle. The speckle pattern is given by the covariance matrix of $\mathbf{s}_{i,t}$ and represents the parameter of interest in localizing the respective target, leading to the perception of speckle as a multiplicative model.

Whenever scattering from rough surfaces is involved [17, 154], $\mathcal{S}(\cdot)$ is considered to be a white process, that is

$$\mathbb{E}\{\mathcal{S}(\phi; \mathbf{x}_{i,t}) \mathcal{S}^*(\phi'; \mathbf{x}_{i,t})\} = P\, \rho(\phi; \mathbf{x}_{i,t}) \delta(\phi - \phi')$$

where $\delta(\cdot)$ is the Dirac impulse. P is the mean power of the target and $\rho(\phi; \mathbf{x}_{i,t})$ is the power density function of the target signal. Examples of $\rho(\cdot)$ are given in [155], and include uniform, Gaussian or polynomial. In this work we consider a Gaussian shape for $\rho(\cdot)$, as in [155, Sec. 2.2]:

$$\rho(\phi; \mathbf{x}_{i,t}) = \frac{1}{\sqrt{2\pi\sigma_\phi^2}} \exp\left(-\frac{(\phi - \phi_c)^2}{2\sigma_\phi^2}\right), \tag{IV.14}$$

where $\sigma_\phi \ll \pi$ controls the angular spread of $\rho(\cdot)$. The target-centroid DOA ϕ_c, signal power P and angular spread σ_ϕ are the main parameters of the extended target. Note that P and σ_ϕ are appended to θ_c (or equivalently $\phi_c \triangleq \frac{2\pi}{\lambda}\Delta\sin(\theta_c)$) alongside kinematic terms to form the state vector $\mathbf{x}_{i,t}$, as described later in Section IV.3.2.

Similarly to [156], by considering the elementary backscattered signal conditioned on $\mathbf{x}_{i,t}$ as circular symmetric Gaussian (i.e. $\mathcal{S}(\phi;\mathbf{x}_{i,t})|\mathbf{x}_{i,t} \sim \mathcal{CN}(0, P\,\rho(\phi;\mathbf{x}_{i,t}))$), from Eq. (IV.13) we have

$$\mathbf{s}_{i,t}|\mathbf{x}_{i,t} \sim \mathcal{CN}(\mathbf{0}, \mathbf{R}(\mathbf{x}_{i,t})), \tag{IV.15a}$$

$$[\mathbf{R}(\mathbf{x}_{i,t})]_{m,n} = P\, e^{-\frac{(n-m)^2\sigma_\phi^2}{2}} e^{j\,(n-m)\phi_c}. \tag{IV.15b}$$

As previously stated, the array observation signal $\mathbf{y}_t \in \mathbb{C}^M$ is

$$\mathbf{y}_t = \sum_{i=1}^{n_t} \mathbf{g}_{i,t} + \mathbf{w}_t, \tag{IV.16}$$

where both the contribution of the i-th extended target $\mathbf{g}_{i,t}$ and the additive observation noise $\mathbf{w}_t \in \mathbb{C}^M$ are SIRV processes.

A joint-SIRV model is employed for the array observation, as described in Eq. (IV.11). The target signals and observation noise become:

$$\mathbf{g}_{i,t} = \sqrt{u_t}\,\mathbf{s}_{i,t} \tag{IV.17a}$$

$$\mathbf{w}_t = \sqrt{u_t}\,\mathbf{n}_t \tag{IV.17b}$$

$$\mathbf{n}_t \sim \mathcal{CN}(\mathbf{0}, \sigma_t^2\mathbf{I}_M), \tag{IV.17c}$$

where u_t, $\mathbf{n}_t$ and $\{\mathbf{s}_{i,t}|i = 1,\dots,n_t\}$ are independent. $\mathbf{s}_{i,t}$ is the target signal, or target mark, given in Eq. (IV.13) and with distribution (IV.15a). σ_t^2 is the additive noise variance. $\mathbf{I}_M$ is the identity matrix of size M. The texture is considered to have unitary second-order moment $\mathbb{E}\{u_t^2\} = 1$, hence the Signal-to-Noise Ratio (SNR) of the i-th target is given by $SNR = \frac{P}{\sigma_t^2}$. As described in Sec. IV.2.1, the distribution of the non-negative texture controls the impulsive character of the target signal. A detailed analysis of the joint-DIRV model is given in Sec. IV.2.2. Here, we briefly note that the texture u_t is identical for all targets and noise, leading to a SIRV observation vector $\mathbf{y}_t$. Under such a model, the physical property of uncorrelated target marks $\mathbf{g}_{i,t}$ and additive noise is kept. However, the target marks and noise are no longer independent. Independence only being achieved for the special case of Gaussian signals, i.e. non-random texture with $u_t = 1$.

In this chapter, we will particularly consider the complex multivariate Laplace distribution for $\mathbf{y}_t$, which was shown in [92, 131] and Appendix H via goodness-of-fit tests to match complex phased-array sonar signals. The complex multivariate Laplace distribution is obtained by considering an exponential texture $u_t \sim \text{Exp}(1)$, see Eq. (IV.6). However, the filter derivation is valid for all SIRV observation processes, by employing a generic distribution for u_t. The conditional distribution $p(\mathbf{y}_t|u_t, X_t)$ is complex circular Gaussian with zero mean and covariance $\mathbf{\Gamma}_t = \sum_{i=1}^{n_t}\mathbf{R}(\mathbf{x}_{i,t}) + \sigma_t^2\mathbf{I}_M$. This follows from the independence of individual target marks, when conditioned on u_t, and their Gaussian distributions, given in Eq. (IV.15a). By employing the exponential texture, we obtain the multivariate Laplace distribution for the array observation $p(\mathbf{y}_t|X_t) = \mathcal{L}(\mathbf{y}_t; \mathbf{0}, \mathbf{\Gamma}_t)$ given in Eq. (IV.6).

IV.3.2 Marked process for extended and impulsive target signals

In a similar fashion to Sec. III.6.2, we introduce a marked process to model the multiple targets and their associated source signals. The multi-target process X_t is an independent

and identically distributed cluster (iidc) process (see Sec. III.3.1), with the distribution of the number of targets denoted as $p_t(n)$ and iid target state vectors with pdf $v_t(\mathbf{x})$. A compact representation for the iidc processes is achieved via the multi-target density. Using the set notations of Sec. III.2.3, and from Eq. (III.15), we have

$$p_{X_t}(X) \triangleq p_t(X) = p_t(n)n! \prod_{\mathbf{x}\in X_t} v_t(\mathbf{x}). \tag{IV.18}$$

Furthermore, the intensity (or PHD) of X_t [see Eq. III.16] is given by:

$$D_t(\mathbf{x}) = \bar{n}_t v_t(\mathbf{x}), \tag{IV.19}$$

where $\bar{n}_t = \sum_{n=0}^{\infty} n p_t(n)$ is the mean of the number of targets present at time t. We assume that targets evolve according to the linear state equation

$$\mathbf{x}_t = \mathbf{F}_t\, \mathbf{x}_{t-1} + \mathbf{v}_t, \tag{IV.20}$$

where $\mathbf{F}_t$ is the state transition matrix and $\mathbf{v}_t$ is the model noise. We assume $\mathbf{v}_t$ to be a zero mean, white Gaussian process with covariance matrix $\mathbf{Q}_t$, i.e. $\mathbf{v}_t \sim \mathcal{N}(\mathbf{0}, \mathbf{Q}_t)$. Since SMC (Sequential Monte Carlo) techniques are employed to implement the proposed filter, the subsequent derivations would apply similarly for any non-linear state equation. In this work, we consider a nearly constant velocity model [74, Ch. 6.3.1] in the angular domain θ. Furthermore, we consider the logarithm of the target-signal power and of the target spread as part of the target-state vector, with a random walk evolution model. Thus, the target state is $\mathbf{x}_t = [\theta_t, \dot{\theta}_t, \log(P_t), \log(\sigma_{\phi,t})]^T$. Note that the in Eq. (IV.15b) the target angular spread and signal power were explicitly made dependent on the target state. The logarithm of the target spread and signal power are necessary to ensure their positivity. A similar scheme has been employed for the noise variance in time-varying auto-regressive models in [157, Ch. 7]. More involved models that relate the signal power to the target spread can be envisaged, however, they do not represent the scope of this work. Different methods that cope with unknown parameters, such as signal power or target spread, have been proposed in [157, Ch. 10]. However, for simplicity, they will not be considered in this work.

Knowledge of the cardinality distribution $p_t(n)$ and the individual target distribution $v_t(\mathbf{x})$ is sufficient to infer the number of targets and their locations. More specifically, the number of targets is estimated from $p_t(n)$, and afterwards the target locations are given by the peaks of $v_t(\mathbf{x})$. Next we consider the process formed by $\widetilde{X}_t = \{(\mathbf{x}, \mathbf{s}) | \, \mathbf{x} \in X_t \text{ and } \mathbf{s}|\mathbf{x} \sim \mathcal{CN}(\mathbf{0}, \mathbf{R}(\mathbf{x}))\}$, referred to as the marked multi-target process, or marked point process in point process terminology. X_t is usually referred to as the ground multi-target process. Note that the cardinality of the marked process is equal to that of the ground process, i.e. $|\widetilde{X}_t| = |X_t|$. The mark $\mathbf{s}$ depends only on the target state as given by Eq. (IV.13), or in other words, the target signal is dependent on the parameters of the target that generated (or backscattered) that signal. Conditionally to the target states, the marks are independent and the marked-process PHD is given by the marking theorem: $\widetilde{D}(\tilde{\mathbf{x}}) = D(\mathbf{x})\mathcal{CN}(\mathbf{s}; \mathbf{0}, \mathbf{R}(\mathbf{x}))$ [94, Prop. 3.9] and [93, p. 55], where $\tilde{\mathbf{x}}$ denotes the pair $(\mathbf{x}, \mathbf{s}(\mathbf{x}))$ and $\mathbf{R}(\mathbf{x})$ is given by Eq. (IV.15b). Since the ground process is iidc and the marks are independent, the marked process is iidc with density:

$$p_t(\widetilde{X}) = p_t(n)n! \prod_{\{(\mathbf{x},\mathbf{s})\}\in\widetilde{X}_t} v_t(\mathbf{x})\mathcal{CN}(\mathbf{s}; \mathbf{0}, \mathbf{R}(\mathbf{x})). \tag{IV.21}$$

We choose to interpret $\widetilde{X}_t$ as a marked process for two reasons. Firstly, it has an intuitive interpretation: a target generates a mark, here the backscattered signal. Secondly, in the update step (Sec. IV.4.2 and IV.4.3) of the CPHD filter, we show that target signals can be analytically integrated-out, without requiring a posterior defined on an extended space. This is especially important for particle filter implementations, where sampling from higher-dimensional posteriors is always less efficient. The PHD of the marked process intervenes in the array likelihood function.

IV.4 Phased-array TBD-CPHD filter

In this section, we derive the filtering equations for tracking extended targets via phased-array observations. We aim to derive the PHD $D_{t|t}(\mathbf{x})$ and cardinality distribution $p_{t|t}(n)$ of the posterior ground process $X_t|\mathbf{y}_{0:t}$, given the past and current array observations denoted as $\mathbf{y}_{0:t}$. The filter comprises two stages: prediction (Section IV.4.1) and update. The latter supposes the update of the intensity/PHD function (Section IV.4.2) and the cardinality distribution (Section IV.4.3). In the prediction stage, starting from $D_{t-1|t-1}(\mathbf{x})$ and $p_{t-1|t-1}(n)$ we give the exact formulas for the predicted intensity $D_{t|t-1}(\mathbf{x})$ and $p_{t|t-1}(n)$. We take into account target kinematics as dictated by the law of motion of Eq. (IV.20), as well as target death and birth. The update stage intends to correct the predicted PHD and cardinality with the current observation $\mathbf{y}_t$. Closed-form formulas are not available for the updated intensity and cardinality, and an approximation similar to that in [28] is proposed.

IV.4.1 Phased-array TBD-CPHD prediction

The array model of Section IV.3.1 only impacts the update step, as prediction is carried out with the classical formulas of [122], which are recalled here. A target with state $\mathbf{x}_{t-1}$ at time $t-1$, will survive at time t with probability $p_s(\mathbf{x}_{t-1})$. Each target survival is independent of other target survivals. Surviving targets undergo a kinematic transformation dictated by the transition density kernel $f(\mathbf{x}_t|\mathbf{x}_{t-1}) = \mathcal{N}(\mathbf{x}_t; \mathbf{F}_t\mathbf{x}_{t-1}, \mathbf{Q}_t)$ resulting from the kinematic model in Eq. (IV.20). Furthermore, to account for target birth, a process with intensity $\gamma_t(\cdot)$ is superposed to the transformed process. In virtue of the superposition theorem [93, Ch. 2.2], the predicted intensity is given by

$$D_{t|t-1}(\mathbf{x}_t) = \gamma_t(\mathbf{x}_t) + \int f(\mathbf{x}_t|\mathbf{x}_{t-1})p_s(\mathbf{x}_{t-1}), D_{t-1|t-1}(\mathbf{x}_{t-1})d\mathbf{x}_{t-1}. \tag{IV.22}$$

The predicted intensity model captures target death, birth and kinematics. Furthermore, the probability density of targets is obtained by normalizing the intensity function:

$$v_{t|t-1}(\mathbf{x}) = \frac{D_{t|t-1}(\mathbf{x})}{\int D_{t|t-1}(\mathbf{x})d\mathbf{x}}. \tag{IV.23}$$

The marked process $\widetilde{X}_{t|t-1}$ is obtained by marking each element of $X_{t|t-1}$ with the corresponding source/target signal, i.e. mark $\mathbf{s} \in \mathbb{K}$, with $\mathbb{K} \subseteq \mathbb{C}^M$. Conditionally on the target state $\mathbf{x}$, its mark is $\mathbf{s} \sim \mathcal{CN}(\mathbf{0}, \mathbf{R}(\mathbf{x}))$ as described in Sec. IV.3.2. Hence, the pdf of the marked target $\tilde{\mathbf{x}} \triangleq (\mathbf{x}, \mathbf{s})$ is

$$\tilde{v}_{t|t-1}(\tilde{\mathbf{x}}) = v_{t|t-1}(\mathbf{x})\mathcal{CN}(\mathbf{s}; \mathbf{0}, \mathbf{R}(\mathbf{x})). \tag{IV.24}$$

Whereas the intensity function of the marked process is

$$\widetilde{D}_{t|t-1}(\tilde{\mathbf{x}}) = D_{t|t-1}(\mathbf{x})\mathcal{CN}(\mathbf{s}; \mathbf{0}, \mathbf{R}(\mathbf{x})). \tag{IV.25}$$

As shown in the following section, the propagation of $D_{t|t}(\mathbf{x})$ is sufficient, with the marked intensity intervening in the array likelihood model. This leads to an efficient implementation propagating only a particle approximation of $D_{t|t}(\mathbf{x})$.

The predicted cardinality $p_{t|t-1}(n)$, identical for both $X_{t|t-1}$ and $\widetilde{X}_{t|t-1}$, is from [122]:

$$p_{t|t-1}(n) = \sum_{j=0}^{n} p_b(n-j) \left(\sum_{l=j}^{\infty} \binom{l}{j} \frac{\langle p_s, D_{t|t-1}\rangle^j \langle 1 - p_s, D_{t|t-1}\rangle^{l-j}}{\langle 1, D_{t|t-1}\rangle^l} p_{t-1|t-1}(l) \right), \tag{IV.26}$$

where $p_b(j)$ is the probability of having j newly birthed targets and

$$\langle a, b \rangle = \int_{\mathbb{X}} a(\mathbf{x}) b(\mathbf{x}) d\mathbf{x}$$

is the inner product on $\mathbb{X}$.

In the case of a constant probability of survival, i.e. $p_s(\mathbf{x}) \triangleq p_s \, \forall \mathbf{x} \in \mathbb{X}$, the predicted cardinality $p_{t|t-1}(n)$ (identical for both $X_{t|t-1}$ and $\widetilde{X}_{t|t-1}$) is from [122]

$$p_{t|t-1}(n) = \sum_{j=0}^{n} p_b(n-j) \left(\sum_{l=j}^{\infty} \binom{l}{j} p_s^j (1-p_s)^{l-j} p_{t-1|t-1}(l) \right). \tag{IV.27}$$

This above prediction equations will be employed in the TBD-CPHD filter, while update equations are derived in the following sections for both the intensity function and cardinality distribution.

IV.4.2 Phased-array TBD-CPHD intensity update

The updated PHD $D_{t|t}(\cdot)$ can be obtained from the set integral (see Eq. III.10)

$$D_{t|t}(\mathbf{x}) = \int p_{t|t}(\{\mathbf{x}\} \cup W) \delta W, \tag{IV.28}$$

where $p_{t|t}(W)$ is a the posterior distribution of the multi-target process $X_t | \mathbf{y}_{0:t}$.

In a similar fashion to Sec. III.6.3.b, by applying the Bayes rule for the posterior $p_{t|t}(W)$, we obtain:

$$D_{t|t}(\mathbf{x}) = \frac{\int p_t(\mathbf{y}_t | \{\mathbf{x}\} \cup W) p_{t|t-1}(\{\mathbf{x}\} \cup W) \delta W}{\int p_t(\mathbf{y}_t | W) p_{t|t-1}(W) \delta W}. \tag{IV.29}$$

To make the above integrals tractable, we employ the specific factorization of SIRV random vectors [Eq. (IV.17a)]. The array likelihood is written as

$$p_t(\mathbf{y}_t | W) = \int_0^{\infty} p_t(\mathbf{y}_t | W, u_t) p(u_t) du_t.$$

In particular, for Laplace signals, u_t is an exponentially distributed scalar. Further accounting for the target marks $\mathbf{s}$ of Eq. (IV.15a), the array likelihood becomes

$$p_t(\mathbf{y}_t | W, u_t) = \int_{\mathbb{X}^{|W|}} p_t(\mathbf{y}_t | \widetilde{W}, u_t) \prod_{\{(\mathbf{w},\mathbf{s})\} \in \widetilde{W}} \left[\mathcal{CN}(\mathbf{s}; \mathbf{0}, \mathbf{R}(\mathbf{w})) d\mathbf{s} \right],$$

where $\widetilde{W} = \{\tilde{\mathbf{w}} \triangleq (\mathbf{w}, \mathbf{s}) | \mathbf{w} \in W \text{ and } \mathbf{s} | \mathbf{w} \sim \mathcal{CN}(\mathbf{0}, \mathbf{R}(\mathbf{w}))\}$ is the marked process obtained by appending the target signals to each target state of the predicted process at time t. Both the ground and marked processes have the same cardinality, denoted by $|W|$ and $|\widetilde{W}|$ respectively. Considering this specific form of the likelihood, and employing the iidc distribution of Eq.

(III.15), the nominator of Eq. (IV.29) is factored as

$$\begin{aligned}
&\int p_t(\mathbf{y}_t|\{\mathbf{x}\}\cup W)p_{t|t-1}(\{\mathbf{x}\}\cup W)\delta W = \\
&\quad= \sum_{n=0}^{\infty}\frac{1}{n!}\int_0^{\infty} p(u_t)\int_{\mathbb{K}}\mathcal{CN}(\mathbf{s};\mathbf{0},\mathbf{R}(\mathbf{x}))\int_{(\mathbb{X}\times\mathbb{K})^n} p_t(\mathbf{y}_t|u_t,(\mathbf{x},\mathbf{s}),\{(\mathbf{w}_i,\mathbf{s}_i)|i=1,\dots,n\}) \\
&\qquad\qquad\times(n+1)!\,p_{t|t-1}(n+1)v(\mathbf{x})\prod_{i=1}^{n}\left[v_{t|t-1}(\mathbf{w}_i)\mathcal{CN}(\mathbf{s}_i;\mathbf{0},\mathbf{R}(\mathbf{w}_i))d\mathbf{w}_i d\mathbf{s}_i\right]d\mathbf{s}du_t \\
&\quad= v(\mathbf{x})\sum_{n=0}^{\infty}\frac{1}{n!}\int_0^{\infty} p(u_t)\int_{\mathbb{K}}\mathcal{CN}(\mathbf{s};\mathbf{0},\mathbf{R}(\mathbf{x}))\int_{(\mathbb{X}\times\mathbb{K})^n} p_t(\mathbf{y}_t|u_t,\tilde{\mathbf{x}},\{\tilde{\mathbf{w}}_i|i=1,\dots,n\}) \\
&\qquad\qquad\times(n+1)!\,p_{t|t-1}(n+1)\prod_{i=1}^{n}\left[\tilde{v}_{t|t-1}(\tilde{\mathbf{w}}_i)d\tilde{\mathbf{w}}_i\right]d\mathbf{s}du_t \\
&\quad= D_{t|t-1}(\mathbf{x})\int_0^{\infty} p(u_t)\int_{\mathbb{K}}\mathcal{CN}(\mathbf{s};\mathbf{0},\mathbf{R}(\mathbf{x}))\int p_t(\mathbf{y}_t|u_t,\widetilde{W}\cup\tilde{\mathbf{x}})p_{t|t-1,\tilde{\mathbf{x}}}(\widetilde{W})\delta\widetilde{W}d\mathbf{s}du_t,
\end{aligned}$$

where, in the last equality, we introduced for a fixed $\tilde{\mathbf{x}}\in\mathbb{X}\times\mathbb{K}$ the multi-target process with distribution $p_{t|t-1,\tilde{\mathbf{x}}}(\widetilde{W})$ as

$$p_{t|t-1,\tilde{\mathbf{x}}}(\widetilde{W}) = \frac{p_{t|t-1}(\{\tilde{\mathbf{x}}\}\cup\widetilde{W})}{\widetilde{D}_{t|t-1}(\tilde{\mathbf{x}})}$$

where $\widetilde{D}_{t|t-1}(\cdot)$ is the marked intensity function of Eq. (IV.25). Note that $p_{t|t-1,\tilde{\mathbf{x}}}(\widetilde{W})$ is a true multi-target probability distribution since $\int p_{t|t-1,\tilde{\mathbf{x}}}(\widetilde{W})\delta\widetilde{W}=1$. This is easily seen by using the definition of the intensity function of Eq. (III.11). Note that in [116], a similar process is defined for the non-marked case.

Proceeding in a similar manner for the denominator of Eq. (IV.29), the updated intensity function becomes:

$$D_{t|t}(\mathbf{x}) = D_{t|t-1}(\mathbf{x})\frac{\int_0^{\infty}p(u_t)\int\mathcal{CN}(\mathbf{s};\mathbf{0},\mathbf{R}(\mathbf{x}))\int p_t(\mathbf{y}_t|\widetilde{W},\tilde{\mathbf{x}},u_t)p_{t|t-1,\tilde{\mathbf{x}}}(\widetilde{W})\delta\widetilde{W}d\mathbf{s}du_t}{\int_0^{\infty}p(u_t)\int p_t(\mathbf{y}_t|\widetilde{W},u_t)p_{t|t-1}(\widetilde{W})\delta\widetilde{W}du_t}. \tag{IV.30}$$

By employing the change of variables formula proposed in [118, Prop 4., p.180], that is, denoting $\mathbf{z}\triangleq\sum_{\{(\mathbf{w},\mathbf{s})\}\in\widetilde{W}}\mathbf{s}(\mathbf{w})$, the inner integral of the denominator of Eq. (IV.30) becomes:

$$\int p_t(\mathbf{y}_t|\widetilde{W},u_t)p_{t|t-1}(\widetilde{W})\delta\widetilde{W} = \int\mathcal{CN}(\mathbf{y}_t;\sqrt{u_t}\mathbf{z},u_t\sigma_t^2\mathbf{I}_M)p(\mathbf{z})d\mathbf{z}.$$

The set integrals are now reduced to ordinary integrals, where $p(\mathbf{z})$ is the distribution induced by the change of variables. As proposed in [28], under the approximation: $p(\mathbf{z})\approx\mathcal{CN}(\mathbf{z};\boldsymbol{\mu},\boldsymbol{\Sigma})$, we obtain an analytic formula for the updated intensity. The first and second order moments of $p(\mathbf{z})$ are obtainable from the marked predicted iidc process $\widetilde{X}$, with distribution $p_{t|t-1}(\widetilde{X})$ [Eq. (IV.21)]. In [116, Eq. (43) and (44)], the authors derived such moments for the non-marked iidc case. The extension to the marked process is obtained by replacing the iidc intensity with the marked intensity of Eq. (IV.25), the result is: $\boldsymbol{\mu}=\bar{n}\tilde{\boldsymbol{\mu}}$ and $\boldsymbol{\Sigma}=\bar{n}\tilde{\boldsymbol{\Sigma}}$, where $\bar{n}=\sum_{n=1}^{\infty}n\,p_{t|t-1}(n)$ is the mean of the predicted cardinality distribution $p_{t|t-1}(n)$ [given in either Eq. (IV.26) or Eq. (IV.27)] and

$$\begin{aligned}
\tilde{\boldsymbol{\mu}} &= \int_{\mathbb{X}\times\mathbb{K}}\mathbf{s}\,\tilde{v}_{t|t-1}(\tilde{\mathbf{x}})d\tilde{\mathbf{x}} \\
&= \int_{\mathbb{K}}\int_{\mathbb{X}}\mathbf{s}\,v_{t|t-1}(\mathbf{x})\,\mathcal{CN}(\mathbf{s};\mathbf{0},\mathbf{R}(\mathbf{x}))d\mathbf{x}d\mathbf{s}=\mathbf{0} &\text{(IV.31a)}\\
\tilde{\boldsymbol{\Sigma}} &= \int_{\mathbb{X}\times\mathbb{K}}\mathbf{s}\mathbf{s}^H\,\tilde{v}_{t|t-1}(\tilde{\mathbf{x}})d\tilde{\mathbf{x}} \\
&= \int_{\mathbb{X}}\mathbf{R}(\mathbf{x})\,v_{t|t-1}(\mathbf{x})d\mathbf{x}, &\text{(IV.31b)}
\end{aligned}$$

where $\tilde{v}(\tilde{\mathbf{x}})$ is the marked target pdf and is defined in Eq. (IV.24). $\{\cdot\}^H$ represents the transpose-conjugate operator. Employing the aforementioned change of variables and under the approximation $p(\mathbf{z}) \approx \mathcal{CN}(\mathbf{z}; \mathbf{0}, \boldsymbol{\Sigma})$, the denominator of Eq. (IV.30) becomes

$$\int_0^\infty p(u_t) \int \mathcal{CN}(\mathbf{y}_t; \sqrt{u_t}\mathbf{z}, u_t\sigma_t^2\mathbf{I}_M)p(\mathbf{z})d\mathbf{z}du_t \approx \int_0^\infty p(u_t)\mathcal{CN}(\mathbf{y}_t; \mathbf{0}, u_t(\sigma_t^2\mathbf{I}_M + \bar{n}\widetilde{\boldsymbol{\Sigma}}))du_t. \quad \text{(IV.32)}$$

Similarly for the numerator of Eq. (IV.30) we get:

$$\int p(\mathbf{y}_t|\widetilde{W}, \tilde{\mathbf{x}}, u_t)p_{t|t-1,\tilde{\mathbf{x}}}(\widetilde{W})\delta\widetilde{W} = \int \mathcal{CN}(\mathbf{y}_t - \sqrt{u_t}\mathbf{s}; \sqrt{u_t}\mathbf{z}, u_t\sigma_t^2\mathbf{I}_M)p_{\tilde{\mathbf{x}}}(\mathbf{z})d\mathbf{z},$$

where $p_{\tilde{\mathbf{x}}}(\mathbf{z})$ is the probability distribution induced by the change of variables. Again, we assume $p_{\tilde{\mathbf{x}}}(\mathbf{z}) \approx \mathcal{CN}(\mathbf{z}, \boldsymbol{\mu}_{\tilde{\mathbf{x}}}, \boldsymbol{\Sigma}_{\tilde{\mathbf{x}}})$. The first and second-order moments for non-marked multi-target distributions have been computed in [116, Eq. (69) and (70)]. Here, similar results can be obtained, by replacing the multi-target intensity with the marked intensity $\boldsymbol{\mu}_{\tilde{\mathbf{x}}} = \mathbf{0}$ and $\boldsymbol{\Sigma}_{\tilde{\mathbf{x}}} = \bar{n}^{-1}G^{(2)}(1)\widetilde{\boldsymbol{\Sigma}}$, where $\bar{n}$ is the mean and $G^{(2)}(1) = \sum_{n=2}^\infty n(n-1)\, p_{t|t-1}(n)$ is the second-order factorial moment of the predicted cardinality distribution $p_{t|t-1}(n)$.

By employing the above Gaussian approximation for $p_{\tilde{\mathbf{x}}}(\mathbf{z})$, the updated intensity/PHD is

$$D_{t|t}(\mathbf{x}) = D_{t|t-1}(\mathbf{x})L_{\mathbf{y}_t}(\mathbf{x}), \quad \text{(IV.33)}$$

where the pseudo-likelihood $L_{\mathbf{y}_t}(\mathbf{x})$ is approximately given by:

$$L_{\mathbf{y}_t}(\mathbf{x}) \approx \frac{\int_0^\infty p(u_t)\mathcal{CN}(\mathbf{y}_t; \mathbf{0}, u_t(\mathbf{R}(\mathbf{x}) + \sigma_t^2\mathbf{I}_M + \boldsymbol{\Sigma}_{\tilde{\mathbf{x}}})du_t}{\int_0^\infty p(u_t)\mathcal{CN}(\mathbf{y}_t; \mathbf{0}, u_t(\sigma_t^2\mathbf{I}_M + \bar{n}\widetilde{\boldsymbol{\Sigma}}))du_t}.$$

Employing an exponential texture $u_t \sim \text{Exp}(1)$, we obtain:

$$L_{\mathbf{y}_t}(\mathbf{x}) \approx \frac{\mathcal{L}(\mathbf{y}_t; \mathbf{0}, \mathbf{R}(\mathbf{x}) + \sigma_t^2\mathbf{I}_M + \bar{n}^{-1}G^{(2)}(1)\widetilde{\boldsymbol{\Sigma}})}{\mathcal{L}(\mathbf{y}_t; \mathbf{0}, \sigma_t^2\mathbf{I}_M + \bar{n}\widetilde{\boldsymbol{\Sigma}})}, \quad \text{(IV.34)}$$

where $\mathcal{L}(\cdot; \mathbf{0}, \boldsymbol{\Sigma})$ denotes a centered and complex multivariate Laplace density of Eq. (IV.6) and covariance $\boldsymbol{\Sigma}$.

IV.4.3 Phased-array TBD-CPHD cardinality update

The updated cardinality distribution $p_{t|t}(n)$ is by definition [24, Eq. 11.109]:

$$\begin{aligned} p_{t|t}(n) &= \int_{|X|=n} p_{t|t}(X)\delta X \\ &= \frac{\int_{|X|=n} p(\mathbf{y}_t|X)p_{t|t-1}(X)\delta X}{\int p(\mathbf{y}_t|X)p_{t|t-1}(X)\delta X}. \end{aligned} \quad \text{(IV.35)}$$

Note that the denominator of Eq. (IV.35) was solved in the preceding section and is equal to the denominator of Eq. (IV.34). By employing the marginalized likelihood and the marked predicted iidc $\widetilde{X}$, the numerator of Eq. (IV.35) is equivalent to:

$$\begin{aligned} \int_{|X|=n} p(\mathbf{y}_t|W)p_{t|t-1}(W)\delta W &= \int_0^\infty p(u_t) \int_{|X|=n} p(\mathbf{y}_t|\widetilde{W}, u_t)p_{t|t-1}(\widetilde{W})\delta\widetilde{W}du_t \\ &= p_{t|t-1}(n) \quad \int_0^\infty p(u_t) \int p(\mathbf{y}_t|\widetilde{W}, u_t)p_{t|t-1,n}(\widetilde{W})\delta\widetilde{W}du_t, \end{aligned} \quad \text{(IV.36)}$$

where we introduced for fixed cardinality n the marked multi-target process with distribution

$$p_{t|t-1,n}(\widetilde{W}) = p_{t|t-1}(n)^{-1}\, \delta_{|\widetilde{W}|,n}\, p_{t|t-1}(\widetilde{W}),$$

with $\delta_{.,.}$ representing the Kronecker symbol.

By introducing the change in variables

$$\begin{aligned}\int p(\mathbf{y}_t|\widetilde{W},u_t)p_{t|t-1,n}(\widetilde{W})\delta\widetilde{W} &= \int \mathcal{CN}\left(\mathbf{y}_t;\sqrt{u_t}\mathbf{z},u_t(\sigma^2\mathbf{I}_M)\right)p_n(\mathbf{z})d\mathbf{z}\\ &\approx \mathcal{CN}(\mathbf{y}_t;\sqrt{u_t}\mu_n,u_t(\sigma_t^2\mathbf{I}_M+\mathbf{\Sigma}_n)),\end{aligned} \tag{IV.37}$$

where we introduce the approximation $p_n(\mathbf{z}) \approx \mathcal{CN}(\mathbf{z};\boldsymbol{\mu}_n,\mathbf{\Sigma}_n)$. The first-order moment densities of non-marked distributions of the type $p_{t|t-1,n}(W)$ have been computed in [116, Eq. (54) and (55)]. The extension to the marked process is obtained simply by replacing the respective intensity with the marked intensity of Eq. (III.29). Thus, $\boldsymbol{\mu}_n = \mathbf{0}$ and $\mathbf{\Sigma}_n = n\widetilde{\mathbf{\Sigma}}$. Gathering the results of Eqs. (IV.35)-(IV.37), the updated cardinality becomes:

$$p_{t|t}(n) \propto p_{t|t-1}(n)l_{\mathbf{y}_t}(n), \tag{IV.38}$$

where the pseudo-likelihood $l_{\mathbf{y}_t}(n)$ is given by:

$$l_{\mathbf{y}_t}(n) \approx \frac{\int_0^\infty p(u_t)\mathcal{CN}(\mathbf{y}_t;\mathbf{0},u_t(\sigma_t^2\mathbf{I}_M+n\widetilde{\mathbf{\Sigma}})du_t}{\int_0^\infty p(u_t)\mathcal{CN}(\mathbf{y}_t;\mathbf{0},u_t(\sigma_t^2\mathbf{I}_M+\bar{n}\widetilde{\mathbf{\Sigma}}))du_t}.$$

For the particular case of an exponential texture u_t, the pseudo-likelihood becomes:

$$l_{\mathbf{y}_t}(n) \approx \frac{\mathcal{L}(\mathbf{y}_t;\mathbf{0},\sigma_t^2\mathbf{I}_M+n\widetilde{\mathbf{\Sigma}})}{\mathcal{L}(\mathbf{y}_t;\mathbf{0},\sigma_t^2\mathbf{I}_M+\bar{n}\widetilde{\mathbf{\Sigma}})}, \tag{IV.39}$$

where $\mathcal{L}(\cdot;\mathbf{0},\mathbf{\Sigma})$ denotes a centered and complex multivariate Laplace density of Eq. (IV.6) and covariance $\mathbf{\Sigma}$. Note that the normalization factor of Eq. (IV.38) requires the convergence of the sum $\sum_{n=0}^{\infty} p_{t|t-1}(n)l_{\mathbf{y}_t}(n)$. As shown in [116, Eqs. (97-99)], this is verified as long as there exists an n_0 for which $p_{t|t-1}(n) < 1/n\ \forall n > n_0$. This condition posses no real limitation, since in practice we will always employ a maximum number of allowed targets $N_{\max}$, for which $p_{t|t-1}(n) = 0\ \forall n > N_{\max}$.

IV.4.4 TBD-CPHD Monte Carlo Implementation

In the context of sonar signals with impulsive distributions, e.g. Laplace, analytic solutions to the PHD and cardinality update equations are unfeasible. This is also the case even with Gaussian-mixture intensity/PHD functions. The alternative is to employ Sequential Monte Carlo (SMC) methods, i.e. particle approximations, to the PHD function. For TWS frameworks, the standard SMC-PHD filter was first proposed in [97], with subsequent improvements in [158], [159], [160] and [161]. The TWS framework offers the advantage of point observations, around which adaptive birth and/or nearly optimal Importance Sampling (IS) distributions can be constructed. In [158], the authors construct an adaptive birth intensity, by placing samples around the observation points. In [159] a similar adaptive-birth intensity is defined, and the update step is achieved by applying the unscented transform to a set of gated observations (i.e. observations falling in a gate around the predicted value). For high-density clutter, in [160] an efficient SMC-PHD implementation is achieved by employing only the gated observations around the predicted PHD particles. A rigorous auxiliary SMC-PHD is given in [161], where both the predictive IS and the birth IS are constructed by incorporating the new observation. In [162], the author divides the set of persistent particles of the PHD based on the current point observations, in order to construct efficient IS proposals for each particle partition.

For TBD-PHD filters, adaptive-birth intensities and IS distributions are less obvious, since the observation is a continuous process rather than a set of points. In [28], the authors use an

auxiliary step for birth particles in order to concentrate them around newly-birthed targets. However, for the previous time-step, i.e. persistent PHD particles, the authors resort to the bootstrap PHD filter. Here, we propose a complete auxiliary SMC-PHD filter for the array processing problem, which employs the current observation in the construction of the IS distributions for both persistent and newly birthed particles. For persistent particles, the fully adapted auxiliary SMC implementation (in the terminology of Pitt and Shepard [163]) is unobtainable. Additionally, for the birth particles we devise an adaptive-birth IS distribution by using the angular-power spectrum of the current array observation.

IV.4.4.a Optimal IS proposals

The auxiliary step of the SMC-PHD filter aims to select from the previous and birth particles, only those particles that best "explain" the current observation and then perform the prediction and update step. In order to introduce the IS distributions, we consider the evaluation of the following integral

$$\bar{\varphi} = \int \varphi(\mathbf{x}_t) D_{t|t}(\mathbf{x}_t) d\mathbf{x}_t, \tag{IV.40}$$

where $\varphi(\cdot)$ is any test function defined on $\mathbb{X}$, for which $\bar{\varphi}$ is defined. By employing the prediction (III.21) and update (IV.33) equations, as well as importance sampling, $\bar{\varphi}$ rewrites

$$\begin{aligned}\bar{\varphi} = &\iint \varphi(\mathbf{x}_t) \frac{L_{\mathbf{y}_t}(\mathbf{x}_{t-1}) p_s(\mathbf{x}_{t-1}) f(\mathbf{x}_t|\mathbf{x}_{t-1}) D_{t-1|t-1}(\mathbf{x}_{t-1})}{q_{t,p}(\mathbf{x}_t, \mathbf{x}_{t-1}|\mathbf{y}_t)} q_{t,p}(\mathbf{x}_t, \mathbf{x}_{t-1}|\mathbf{y}_t) d\mathbf{x}_{t-1} d\mathbf{x}_t \\ &+ \int \varphi(\mathbf{x}_t) \frac{L_{\mathbf{y}_t}(\mathbf{x}_t)\gamma(\mathbf{x}_t)}{q_{t,b}(\mathbf{x}_t|\mathbf{y}_t)} q_{t,b}(\mathbf{x}_t|\mathbf{y}_t) d\mathbf{x}_t,\end{aligned} \tag{IV.41}$$

where $q_{t,p}(\cdot,\cdot|\mathbf{y}_t)$ and $q_{t,b}(\cdot|\mathbf{y}_t)$ are the persistent and birth IS distributions that take into account the current observation $\mathbf{y}_t$. Note that the support of functions $q_{t,p}(\cdot)$ and $q_{t,b}(\cdot)$ is supposed to include the support of their respective target distributions, in order for Eq. (IV.41) to be valid. Hence, evaluating $\bar{\varphi}$ is achieved by providing a sample-based approximation to the aforementioned IS distributions. In a similar way to [161], we employ the following proposal for the IS persistent distribution:

$$q_{t,p}(\mathbf{x}_t, \mathbf{x}_{t-1}|\mathbf{y}_t) = q_{t,p}(\mathbf{x}_t|\mathbf{x}_{t-1}, \mathbf{y}_t) \frac{V_{\mathbf{y}_t}(\mathbf{x}_{t-1}) D_{t-1|t-1}(\mathbf{x}_{t-1})}{\int V_{\mathbf{y}_t}(\mathbf{x}_{t-1}) D_{t-1|t-1}(\mathbf{x}_{t-1}) d\mathbf{x}_{t-1}}. \tag{IV.42}$$

The potential function $V_{\mathbf{y}_t} : \mathbb{X} \to \mathbb{R}^+$ represents the "first stage" weights of the auxiliary particle filter [163]. $V_{\mathbf{y}_t}$ weights each of the previous PHD particles by taking into account the current observation $\mathbf{y}_t$. As showcased in Sec. IV.5, this step improves the performance of our proposed auxiliary SMC-PHD as opposed to [28].

Having defined both IS proposals, we can draw iid samples $\{\mathbf{x}_{t,p}^{(i)}, \mathbf{x}_{t-1,p}^{(i)}\}_{i=1}^{N_{t,p}}$ from $q_{t,p}(\cdot,\cdot|\mathbf{y}_t)$ and $\{\mathbf{x}_{t,b}^{(i)}\}_{i=1}^{N_{t,b}}$ from $q_{t,b}(\cdot|\mathbf{y}_t)$, and $\bar{\varphi}$ can be approximated as

$$\bar{\varphi} \approx \sum_{i=1}^{N_{t,p}} \varphi(\mathbf{x}_{t,p}^{(i)}) w_{t,p}^{(i)} + \sum_{i=1}^{N_{t,b}} \varphi(\mathbf{x}_{t,b}^{(i)}) w_{t,b}^{(i)}, \tag{IV.43}$$

where the IS persistent weights are given by

$$\begin{aligned} w_{t,p}^{(i)} &= \frac{1}{N_{t,p}} \frac{L_{\mathbf{y}_t}(\mathbf{x}_{t,p}^{(i)}) p_s(\mathbf{x}_{t-1,p}^{(i)}) f(\mathbf{x}_{t,p}^{(i)}|\mathbf{x}_{t-1,p}^{(i)}) D_{t-1|t-1}(\mathbf{x}_{t-1,p}^{(i)})}{q_{t,p}(\mathbf{x}_{t,p}^{(i)}, \mathbf{x}_{t-1,p}^{(i)}|\mathbf{y}_t)} \\ &= \frac{1}{N_{t,p}} \frac{L_{\mathbf{y}_t}(\mathbf{x}_{t,p}^{(i)}) p_s(\mathbf{x}_{t-1,p}^{(i)}) f(\mathbf{x}_{t,p}^{(i)}|\mathbf{x}_{t-1,p}^{(i)})}{q_{t,p}(\mathbf{x}_{t,p}^{(i)}|\mathbf{x}_{t-1,p}^{(i)}, \mathbf{y}_t)} \frac{\sum_{j=1}^{N_{t,p}} V_{\mathbf{y}_t}(\mathbf{x}_{t-1}^{(i)}) D_{t-1|t-1}(\mathbf{x}_{t-1}^{(i)})}{V_{\mathbf{y}_t}(\mathbf{x}_{t-1}^{(i)})}, \end{aligned} \tag{IV.44}$$

while IS birth weights are given by

$$w_{t,b}^{(i)} = \frac{1}{N_{t,b}} \frac{L_{\mathbf{y}_t}(\mathbf{x}_{t,b}^{(i)})\gamma(\mathbf{x}_{t,b}^{(i)})}{q_{t,b}(\mathbf{x}_{t,b}^{(i)}|\mathbf{y}_t)}. \tag{IV.45}$$

Constructing IS proposals that minimize the variance of the IS weights in Eqs. (IV.44) and (IV.45), leads to the optimal IS proposals. The optimal choice for the persistent IS proposal is given by

$$q_{t,p}^{\text{opt}}(\mathbf{x}_t|\mathbf{x}_{t-1}, \mathbf{y}_t) = \frac{L_{\mathbf{y}_t}(\mathbf{x}_t)p_s(\mathbf{x}_{t-1})f(\mathbf{x}_t|\mathbf{x}_{t-1})}{\int L_{\mathbf{y}_t}(\mathbf{x}_t)p_s(\mathbf{x}_{t-1})f(\mathbf{x}_t|\mathbf{x}_{t-1})d\mathbf{x}_t} \tag{IV.46}$$

$$V_{\mathbf{y}_t}^{\text{opt}}(\mathbf{x}_{t-1}) = \int L_{\mathbf{y}_t}(\mathbf{x}_t)p_s(\mathbf{x}_{t-1})f(\mathbf{x}_t|\mathbf{x}_{t-1})d\mathbf{x}_t, \tag{IV.47}$$

while the optimal birth IS proposal is

$$q_{t,b}^{\text{opt}}(\mathbf{x}_t|\mathbf{y}_t) = L_{\mathbf{y}_t}(\mathbf{x}_t)\gamma(\mathbf{x}_t). \tag{IV.48}$$

The aforementioned optimal IS distributions lead to IS weights that do not depend on $\mathbf{x}_t$, $\mathbf{x}_{t-1}$ and $\mathbf{y}_t$ and hence, are of zero variance.

IV.4.4.b Practical IS proposals

Optimal IS distributions are unfeasible in the context of the highly non-linear observation equation (II.2) and with multiplicative and non-Gaussian noise (i.e. the target signals). Hence, we resort to the state transition kernel

$$q_{t,p}(\mathbf{x}_t|\mathbf{x}_{t-1}, \mathbf{y}_t) = f(\mathbf{x}_t|\mathbf{x}_{t-1}), \tag{IV.49}$$

while for the potential function we employ the following approximation (first proposed in [163])

$$V_{\mathbf{y}_t}(\mathbf{x}_{t-1}) = L_{\mathbf{y}_t}(\bar{\mathbf{x}}_{t-1}), \tag{IV.50}$$

$$\bar{\mathbf{x}}_{t-1} = \int f(\mathbf{x}_t|\mathbf{x}_{t-1})d\mathbf{x}_t.$$

Tampering is employed, as described in [161], in order to avoid $V_{\mathbf{y}_t}(\cdot)$ becoming too concentrated as opposed to $V_{\mathbf{y}_t}^{\text{opt}}(\cdot)$.

Concerning the birth IS proposal, since constructing a distribution based on the exact shape of $L_{\mathbf{y}_t}(\cdot)$ is impractical, we opt for a construction based on the observation spectrogram. By constructing a spectrogram $S_t(\phi)$ of the array observation, we obtain an angular-power distribution of $\mathbf{y}_t$. Basically the peaks of $S_t(\phi)$ represent possible targets, and this information can be used to construct an adaptive IS proposal. We construct $q_{t,b}(\cdot)$ as a Gaussian mixture so as to drive birth samples around the peaks of the spectrogram $S_t(\phi)$:

$$q_{t,b}^{\text{spect}}(\phi_t|\mathbf{y}_t) = \sum_{i=1}^{N^{\text{spect}}} w_{t,i}^{\text{spect}} \mathcal{N}(\phi_t; \hat{\phi}_{t,i}^{\text{spect}}, P_{t,i}^{\text{spect}}), \tag{IV.51}$$

where the Gaussian mixture parameters are estimated from the observation spectrogram. In this work, we opted for instantaneous beamforming: $S_t(\phi) = |\frac{1}{M}\mathbf{a}(\phi)^H\mathbf{y}_t|^2$. However, other spectrogram options are possible, such as Capon [56, Ch. 5.4] or MUSIC [56, Ch. 4.5], which are computed over a window of array observations. In Eq. (IV.51) N^{spect} is a fixed parameter, equal to an imposed maximum number of targets for the filter. The means $\hat{\phi}_{t,i}^{\text{spect}}$ are obtained as the locations of the N^{spect} peaks of the spectrogram. Furthermore, only the peaks not interfering

with the persistent intensity are retained. Component weights can be adaptively constructed as $w_{t,i}^{\text{spect}} \propto S_t(\hat{\phi}_{t,i}^{\text{spect}})$, and then normalized. The component variances $P_{t,i}^{\text{spect}}$ are taken to be identical. For simplicity, other state parameters are directly sampled from the birth intensity. The aforementioned construction of the birth IS distribution is reminiscent of the pre-processor in TWS systems (see Sec. II.2). In TWS systems, the tracking system processes the positions of spectrogram maxima. In contrast, the TBD-CPHD filter processes the phased-array observation $\mathbf{y}_t$, while the spectrogram maxima are employed only for the construction of the birth IS distribution.

IV.4.4.c The estimation of $\widetilde{\boldsymbol{\Sigma}}$

Throughout the previous section, the pseudo-likelihood function $L_{\mathbf{y}_t}(\mathbf{x})$ was assumed to be known. However, as seen from the PHD (IV.34) and the cardinality (IV.39) pseudo-likelihoods, the covariace matrix $\widetilde{\boldsymbol{\Sigma}}$ needs to be estimated from the predicted PHD function (IV.31b). Since the non-linear form of the integrand in Eq. (IV.31b) prohibits an exact computation of $\widetilde{\boldsymbol{\Sigma}}$, we resort to a MC approximation, based on the particles of the predicted and normalized PHD function $v_{t|t-1}(\cdot)$. We compute an approximation to $\widetilde{\boldsymbol{\Sigma}}$ by employing the samples from the IS posteriors $q_{t,p}(\cdot,\cdot|\mathbf{y}_t)$ and $q_{t,b}(\cdot|\mathbf{y}_t)$:

$$\widetilde{\boldsymbol{\Sigma}} = \frac{1}{K_D}\left[\iint \mathbf{R}(\mathbf{x}_t)\frac{p_s(\mathbf{x}_{t-1})f(\mathbf{x}_t|\mathbf{x}_{t-1})D_{t-1|t-1}(\mathbf{x}_{t-1})}{q_{t,p}(\mathbf{x}_t,\mathbf{x}_{t-1}|\mathbf{y}_t)}q_{t,p}(\mathbf{x}_t,\mathbf{x}_{t-1}|\mathbf{y}_t)d\mathbf{x}_{t-1}d\mathbf{x}_t \right.$$
$$\left. + \int \mathbf{R}(\mathbf{x}_t)\frac{\gamma(\mathbf{x}_t)}{q_{t,b}(\mathbf{x}_t|\mathbf{y}_t)}q_{t,b}(\mathbf{x}_t|\mathbf{y}_t)d\mathbf{x}_t\right],$$

where the normalization constant, $K_D = \int_{\mathbb{X}} D_{t|t-1}(\mathbf{x})d\mathbf{x}$, is required because $\widetilde{\boldsymbol{\Sigma}}$ is computed from the normalized intensity (i.e. target pdf) $v_{t|t-1}(\cdot)$ [see Eq. (IV.31b)].

Employing the previously sampled particles $\{\mathbf{x}_{t,p}^{(i)}, \mathbf{x}_{t-1,p}^{(i)}\}_{i=1}^{N_{t,p}}$ and $\{\mathbf{x}_{t,b}^{(i)}\}_{i=1}^{N_{t,b}}$ from the proposals $q_{t,p}(\cdot,\cdot|\mathbf{y}_t)$ and $q_{t,b}(\cdot|\mathbf{y}_t)$, we obtain the approximation

$$\widetilde{\boldsymbol{\Sigma}} \approx \frac{1}{K_D}\left[\sum_{i=1}^{N_{t,p}} \mathbf{R}(\mathbf{x}_{t,p}^{(i)})\tilde{w}_{t,p}^{(i)} + \sum_{i=1}^{N_{t,b}} \mathbf{R}(\mathbf{x}_{t,b}^{(i)})\tilde{w}_{t,b}^{(i)}\right], \tag{IV.52}$$

where $K_D = \sum_{i=1}^{N_{t,p}} \tilde{w}_{t,p}^{(i)} + \sum_{i=1}^{N_{t,b}} \tilde{w}_{t,b}^{(i)}$, and the IS weights are given by

$$\begin{aligned}\tilde{w}_{t,p}^{(i)} &= \frac{1}{N_{t,p}}\frac{p_s(\mathbf{x}_{t-1,p}^{(i)})f(\mathbf{x}_{t,p}^{(i)}|\mathbf{x}_{t-1,p}^{(i)})D_{t-1|t-1}(\mathbf{x}_{t-1,p}^{(i)})}{q_{t,p}(\mathbf{x}_{t,p}^{(i)},\mathbf{x}_{t-1,p}^{(i)}|\mathbf{y}_t)} \\ \tilde{w}_{t,b}^{(i)} &= \frac{1}{N_{t,b}}\frac{\gamma(\mathbf{x}_{t,b}^{(i)})}{q_{t,b}(\mathbf{x}_{t,b}^{(i)}|\mathbf{y}_t)},\end{aligned} \tag{IV.53}$$

where we employ the practical IS proposals of Eqs. (IV.49) and (IV.50).

IV.4.4.d Algorithm description

A pseudo-algorithm is given in Table IV.1 for one iteration of the proposed auxiliary CPHD filter. The auxiliary step for persistent particles is presented at lines 6 to 10 of Fig. IV.1. Observe the tampering of weights with parameter $0 < \epsilon < 1$, as proposed in [161]. A first approximation of $\widetilde{\boldsymbol{\Sigma}}$ is given at line 5, where we employed the normalized spectrogram $S_t(\phi)$ to approximate the current intensity. Furthermore, $\hat{P}$ and $\hat{\sigma}_\phi$ are the means of the initial distribution of the target

$D_{t-1|t-1}(\mathbf{x}_{t-1}) \approx \sum_{i=1}^{N_{t-1}} w_{t-1}^{i} \delta_{\mathbf{x}_{t-1}^{i}}(d\mathbf{x}_{t-1})$
$N_{t,p} = N_{t-1}$
Cardinality prediction: $p_{t|t-1}(n)$ by Eq. (IV.27)
First stage for persistent and birth PHD
$[\widetilde{\boldsymbol{\Sigma}}]_{m,n} \approx \hat{P} \exp\left(-\frac{(n-m)^2 \hat{\sigma}_{\phi}^2}{2}\right) \frac{\int e^{j\,(n-m)\phi} S_t(\phi) d\phi}{\int S_t(\phi) d\phi}$
for $i = 0$ **do** to $N_{t,p}$
    $V_{\mathbf{y}_t}(\mathbf{x}_{t-1}^{(i)}) = L_{\mathbf{y}_t}(\bar{\mathbf{x}}_{t-1}^{(i)})$ ▷ First stage weights
end for
Resample previous particles:
$\{\mathbf{x}_{t-1}^{(i)}, [V_{\mathbf{y}_t}(\mathbf{x}_{t-1}^{(i)}) w_{t-1}^{(i)}]^{\epsilon}\}_{i=1}^{N_{t,p}} \rightarrow \{\mathbf{x'}_{t-1,p}^{(i)}, w'^{(i)}_{t-1}\}_{i=1}^{N_{t,p}}$
for $i = 0$ **do** to $N_{t,b}$
    $\mathbf{x}_{t,b}^{(i)} \sim q_{t,b}^{\text{spect}}(\mathbf{x}_t|\mathbf{y}_t)$
    $\tilde{w}_{t,b}^{(i)} = \frac{\gamma(\mathbf{x}_{t,b}^{(i)})}{N_{t,b}\, q_{t,b}^{\text{spect}}(\mathbf{x}_{t,b}^{(i)}|\mathbf{y}_t)}$
end for
Second stage persistent PHD
for $i = 0$ **do** to $N_{t,p}$ ▷ Second stage sampling
    $\mathbf{x}_{t,p}^{(i)} \sim f(\mathbf{x}_t|\mathbf{x'}_{t-1}^{(i)})$
    $\tilde{w}_{t,p}^{(i)} = \frac{p_s(\mathbf{x'}_{t-1}^{(i)}) \sum_{j=1}^{N_{t,p}} V_{\mathbf{y}_t}(\mathbf{x'}_{t-1}^{(j)}) w'_{t-1}^{(j)}}{N_{t,p}\, V_{\mathbf{y}_t}(\mathbf{x'}_{t-1}^{(i)})}$
end for
Estimate $\widetilde{\boldsymbol{\Sigma}}$ by Eq. (IV.52)
Final weights for persistent and birth PHD
for $i = 1$ to $N_{t,p}$ **do** ▷ Persistent weights
    $w_{t,p}^{(i)} = \tilde{w}_{t,p}^{(i)}\, L_{\mathbf{y}_t}(\mathbf{x}_{t,p}^{(i)})$
end for
for $i = 1$ to $N_{t,b}$ **do** ▷ Birth weights
    $w_{t,b}^{(i)} = \tilde{w}_{t,b}^{(i)}\, L_{\mathbf{y}_t}(\mathbf{x}_{t,b}^{(i)})$
end for
Update cardinality $p_{t|t}(n) \propto p_{t|t-1}(n)\, l_{\mathbf{y}_t}(n)$
MAP cardinality estimate:
$\hat{n}_{t|t}^{\text{MAP}} = \underset{n}{\text{argmax}}\; p_{t|t}(n)$
Resample $N_t = \hat{n}_{t|t}^{\text{MAP}} N_{ppt}$ **particles**:
$\{\mathbf{x}_{t,p}^{(i)}, w_{t,p}^{(i)}\} \cup \{\mathbf{x}_{t,b}^{(i)}, w_{t,b}^{(i)}\} \rightarrow \{\mathbf{x}_t^{(i)}, w_t^{(i)}\}_{i=1}^{N_t}$
Clustering:
$\{\hat{\mathbf{x}}_{t|t}^{(i)}\}_{i=1}^{\hat{n}_{t|t}} \leftarrow \text{Clustering}\left(\{\mathbf{x}_t^{(i)}\}_{i=1}^{N_t}, \hat{n}_{t|t}^{\text{MAP}}\right)$
$D_{t|t}(\mathbf{x}_t) \approx \sum_{i=1}^{N_t} w_t^{i} \delta_{\mathbf{x}_t^{i}}(d\mathbf{x}_t)$ ▷ New PHD

Figure IV.1: Pseudo-algorithm for one iteration for the proposed auxiliary SMC-CPHD filter for array processing.

1: **function** CLUSTERING($\{\mathbf{x}_t^{(i)}\}_{i=1}^{N_t}$, $\hat{n}_{t|t}^{\text{MAP}}$)
2: $\left(\{\mathbf{x}_{\text{DBSCAN}}^{(i)}\}_{i=1}^{\hat{n}_{\text{DBSCAN}}}, \{\mathbf{x}_{\text{outlier}}^{(i)}\}_{i=1}^{N_{\text{outlier}}}\right) = \text{DBSCAN}\left(\{\mathbf{x}_{t+1}^{(i)}\}_{i=1}^{N_{t+1}}, N_{\min}, \epsilon\right)$
3: $\{\mathbf{x}_t^{(i)}\}_{i=1}^{N_t} \setminus \{\mathbf{x}_{\text{outlier}}^{(i)}\}_{i=1}^{N_{\text{outlier}}} = \{\mathbf{x}_{\overline{\text{outlier}}}^{(i)}\}_{i=1}^{N_{\overline{\text{outlier}}}}$
4: $\{\hat{\mathbf{x}}_{\text{KMEANS}}^{(i)}\}_{i=1}^{\hat{n}_{\text{KMEANS}}} = \text{k-means}\left(\{\mathbf{x}_{\overline{\text{outlier}}}^{(i)}\}_{i=1}^{N_{\overline{\text{outlier}}}}, \hat{n}_{t|t}^{\text{MAP}}\right)$
5: $\{\hat{\mathbf{x}}_{\text{OUT}}^{(i)}\}_{i=1}^{\hat{n}_{\text{OUT}}} = \{\hat{\mathbf{x}}_{\text{KMEANS}}^{(i)}\}_{i=1}^{\hat{n}_{\text{KMEANS}}}$
6: **if** $(\hat{n}_{\text{DBSCAN}} > 1) \wedge (\hat{n}_{\text{KMEANS}} > 1)$ **then**
7: $s_{\text{DBSCAN}} = \text{Silhouette}\left(\{\hat{\mathbf{x}}_{\text{DBSCAN}}^{(i)}\}_{i=1}^{\hat{n}_{\text{DBSCAN}}}\right)$
8: $s_{\text{KMEANS}} = \text{Silhouette}\left(\{\hat{\mathbf{x}}_{\text{KMEANS}}^{(i)}\}_{i=1}^{\hat{n}_{\text{KMEANS}}}\right)$
9: **if** $s_{\text{DBSCAN}} > s_{\text{KMEANS}}$ **then**
10: $\{\hat{\mathbf{x}}_{\text{OUT}}^{(i)}\}_{i=1}^{\hat{n}_{\text{OUT}}} = \{\hat{\mathbf{x}}_{\text{DBSCAN}}^{(i)}\}_{i=1}^{\hat{n}_{\text{DBSCAN}}}$
11: **end if**
12: **end if**
13: **return** $\{\hat{\mathbf{x}}_{\text{OUT}}^{(i)}\}_{i=1}^{\hat{n}_{\text{OUT}}}$
14: **end function**

Figure IV.2: Pseudo-algorithm of the proposed clustering method.

signal power and angular spread. Thus, we obtain a computationally inexpensive approximation of $\widetilde{\mathbf{\Sigma}}$ at time t.

Birth samples are drawn from the adaptive IS distribution in lines 11 to 14. Prediction for persistent particles is achieved next in lines 16 to 19 and the estimated covariance matrix $\widetilde{\mathbf{\Sigma}}$ is recomputed at line 20. The matrix $\widetilde{\mathbf{\Sigma}}$ is required in the computation of the pseudo-likelihoods $L_{\mathbf{y}_t}(\cdot)$ and $l_{\mathbf{y}_t}(\cdot)$ employed for the final weighting stage of persistent and birth particles (lines 22 to 28). Resampling and clustering are conducted next.

Recent results, presented in [88, 89], of density-based clustering algorithms (e.g. DBSCAN) showcase their ability to reject outlier particles and the capability of non-linear cluster separation. DBSCAN [120] estimates both the number of clusters and their centers. Outlier particles, i.e. particles not belonging to any cluster, are present due to the uniform birth intensity $\gamma_t(\cdot)$. The k-means clustering method minimizes the within-cluster sum of squares and hence behaves poorly in the presence of such outliers. Our proposed clustering method, presented in Fig. IV.2, considers the application of DBSCAN in order to identify outlier particles and eliminate them from subsequent clustering. Note that on line 3 of Fig. IV.2, outliers are eliminated from the current set of particles ($\setminus$ symbolizing set difference). Next, the k-means is applied with the number of clusters specified by the cardinality MAP estimator. At this stage, two sets of clusters are available, by DBSCAN and k-means. In order to evaluate the two clustering results, we compute their silhouettes [119], and pick the clustering method with the largest mean silhouette value. Note that these silhouettes are computed only when both methods detect at least two clusters. Whenever this is not verified, we choose the k-means method by default. This methodology eliminates outliers, and is shown to confer better results than using the k-means algorithm solely. The DBSCAN algorithm (line 2) requires two parameters: the minimum number of points that form a cluster $N_{\min}$ and the neighborhood distance ϵ. The outlier particles detected by DBSCAN are then eliminated from the available particle set (line 4) before applying the k-means clustering method. The two mean-silhouettes values are given by: s_{DBSCAN} and s_{KMEANS}.

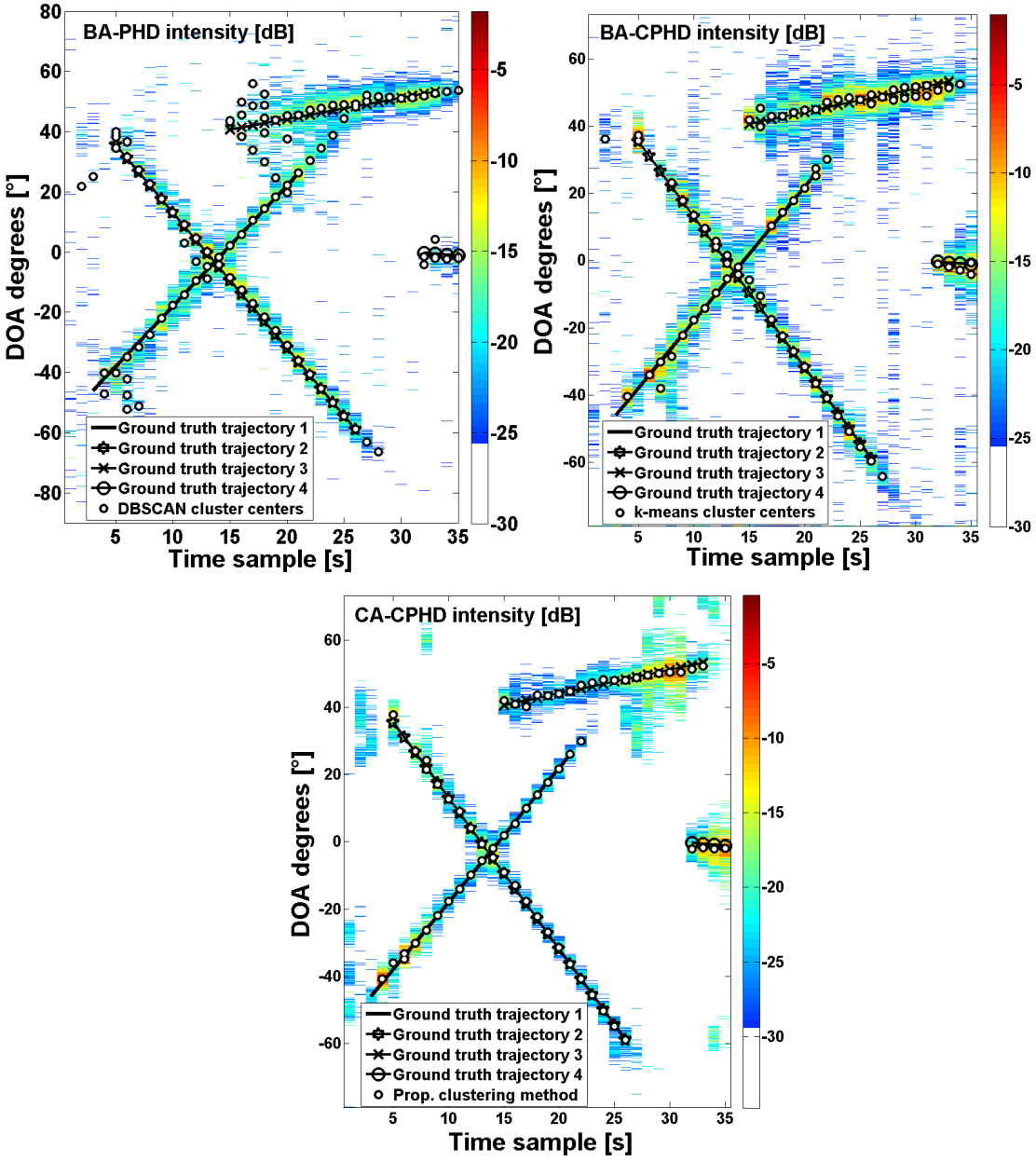

Figure IV.3: Different PHD filter intensities and clustering results.

IV.5 Simulation Results

In this section, we provide filtering results with the proposed method for simulated phased-array signals. In the first scenario, presented in IV.5.1, we simulate multiple targets with a wide range of target speeds and exhibiting crossing targets. Secondly, in Sec. IV.5.2 we assess the angular-resolution capabilities of our proposed filter.

IV.5.1 Tracking results

In this section, a ULA of $M = 30$ receivers and half-wavelength spacing is considered. Tracking is conducted with a nearly constant angular velocity model, obeying Eq. (IV.20). Target-generated signals and observation noise are mutually Laplace random vectors, obeying the SIRV model of Eq. (IV.17a) and Eq. (IV.17b). Conducting tracking in the angular domain, as opposed to

the Cartesian, is possible whenever pseudo-accelerations are small [117, Ch. 1.5]. Furthermore, this allows a simpler definition and interpretation of the birth intensity. The state vectors also contain the logarithms of the target-signal power and angular spread, as described in section IV.3.2. Thus the state-transition matrix is defined as: $\mathbf{F}_t = \begin{bmatrix} \mathbf{F}_t^k & \mathbf{0}_2 \\ \mathbf{0}_2 & \mathbf{I}_2 \end{bmatrix}$ where $\mathbf{F}_t^k = \begin{bmatrix} 1 & T_s \\ 0 & 1 \end{bmatrix}$ represents the kinematic-transition matrix, $\mathbf{0}_n$ is the zero matrix of size n and $T_s = 1$s is the sampling period. The kinematic-covariance matrix is given by the nearly-constant velocity model [74, Ch. 6.3.2].

A first tracking example is presented in Fig. IV.3, where we employ an angular acceleration deviation of $0.1^o/\text{s}$ for the kinematic model. All targets generate signals with equal power, assuring an SNR of 5dB and angular spread of $\sigma_\phi = 0.1$rad. Tracking is conducted with our proposed method, which we shall refer to as the Complete Auxiliary CPHD (CA-CPHD), as opposed to the Birth Auxiliary PHD and CPHD (BA-PHD and BA-CPHD) proposed in [28]. For all algorithms, we employ a number of $N_{ppt} = 1000$ particles per target, a constant target survival probability of $p_s = 0.9$ and a uniform birth intensity for the centroid DOA in the physical angle coordinates: $\gamma_t(\theta) \propto \mathbb{1}_{[-\pi/2,\pi/2]}(\theta)$, while for the speed we employ $\gamma_t(\dot{\theta}) \propto \mathbb{1}_{[-7,7]}(\dot{\theta})$. The birth intensity is constructed in order to ensure $\int \gamma_t(\mathbf{x})d\mathbf{x} = 0.3$, a commonly used value. Thus, we assume that births may occur anywhere in the state space, with a wide variety of speeds. For the CPHD algorithms, the cardinality of the birth process is fixed at $p_b(0) = 0.7$, $p_b(1) = 0.3$ and $p_b(n) = 0\ \forall n > 1$. The birth IS distribution is obtained by employing the peaks of the signal spetrogram, as detailed in Sec. IV.4.4.b, with a number of components $N^{\text{spect}} = 5$ and $\sqrt{P^{\text{spect}}} = (1)^o$. Fig. IV.3 presents the particular approximation of the intensities of the three filtering methods: BA-PHD, BA-CPHD and CA-CPHD, and the respective clustering results. Note that we employ the DBSCAN clustering method for the BA-PHD method with the following parameters: the minimum number of points to form a cluster (set to 50) and the neighborhood distance (set to 2). The k-means was employed for the BA-CPHD, with outlier rejection as described in Sec. IV.4.4.d, and the proposed clustering for the CA-CPHD filter. Observe the improved results of the CA-CPHD filter.

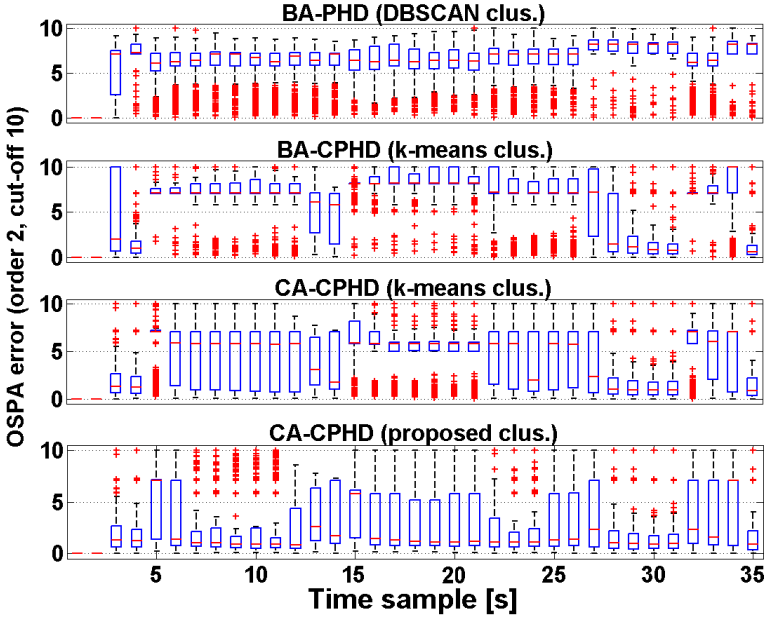

Figure IV.4: Box and whiskers plot of the OSPA error (order 2 and cut-off 10), as a function of time. On each box, the central mark is the median, the edges of the box are the 25th and 75th percentiles, the whiskers extend to the most extreme data points not considered outliers, and outliers are plotted individually.

A Monte Carlo analysis is carried out by simulating 400 runs of the above scenario. The OSPA metric of Sec. III.4, which takes into account both position and cardinality errors, is used to quantify the statistical error. We employ the OSPA metric with order $p = 2$ (i.e. the Euclidean distance) for positioning errors and various cut-off parameter values. The cut-off c controls cardinality errors and acts as a threshold for the Euclidean distance between two points. If the distance between two points is greater than the cut-off, then they are considered unrelated and the error is fixed at the cut-off value. Hence, cardinality errors become more visible at higher values of c. In Fig. IV.4, box and whisker plots conducted for the OSPA error over the 400 runs are presented for the different tracking methods. Note the reduced median values for the CA-CPHD with k-means clustering, and furthermore for the CA-CPHD with the proposed clustering. A more compact error representation is given by the mean OSPA error (averaged over the duration of the simulation) presented in Table IV.1. Furthermore, we compute the OSPA errors for several cut-off and SNR values. Observe that the CA-CPHD outperforms the BA-PHD and BA-CPHD even at very-low SNR values. The CA-CPHD is further improved by employing the proposed clustering method as opposed to the k-means. For increasing cut-off values the OSPA error increases, highlighting cardinality errors for both BA-PHD and BA-CPHD.

Table IV.1: Average OSPA error of various filters computed over 400 runs.

Mean OSPA error values					
SNR	cut-off	BA PHD	BA CPHD	CA CPHD k-means	CA CPHD (prop. clust.)
0dB	$c = 1$	0.91	0.86	0.82	0.78
	$c = 2.5$	2.03	1.89	1.64	1.45
	$c = 5$	3.82	3.48	2.80	2.24
5dB	$c = 1$	0.87	0.824	0.747	0.70
	$c = 2.5$	1.89	1.75	1.45	1.22
	$c = 5$	3.46	3.2	2.45	1.80
10dB	$c = 1$	0.84	0.78	0.72	0.68
	$c = 2.5$	1.81	1.67	1.34	1.14
	$c = 5$	3.27	2.95	2.22	1.71
20dB	$c = 1$	0.82	0.758	0.70	0.65
	$c = 2.5$	1.73	1.59	1.33	1.09
	$c = 5$	3.1	2.88	2.17	1.60

Cardinality errors are more easily visualized by cardinality histograms, where for the 400 runs, the cardinality of the estimated set is recorded in a histogram. In Fig. IV.5, we observe the cardinality histograms for the scenario presented in Fig. IV.3, at an SNR of 5dB. Cardinality histograms showcase the improved cardinal estimation of the CA-CPHD while the proposed clustering further improves the cardinality of the estimated target set. Essentially, the proposed clustering performs a fusion of k-means and DBSCAN. DBSCAN is density-based, hence if the estimated PHD function has the same number of modes as the true multi-target intensity, then DBSCAN offers the correct cardinality estimate. Note that the CPHD offers not only the cardinality distribution, but also an improved estimate of the intensity function. This is especially true in the case of superpositional models, where the approximations made to the PHD-update equation lead to a highly fluctuant intensity mass, and hence an inaccurate $\tilde{\mathbf{\Sigma}}$. However, the CPHD normalizes the mass of the intensity with the average number of targets obtained from the cardinality distribution. This greatly decreases the fluctuations of the intensity mass, and

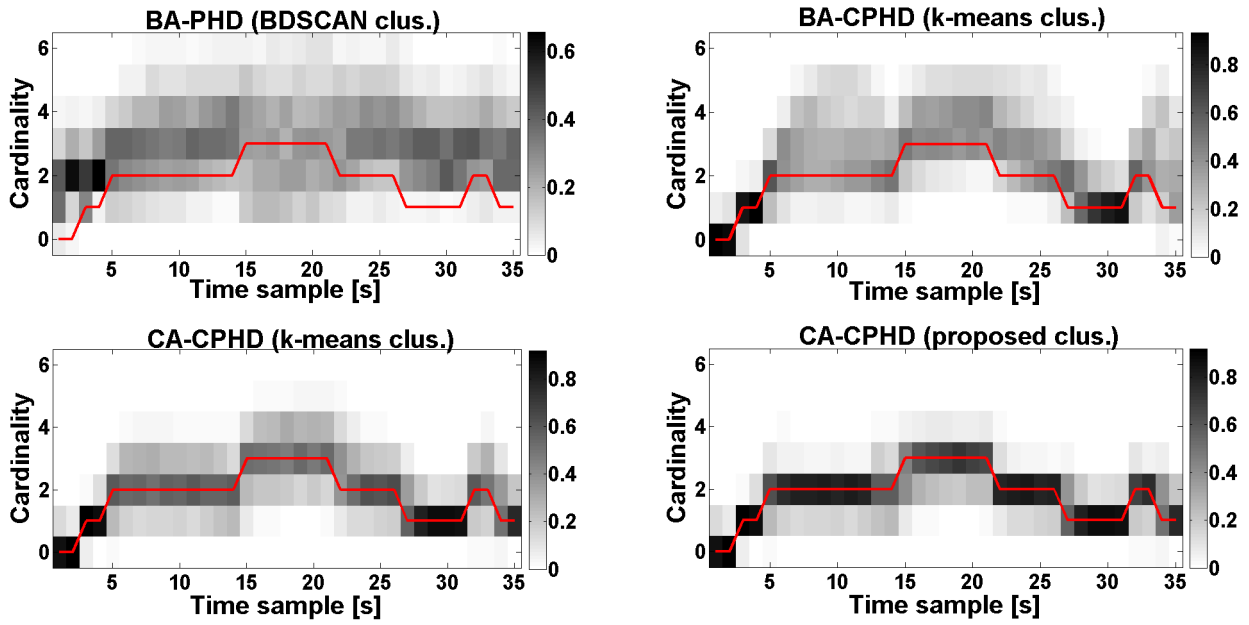

Figure IV.5: Cardinal histograms for different filtering methods at SNR $5dB$. Ground truth cardinality is represented by the red line.

thus provides better approximations for the covariance estimate $\bar{n}_{t+1|t}\boldsymbol{\Sigma}$. Whenever the MAP cardinality estimate is slightly off the true cardinality value but the intensity function exhibits the correct number of modes, the proposed clustering offers the correct cardinality estimate.

The computation time of the different algorithms is given in Table IV.2, where we observe the mean duration of one iteration for the various filters. Computational times are reported for 400 runs of the aforementioned scenario at 5dB. All filters are implemented in MATLAB on a 3.6GHz CPU. The increased computational time of the BA-PHD filter is explained by the fact that the number of particles per target is controlled by the mass of the estimated intensity function, which is often higher than the true mean cardinality. The cardinalized PHD filters eliminate this issue by employing the estimated cardinality distribution in order to determine the number of particles to be resampled. As proposed in [28], for the BA algorithms an auxiliary step for birth particles is achieved by resampling from a Gaussian mixture, with the mixture components given by all first-stage birth particles. This is time-consuming, as opposed to direct sampling from an $N^{\text{spect}} = 3$ component Gaussian mixture in the CA-CPHD filter. Indeed, the mean computation time of one algorithm iteration is greater for the both BA-PHD and BA-CPHD than the CA-CPHD, even with the proposed clustering scheme.

Table IV.2: Average time duration of one iteration of various filters.

Algorithm	Mean duration	Std. duration
BA-PHD	3.12s	0.07s
BA-CPHD	2.29s	0.06s
CA-CPHD (prop. clust.)	1.67s	0.112s

IV.5.2 Angular resolution analysis

In this section, we compare the resolution capabilities of our proposed algorithm with array processing methods. For extended (or angularly distributed) targets, two widely-employed methods are the generalized Capon [164] and the DSPE [16]. The generalized Capon is a beamformer for distributed targets while DSPE generalizes the MUSIC algorithm for extended targets. The two algorithms employ a parametric description of the array signal and resort to eigen-analysis of the array signal covariance. The array covariance is estimated on a sliding window of array observations of 34 samples. Furthermore, both array processing methods assume the exact number of targets, while the CA-CPHD intensity is initialized on a uniform interval of angles. There are two scenarios of interest: a stationary case with targets having constant DOAs and parameters, and a slightly non-stationary case where the target DOAs evolves slowly. Results of the first scenario, with two targets placed at $\pm 5^o$, are presented in the top row of Fig. IV.6. All three methods resolve the targets and correctly estimate both DOA trajectories. In the second row of Fig. IV.6, results on the second scenario are presented. The generalized Capon and DSPE have difficulties resolving the two targets when the angle between them is less than 8^o, while the CA-CPHD still achieves target separation and correctly estimates the target tracks. Note that an analysis with crossing targets is not possible, since neither the Capon nor the DSPE method resolves such closely spaced targets, and additional target characteristics, such as target-speed, are necessary. Mean OSPA error (see Sec. III.4) results, conducted by simulating 400 runs for both scenarios, are presented in Table IV.3. Note that, for scenario # 1, with a stationary process $\mathbf{y}_t$ and a known number of targets, DSPE slightly outperforms CA-CPHD. However, for scenario # 2, CA-CPHD outperforms both DSPE and the generalized Capon beamformer.

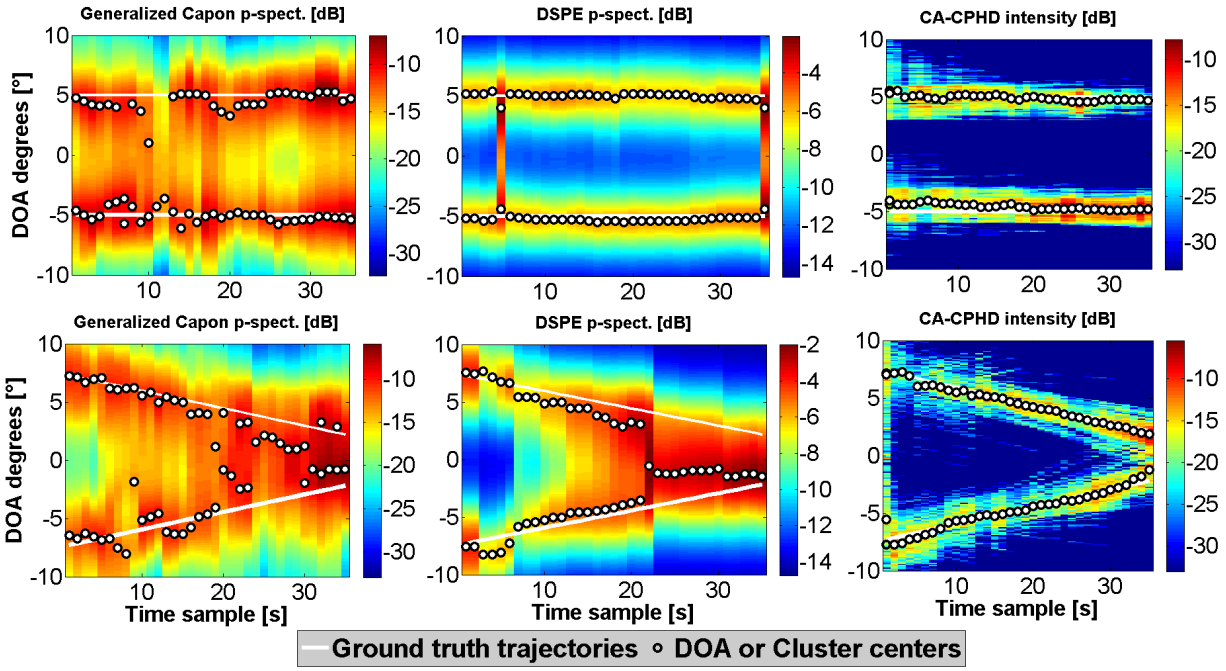

Figure IV.6: Angular resolution analysis with closely spaced targets scenario: stationary case → upper row, non-stationary case → bottom row.

Table IV.3: Average OSPA error computed over 400 runs.

Mean OSPA error values				
SNR	cut-off	Generalized Capon	DSPE	CA-CPHD (prop. clust.)
Scenario #1	$c = 1$	0.53	0.46	0.39
	$c = 2.5$	0.63	0.47	0.5
	$c = 5$	0.67	0.48	0.65
Scenario #2	$c = 1$	0.739	0.734	0.5
	$c = 2.5$	1.19	1.3	0.73
	$c = 5$	1.54	1.86	0.97

IV.6 Real sonar data results

In this section, the CA-CPHD is applied to bathymetric sonar data, with the aim of separating the different echoes backscattered by the sea-bottom and various objects. Although in such applications the targets of interest are no longer kinematic in nature, the relevance of adaptively filtering the multiple echoes impinging the sonar array was showcased in Chapter II.

The phased-array data was obtained with an EdgeTech 4600 side-scan (i.e. side looking) sonar in a shallow-water canal (average depth of 15m). In Appendix H, the impulsive character of the EdgeTech 4600 sonar signals is demonstrated, whit the complex multivariate Laplace [see Eq. (IV.6)] providing a good fit. Therefore, in this section, the Laplace density is employed as the phased-array likelihood function. For more details on the sonar array, we direct the reader to Sec. II.2 and Appendix G. Two real-data scenarios are presented. First, for one data ping, we compare the DOA estimates of the Capon beamforming method [Fig. IV.7 a)] to our CA-CPHD filter [Fig. IV.7 b)]. In both figures, we employ the Capon beamforming spectrogram as background, to showcase the angular distribution of the phased-array signal power. Notice the arch-shaped curve representing the line-of-site echo from a flat sea-bottom and the interfering echoes, involving sea-surface reflections and causing spurious DOA estimates. In Fig. IV.7 a) the DOA estimates (represented as +) are obtained as the instantaneous maxima of the Capon spectrogram. In Fig. IV.7 b) the DOA centroids of the CA-CPHD filter are overlaid

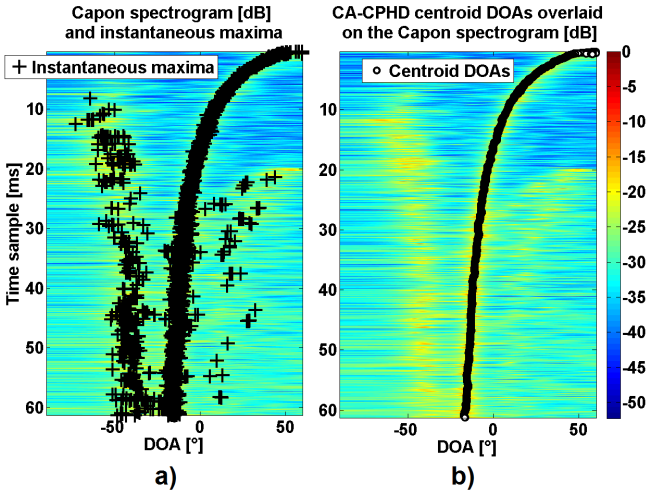

Figure IV.7: DOA estimates as the instantaneous maxima (a) of the Capon spectrogram an the CA-CPHD filter results (b), overlaid on the CAPON spectrogram.

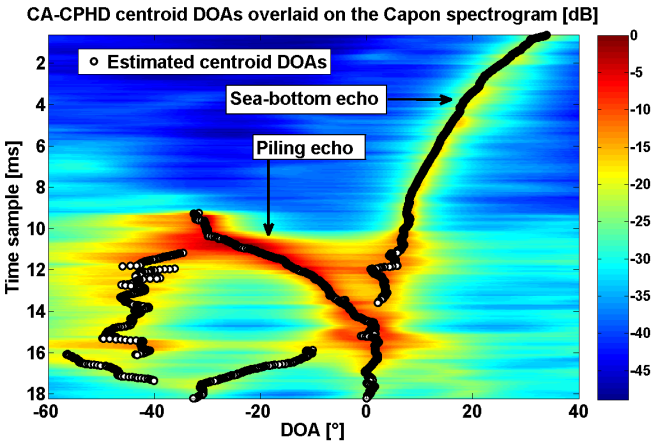

Figure IV.8: CA-CPHD filter centroid DOA estimates for a multiple echo scenario.

on the Capon spectrogram. Notice the spurious-free filtered DOA estimates supplied by the CA-CPHD filter.

The second scenario involves the vertical piling (a man-made object) of Sec. II.5.2.b. Fig. IV.8 presents the results of the CA-CPHD filter on a single ping of the piling data-set, where the "informative" echoes are generated by the sea-bottom and the vertical piling, i.e. a large cylinder. The sea-bottom echo has the same arch-shaped curve, indicating a relatively flat sea-bottom. The sonar insonifies a narrow strip along the length of the piling, leading to the piling to be perceived as a locally flat vertical surface. Therefore, the piling echo has a similar curve as the bottom echo but arched in the opposite direction. Notice the filtered DOA estimates of the proposed method and also some residual echoes being received after the piling echo. Echoes received after the piling echo are not line-of-sight and involve higher-order paths, e.g. reflections from the sea-surface, and should be eliminated for bathymetry. Note that the estimated centroid DOAs do not constitute echo trajectories. The recently introduced labeled sets [33, 34], where each element (or target) has a unique label throughout time, can be employed to identify and separate echo tracks/trajectories. Additionally, labeled approaches can facilitate the rejection of residual echoes that involve higher-order propagation paths.

IV.7 Chapter conclusions

A track-before-detect intensity filter is proposed for non-Gaussian phased-array observations, modeled as SIRV processes, and generated by angularly distributed (extended) targets. The target (or source) signals are analytically integrated-out from the filter update equation, ensuring an efficient implementation of the intensity filter. As an improvement to the TBD-PHD filter, we developed the TBD-CPHD filter that, additionally to the intensity function, also propagates the distribution of the number of targets, referred to as cardinality distribution. The cardinality distribution not only improves the state-inference stage from the intensity function, but also the accuracy of the intensity function itself. This vastly improves performances over the TBD-PHD filter. Furthermore, in an effort to approach real-data scenarios, the TBD-CPHD is developed for a distributed (extended) target model within an impulsive-noise context. Underwater acoustic environments have been shown to exhibit impulsive (i.e. heavier tails than the Gaussian) or even heavy-tailed distribution signals. In this work, we employ the general SIRV-signal model capable of describing both impulsive and heavy-tailed signals, with the more specific multivariate Laplace distribution for the real-data experiments. An improved particle-filter implementation is proposed that employs an auxiliary step for persistent particles and an adaptive-birth IS distribution, which accounts for the current observation. Results on simulated data demonstrate the improved performance of the proposed filter as compared to recent methods. Furthermore, the proposed filter is applied to real bathymetric sonar data.

One of the major limitations of all intensity filters, as pointed out for TBD-CPHD real-sonar data results, is the inability to identify track (or trajectories). This is intrinsic to the intensity function, where only target states are represented and no target history, i.e. trajectory, is kept. The importance of such trajectory identifications are prevalent in the echo-tracking example of Fig. IV.8, where the TBD-CPHD filter correctly infers the DOAs of several echoes, even dough several echos have no bathymetric relevance. In order to achieve the separation of bathymetrically relevant echoes from irrelevant ones, we need a clear separation and identification of trajectories and not just of filtered DOAs. The newly proposed labeled RFS [33, 34], appear to resolve this issue by labeling the different targets. The target labels being unique, can be employed to reconstruct the entire trajectory of a specific target.

Chapter V

Conclusions and perspectives

Finished products are for decadent minds.

Isaac Asimov

Foundation's Edge [165]

Conclusions

In this work, the problem of DOA tracking of multiple targets with phased arrays is addressed. Several possible solutions are presented and classified into the TWS and TBD frameworks. The proposed solutions are tested on the problem of bathymetry recovery in underwater sonar-array processing.

The first contribution presented, relies on the TWS modular processing chain, with pre-processing methods forming point-observation sets that are subsequently filtered by the tracking module. This is by far the most common tracking implementation and has the advantage of a relatively low-complexity and straightforward implementation. Tracking is perceived as a model-based filter and ensures trajectory formation and separation of echoes from clutter and interfering multi-path for 3D image reconstruction. The proposed filter processes DOA estimates, obtained with classical array-processing methods, as observations and is implemented on the basis of the unscented Kalman filter. Geometric models are employed to characterize the DOA trajectories of echoes in a bathymetric context. Multiple models are employed in parallel in order to increase the adaptability of the proposed filter. Furthermore, the models are also shown to effectively segment the 3D image and provide useful information for infrastructure identification purposes. Trajectory interruptions, due to acoustical shadows, are detected via a measure of trajectory existence probability. Goodness-of-fit tests validate the proposed model processors on simulated and real data.

A second contribution represents a TBD-PHD filter for phased-arrays. For the TBD framework, where no pre-processing is done, better performances can be achieved but at the cost of a higher-complexity filter implementation. As opposed to TWS, TBD also renders difficult the proposal of ad-hoc methods for target initialization and death. Therefore, we opt for the point-process formalism and intensity filters, that circumvent this problem by considering the multi-target state as an unordered collection of points, i.e. a set. The intensity function (or PHD function) is the first-order moment density of a point process, which describes both the random number of targets and their random-state vectors. Thus, an intensity filter is viewed as a first-order filter, propagating an approximation to the true posterior distribution. Based on the superpositional PHD filter, the TBD-PHD filter is proposed, that is capable of tracking multiple-targets directly from phased-array observations. The proposed filter employs marked point processes and avoids an augmented state by analytically integrating-out the target signals

in the update stage of the filter. This leads to an efficient particle-filter implementation, that does not require sampling from the higher-dimensional posterior of the augmented state. Furthermore, in the proposed filter an improved clustering mechanism is employed, that estimates both the number of clusters and their centers in the presence of outliers. The proposed TBD-PHD filter is general, in the sense that it does not suppose any assumptions on the type of target kinematics. The TBD-PHD filter does, however assume Gaussian source signals generated by the point-target model and Gaussian additive noise. These hypotheses, although sufficient in various applications, are too restrictive for sonar applications.

The TBD-PHD filter is further generalized to angularly-distributed (extended) targets and impulsive non-Gaussian signals. Additionally, to improve the filtering performance a cardinalized version of the PHD filter is considered. The resulting TBD-CPHD filter propagates both the intensity function and the cardinality distribution. Here again, filtering is achieved without augmenting the state vector with source signals, i.e. the marks. SIRV distributions are employed to model source signals and noise, in a joint-SIRV model. The SIRV distribution family is very general and encompasses most distributions employed to model signals and clutter in sonar/radar applications. For example, in the real-data experiments, we employ the complex multivariate Laplace SIRV as the array observation likelihood. An improved particle filter implementation is proposed that employs an auxiliary step for persistent particles and an adaptive birth IS distribution, which accounts for the current observation. The performance of the TBD-CPHD filter is evaluated in relationship to classical array-processing methods and to state-of-the-art PHD tracking filters.

Perspectives

Potential axes of research can be classified in two distinct, nevertheless interconnected, directions: model and filter improvements.

As pointed out in Appendix H, the impulsive nature of the sonar signals is shown to vary, possibly with the incidence angle and/or distance between source and receiver. However, the lack of sufficient data hampers the proposal of an adaptive distribution, that is, a distribution that depends on the incidence angle. This could be achieved by acquiring more data in a controlled environment, e.g. homogeneous sea-floor and propagation conditions. Without changing the current filtering equations, the K-distribution could be employed with a shape parameter dependent on the incidence angle, and hence on the DOA of the source signal. This could lead to a "sharper" likelihood function and improve the precision of the DOA estimate. Such methods are reminiscent of *shape-from shading*, where a model of the amplitude of the reverberated signal as a function of the incident angle is employed. Both models for shape parameter and echo intensity can be employed in the proposed filter without requiring additional changes. Another model improvement could be achieved by considering different distributions for the source signals and noise. In the current joint-SIRV model, the texture is considered identical for the different sources and the noise. This arises mainly from the need to fit a distribution to the overall array observation and not having access to samples from individual source signals or noise. However, for independent non-Gaussian distributed source signals and noise, a general analytic formula for the resulting distribution is not known. The case where all signals are independent Complex Elliptically Symmetric (CES) variables and have the same dispersion matrix, leads after summation to a new CES distributed variable [35]. Unfortunately, for array processing, this is of no interest because distinct sources have distinct dispersion matrices while the spatially-white noise has a dispersion matrix proportional to the identity matrix. A more promising alternative comes from the family of α-stable distributions [36]. The stability property of α-stable distributions, requires that the source signals and noise are independent α-stable random variables with the same α parameter, in order for their sum to be α-stable.

The constraint of source signals and noise having the same α parameter amends to having the same "degree of impulsiveness", which is a less stringent condition than supposing a common texture. Indeed, the common texture of the joint-SIRV model implies that the different source signals and noise are mutually uncorrelated but dependent, while α-stable distributions suppose their independence. However, changing to α-stable distributions also requires changes in the filtering equations.

The second axis of research involves improving the filtering method itself. As pointed out for TBD-CPHD real-sonar data results, intensity filters are incapable of identifying tracks (or trajectories). Even the notion of trajectory is not defined in intensity filters. In general, the point-processes framework poses this problem since we only have measures that yield the mean number of targets in any region of space. The importance of such trajectory identifications are prevalent in the echo-tracking example of Fig. IV.8, where the TBD-CPHD filter correctly infers the DOAs of several echoes, even though several have no bathymetric relevance. In order to achieve the separation between bathymetrically relevant echoes and irrelevant ones, we need a clear separation and identification of trajectories and not just of filtered DOAs. Furthermore, with identified target trajectories, clustering would no longer be required, the latter representing a source of error in PHD filters. The newly proposed labeled RFS [33, 34] filters, seem to resolve this issue by labeling the different targets. The target labels are unique and can be employed to reconstruct the entire trajectory of a specific target. However, labeled RFS filters are not intensity filters, that is, filters propagating a first-order approximation, but resort to the propagation of a truncated version of the multi-target posterior density. Therefore, labeled RFS filters are in general more computationally demanding. Moreover, for bathymetric echo tracking, the labeled version of the standard multi-target processes (or RFS) seems promising.

Bibliography

[1] J. S. Helmick, "Port and maritime security: A research perspective," *Journal of Transportation Security*, vol. 1, no. 1, pp. 15–28, 2008.

[2] J. P. Vesky, Ed., *Port and Maritime Security*. New York: Nova Science Publishers, Inc., 2008.

[3] D. Zeng, A. Benilov, B. Bunin, and R. Martini, "Long-wavelength IR imaging system to scuba diver detection in three dimensions," *IEEE Sensors Journal*, vol. 10, no. 3, pp. 760–764, March 2010.

[4] R. Stolkin, L. Vickers, and J. Nickerson, "Using environmental models to optimize sensor placement," *IEEE Sensors Journal*, vol. 7, no. 3, pp. 319–320, March 2007.

[5] R. Kessel, T. Pastore, A. Crawford, and V. Crowe, "Commercial imaging sonars for observing underwater intruders," in *Proceedings of the 1st International Conference on Waterside security, WSS2008, Copenhagen, Denmark*, 2008.

[6] (2015, October) 4600 swath bathymetry and side-scan sonar brochure. [Online]. Available: http://measutronics.com/wp-content/uploads/2013/05/4600_brochure_033111.pdf

[7] B. Ferguson and R. Wyber, "Generalized framework for real aperture, synthetic aperture, and tomographic sonar imaging," *Oceanic Engineering, IEEE Journal of*, vol. 34, no. 3, pp. 225–238, July 2009.

[8] R. E. Hansen, H. J. Callow, T. O. Sæbø, and S. A. V. Synnes, "Challenges in seafloor imaging and mapping with synthetic aperture sonar," *IEEE Transactions on Geoscience and Remote Sensing*, vol. 49, no. 10, pp. 3677 – 3687, October 2011.

[9] P. Blondel, "Automatic mine detection by textural analysis of COTS sidescan sonar imagery," *International Journal of Remote Sensing*, vol. 21, no. 16, pp. 3115–3128, 2000.

[10] C. Sintes and G. Llort-Pujol, "Empirical interferometric phase variance formulas for bathymetric applications," *IEEE Transactions on Geoscience and Remote Sensing*, vol. 50, no. 2, pp. 2079–2097, June 2012.

[11] P. Blondel, *The Handbook of Sidescan Sonar*. Chichester, UK: Springer and Praxis, January 2009.

[12] V. Murino and A. Trucco, "Three-dimensional image generation and processing in underwater acoustic vision," *Proceedings of the IEEE*, vol. 88, no. 12, pp. 1903 – 1948, December 2000.

[13] S. K. Pearce and J. S. Bird, "Sharpening sidescan sonar images for shallow-water target and habitat classification with a vertically stacked array," *IEEE Journal of Oceanic Engineering*, vol. 38, no. 3, pp. 455 – 469, July 2013.

[14] A. E. A. Blomberg, A. Austeng, R. E. Hansen, and S. A. V. Synnes, "Improving sonar performance in shallow water using adaptive beamforming," *IEEE Journal of Oceanic Engineering*, vol. 38, no. 2, pp. 297–307, April 2013.

[15] T. E. Giddings and J. J. Shirron, "A model for sonar interrogation of complex bottom and surface targets in shallow-water waveguides," *Journal of the Acoustical Society of America*, vol. 123, no. 4, pp. 2024 –2034, April 2008.

[16] S. Valaee, B. Champagne, and P. Kabal, "Parametric localization of distributed sources," *IEEE Transactions on Signal Processing*, vol. 43, no. 9, pp. 2144–2153, Sep 1995.

[17] S. Shahbazpanah, S. Valaee, and A. Gershman, "A covariance fitting approach to parametric localization of multiple incoherently distributed sources," *IEEE Transactions on Signal Processing*, vol. 52, no. 3, pp. 592–600, March 2004.

[18] S. Shahbazpanah, S. Valaee, and M. H. Bastani, "Distributed source localization using ESPRIT algorithm," *IEEE Transactions on Signal Processing*, vol. 49, no. 10, pp. 2169–2178, Oct 2001.

[19] J. Abou Chaaya, J. Picheral, and S. Marcos, "Localization of spatially distributed near-field sources with unknown angular spread shape," *Signal Processing*, vol. 106, pp. 259–265, Jan. 2015.

[20] E. Ollila, D. Tyler, V. Koivunen, and H. Poor, "Complex elliptically symmetric distributions: Survey, new results and applications," *Signal Processing, IEEE Transactions on*, vol. 60, no. 11, pp. 5597–5625, Nov 2012.

[21] P. Tsakalides and C. Nikias, "The robust covariation-based MUSIC (ROC-MUSIC) algorithm for bearing estimation in impulsive noise environments," *IEEE Transactions on Signal Processing*, vol. 44, no. 7, pp. 1623–1633, Jul 1996.

[22] E. Ollila and V. Koivunen, "Influence function and asymptotic efficiency of scatter matrix based array processors: Case mvdr beamformer," *Signal Processing, IEEE Transactions on*, vol. 57, no. 1, pp. 247–259, Jan 2009.

[23] W.-J. Zeng, H. So, and L. Huang, "ℓ_p -MUSIC: Robust direction-of-arrival estimator for impulsive noise environments," *IEEE Transactions on Signal Processing*, vol. 61, no. 17, pp. 4296–4308, Sept 2013.

[24] R. Mahler, *Statistical Multisource-Multitarget Information Fusion.* Norwood, MA: Artech House, 2007.

[25] S. Blackman and R. Popoli, *Design and Analysis of Modern Tracking Systems.* Norwood, MA: Artech House, August 1999.

[26] Y. Bar-Shalom, F. Daum, and J. Huang, "The probabilistic data association filter," *IEEE Control Systems Magazine*, vol. 29, no. 6, pp. 82–100, December 2009.

[27] R. Mahler, "Multitarget Bayes filtering via first-order multitarget moments," *IEEE Transactions on Aerospace and Electronic Systems*, vol. 39, no. 4, pp. 1152 – 1178, October 2003.

[28] S. Nannuru, M. Coates, and R. Mahler, "Computationally-tractable approximate PHD and CPHD filters for superpositional sensors," *IEEE Journal of Selected Topics in Signal Processing*, vol. 7, no. 3, pp. 410 – 420, June 2013.

[29] J. Preston and D. Abraham, "Statistical analysis of multistatic echoes from a shipwreck in the malta plateau," *Oceanic Engineering, IEEE Journal of*, vol. 40, no. 3, pp. 643–656, July 2015.

[30] G. Le Chenadec, J.-M. Boucher, and X. Lurton, "Angular dependence of K-distributed sonar data," *Geoscience and Remote Sensing, IEEE Transactions on*, vol. 45, no. 5, pp. 1224–1235, May 2007.

[31] C. De and B. Chakraborty, "Model-based acoustic remote sensing of seafloor characteristics," *IEEE Transactions on Geoscience and Remote Sensing*, vol. 49, no. 10, pp. 3868–3877, Oct 2011.

[32] K. Landmark, A. Schistad Solberg, A. Austeng, and R. Hansen, "Bayesian seabed classification using angle-dependent backscatter data from multibeam echo sounders," *Oceanic Engineering, IEEE Journal of*, vol. 39, no. 4, pp. 724–739, Oct 2014.

[33] B.-T. Vo and B.-N. Vo, "Labeled random finite sets and multi-object conjugate priors," *IEEE Transactions on Signal Processing*, vol. 61, no. 13, pp. 3460–3475, July 2013.

[34] B.-N. Vo, B.-T. Vo, and D. Phung, "Labeled random finite sets and the Bayes multi-target tracking filter," *IEEE Transactions on Signal Processing*, vol. 62, no. 24, pp. 6554–6567, Dec 2014.

[35] G. Frahm, "Generalized elliptical distributions: Theory and applications," Ph.D. dissertation, Universität zu Köln, 2004.

[36] G. Samorodnitsky and M. S. Taqqu, *Stable non-Gaussian random processes : stochastic models with infinite variance*, ser. Stochastic modeling. New York: Chapman & Hall, 1994.

[37] K. Zwolak, "Underwater objects' detection system choice for harbor surveillance purposes," *Scientific Journal of the Polish Naval Academy*, no. 1, 2015.

[38] J.-R. Larocque, J. P. Reilly, and W. Ng, "Particle filters for tracking an unknown number of sources," *IEEE Transactions on Signal Processing*, vol. 50, no. 12, pp. 2926 – 2937, December 2002.

[39] G. Llort-Pujol, C. Sintes, T. Chonavel, A. Morrison, and S. Daniel, "Advanced interferometric techniques for high-resolution bathymetry," *Marine Technology Society Journal*, vol. 46, no. 2, pp. 9–31, April 2012.

[40] S. Haykin and K. Ray Liu, *Handbook on Array Processing and Sensor Networks*. Wiley-Blackwell, 2010.

[41] H. L. Van Trees, *Detection, Estimation, and Modulation Theory: Optimum Array Processing*. New York: John Wiley and Sons, 2002, vol. IV.

[42] N. Debese, R. Moitié, and N. Seube, "Multibeam echosounder data cleaning through a hierarchic adaptive and robust local surfacing," *Computers & Geosciences*, vol. 46, pp. 330–339, September 2012.

[43] B. Sharif and F. Kamalabadi, "Optimal sensor array configuration in remote image formation," *IEEE Transactions on Image Processing*, vol. 17, no. 2, pp. 155 – 166, February 2008.

[44] S. Affes, S. Gazor, and Y. Grenier, "An algorithm for multisource beamforming and multitarget tracking," *IEEE Transactions on Signal Processing*, vol. 44, no. 6, pp. 1512–1522, Jun 1996.

[45] S. Affes and Y. Grenier, "A signal subspace tracking algorithm for microphone array processing of speech," *IEEE Transactions on Speech and Audio Processing*, vol. 5, no. 5, pp. 425 – 437, September 1997.

[46] A. Masmoudi, F. Bellili, S. Affes, and A. Stéphenne, "A maximum likelihood time delay estimator in a multipath environment using importance sampling," *IEEE Transactions on Signal Processing*, vol. 61, no. 1, pp. 182 – 193, January 2013.

[47] P. Setlur, G. Alli, and L. Nuzzo, "Multipath exploitation in through-wall radar imaging via point spread functions," *IEEE Transactions on Image Processing*, vol. 22, no. 12, pp. 4571–4586, December 2013.

[48] G. E. Smith and B. G. Mobasseri, "Analysis and exploitation of multipath ghosts in radar target image classification," *IEEE Transactions on Image Processing*, vol. 23, no. 4, pp. 1581 – 1592, April 2014.

[49] A. Levy, S. Gannot, and E. Habets, "Multiple-hypothesis extended particle filter for acoustic source localization in reverberant environments," *Audio, Speech, and Language Processing, IEEE Transactions on*, vol. 19, no. 6, pp. 1540–1555, Aug 2011.

[50] A. Masnadi-Shirazi and B. Rao, "An ICA-SCT-PHD filter approach for tracking and separation of unknown time-varying number of sources," *Audio, Speech, and Language Processing, IEEE Transactions on*, vol. 21, no. 4, pp. 828–841, April 2013.

[51] J. V. Candy, "Bootstrap particle filtering," *IEEE Signal Processing Magazine*, vol. 73, July 2007.

[52] M. Wax and T. Kailath, "Detection of signals by information theoretic criteria," *IEEE Transactions on Acoustics, Speech and Signal Processing*, vol. 33, no. 2, pp. 387 – 392, April 1985.

[53] R. O. Schmidt, "Multiple emitter location and signal parameter estimation," *IEEE Transactions on Antennas and Propagation*, vol. 34, no. 3, pp. 276–280, March 1986.

[54] J. Capon, "High-resolution frequency-wavenumber spectrum analysis," *Proceedings of the IEEE*, vol. 57, no. 8, pp. 1408 – 1418, August 1969.

[55] S. Kay, *Modern Spectral Estimation: Theory and Application*. Prentice Hall, 1999.

[56] P. Stoica and R. L. Moses, *Spectral Analysis of Signals*. Prentice Hall, 2005.

[57] E. Fishler, M. Grosmann, and H. Messer, "Detection of signals by information theoretic criteria: General asymptotic performance analysis," *IEEE Transactions on Signal Processing*, vol. 50, no. 5, pp. 1027 – 1036, May 2002.

[58] B. Nadler, "Nonparametric detection of signals by information theoretic criteria: Performance analysis and an improved estimator," *IEEE Transactions on Signal Processing*, vol. 58, no. 5, pp. 2746 – 2756, May 2010.

[59] T. L. Song, D. Mušicki, and K. D. Sol, "Target tracking with target state dependent detection," *IEEE Transactions on Signal Processing*, vol. 59, no. 3, pp. 1063 – 1074, March 2011.

[60] R. Kalman, "A new approach to linear filtering and prediction problems," *Transactions of the ASME - Journal of Basic Engineering*, vol. 82, pp. 35–45, 1960.

[61] S. J. Julier and J. K. Uhlmann, "Unscented filtering and nonlinear estimation," *Proceedings of the IEEE*, vol. 92, no. 3, pp. 401–422, March 2004.

[62] ——, "Corrections to "Unscented Filtering and Nonlinear Estimation"," *Proceedings of the IEEE*, vol. 92, no. 12, p. 1958, December 2004.

[63] D. Mušicki, R. Evans, and S. Stankovic, "Integrated probabilistic data association," *IEEE Transactions on Automatic Control*, vol. 39, no. 6, pp. 1237 – 1241, June 1994.

[64] D. Mušicki, S. Challa, and S. Suvorova, "Automatic track initiation of manoeuvring target in clutter," *5th Asian Control Conference*, vol. 2, pp. 1009 – 1015, July 2004.

[65] D. Mušicki and S. Suvorova, "Tracking in clutter using IMM-IPDA-based algorithms," *IEEE Transactions on Aerospace and Electronic Systems*, vol. 44, no. 1, pp. 111–126, January 2008.

[66] B. Habtemariam, R. Tharmarasa, T. Thayaparan, M. Mallick, and T. Kirubarajan, "A multiple-detection joint probabilistic data association filter," *IEEE Journal of Selected Topics in Signal Processing*, vol. 7, no. 3, pp. 461 – 471, June 2013.

[67] Y. Bar-Shalom, Ed., *Multitarget-Multisensor Tracking: Advanced Applications*. Norwood, MA: Artech House, 1990.

[68] R. Urick, *Principles of Underwater Sound*. Los Altos, California: Peninsula Publishing, 1983.

[69] A. Moghaddamjoo and R. L. Kirlin, "Robust adaptive Kalman filtering with unknown inputs," *IEEE Transactions on Acoustics Speech and Signal Processing*, vol. 37, no. 8, pp. 1166 – 1175, August 1989.

[70] J. Candy, *Model-Based Signal Processing*. Hoboken, NJ: John Wiley and Sons / IEEE Press, 2006.

[71] ——, *Bayesian Signal Processing: Classical, Modern and Particle Filtering Methods*. Hoboken, NJ: John Wiley and Sons / IEEE Press, April 2009.

[72] C. H. Papadimitriou and K. Steiglitz, *Combinatorial Optimization: Algorithms and Complexity*. Englewood Cliffs, NJ: Prentice Hall, January 1998.

[73] Y. Bar-Shalom, K. Chang, and H. Blom, "Tracking a maneuvering target using input estimation versus the interacting multiple model algorithm," *IEEE Transactions on Aerospace and Electronic Systems*, vol. 25, no. 2, pp. 296–300, Mar 1989.

[74] Y. Bar-Shalom, X. Rong Li, and T. Kirubarajan, *Estimation with Applications to Tracking and Navigation: Algorithms and Software for Information Extraction.* Hoboken, NJ: John Wiley and Sons, July 2001.

[75] H. A. P. Blom and Y. Bar-Shalom, "The interacting multiple model algorithm for systems with Markovian switching coefficients." *IEEE Transactions on Automatical Control*, vol. 33, no. 8, pp. 780–783, August 1988.

[76] S. Jeong and J. K. Tugnait, "Multisensor tracking of a maneuvering target in clutter using IMMPDA filtering with simultaneous measurement update," *IEEE Transactions on Aerospace and Electronic Systems*, vol. 41, no. 3, pp. 1122 – 1131, July 2005.

[77] C. Hubert-Carol, N. Balakrishnan, M. S. Nikulin, and M. Mesbah, Eds., *Goodness-of-Fit Tests and Model Validity.* Boston: Birkhäuser, 2002.

[78] G. E. P. Box and D. A. Pierce, "Distribution of residual autocorrelations in autoregresive-integrated moving average time series models," *Journal of American Statistical Association*, vol. 65, no. 332, pp. 1509–1526, December 1970.

[79] G. M. Ljung and G. E. P. Box, "On a measure of lack of fit in time series models," *Biometrika*, vol. 65, no. 2, pp. 297–303, 1978.

[80] P. Stoica, "A test for whiteness," *IEEE Transactions on Automatic Control*, vol. 22, no. 6, pp. 992 – 993, December 1977.

[81] T. J. Cox and P. D'Antonio, *Acoustic Absorbers and Diffusers: Theory, Design and Application.* New York: Taylor and Francis, 2009.

[82] V. Pratt, "Direct least-squares fitting of algebraic surfaces," in *Proceedings of the 14th annual conference on Computer graphics and interactive techniques*, vol. 21, no. 4, July 1987, pp. 145–152.

[83] D. J. Murdoch, Y.-L. Tsai, and J. Adcock, "P-values are random variables," *The American Statistician*, vol. 62, no. 3, pp. 242–245, August 2008.

[84] D. Mušicki and R. Evans, "Joint integrated probabilistic data association: JIPDA," *IEEE Aerospace and Electronic Systems Magazine*, vol. 40, no. 3, pp. 1093 – 1099, July 2004.

[85] D. J. Daley and D. Vere-Jones, *An Introduction to the Theory of Point Processes.* New York: Springer-Verlag, 2003, vol. I.

[86] S. Nannuru, Y. Li, Y. Zeng, M. Coates, and B. Yang, "Radio-frequency tomography for passive indoor multitarget tracking," *IEEE Transactions on Mobile Computing*, vol. 12, no. 12, pp. 2322 – 2333, December 2013.

[87] B. Balakumar, A. Sinha, T. Kirubarajan, and J. P. Reilly, "PHD filtering for tracking an unknown number of sources using an array of sensors," in *Proceedings of the 13th IEEE Workshop on Statistical Signal Processing*, 2005.

[88] A.-A. Saucan, T. Chonavel, C. Sintes, and J.-M. Le Caillec, "Marked Poisson point process PHD filter for DOA tracking," in *Proceedings of the 23rd European Signal Processing Conference (EUSIPCO)*, Nice, France, Sept 2015.

[89] ——, "Track before detect DOA tracking of extended targets with marked Poisson point processes," in *Proceedings of the 18th International Conference on Information Fusion (Fusion 2015)*, Washington, USA, Jul. 2015.

[90] A.-A. Saucan, C. Sintes, T. Chonavel, and J.-M. Le Caillec, "Enhanced sonar bathymetry tracking in multi-path environment," in *Oceans*, Oct 2012, pp. 1–8.

[91] A. Saucan, T. Chonavel, C. Sintes, and J.-M. Le Caillec, "Interacting multiple model particle filters for side scan bathymetry," in *Proceedings of IEEE Oceans International Conference*, 2013.

[92] A.-A. Saucan, C. Sintes, T. Chonavel, and J.-M. Le Caillec, "Robust, track before detect particle filter for bathymetric sonar application," in *Proceedings of the 17th International Conference on Information Fusion (FUSION)*, 2014.

[93] J. Kingman, *Poisson Processes*. Oxford, UK: Clarendon Press, 1993.

[94] J. Møller and R. Waagepetersen, *Statistical Inference and Simulation for Spatial Point Processes*, ser. Chapman & Hall/CRC Monographs on Statistics & Applied Probability. CRC Press, 2004.

[95] O. E. Barndorff-Nielsen, W. S. Kendall, and M. N. M. Van Lieshout, Eds., *Stochastic geometry : likelihood and computation*, ser. Monographs on statistics and applied probability. Boca Raton, Fla. Chapman & Hall/CRC, 1999.

[96] R. L. Streit, *Poisson Point Processes*. New York: Springer-Verlag, 2010.

[97] B.-N. Vo, S. R. Sigh, and A. Doucet, "Sequential Monte Carlo methods for multi-target filtering with random finite sets," *IEEE Transactions on Aerospace and Electronic Systems*, vol. 41, no. 4, pp. 1224 – 1245, October 2005.

[98] B. N. Vo and W. K. Ma, "The Gaussian mixture probability hypothesis density filter," *IEEE Transactions on Signal Processing*, vol. 54, no. 11, pp. 4091–4104, November 2006.

[99] R. Mahler, "PHD filters of higher order in target number," *IEEE Transctions on Aerospace and Electronic Systems*, vol. 43, no. 4, pp. 1523 – 1543, October 2007.

[100] D. Schuhmacher, B.-T. Vo, and B.-N. Vo, "A consistent metric for performance evaluation of multi-object filters," *IEEE Transactions on Signal Processing*, vol. 56, no. 8, pp. 3447–3457, August 2008.

[101] B.-T. Vo, B.-N. Vo, and A. Cantoni, "The cardinality balanced multi-target multi-Bernuli filter and its implementations," *IEEE Transactions on Signal Processing*, vol. 57, no. 2, pp. 409 – 423, February 2009.

[102] W. Ma, B. Vo, S. Sigh, and A. Baddeley, "Tracking an unknown time-varying number of speakers using TDOA measurements: A random finite set approach," *IEEE Transactions on Signal Processing*, vol. 54, no. 9, pp. 3291 – 3304, September 2006.

[103] S. S. Singh, B.-N. Vo, A. Baddeley, and S. Zuyev, "Filters for spatial point processes," *SIAM Journal on Control and Optimization*, pp. 2275–2295, 2009.

[104] R. L. Streit and L. D. Stone, "Bayes derivation of multitarget intensity filters," in *Proceedings of the 11th International Conference on Information Fusion (FUSION)*, June 2008, pp. 1–8.

[105] T. Jebara, *Machine Learning : Discriminative and Generative*, ser. The Kluwer International series in Engineering and Computer Science. Dordrecht, Boston, Londres: Kluwer academic publishers, 2004.

[106] R. L. Streit, "Marked multitarget intensity filters," in *Proceedings of the 13th Conference on Information Fusion (FUSION)*, July 2010, pp. 1–7.

[107] S. Challa, B.-N. Vo, and X. Wang, "Bayesian approaches to track existence - IPDA and random sets," in *Proceedings of the 5th International Conference on Information Fusion (FUSION)*, vol. 2, July 2002, pp. 1228–1235 vol.2.

[108] A.-A. Saucan, T. Chonavel, C. Sintes, and J.-M. Le Caillec, "3-D bathymetric reconstruction in multi-path and reverberant underwater environments," in *Proceedings of the 21st International Conference on Image Processing (ICIP)*, 2014.

[109] A.-A. Saucan, C. Sintes, T. Chonavel, and J.-M. Le Caillec, "Model-based adaptive 3D sonar reconstruction in reverberating environments," *IEEE Transactions on Image Processing*, vol. 24, no. 10, pp. 2928–2940, Oct 2015.

[110] R. Georgescu and P. Willett, "The GM-CPHD tracker applied to real and realistic multistatic sonar data sets," *Oceanic Engineering, IEEE Journal of*, vol. 37, no. 2, pp. 220–235, April 2012.

[111] ——, "The multiple model CPHD tracker," *Signal Processing, IEEE Transactions on*, vol. 60, no. 4, pp. 1741–1751, April 2012.

[112] E. Maggio and A. Cavallaro, "Learning scene context for multiple object tracking," *Image Processing, IEEE Transactions on*, vol. 18, no. 8, pp. 1873–1884, Aug 2009.

[113] C. S. Lee, S. Nagappa, N. Palomeras, D. Clark, and J. Salvi, "SLAM with SC-PHD filters: An underwater vehicle application," *Robotics Automation Magazine, IEEE*, vol. 21, no. 2, pp. 38–45, June 2014.

[114] B.-N. Vo, B.-T. Vo, N.-T. Pham, and D. Suter, "Joint detection and estimation of multiple objects from image observations," *IEEE Transactions on Signal Processing*, vol. 58, no. 10, pp. 5129–5141, Oct 2010.

[115] P. B. Choppala, P. D. Teal, and M. Frean, "Adapting the Multi-Bernoulli filter to phased array observations using MUSIC as pseudo-likelihood," in *Preceedings of the 17th International Conference on Information Fusion (FUSION)*, 2014.

[116] R. Mahler and A. El-Fallah, "An approximate CPHD filter for superpositional sensors," in *Proceedings of SPIE International Conference*, 2012.

[117] E. Brookner, *Tracking and Kalman Filtering Made Easy.* New York: John Wiley and Sons, 1998.

[118] I. Goodman, R. Mahler, and H. Nguyen, *Mathematics of Data Fusion.* New York: Kluwer Academic Publishers, 1997.

[119] P. J. Rousseeuw, "Silhouettes: A graphical aid to the interpretation and validation of cluster analysis," *Journal of Computational and Applied Mathematics*, vol. 20, pp. 53 – 65, 1987.

[120] M. Ester, H. Kriegel, J. Sander, and X. Xu, "A density-based algorithm for discovering clusters in large spatial databases with noise," in *International Conference on Knowledge Discovery and Data Mining*, 1996.

[121] E. T. Jaynes, "Bayesian methods: General background," in *Maximum Entropy and Bayesian Methods in Applied Statistics: Proceedings of the Fourth Maximum Entropy Workshop University of Calgary*, 1986.

[122] R. Mahler, B. Vo, and B. Vo, "CPHD filtering with unknown clutter rate and detection profile," *IEEE Transactions on Signal Processing*, vol. 59, no. 8, pp. 3497 – 3513, August 2011.

[123] J. B. Billingsley, "Ground clutter measurements for surface-sited radar," Massachusetts Institute of Technology, Cambridge, MA, Tech. Rep., Feb. 1993.

[124] S. Watts, "Radar detection prediction in sea clutter using the compound K-distribution model," *IEE Proceedings on Communications, Radar and Signal Processing*, vol. 132, no. 7, pp. 613–620, December 1985.

[125] ——, "Modeling and simulation of coherent sea clutter," *IEEE Transactions on Aerospace and Electronic Systems*, vol. 48, no. 4, pp. 3303–3317, October 2012.

[126] J. Billingsley, A. Farina, F. Gini, M. Greco, and L. Verrazzani, "Statistical analyses of measured radar ground clutter data," *IEEE Transactions on Aerospace and Electronic Systems*, vol. 35, no. 2, pp. 579–593, Apr 1999.

[127] K. Sangston, F. Gini, and M. Greco, "Coherent radar target detection in heavy-tailed compound-Gaussian clutter," *IEEE Transactions on Aerospace and Electronic Systems*, vol. 48, no. 1, pp. 64–77, Jan 2012.

[128] G. G. Panayiotis and C. Kyriakakis, "Robust maximum likelihood source localization: The case for sub-Gaussian versus Gaussian," *IEEE Transactions on Audio, Speech and Language Processing*, vol. 14, no. 4, pp. 1470–1480, July 2006.

[129] D. A. Abraham and A. P. Lyons, "Editorial: Non-rayleigh reverberation and clutter," *IEEE Journal of Oceanic Engineering*, vol. 35, no. 2, pp. 147–151, April 2010.

[130] D. Abraham, "Detection-threshold approximation for non-gaussian backgrounds," *IEEE Journal of Oceanic Engineering*, vol. 35, no. 2, pp. 355–365, April 2010.

[131] N. Klausner and M. R. Azimi-Sadjadi, "Non-Gaussian target detection in sonar imagery using the multivariate Laplace distribution," *Oceanic Engineering, IEEE Journal of*, vol. 40, no. 2, pp. 452–464, April 2015.

[132] F. Pascal, P. Forster, J. Ovarlez, and P. Larzabal, "Performance analysis of covariance matrix estimates in impulsive noise," *Signal Processing, IEEE Transactions on*, vol. 56, no. 6, pp. 2206–2217, June 2008.

[133] P. Formont, F. Pascal, G. Vasile, J. Ovarlez, and L. Ferro-Famil, "Statistical classification for heterogeneous polarimetric SAR images," *Selected Topics in Signal Processing, IEEE Journal of*, vol. 5, no. 3, pp. 567–576, June 2011.

[134] M. Rupp and R. Frenzel, "Analysis of LMS and NLMS algorithms with delayed coefficient update under the presence of spherically invariant processes," *IEEE Transactions on Signal Processing*, vol. 42, no. 3, pp. 668–672, Mar 1994.

[135] K. Yao, "Spherically invariant random processes: Theory and applications," in *Communications, Information and Network Security*, ser. The Springer International Series in Engineering and Computer Science, V. Bhargava, H. Poor, V. Tarokh, and S. Yoon, Eds. Springer US, 2003, vol. 712, pp. 315–331.

[136] L. Belkacem, J. L. Vhel, and C. Walter, "CAPM, risk and portfolio selection in alpha-stable markets," *Fractals 8*, pp. 99 –115, 2000.

[137] A.-A. Saucan, T. Chonavel, C. Sintes, and J.-M. Le Caillec, "CPHD-DOA tracking of multiple extended sonar targets in implulsive noise environments," in *Accepted to IEEE Transactions on Signal Processing*, 2015.

[138] V. V. Ol'shevskii, *Characteristics of Sea Reverberation*. Springer US, 1967.

[139] W. Burdic, *Underwater Acoustic System Analysis*, ser. Prentice Hall Signal Processing Series. Pearson Education Canada, 1984.

[140] V. Seshadri, *The inverse Gaussian distribution: statistical theory and applications*, ser. Lecture notes in statistics. Oxford, NY: Springer, 1999.

[141] S. Foss, D. Korshunov, and S. Zachary, *An Introduction to Heavy-Tailed and Subexponential Distributions*. Springer-Verlag New York, 2013.

[142] Y. Kano, "Consistency property of elliptic probability density functions," *Journal of Multivariate Analysis*, vol. 51, no. 1, pp. 139 – 147, 1994.

[143] M. Rangaswamy, D. Weiner, and A. Ozturk, "Non-gaussian random vector identification using spherically invariant random processes," *IEEE Transactions on Aerospace and Electronic Systems*, vol. 29, no. 1, pp. 111–124, Jan 1993.

[144] K. Samuel, K. Tomasz, and P. Krzystof, *The Laplace Distribution and Generalizations*. Birkhäuser Boston, 2001.

[145] S. Gazor and W. Zhang, "Speech probability distribution," *Signal Processing Letters, IEEE*, vol. 10, no. 7, pp. 204–207, July 2003.

[146] ——, "Speech enhancement employing laplacian-gaussian mixture," *Speech and Audio Processing, IEEE Transactions on*, vol. 13, no. 5, pp. 896–904, Sept 2005.

[147] J. Portilla, V. Strela, M. Wainwright, and E. Simoncelli, "Image denoising using scale mixtures of gaussians in the wavelet domain," *Image Processing, IEEE Transactions on*, vol. 12, no. 11, pp. 1338–1351, Nov 2003.

[148] M. Abramowitz, *Handbook of Mathematical Functions, With Formulas, Graphs, and Mathematical Tables,*. New York: Dover Publications, Incorporated, 1974.

[149] G. N. Watson, *A Treatise on the Theory of Bessel Functions*. Cambridge, England: Cambridge University Press, 1944.

[150] K. Ward, "Compound representation of high resolution sea clutter," *Electronics Letters*, vol. 17, no. 16, pp. 561–563, August 1981.

[151] G. Panayiotis and C. Kyriakakis, "Maximum likelihood parameter estimation under impulsive conditions, a sub-gaussian signal approach," *Elsevier Signal Processing*, vol. 86, pp. 3061–3075, February 2006.

[152] Y. I. Abramovich, B. A. Johnson, and O. Besson, "Maximum likelihood and robust G-MUSIC performance in K-distributed noise," in *Proceedings of the 23rd European Signal Processing Conference (EUSIPCO)*, 2015.

[153] F. T. Ulaby and D. G. Long, *Microwave Radar and Radiometric Remote Sensing*. Ann Arbor, MI: The University of Michigan Press, 2014.

[154] P. Beckmann and A. Spizzichino, *The Scattering of Electromagnetic Waves from Rough Surfaces*. Norwood, MA.: Artech House, 1987.

[155] Y. Meng, P. Stoica, and K. Wong, "Estimation of the directions of arrival of spatially dispersed signals in array processing," *Radar, Sonar and Navigation, IEE Proceedings* -, vol. 143, no. 1, pp. 1–9, Feb 1996.

[156] R. Raich, J. Goldberg, and H. Messer, "Bearing estimation for a distributed source: modeling, inherent accuracy limitations and algorithms," *IEEE Transactions on Signal Processing*, vol. 48, no. 2, pp. 429–441, Feb 2000.

[157] A. Doucet, N. de Freitas, and N. Gordon, *Sequantial Monte Carlo Methods in Practice*. New York: Springer-Verlag, 2001.

[158] B. Ristic, D. Clark, B.-N. Vo, and B.-T. Vo, "Adaptive target birth intensity for PHD and CPHD filters," *IEEE Transactions on Aerospace and Electronic Systems*, vol. 48, no. 2, pp. 1656–1668, APRIL 2012.

[159] J. H. Yoon, D. Y. Kim, and K.-J. Yoon, "Efficient importance sampling function design for sequential Monte Carlo PHD filter," *Signal Processing*, vol. 92, no. 9, pp. 2315 – 2321, 2012.

[160] T. Li, S. Sun, and T. P. Sattar, "High-speed sigma-gating SMC-PHD filter," *Signal Processing*, vol. 93, no. 9, pp. 2586 – 2593, 2013.

[161] N. Whiteley, S. Sumeetpal, and S. Godsill, "Auxiliary particle implementation of probability hypothesis density filter," *IEEE Transactions on Aerospace and Electronic Systems*, vol. 46, no. 3, pp. 1437 – 1454, July 2010.

[162] B. Ristic, "Efficient update of persistent particles in the SMC-PHD filter," in *IEEE International Conference on Acoustics, Speech and Signal Processing (ICASSP)*, 2015.

[163] M. K. Pitt and N. Shephard, "Filtering via simulation: Auxiliary particle filters," *Journal of the American Statistical Association*, vol. 94, no. 446, pp. 590–599, 1999.

[164] A. Hassanien, S. Shahbazpanahi, and A. Gershman, "A generalized Capon estimator for localization of multiple spread sources," *Signal Processing, IEEE Transactions on*, vol. 52, no. 1, pp. 280–283, Jan 2004.

[165] I. Asimov, *Foundation's Edge*, ser. Foundation Novels. New York City, NY: Bantam Books, 1991.

[166] X. Rong Li and Ning Li, "Intelligent PDAF: Refinement of IPDAF for tracking in clutter," *Proceedings of the Twenty-Ninth Southeastern Symposium on System Theory*, pp. 133–137, March 1997.

[167] G. E. P. Box, G. M. Jenkins, and G. C. Reinsel, *Time Series Analysis Forcasting and Control*. Wiley, 2008.

[168] J. C. W. Rayner and D. J. Best, *Smooth Tests of Goodness of Fit*. Oxford Univercity press, 1989.

[169] T. R. C. Read and N. A. C. Cressie, *Goodness-of-Fit Statistics for Discrete Multivariate Data*. Springer-Verlag, 1988.

[170] X. R. Li and X. B. Li, "Common fallacies in applying hypothesis testing," in *Proc. Int. Conf. Inf. Fusion*, 2008, pp. 1085 –1092.

[171] A. Papoulis and S. Unnikrishna Pillai, *Probability, Random Variables and Stochastic Processes*. McGraw-Hill, 2002.

[172] M. G. Kendall and A. Stuart, *The Advanced Theory of Statistics*. Wiley, 1976, vol. III.

[173] K. Drouiche, "A new test for whiteness," *IEEE Transactions on Signal Processing*, vol. 48, no. 7, pp. 1864 – 1871, July 2000.

[174] B. Ristic, S. Arulampalam, and N. Gordon, *Beyond the Kalman Filter: Particle Filters for Tracking Applications*. Artech House, 2004.

[175] M. B. Wilkand and R. Gnanadesikan, "Probability plotting methods for the analysis of data," *Biometrika*, vol. 55, no. 1, pp. 1–17, 1968.

[176] D. Abraham and A. Lyons, "Reliable methods for estimating the K-distribution shape parameter," *IEEE Journal of Oceanic Engineering*, vol. 35, no. 2, pp. 288–302, April 2010.

[177] E. Coiras, Y. Petillot, and D. Lane, "Multiresolution 3-D reconstruction from side-scan sonar images," *IEEE Transactions on Image Processing*, vol. 16, no. 2, pp. 382–390, Feb 2007.

[178] A. Bors, E. Hancock, and R. Wilson, "Terrain analysis using radar shape-from-shading," *IEEE Transactions on Pattern Analysis and Machine Intelligence*, vol. 25, no. 8, pp. 974–992, Aug 2003.

[179] R. Zhang, P.-S. Tsai, J. Cryer, and M. Shah, "Shape-from-shading: a survey," *IEEE Transactions on Pattern Analysis and Machine Intelligence*, vol. 21, no. 8, pp. 690–706, Aug 1999.

[180] T. W. Anderson and D. A. Darling, "Asymptotic theory of certain goodness of fit criteria based on stochastic processes," *Annals of Mathematical Statistics*, vol. 23, pp. 193–212, 1952.

Appendix A

Integrated PDAF (IPDAF)

In this appendix, we derive of the trajectory (or track) existence probability of the IPDA [63] filter. The propagation equations: prediction and update for the track-existence probability are derived and presented in detail. As an interesting sidenote, it has been noted in [24, 27] that the PDAF coupled with the probability of track existence is reminiscent of the Probability Hypothesis Density filter (PHD) proposed by Mahler. In the PHD filter, the intensity function plays a double role: its peaks denote the presence of a target while the peak location represents a target position estimate. Thus, thresholding the intensity function in order to detect targets is reminiscent of thresholding the track-existence probability.

In the following, since we will only consider the trajectory existence probability of one target, we drop the index i, that was employed to denote the i-th target in Chapter II. Throughout this appendix, various probabilities are conditioned on the set of observations, denoted with $Z_{0:t}$ (or $Z_{0:t-1}$). However, to update the filter estimates we only employ the set of validated observations $\tilde{Z}_t \triangleq \{\tilde{\mathbf{z}}_t^1, \ldots, \tilde{\mathbf{z}}_t^{\tilde{m}_t}\}$. Note that $\tilde{Z} \subseteq Z$, while the observation validation process is described in Chapter II. We consider at time $t-1$ the following state-mean and covarince estimates: $\hat{\mathbf{x}}_{t-1|t-1}$ and $\mathbf{P}_{t-1|t-1}$; and of the probability of track existence $\nu_{t-1|t-1} \triangleq Pr\{\zeta_{t-1} = 1|Z_{1:t-1}\}$.

The *apriori* probability of track existence at time-step t is given by:

$$\begin{aligned} \nu_{t|t-1} &\triangleq Pr\{\nu_t = 1|Z_{1:t-1}\} = \pi_{11}\nu_{t-1|t-1} + \pi_{01}(1 - \nu_{t-1|t-1}), \\ 1 - \nu_{t|t-1} &\triangleq Pr\{\nu_t = 0|Z_{1:t-1}\} = \pi_{10}\nu_{t-1|t-1} + \pi_{00}(1 - \nu_{t-1|t-1}). \end{aligned} \tag{A.1}$$

The hidden Markov chain ζ_t models the existence of the target of interest, thus the event $\zeta_t = 0$ implies that the target is not present, while the event $\zeta_t = 1$ implies the contrary. Since the pre-processor detects targets with a non-unity probability p_D, the presence of the target doesn't necessarily imply a detection. In such, a different process, denoted ξ_t, needs to be introduced. $\xi_t = 0$ denotes that no target-originated observation is present in the validated set (although clutter might be present). $\xi_t = i$ denotes that the i-th observation of the $\tilde{m}_t$ validated observations was generated by the target. Events $\zeta_t = 0$ and $\xi_t = 0$ are distinct, since a target observation is obtained with probability $p_D p_W$, corresponding to the processes of detection and validation (supposed independent). The event $\zeta_t = 0$ necessarily implies $\xi_t = 0$ (i.e. when the target is not present, there are no target-originated measurements), while the contrary is not necessarily true. Supposing the processes of target detection and observation validation as independent, we can write

$$\begin{aligned} Pr\{\xi_t = 0, \zeta_t = 1|Z_{1:t-1}\} &= Pr\{\xi_t = 0|Z_{1:t-1}, \zeta_t = 1\}Pr\{\zeta_t = 1|Z_{1:t-1}\}, \\ &= Pr\{\xi_t = 0|\zeta_t = 1\}Pr\{\zeta_t = 1|Z_{1:t-1}\}, \\ &= \Big((1 - p_D) + p_D(1 - p_W)\Big)\,\nu_{t|t-1}, \\ &= (1 - p_D\,p_W)\,\nu_{t|t-1}. \end{aligned} \tag{A.2}$$

Whenever the validated-observation set is non-empty, i.e. $Z_t \neq \emptyset$, and considering that all observations are equally likely of originating from the target of interest, we can write the *apriori*

probability that the i-th observation originates from the target

$$Pr\{\xi_t = i|\zeta_t = 1, \tilde{m}_t, Z_{1:t-1}\} = \frac{p_D\, p_W}{\tilde{m}_t} \qquad \forall i = 1, \cdots, \tilde{m}_t. \tag{A.3}$$

Marginalizing in relationship with the $\zeta_t = 1$ process, we can write

$$\begin{aligned} Pr\{\xi_t = 0|Z_{1:t-1}\} &= \overbrace{Pr\{\xi_t = 0, \zeta_t = 1|Z_{1:t-1}\}}^{\text{track exists but no measurement from track}} + \overbrace{Pr\{\zeta_t = 0|Z_{1:t-1}\}}^{\text{track does not exist}}, \\ &= (1 - p_D\, p_W) Pr\{\zeta_t = 1|Z_{1:t-1}\} + 1 - Pr\{\zeta_t = 1|Z_{1:t-1}\}, \\ &= 1 - p_D\, p_W \nu_{t|t-1}. \end{aligned} \tag{A.4}$$

Taking into account the current validated set of measurements Z_t, we can express the updated probability of track existence:

$$\begin{aligned} Pr\{\zeta_t = 1|Z_{1:t}\} &= \overbrace{Pr\{\xi_t = 0, \zeta_t = 1|Z_{1:t}\}}^{\text{track exists but no measurement from track}} + \sum_{i=1}^{\tilde{m}_t} \overbrace{Pr\{\zeta_t = 1, \xi_t = i|Z_{1:t}\}}^{\text{track exists and measurement } i \text{ is target originated}}, \\ &= Pr\{\xi_t = 0|Z_{1:t}\} - Pr\{\zeta_t = 0|Z_{1:t}\} + \sum_{i=1}^{\tilde{m}_t} Pr\{\xi_t = i|Z_{1:t}\}. \end{aligned} \tag{A.5}$$

From Eq. (A.5), but also according to the formula of total probability, we can write

$$Pr\{\xi_t = 0|Z_{1:t}\} + \sum_{i=1}^{\tilde{m}_t} Pr\{\xi_t = i|Z_{1:t}\} = Pr\{\zeta_t = 1|Z_{1:t}\} + Pr\{\zeta_t = 0|Z_{1:t}\} = 1. \tag{A.6}$$

The computation of $Pr\{\xi_t = 0|Z_{1:t}\}$ reads:

$$\begin{aligned} Pr\{\xi_t = 0|Z_{1:t}\} &= Pr\{\xi_t = 0|Z_t, \tilde{m}_t, Z_{1,t-1}\}, \\ &= \frac{p(\{\tilde{\mathbf{z}}_t^1, \ldots, \tilde{\mathbf{z}}_t^{\tilde{m}_t}\}|\xi_t = 0, \tilde{m}_t, Z_{1,t-1}) Pr\{\tilde{m}_t|\xi_t = 0, Z_{1,t-1}\} Pr\{\xi_t = 0|Z_{1,t-1}\}}{Pr\{\widetilde{Z}_t, \tilde{m}_t|Z_{1,t-1}\}}. \end{aligned} \tag{A.7}$$

Although the above probability is conditioned on $Z_{0:t}$, we only consider the gated/validated observations $\widetilde{Z}_t \triangleq \{\tilde{\mathbf{z}}_t^1, \ldots, \tilde{\mathbf{z}}_t^{\tilde{m}_t}\}$ for update. False observations, generated by clutter, are considered uniformly distributed in the validation gate area, hence:

$$p(\{\tilde{\mathbf{z}}_t^1, \ldots, \tilde{\mathbf{z}}_t^{\tilde{m}_t}\}|\xi_t = 0, \tilde{m}_t, Z_{1,t-1}) = \prod_{i=1}^{\tilde{m}_t} \frac{1}{\mathcal{V}_t}. \tag{A.8}$$

Furthermore, the number of false measurements K is distributed according to a Poisson density of parameter λ:

$$p_K(k) = e^{-\lambda \mathcal{V}_t} \frac{(-\lambda \mathcal{V}_t)^k}{k!}. \tag{A.9}$$

When λ is known apriori, the filter is referred to as a parametric filter and respectively non-parametric when λ is estimated. Several estimation schemes exist for λ, the simplest of which is $\hat{\lambda} = \tilde{m}_t / \mathcal{V}_t$. In [63], the alternative (but still heuristic) estimator is proposed:

$$\hat{\lambda} = \frac{\hat{m}_t}{\mathcal{V}_t} \qquad \text{where} \qquad \hat{m}_t = \begin{cases} 0 & \text{if } \tilde{m}_t = 0 \\ \tilde{m}_t - p_D\, p_W \nu_{t|t-1} & \text{if } \tilde{m}_t > 0. \end{cases} \tag{A.10}$$

A recursive estimator for λ was proposed in [166], that is $\hat{\lambda}_{t|t} = p(\lambda_t|Z_{1:t})$ is predicted and updated with each newly-available set of validated measurements $\widetilde{Z}_t$. The number of false observations inside the validation gate is $\tilde{m}_k$ in the case of $\xi_t = 0$ and $\tilde{m}_t - 1$ when $\xi_t = 1$.

If we denote $c_t^{-1} = Pr\{\widetilde{Z}_t, \tilde{m}_t | Z_{1,t-1}\}$, and gathering the results of Eqs. (A.8), (A.9) and (A.4) in Eq. (A.7), then we obtain

$$\begin{aligned} Pr\{\xi_t = 0 | Z_{1:t}\} &= c_t^{-1} \prod_{i=1}^{\tilde{m}_t} \mathcal{V}_t^{-1} e^{-\hat{m}_t} \frac{(\hat{m}_t)^{\tilde{m}_t}}{\tilde{m}_t!} (1 - p_D\, p_W \nu_{t|t-1}), \\ &= C_t^{-1} \mathcal{V}_t^{-1} \hat{m}_t (1 - p_D\, p_W \nu_{t|t-1}), \end{aligned} \tag{A.11}$$

where $C_t^{-1} = c_t^{-1} \mathcal{V}_t^{\tilde{m}_t - 1} e^{-\hat{m}_t} \frac{(\hat{m}_t)^{\tilde{m}_t - 1}}{\tilde{m}_t!}$.

In a similar fashion, we can derive:

$$Pr\{\zeta_t = 1, \xi_t = 0 | Z_{1:t}\} = C_t^{-1} \mathcal{V}_t^{-1} \hat{m}_t (1 - p_D\, p_W) \nu_{t|t-1}. \tag{A.12}$$

The derivation of $Pr\{\zeta_t = 1, \xi_t = i | Z_{1:t}\}$ follows:

$$\begin{aligned} Pr\{\zeta_t = 1, \xi_t = i | Z_{1:t}\} &= Pr\{\zeta_t = 1, \xi_t = i | \widetilde{Z}_t, \tilde{m}_t, Z_{1,t-1}) \\ &= p(\widetilde{Z}_t | \zeta_t = 1, \xi_t = i, \tilde{m}_t, Z_{1,t-1}) Pr\{\tilde{m}_t | \zeta_t = 1, \xi_t = i, Z_{1,t-1}\} \\ &\quad \times Pr\{\xi_t = i | \zeta_t = 1, Z_{1,t-1}\} Pr\{\zeta_t = 1 | Z_{1:t-1}\} \left[Pr\{Z_t, \tilde{m}_t | Z_{1,t-1}\}\right]^{-1} \\ &= c_t^{-1} p(\tilde{\mathbf{z}}_t^i | \xi_t = i, Z_{1:t-1}) \prod_{\substack{j=1 \\ j \neq i}}^{\tilde{m}_t} \mathcal{V}_t^{-1} e^{-\hat{m}_t} \frac{(\hat{m}_t)^{\tilde{m}_t - 1}}{(\tilde{m}_t - 1)!} \frac{p_D\, p_W}{\tilde{m}_t} \nu_{t|t-1} \\ &= C_t^{-1} p(\tilde{\mathbf{z}}_t^i | \xi_t = i, Z_{1:t-1}) p_D\, p_W \nu_{t|t-1}. \end{aligned} \tag{A.13}$$

Replacing Eqs. (A.11) and (A.13) in Eq. (A.6), we obtain an expression for C_t^{-1}:

$$C_t = \mathcal{V}_t^{-1} \hat{m}_t (1 - p_D\, p_W \nu_{t|t-1}) + p_D\, p_W \sum_{i=1}^{\tilde{m}_t} p(\tilde{\mathbf{z}}_t^i | \xi_t = i, Z_{1:t-1}) \nu_{t|t-1}, \tag{A.14}$$

where $p(\tilde{\mathbf{z}}_t^i | \xi_t = i, Z_{1:t-1})$ has first and second order moments $\mathbf{H}_t \hat{\mathbf{x}}_{t|t-1}$ and $\mathbf{P}_{t|t-1}$. In practice, we suppose a Gaussian pdf $p(\tilde{\mathbf{z}}_t^i | \xi_t = i, Z_{1:t-1}) = \mathcal{N}(\tilde{\mathbf{z}}; \mathbf{H}_t \hat{\mathbf{x}}_{t|t-1}, \mathbf{P}_{t|t-1})$.

The final form of the filtering equations and the track existence probability will be given considering two distinct cases:

- $\tilde{m}_t = 0$

  The updated track existence probability is given by:

$$\begin{aligned} \nu_{t|t} = Pr\{\zeta_t = 1 | Z_{1:t}\} &= Pr\{\zeta_t = 1 | \overbrace{\widetilde{Z}_t}^{\emptyset}, Z_{1:t-1}\} \\ &= Pr\{\zeta_t = 1 | \xi_t = 0, Z_{1:t-1}\} \\ &= \frac{Pr\{\zeta_t = 1, \xi_t = 0 | Z_{1:t-1}\}}{Pr\{\xi_t = 0 | Z_{1:t-1}\}} \\ &= \frac{1 - p_D\, p_W}{1 - p_D\, p_W \nu_{t|t-1}} \nu_{t|t-1}. \end{aligned} \tag{A.15}$$

  In the last line of Eq. (A.15), we used Eqs. (A.2) and (A.4), also observe that $Pr\{\zeta_t = 1 | Z_{1:t}\}$ does not depend on $\widetilde{Z}_t = \emptyset$. In the following, we compare the updated $\nu_{t|t}$ against $\nu_{t|t-1}$:

$$\begin{aligned} \nu_{t|t} < \nu_{t|t-1} &\iff \frac{(1 - p_D\, p_W) \nu_{t|t-1}}{1 - p_D\, p_W \nu_{t|t-1}} < \nu_{t|t-1} \\ &\iff \nu_{t|t-1} < 1, \end{aligned} \tag{A.16}$$

which is verified, since $\nu_{t|t-1}$ is a probability. This verifies that when $\tilde{m}_t = 0$, the track existence probability decreases. Regarding the state-mean and covariance estimates, we opt to perform only prediction in this case, until the track is deleted or a new observation appears.

$$\hat{\mathbf{x}}_{t|t} = \hat{\mathbf{x}}_{t|t-1}$$
$$\mathbf{P}_{t|t} = \mathbf{P}_{t|t-1}.$$

- $\tilde{m}_t > 0$

  Concerning the updated track existence probability, replacing Eq. (A.12) and Eq. (A.13) in Eq. (A.5), we can write:

$$\begin{aligned}
\nu_{t|t} &= Pr\{\zeta_t = 1, \xi_t = 0 | Z_{1:t}\} + \sum_{i=1}^{\tilde{m}_t} Pr\{\zeta_t = 1, \xi_t = i | Z_{1:t}\} \\
&= C_t^{-1} \mathcal{V}_t^{-1} \hat{m}_t (1 - p_D\, p_W) \nu_{t|t-1} + \sum_{i=1}^{\tilde{m}_t} C_t^{-1} p(\tilde{\mathbf{z}}_t^i | \xi_t = i, Z_{1:t-1}) p_D\, p_W \nu_{t|t-1} \\
&= \frac{1 - p_D\, p_W + \frac{\mathcal{V}_t}{\hat{m}_t} \sum_{i=1}^{\tilde{m}_t} p_D\, p_W p(\tilde{\mathbf{z}}_t^i | \xi_t = i, Z_{1:t-1})}{1 - \left[p_D\, p_W - \frac{\mathcal{V}_t}{\hat{m}_t} \sum_{i=1}^{\tilde{m}_t} p_D\, p_W p(\tilde{\mathbf{z}}_t^i | \xi_t = i, Z_{1:t-1}) \right] \nu_{t|t-1}} \nu_{t|t-1} \\
&= \frac{1 - \delta_t}{1 - \delta_t \nu_{t|t-1}} \nu_{t|t-1}, \qquad \text{(A.17)}
\end{aligned}$$

  where $\delta_t \triangleq p_D\, p_W - \frac{\mathcal{V}_t}{\hat{m}_t} \sum_{i=1}^{\tilde{m}_t} p_D\, p_W p(\tilde{\mathbf{z}}_t^i | \xi_t = i, Z_{1:t-1})$ and the individual observation likelihood is supposed Gaussian $p(\tilde{\mathbf{z}}_t^i | \xi_t = i, Z_{1:t-1}) = \mathcal{N}(\tilde{\mathbf{z}}; \mathbf{H}_t \hat{\mathbf{x}}_{t|t-1}, \mathbf{P}_{t|t-1})$.

The individual association probabilities are given by the classical PDA filter [26], and using the δ_t notation we have:

$$\beta_t^i = \begin{cases} \dfrac{p_D\, p_W \frac{\mathcal{V}_t}{\hat{m}_t} p(\tilde{\mathbf{z}}_t^i | \xi_t = i, Z_{1:t-1})}{1 - \delta_t} & \text{if } i = 1, \cdots, \tilde{m}_t \\ \dfrac{1 - p_D\, p_W}{1 - \delta_t} & \text{if } i = 0. \end{cases} \qquad \text{(A.18)}$$

The state-mean update follows:

$$\hat{\mathbf{x}}_{t|t} = \hat{\mathbf{x}}_{t|t-1} + \mathbf{K}_t\, \boldsymbol{\epsilon}_t. \qquad \text{(A.19)}$$

$$\text{where} \qquad \boldsymbol{\epsilon}_t \triangleq \sum_{i=1}^{\tilde{m}_t} \beta_t^i \boldsymbol{\epsilon}_t^i.$$

$$\boldsymbol{\epsilon}_t^i \triangleq \tilde{\mathbf{z}}_t^i - \mathbf{H}_t \hat{\mathbf{x}}_{t|t-1}, \qquad \text{(A.20)}$$

$\boldsymbol{\epsilon}_t$ represents the total innovation of the filter while $\boldsymbol{\epsilon}_t^i$ represents the individual association innovation, and $\mathbf{K}_t$ is the Kalman filter gain of Eq. (II.10).

The covariance is updated as follows:

$$\begin{aligned}
\mathbf{P}_{t|t} &= \mathbf{P}_{t|t-1} - (1 - \beta_t^0) \mathbf{K}_t \mathbf{S}_{t|t-1} \mathbf{K}_t^T + \check{\mathbf{P}}_t, \qquad \text{(A.21)} \\
\text{where} \qquad \check{\mathbf{P}}_t &\triangleq \mathbf{K}_t \left[\sum_{i=1}^{\tilde{m}_t} \beta_t^i \boldsymbol{\epsilon}_t^i (\boldsymbol{\epsilon}_t^i)^T - \boldsymbol{\epsilon}_t \boldsymbol{\epsilon}_t^T \right] \mathbf{K}_t^T.
\end{aligned}$$

The term $\check{\mathbf{P}}_t$ represents the spread of means in the approximation of a Gaussian mixture with a single Gaussian pdf [74, Ch.1]. Observe the differences between Eq. (A.21) and the

classical Kalman filter covariance update equation. The no-observation association probability β_t^0 weights the update term in $\mathbf{P}_{t|t}$. If observations are not present inside the validation gate, then β_t^0 is close to unitary and $\mathbf{P}_{t|t}$ is not decreased (via the update step). However, when measurements are present, β_t^0 will decrease, which brings about the decrease of $\mathbf{P}_{t|t}$, indicating an increased confidence in the filtered state. Whenever measurements are present, $\check{\mathbf{P}}_t$ quantifies the origin uncertainty of measurements. Situations with a large number of observations that fall "far" from their predicted values, lead to an increase of uncertainty, that is, an increase of $\check{\mathbf{P}}_t$, and eventually of $\mathbf{P}_{t|t}$. Indeed, the presence of observations alone is not enough to guarantee a decrease in the uncertainty of the system, and the positioning of observations in relationship to the model predictions also dictates the increase/decrease of uncertainty.

Appendix B

Observation noise covariance estimation

In [69] and the references herein, robust Kalman filters are proposed that estimate the covariance matrices of the observation and model-noise terms. Here, we propose the estimation of the observation-noise covariance in the case of the NN-IPDA-UKF. For clarity, the superscripts i are dropped in this appendix. Consider the observation-noise covariance $\mathbf{R}_t$ to evolve slowly. In such, $\mathbf{R}_t$ is considered nearly constant for a duration T, in order to have $\mathbf{R}_t = \mathbf{R}_{t-\tau}$, with $\tau \in \{1, \cdots, T\}$. We compute $\hat{\mathbf{R}}_t$ using a "batch" limited-memory estimator given by the following theorem.

Proposition. *Given the innovation term $\boldsymbol{\epsilon}_t$, formed after the PDA phase in eq. (A.19), a batch estimator for $\mathbf{R}_t$ using the method of moments is*

$$\hat{\mathbf{R}}_t = \frac{1}{T-1} \sum_{\tau=t-T+1}^{t} \{(\boldsymbol{\epsilon}_\tau - \bar{\boldsymbol{\epsilon}}_t)(\boldsymbol{\epsilon}_\tau - \bar{\boldsymbol{\epsilon}}_t)^T - \frac{T-1}{T} \mathbf{H}_\tau \mathbf{P}_{\tau|\tau-1} \mathbf{H}_\tau^T\}, \tag{B.1}$$

where $\bar{\boldsymbol{\epsilon}}_t = \frac{1}{T} \sum_{\tau=t-T+1}^{t} \boldsymbol{\epsilon}_\tau$ is the unbiased sample-mean estimator.

Proof. The prof of the aforementioned proposition requests that the series $\boldsymbol{\epsilon}_t$ forms a zero mean white time-series. Indeed, whenever the observation series $\mathbf{z}_t$ is generated by the system of Eqs. (II.5a) and (II.5b), the residual series $\boldsymbol{\epsilon}_t$ is white and zero mean. In other words, the proposed model for the system matches the real model used to generate $\mathbf{z}_t$. Note that the validation of the aforementioned assertion forms the topic of appendix C.

Given the series $\boldsymbol{\epsilon}_\tau$ with $\tau \in \{t-T+1, \cdots, t\}$, the unbiased sample covariance estimator, denoted $\bar{\mathbf{C}}$, is given by

$$\bar{\mathbf{C}}_t = \frac{1}{T-1} \sum_{\tau=t-T+1}^{t} (\boldsymbol{\epsilon}_\tau - \bar{\boldsymbol{\epsilon}}_t)(\boldsymbol{\epsilon}_\tau - \bar{\boldsymbol{\epsilon}}_t)^T. \tag{B.2}$$

Considering the model for the observation in Eq. (II.5b), the expectation of $\bar{\mathbf{C}}_t$ gives:

$$\begin{aligned}
\mathbb{E}\{\bar{\mathbf{C}}_t\} &= \frac{1}{T-1} \mathbb{E}\left\{ \sum_{\tau=t-T+1}^{t} \boldsymbol{\epsilon}_\tau \boldsymbol{\epsilon}_\tau^T - T \bar{\boldsymbol{\epsilon}}_t \bar{\boldsymbol{\epsilon}}_t^T \right\} \\
&= \frac{1}{T-1} \mathbb{E}\left\{ \frac{T-1}{T} \sum_{\tau=t-T+1}^{t} \boldsymbol{\epsilon}_\tau \boldsymbol{\epsilon}_\tau^T - \frac{1}{T} \sum_{\tau=t-T+1}^{t} \sum_{\substack{\tau'=t-T+1 \\ \tau' \neq \tau}}^{t} \boldsymbol{\epsilon}_\tau \boldsymbol{\epsilon}_{\tau'}^T \right\} \\
&= \frac{1}{T} \sum_{\tau=t-T+1}^{t} \left(\mathbf{H}_\tau \mathbb{E}\{(\mathbf{x}_\tau - \hat{\mathbf{x}}_{\tau|\tau-1})(\mathbf{x}_\tau - \hat{\mathbf{x}}_{\tau|\tau-1})^T\} \mathbf{H}_\tau^T + \mathbb{E}\{\mathbf{w}_\tau \, \mathbf{w}_\tau^T\} \right) \\
&= \frac{1}{T} \sum_{\tau=t-T+1}^{t} \mathbf{H}_\tau \mathbf{P}_{\tau|\tau-1} \mathbf{H}_\tau^T + \mathbf{R}_t,
\end{aligned} \tag{B.3}$$

where we employed the definition of $\boldsymbol{\epsilon}_t = \mathbf{z}_t - \mathbf{H}_t\hat{\mathbf{x}}_{t|t-1}$ of Eq. (A.19) and $\mathbf{P}_{t|t-1}$ represents the predicted covariance of the state. From Eq. (B.3) we obtain the estimated noise covariance $\hat{\mathbf{R}}_t$ of Eq. (B.1). Note that whenever the observation noise $\mathbf{w}_t$ is not zero mean, Eq. (B.1) still applies, with $\bar{\boldsymbol{\epsilon}}_t$ providing an estimate for the mean of $\mathbf{w}_t$.

■

Observe that $\hat{\mathbf{R}}_t$ of Eq. (B.1) is not guaranteed to be positive definite. Such situations arise for a small amplitude $\mathbf{w}_t$ and due to the fluctuation of sample estimators. A simple solution is to use a small fixed value for $\hat{\mathbf{R}}_t$ whenever such situations arise.

Appendix C

Model validation

For model-based processors, model validation amounts to assessing the adequacy of the model for the respective physical phenomenon [167]. Model validation is also known as Goodness of Fit (GoF), and benefits from an extensive literature [77, 168, 169]. As noted in [170], GoF tests are useful when deciding which models are not adequate for a specific time series rather then searching for the most adequate model. In other words, model inadequacy is signaled by a failed GoF test, but a validated GoF does not rule out the existence of an even better model (i.e. that provides an even better fit to the time series). Generally, the whiteness of the fitting residuals (or filtering residuals, e.g. Kalman filter), is indicative of the capacity of the model to fit the respective time series. Intuitively, residual whiteness indicates that all the information contained in the time series is well described by the model, and only a white-noise term remains within the residuals. Several whiteness test have been proposed, almost all of which suppose the computation of the autocorrelation function of residuals. GoF tests are hypothesis tests, meaning that they test the null hypothesis H_0 of the whiteness of residuals against the alternative hypothesis H_1, that supposes the residuals sequence as correlated. Several statistical tests were derived for univariate residual sequences, namely in [78, 79].

Denoting the univariate (scalar) residual time series by ϵ_t, its estimated auto-correlation function ρ_k is usually computed with the biased sample auto-correlation estimator:

$$\rho_k = \frac{1}{T} \sum_{t=1}^{T-|k|} \epsilon_t \epsilon_{t+|k|} \quad \text{with} \quad k \in \{0, \pm 1, \pm 2, \cdots, \pm(T-1)\}, \tag{C.1}$$

where T represents the length of the residual time series. For large T and under H_0, the random variable ρ_k is asymptotically Gaussian distributed in virtue of the central-limit theorem [171].

One of the first model-validation tests, called the Box-Pierce Portmanteau test [78], has benefited from an extensive study [78, 167, 172]. Box and Pierce proposed the following test statistic

$$Q_{T,K}^{\text{BP}} = T \sum_{k=1}^{K} \left(\frac{\rho_k}{\rho_0} \right)^2. \tag{C.2}$$

A subsequent test statistic was later proposed by Ljung and Box in [79] as

$$Q_{T,K}^{\text{LB}} = T(T+2) \sum_{k=1}^{K} \frac{1}{K-k} \left(\frac{\rho_k}{\rho_0} \right)^2, \tag{C.3}$$

and is usually referred to as the Ljung-Box Portemanteau test.

From hereon, since the hypothesis-testing procedure is identical for both tests, the two statistics $Q_{T,K}^{\text{BP}}$ and $Q_{T,K}^{\text{LB}}$ will be denoted generically with $Q_{T,K}$. Since ρ_k is asymptotically Gaussian distributed, the random variable $Q_{T,K}$ obeys asymptotically a χ^2_{K-p} distribution with $K-p$ degrees of freedom, where p is the model order. The value of K should not be grater than $T/4$, in order to avoid autocorrelation terms computed with relatively few elements. Henceforth, testing for whiteness is reduced to a χ^2 test [77, Ch.2] of the test statistic $Q_{T,K}$. This is conducted

by performing a one-tailed significance test on $Q_{T,K}$, "to see with what degree of certitude we can say that $Q_{T,K}$ was sampled from χ^2_{K-p}". The level of significance of the test α and the associated critical threshold c are defined as

$$\alpha \triangleq Pr\{Q_{T,K} > c|H_0\} \quad \text{or equivalently} \quad c = F^{-1}_{\chi^2}(1-\alpha), \tag{C.4}$$

where $F_{\chi^2}(\cdot)$ represents the distribution of $Q_{T,K}$, i.e. of a χ^2 distributed random variable with $K-p$ degrees of freedom. α is also called *Type I error* or the false-positive rate. In a test, the value of α is imposed and is usually taken to be 0.1 or 0.05. With the given α and the residual series, we are able to compute c from Eq. (C.4) and take the decision:

- If $Q_{N,K} > c$ then it is said that there is evidence within the time series ϵ_t to reject H_0. In other words the series is correlated.
- If $Q_{N,K} \leq c$ then it is said that there is not (enough) evidence within the time series ϵ_t to reject H_0. In other words, there is no reason not to accept H_0.

An equivalent decision scheme is defined using the p-value, defined as

$$p\text{-value} \triangleq Pr\{Q > Q_{T,K}\} \quad \text{where} \quad q \sim \chi^2_{K-p}, \tag{C.5}$$

where $Q_{T,K}$ is the value obtained with Eqs. (C.2) or (C.3) and Q is a χ^2 distributed random variable with $K-p$ degrees of freedom. The p-value is the probability of obtaining a test statistic at least as extreme as the one that was actually observed, assuming that the null hypothesis is true. The p-value does not correspond to the probability that H_0 is true, given the data actually observed. The test now becomes:

- If p-value $< \alpha$ then it is said that there is evidence within the time series ϵ_t to reject H_0. In other words the series is correlated.
- If p-value $\geq \alpha$ then it is said that there is no evidence within the time series ϵ_t to reject H_0. In other words, there is no reason to reject H_0.

Ljung and Box argue that, even though the statistic $Q^{\text{LB}}_{T,K}$ has a larger variance, its lack of bias ensures that $Q^{\text{LB}}_{T,K}$ is better approximated by a χ^2_{K-p} distribution than $Q^{\text{BP}}_{T,K}$. Fundamentally the two statistics differ only by the weighting applied to the autocorrelation lags, with the Ljung and Box statistic favoring higher-lag terms. This also explains the increased variance of the Ljung and Box statistic $Q^{\text{LB}}_{T,K}$. The Ljung-Box statistic is recommended whenever testing for higher-order correlation terms of the residual samples. However, in most practical cases the difference between the two is negligible.

A different whiteness test, first proposed in [80] and used extensively for model testing in [70, 71], supposes that under H_0:

$$|\rho_k| \leq 1.96\frac{\rho_0}{\sqrt{T}} \quad \text{for} \quad k \in \{\pm 1, \pm 2, \cdots, \pm(T-1)\}, \tag{C.6}$$

with about a risk of 5%. Thus, a simple and fast testing strategy is to compute the biased sample autocorrelation sequence from the residues and to count, excepting ρ_0, the number of autocorrelation terms that fall outside the bound imposed by Eq. (C.6). If this number of relative out-of-bound terms is grater than 5%, then the series is deemed correlated.

In [173] a whiteness test is proposed that circumvents the computation of the autocorrelation sequence ρ_k, by assessing the "flatness" of the residual spectrum. This implies the computation of the residual periodogram by means of the Fast-Fourier transform.

Appendix D

Proof of p-value $|H_0 \sim \mathcal{U}(0,1)$

Proposition. *p-values are uniformly distributed under the null hypothesis H_0.*

Proof. Considering the definition of p-values given in Eq. (C.5) we have:

$$p\text{-value} \triangleq Pr\{Q > Q_{T,K}\} = 1 - F_{\chi^2}(Q_{T,K}), \tag{D.1}$$

where Q is a random variable with a χ^2 distribution, $F_{\chi^2}(\cdot)$ being its distribution function.

Under the null hypothesis H_0, the residual series is white, also implying that $Q_{T,K}$ is χ^2 distributed. Hence considering the monotonic transformation $F_{\chi^2}(\cdot)$ we have:

$$Pr\{F_{\chi^2}(Q_{T,K}) \leq u|H_0\} = Pr\{Q_{T,K} \leq F^{-1}_{\chi^2}(u)|H_0\} = F_{\chi^2}\Big(\ F^{-1}_{\chi^2}(u)\Big) = u, \tag{D.2}$$

where $u \in [0,1]$. From Eq. (D.2) we observe that $F_{\chi^2}(Q_{T,K})|H_0 \sim \mathcal{U}(0,1)$. Thus, under H_0 the p-value is distributed as: p-value $= 1 - F_{\chi^2}(Q_{T,K})|H_0 \sim \mathcal{U}(0,1)$.

Note that Eq. (D.2) also represents the proof of the uniform transformation theorem [71, Ch. 3.3.1]. The result of this theorem is employed to generate samples with an arbitrary distribution $F.(\cdot)$, starting from a uniform random generator. This method is usually referred to as the percentile transformation method [171, Eq. 7-154].

■

Appendix E

Quadratic and Gaussian equalities

In this appendix, some general identities are given without proof, regarding the combination of quadratic terms and subsequently Gaussian densities. For symmetric and positive definite matrices $\mathbf{Q}$ and $\mathbf{R}$, the following equality holds

$$\begin{aligned}(\mathbf{z}-\mathbf{H}\mathbf{x}-\mathbf{d})^T\mathbf{R}^{-1}(\mathbf{z}-\mathbf{H}\mathbf{x}-\mathbf{d}) \;+\; & (\mathbf{x}-\mathbf{f})^T\mathbf{Q}^{-1}(\mathbf{x}-\mathbf{f}) = \\ & (\mathbf{x}-\mathbf{a})^T\boldsymbol{\Sigma}^{-1}(\mathbf{x}-\mathbf{a})+(\mathbf{z}-\mathbf{b})^T\mathbf{S}^{-1}(\mathbf{z}-\mathbf{b}), \quad \text{(E.1)}\end{aligned}$$

where

$$\begin{aligned}\boldsymbol{\Sigma}^{-1} &= \mathbf{H}^T\mathbf{R}^{-1}\mathbf{H}+\mathbf{Q}^{-1},\\ \mathbf{S} &= \mathbf{H}\mathbf{Q}\mathbf{H}^T+\mathbf{R},\\ \mathbf{a} &= \mathbf{f}+\boldsymbol{\Sigma}\mathbf{H}^T\mathbf{R}^{-1}(\mathbf{z}-\mathbf{H}\mathbf{f}-\mathbf{d}),\\ \mathbf{b} &= \mathbf{H}\mathbf{f}+\mathbf{d}.\end{aligned}$$

For a proof of Eq. (E.1), see [174, Ch 3.8]. Next, considering the Gaussian probability distribution function $\mathcal{N}(\mathbf{x};\boldsymbol{\mu},\boldsymbol{\Sigma})$ of argument $\mathbf{x}$, mean $\boldsymbol{\mu}$ and covariance $\boldsymbol{\Sigma}$, we can write

$$\mathcal{N}(\mathbf{z};\mathbf{H}\mathbf{x}+\mathbf{d},\mathbf{R})\,\mathcal{N}(\mathbf{x};\mathbf{f},\mathbf{Q}) = \mathcal{N}(\mathbf{x};\mathbf{a},\boldsymbol{\Sigma})\,\mathcal{N}(\mathbf{z};\mathbf{b},\mathbf{S}), \quad \text{(E.2)}$$

$$\int \mathcal{N}(\mathbf{z};\mathbf{H}\mathbf{x}+\mathbf{d},\mathbf{R})\,\mathcal{N}(\mathbf{x};\mathbf{f},\mathbf{Q})d\mathbf{x} = \mathcal{N}(\mathbf{z};\mathbf{b},\mathbf{S}). \quad \text{(E.3)}$$

The aforementioned identities are often employed in the derivation of the Kalman-filtering equations and for direct calculations of integrals involving Gaussian distributions.

Appendix F

On the distribution of random sums

In this appendix we introduce the Gaussian approximation employed for the distribution of random sums, such as encountered in the superpositional observation model. The following developments are valid for the classical superpositional models presented in [28], e.g. amplitude sensors or radio-tomography, as well as for the phased-array observation model. Here, we present the more general case of marked Poisson multi-target process, introduced in Sec. III.6.2 and Sec. IV.3.2, specific for the phased-array observation model.

Suppose the following Poisson multi-target process X and associated marked process $\widetilde{X}$, where the mark $s \in \mathbb{K}$ of a target $\mathbf{x} \in \mathbb{X}$ is distributed according to $s|\mathbf{x} \sim \mathcal{CN}(0, P(\mathbf{x}))$. Note that indices will be dropped in this section for better understanding. The phased-array observation model involves the superposing of individual target contributions as in the following random sum

$$\mathbf{z} = \sum_{\tilde{\mathbf{x}} \in \widetilde{X}} \mathbf{g}(\tilde{\mathbf{x}}).$$

Note that a white noise term has to be added in order to obtain the phased-array observation $\mathbf{y}$ of Sec. III.6.2. The random sum $\mathbf{z}$, where both the number of summation terms and their values are random, is approximated in Sec. III.6.3.b with a Gaussian distribution. In the following we are concerned with the probability distribution of the vector $\mathbf{z}$.

By Campbell's theorem ([93, Ch. 3.2] or [96, Ch. 2.6]) we have the moment-generating function of the random-sum vector $\mathbf{z}$

$$\mathbb{E}\{\mathrm{e}^{\omega^H \mathbf{z}}\} = \exp\left\{\int_{\mathbb{X}\times\mathbb{K}} \left(\mathrm{e}^{\omega^H \mathbf{g}(\tilde{\mathbf{x}})} - 1\right) \widetilde{D}(\tilde{\mathbf{x}}) d\tilde{\mathbf{x}}\right\}, \tag{F.1}$$

where $\widetilde{D}(\tilde{\mathbf{x}})$ is the intensity function of $\widetilde{X}$. Campbell's theorem holds for any complex $\omega \in \mathbb{C}$ whenever the right-hand side of Eq. (F.1) converges, and in particular whenever ω is imaginary. By using the relationship between the intensities of the marked and non-marked intensities, given in Eq. (III.29), we can write

$$\begin{aligned}
\mathbb{E}\{\mathrm{e}^{\omega^H \mathbf{z}}\} &= \exp\left\{\int_{\mathbb{X}}\int_{\mathbb{K}} \left(\mathrm{e}^{\omega^H \mathbf{a}(\tilde{\mathbf{x}})s} - 1\right) \mathcal{CN}(s; 0, P(\mathbf{x})) \widetilde{D}(\mathbf{x}) ds\, d\mathbf{x}\right\} \\
&= \exp\left\{\int_{\mathbb{X}} \left[\int_{\mathbb{K}} \mathrm{e}^{\omega^H \mathbf{a}(\tilde{\mathbf{x}})s} \mathcal{CN}(s; 0, P(\mathbf{x})) ds - 1\right] D(\mathbf{x}) d\mathbf{x}\right\} \\
&= \exp\left\{\int_{\mathbb{X}} \left[\mathrm{e}^{\frac{1}{2}\omega^H \mathbf{a}(\tilde{\mathbf{x}}) P(\mathbf{x}) \mathbf{a}^H(\tilde{\mathbf{x}})\omega} - 1\right] D(\mathbf{x}) d\mathbf{x}\right\},
\end{aligned}$$

where we have employed the moment-generating function of the Gaussian distribution of marks s. Next, by linearizing the inner exponential we obtain

$$\mathbb{E}\{\mathrm{e}^{\omega^H \mathbf{z}}\} \approx \exp\left\{\frac{1}{2}\omega^H \left[\int_{\mathbb{X}} \mathbf{a}(\tilde{\mathbf{x}}) P(\mathbf{x}) \mathbf{a}^H(\tilde{\mathbf{x}}) D(\mathbf{x}) d\mathbf{x}\right] \omega\right\}. \tag{F.2}$$

Observe that the right-hand side of Eq. (F.2) is the moment-generating function of a multivariate Gaussian distribution that is centered and has covariance matrix $\int_{\mathbb{X}} \mathbf{a}(\tilde{\mathbf{x}}) P(\mathbf{x}) \mathbf{a}^H(\tilde{\mathbf{x}}) D(\mathbf{x}) d\mathbf{x}$. Therefore:

$$\mathbf{z} \overset{appr.}{\sim} \mathcal{CN}\left(\mathbf{0}, \int_{\mathbb{X}} \mathbf{a}(\tilde{\mathbf{x}}) P(\mathbf{x}) \mathbf{a}^H(\tilde{\mathbf{x}}) D(\mathbf{x}) d\mathbf{x}\right). \tag{F.3}$$

In this appendix, the above Gaussian approximation is identified in terms of a first-order Taylor expansion of an exponential term in the characteristic function of $\mathbf{z}$. Although the results seems trivial, it appears that we are the first to express the approximation in such a manner. In light of this knowledge, higher-order approximations are theoretically possible. However, these are of little practical interest since they involve tensors.

Appendix G

Array narrow-band condition

In this appendix, the EdgeTech 4600 side-scan sonar array is presented and analyzed. The EdgeTech 4600 consists of an uniform linear array of $M = 8$ with a half of wavelength spacing. Since the phased array is relatively short, the pressure waves received at the M receives can be considered as plane waves. This can be seen from the Fraunhofer distance

$$d_F = \frac{2D^2}{\lambda} \approx 0.068\text{m}, \tag{G.1}$$

where λ is the wavelength and $D = 3.5\lambda$ is the phased-array length. Given the central frequency of the emitted pulse, the Fraunhofer distance is approximately of 7cm. For all practical purposes, the targets of interest are placed in the far-field domain of the antenna, that is, placed farther than 7cm from the phased array. In the available data sets, the objects of interest are placed at distances of at least 10m from the array. Therefore, in this work, we will suppose a plane-wave model for the phased-array signal. The signal or pulse emitted by the single emitter of the

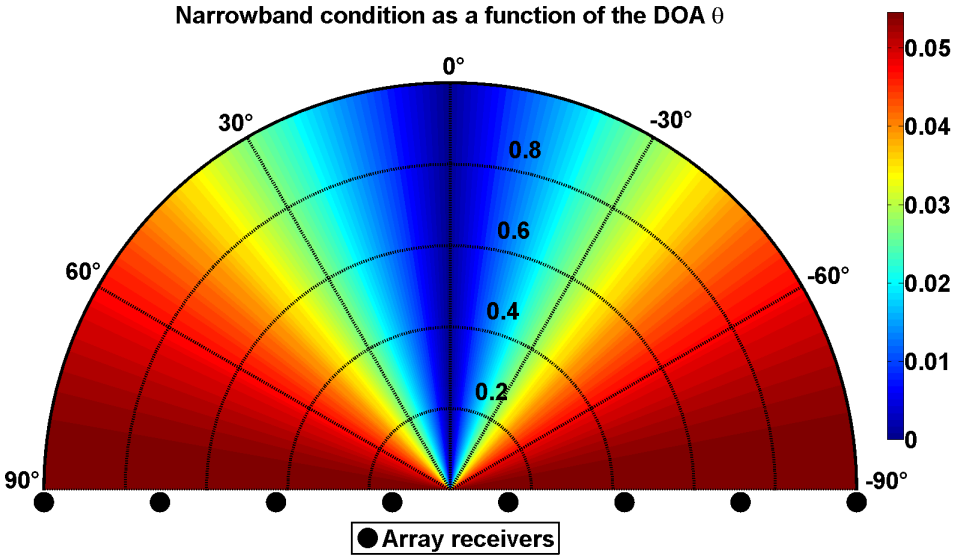

Figure G.1: The narrow-band condition as a function of the DOA θ. The array axis coincides with the abscissa axis. The color represents the condition number $\frac{D\sin(\theta)}{c}B$, which has to be much smaller than 1 for the narrow-band condition to hold.

EdgeTech 4600 sonar is a linear frequency modulated signal. In general target localization is achieved by the difference in arrival times of the target echo on the different array receives. Whenever the narrow-band condition is verified, the time difference of arrival of a source-signal is equivalent to a phase-difference between receiver signals. The narrow-band condition relates the bandwidth of the received signal to the array length, and is not to be mistaken with similarly-named conditions in communication theory where the ratio between bandwidth

and central frequency is employed. For a plane wave impinging the array with DOA θ, the narrow-band condition reads

$$\frac{D}{c}\sin(\theta) \ll \frac{1}{B}, \tag{G.2}$$

where c is the acoustic-wave celerity (typically 1500m/s in water). Stated differently, the narrow-band condition is met if the time needed by the acoustical wave to traverse the array is less than the inverse of the bandwidth of the basebanded signal. The above condition can be visualized in Fig. G.1, where we plotted the term $\frac{D\sin(\theta)}{c}B$ for each angle θ and the specific parameters of the EdgeTech 4600. The narrow-band condition is verified whenever $\frac{D\sin(\theta)}{c}B \ll 1$, which in our case is verified for all values of θ. Usually, only the limiting case of $\theta = 90^o$ is verified, since this corresponds to the longest possible distance traveled by the wave.

Appendix H

Statistical analysis of sonar signals

In this appendix we provide a statistical analysis of data samples acquired with the EdgeTech 4600 side-scan sonar. The analysis is carried out using graphical tools such as the Quantile-Quantile(QQ) plot [175], and with classical acceptance-rejection GoF tests [77, 169] such as the Kolmogorov-Smirnov (KS) and the Anderson-Darling (AD) tests. Tests are conducted on sonar signals acquired with the EdgeTech 4600 side-scan sonar in a shallow-water canal (depth varies between 15m and 20m), that exhibits multi-path propagation and reverberation - specifically reflections from the sea-surface. The sonar data is squired in a relatively flat and homogeneous sea-bottom. The phased-array signal is examined in two cases of interest: near and far range. The impulsive character of the signals is shown to change in relationship to the range, that is, the distance between the sonar and source of the signal. This dependence can also be reformulated in terms of the incidence angle between the incident wavefront and the normal to the target-surface. Incidence-angle dependencies of sonar-envelope distributions are explicitly modeled in [30–32] by using the K-distribution and a model for the shape parameter ν (see Eq. (IV.8)) as a function of the incidence angle. In [29], a K-distribution is fitted to sonar signals backscattered from a shipwreck, where an inverse relationship between the shape parameter ν and the signal SNR is observed. Despite the fact that in our work such dependencies are observed, we do not possess enough data to properly infer a model for the shape parameter ν. Therefore, in this work, we limit ourselves to showcasing the impulsive behavior of the phased-array data and to the fitting of a SIRV distribution. Incorporating an angular-dependent distribution is left as a perspective that can be easily integrated into the proposed processing chains.

The Quantile-Quantile (QQ) plot [175] provides a graphical goodness-of-fit assessment for the distribution of a *test sequence*, representing the phased-array observation $\mathbf{y}_t$. In other words, under hypothesis H_0 the test sequence obeys a hypothetical (theoretical) distribution, referred here as the H_0 distribution. The alternative hypothesis H_1, is chosen when there is sufficient evidence against H_0, that is, whenever the test sequence obeys a different distribution than the H_0 distribution. The QQ plot compares the (empirical) distribution of the test sequence with the H_0 distribution, by plotting their quantiles against each other in a Cartesian plot. Quantiles are values taken at regular intervals from the inverse function of the cumulative distribution function (CDF) of a random variable. For a given data set, in practice, quantiles are obtained by dividing the ordered-data set into q equally-sized subsets; with the quantiles being given by the data values marking the boundaries between the different subsets. While for the theoretical distribution, the quantiles are obtained by dividing the interval of $[0, 1]$ into q equally-sized subintervals and taking the values of the quantile function at the frontiers of these subintervals. If the two distributions being compared are similar, then the points of the QQ plot will approximately lie on the line $y = x$, i.e. the fist-quadrant bisector. Furthermore, whenever the two distributions are linearly related, the points in the QQ plot will form a straight line, but not necessarily the first bisector. Hence, the QQ plot can also be employed to estimate parameters in the location-scale family of distributions. The QQ plot is especially useful in assessing the matching of tails between the two distributions and in detecting the presence of outliers.

Observe the two QQ plots in Figs. H.1 a) and b) for the far-range case. The QQ plot

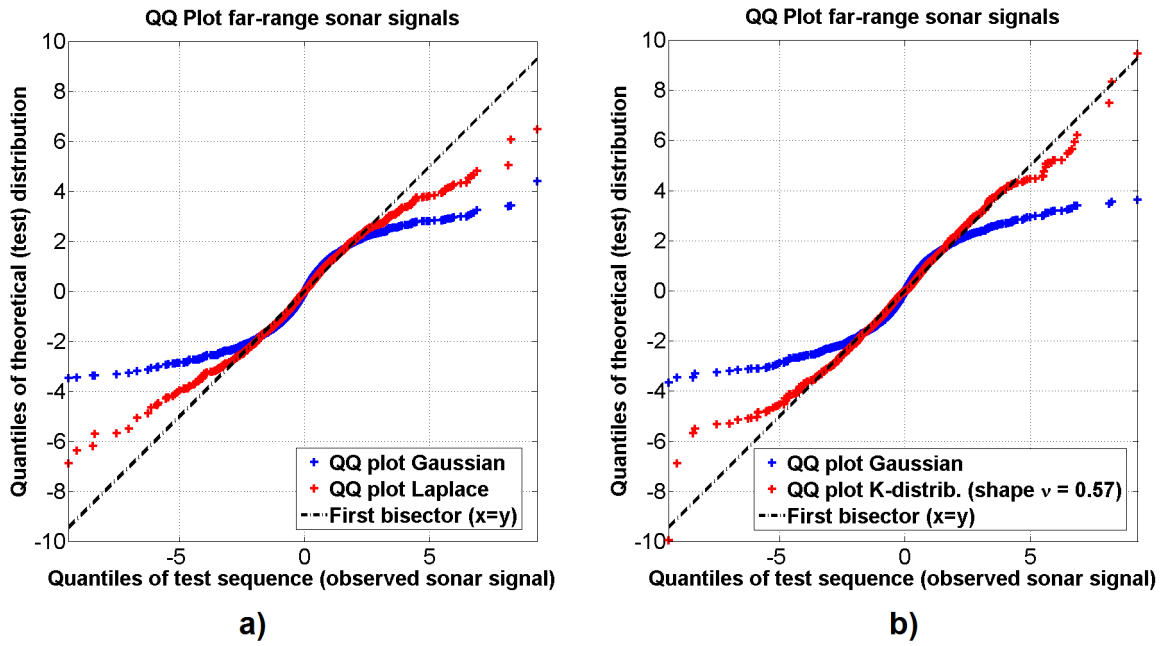

Figure H.1: QQ plot for far range: a) H_0 hypotheses are the Gaussian (blue) and the Laplace (red) distributions, b) H_0 hypotheses are the Gaussian (blue) and K-distributions (red).

of Fig. H.1 a) plots the quantiles of the test sequence against the quantiles of the Gaussian (in blue) and the Laplacian (in red) distributions. The test sequence is a data set containing univariate samples, e.g. the real part of the signal from one receiver of the sonar phased-array. Furthermore, the samples that form the test sequence are selected in order to insure the same environmental conditions, that is, the same range (receiver-source distance), the same sea-floor type, the same DOA. Note that all three distributions are standardized, that is, centered and scaled to have unitary variance. Additionally, the first-quadrant bisector is plotted for reference. A distribution provides a good fit to the test sequence, whenever the QQ plot points align with the first bisector. In the case of the Gaussian distribution, we notice the QQ-plot points forming an "S" shaped curve, highlighting the impulsive nature of the test sequence and the inadequacy of the Gaussian distribution. Having heavier tails than the H_0 distribution, the test sequence exhibits larger variations than the H_0 distribution, leading to an "S" shaped curve in the QQ plot. Also note from Fig. H.1 a) that the Laplace distribution seems to provide a better fit for the tails of the test-sequence distribution than the Gaussian. While in Fig. H.1 b) we can observe the same QQ plot with Gaussian distribution compared with the QQ plot with a K-distribution. Notice a better fit of the K-distribution than the Gaussian for the tails of the test sequence. The value of the K-distribution shape parameter $\nu = 0.57$ was estimated from the test-sequence by means of the method of moments as decried in [176].

Figs. H.2 a) and b) present QQ plots for the near-range case. Again the Laplace, showcased in Fig. H.2 a), and the K-distribution with $\nu = 0.67$ in Fig. H.2 b), present better candidates for the test-sequence distribution than the Gaussian distribution. Therefore, the Laplace and the K-distribution provide a good fit for the sonar data, both at near and at far range values. Regarding the choice of the K-distribution over the Laplace, some minor improvements are noticed in the tail sections of the distribution. However, note that a reliable estimation of ν requires at least 1000 data samples (for the univariate case), which limits the use of K-distributions in online algorithms without a physical model for the evolution of ν. This leads to a different issue, the lack of sufficient data to infer and validate such a model for ν. Various models for ν have been proposed in [30–32]. Ideally, a model of ν with the following parameters: the incidence angle

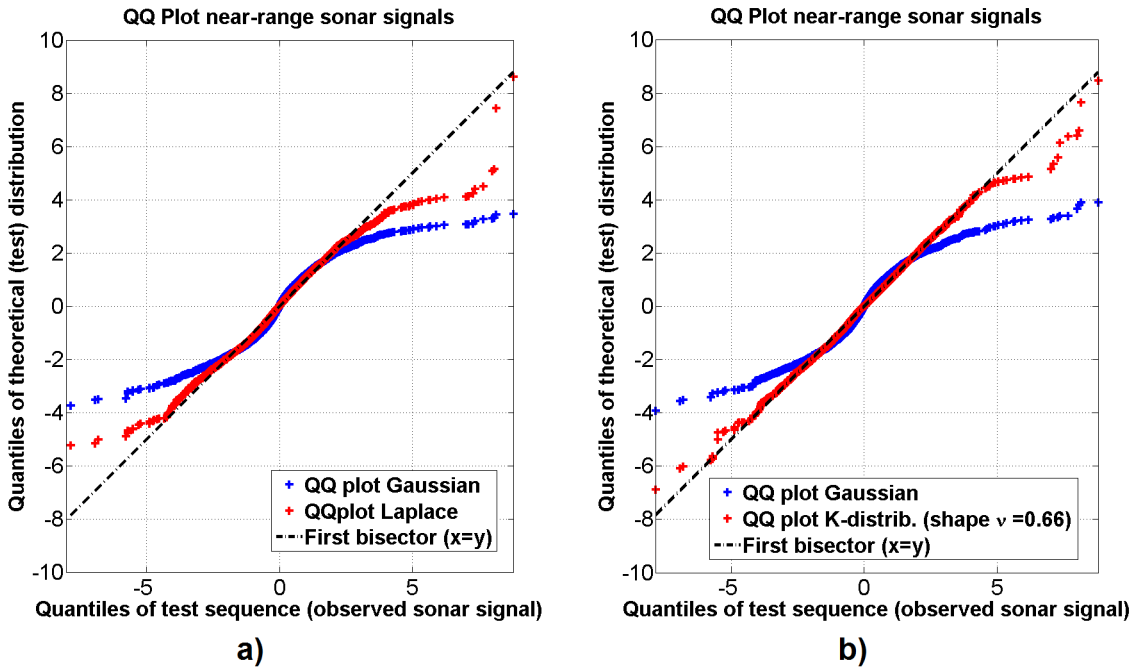

Figure H.2: QQ plot for near range: a) H_0 hypotheses are the Gaussian (blue) and the Laplace (red) distributions, b) H_0 hypotheses are the Gaussian (blue) and K-distributions (red).

(implicitly the DOA), the signal-to-noise ratio and type of sea-floor could be used to improve the efficiency of the online DOA estimators developed in this work. Such algorithms would effectively combine array-processing methods with shape-from-shading techniques [177–179], the latter being currently employed in radar/sonar to reconstruct 3D images from 2D amplitude images. Given that fluctuations of the estimated ν parameter around the value of $\nu = 1$ are observed, in this work we mainly employ the Laplace distribution as the array-data likelihood. The development of a model for ν is left as a perspective.

A quantitative goodness-of-fit analysis, for the Gaussian, Laplace and of the K-distribution, is performed with the Kolmogorov-Smirnov (KS) and Anderson-Darling (AD) tests. The AD test is a modified variant of the KS test that places greater weight on the observations in the tails of the distribution, thus making the test more sensitive to outliers and better at detecting departures from normality in the tails of the distribution [180]. Both AD and KS tests are conducted with three different H_0 distributions: Gaussian, Laplace and K-distribution. The tests are conducted on 2400 test sequences, each containing 400 (univariate) sonar data samples that were selected in the same manner as for the QQ plots. The data samples are selected in a mid-range area. Tests results are summarized in Table H.1, as the percentage of tests that accepted the H_0 distribution at a significance level of $\alpha = 0.05$.

From Table H.1 we observe that the Laplace and K-distribution hypotheses are accepted,

Table H.1: Statistical test results: percentage of tests that accept the H_0 distribution.

H_0 Distribution / Test	Gaussian	Laplace	K-dist.
Anderson-Darling [%]	1.04	84.63	86.75
Kolmogorov-Smirnov [%]	17.79	81.88	90.67

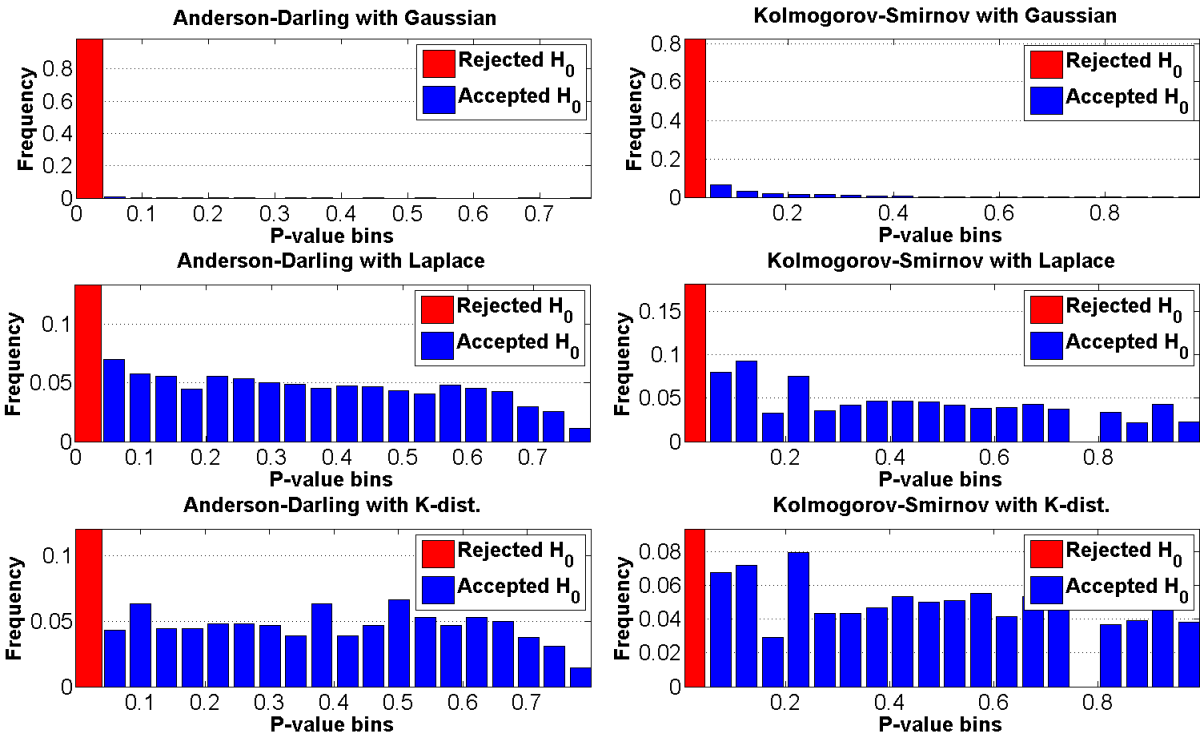

Figure H.3: $p-$value histograms for different tests.

that is, with $p-$values greater than the level of significance $\alpha = 0.05$. Considering the guidelines given in [170], rejection of the Gaussian hypothesis implies the definite inadequacy of the Gaussian distribution to fit the observation. However, the high-acceptance rates of the Laplace and K-distribution do not rule out the possibility of even better-adapted distributions. Distributions such as from the α-stable family are left as a perspective. The $p-$values obtained for each test and for the 6 combinations test-H_0 distribution from Table H.1, are summarized in $p-$value histograms presented in Fig. H.3. $p-$values are expected to be uniformly distributed under the H_0 hypothesis (see Appendix D and [83]). From Fig. H.3 we observe that the $p-$value histograms for the Laplace and K-distributions are relatively uniform, signaling their acceptance. However, the $p-$value histograms for the Gaussian hypothesis are highly non-uniform, again signaling the non-adequacy of the Gaussian distribution for the sonar data. Notice the red bin in all histograms representing the proportion of tests failing to accept the H_0 hypothesis, values which are also obtainable from Table H.1. Outliers account for having slightly taller red bins in the Laplace and K-distribution tests.

In conclusion, the impulsive character of sonar signal has been showcased and appropriate distributions have been proposed in the form of the multivariate Laplace and K-distributions, both part of the SIRV family of distributions. Accordingly, a joint-SIRV (Laplace or K-dist.) model has been proposed for the sonar phased-array likelihood function. Proper justifications of the joint-SIRV model are given for multi-path and echoic (i.e. reverberant) environments in Sec. IV.2.2.

Résumé

Dans ces travaux de doctorat, nous détaillons le problème de la poursuite de la direction d'arrivé (DOA) de cibles multiples avec un réseau d'antennes déphasées sous diverses hypothèses. Les méthodes développées dans ce doctorat sont appliquées au problème de la reconstruction bathymétrique (c'est-à-dire du fond-marin) pour des environnements portuaires. L'environnent portuaire est un environnent « encombré » et la reconstruction bathymétrique de cet environnement pose certaines problématiques, comme les trajets multiples ou la réverbération volumique et surfacique. Les méthodes classiques de traitement d'antennes sont mises en défaut par ces phénomènes induits par cet environnement particulier. Les différentes méthodes, détaillées dans les trois parties de cette thèse, incorporent graduellement des spécificités du signal sonar dans cet environnement. La première approche considère un nombre connu des cibles avec trajectoires déjà initialisées, et traite le problème de filtrage (autrement l'élimination des échos parasites) grâce à un post traitement. Un traitement complet, à partir du signal d'antenne, est proposé ensuite et considère un nombre inconnu et fluctuant de cibles. Le filtre proposé est capable d'estimer le nombre de cibles présentes ainsi que leur positionnement directement à partir du signal d'antenne (sans formation de voies). Dans une troisième partie, une amélioration de l'estimation du nombre des cibles est proposée pour ce filtrage. L'étalement angulaire des cibles sonar (le fond) et la nature impulsionnelle des signaux sonar sont pris en compte dans cette dernière approche. Nous démontrons que l'approche de poursuite multi-échos développée dans ce travail, répond au besoin de reconstruction bathymétrique en présence des interférences observées en milieu portuaire. Les solutions proposées sont testées sur des données sonar bathymétrique acquises dans le port des Everglades en Floride.

Mots-clés : Traitement adaptatif du signal, Traitement d'antennes, Sonar, Estimation de directions d'arrivées, Pistage multi-cibles, Filtrage PHD, Reconstruction d'image en 3D, Bathymétrie

Abstract

In this thesis, we consider the problem of tracking the direction of arrival (DOA) of multiple targets with phased arrays. Different methods are proposed and applied to bathymetry reconstruction in port and canal areas. Bathymetry represents an underwater depth map, that is, a 3D image of the underwater relief, which is obtained by processing sonar phased array data. Port and canal areas pose new challenges, such as multi-path propagation and reverberation, which for classical array processing methods lead to numerous "spurious" DOA estimates (i.e. false detections). The proposed methods are detailed in the three parts of this thesis and gradually incorporate different characteristics of the sonar array signal. The first approach considers a known number of already initialized target trajectories and considers filtering (i.e. the elimination of false detections) as a post processing step. A complete processor is proposed next, that considers an unknown and fluctuant number of targets. The proposed filter is capable of estimating adaptively the number of targets and also their positions, i.e. state vectors. In the third part of this thesis, an improved estimator for the number of targets is considered and the sonar signal model is extended to include angularly distributed targets and impulsive non-Gaussian signals. We show that the multi-target tracking filters proposed in this work solve the problem of bathymetry reconstruction in presence of interfering echoes generated by multi-path and reverberation. The proposed filters are tested on real sonar data acquired in the Everglades Port in Florida, USA.

Keywords : Adaptive signal processing, Array processing, Sonar, Direction of arrival estimation, Multi-target tracking, PHD filter, 3D image reconstruction, Bathymetry

TELECOM Bretagne

n° d'ordre : 2015telb0379
Télécom Bretagne
Technopôle Brest-Iroise - CS 83818 - 29238 Brest Cedex 3
Tél : + 33(0) 29 00 11 11 - Fax : + 33(0) 29 00 10 00